Lattice Boltzmann Simulation of Laminar and Turbulent Two-Phase Flows

Dissertation
zur Erlangung des akademischen Grades

Doktoringenieur
(**Dr.-Ing.**)

von: M.Sc. Amir Eshghinejadfard
geb. am 06. April 1983 in Arak
genehmigt durch die Fakultät für Verfahrens- und Systemtechnik
der Otto-von-Guericke-Universität Magdeburg

Promotionskommission:

Prof. Dr.-Ing. Evangelos Tsotsas
Prof. Dr.-Ing. Dominique Thévenin
Prof. Dr.-Ing. Martin Sommerfeld
Prof. Dr. Berend van Wachem

eingereicht am: 15. Mai 2017

Promotionskolloquium am: 16. November 2017

To my family

Acknowledgements

Along the journey of my studies at University of Magdeburg, I have been encouraged, supported and inspired by many people. Here, I would like to take this opportunity to express my thanks to them for their contribution to the development and completion of this thesis.

First and foremost, I would like to thank my supervisor, Prof. Dominique Thévenin for his consistent support throughout my PhD study, for his patience, motivation, and immense knowledge. It has been a great honor to work under his supervision during these years. Without his passionate help and participation, the completion of this work could not have been successfully conducted. I also would like to acknowledge Dr. Gábor Janiga for his help and guidance in CFD and computer science discussions.

In my daily work I have been blessed with a friendly and scientific atmosphere beside my colleagues at the Institute of Fluid Dynamics and Thermodynamics, University of Magdeburg. Here, I thank them all for support and scientific discussions.

I also appreciate the financial support of the DFG graduate college of “micro-macro-interactions in structured media and particle systems” and International Max-Planck Research School of Magdeburg during this research work.

Last but not least, I must express my very profound gratitude to my wife, Bahar, and my parents, for their consistent support and encouragement throughout my study and research.

Magdeburg,
May 2017 Amir Eshghinejadfard

Declaration

I hereby declare that I prepared the submitted work without inadmissible assistance and without the use of any aids other than those indicated. Facts or ideas taken from other sources, either directly or indirectly have been marked as such.

In particular, I did not use the services of a commercial graduation consultation. Furthermore, I have not made payments to third parties either directly or indirectly for any work connected with the content of the submitted dissertation.

This work has so far not been submitted either in Germany or abroad in same or similar form as a dissertation and has also not yet been published as a whole.

Magdeburg, May, 2017

Amir Eshghinejadfard

Abstract

Multiphase flows are present in many natural and industrial processes including filtration, pollution control, pharmaceutical applications, food industry and fluidized bed reactors. Experimental investigation of such flows, although interesting and ideal, is often associated with many difficulties in constructing and running the set-up. High investment cost is another issue of experimental studies. During the recent years, the computational power of computers has continually and exponentially grown. This provides the researchers with a fertile region for numerical investigation of multiphase flows. In numerical simulation, a variety of geometries with different configurations can be examined. Beside the importance of multiphase flow modeling, another motivation for this dissertation was to use an alternative for classical Navier-Stokes based solvers. Lattice Boltzmann method (LBM) is proven as a profound and robust model since its introduction three decades ago.

This dissertation aims at developing a lattice Boltzmann solver (ALBORZ) for various solid-liquid two-phase flows. The main focus would be on particulate flows and the fluid flow among porous structures. In this regard, both laminar and turbulent flows are considered and non-isothermal applications are studied as well. The dissertation includes seven chapters which can be summarized as follows.

In Chapter 1, the importance of multiphase flow modeling will be presented. A short review on different types of particulate flows and the importance of LBM in CFD studies will be given as well. The complete plan of this dissertation is summarized in the last part of this chapter.

Chapter 2 reviews the fundamentals and the equations of LBM, starting with a brief historical background of the model and explaining the contributions in the model in the last thirty years. Afterwards, the Boltzmann transport equation and single relaxation time model are presented. Comparison of single relaxation time LBM with classical Navier-Stokes based solvers is another topic covered in this chapter. The advantages and shortcomings of single relaxation time-LBM are thoroughly reviewed. Finally, multi-relaxation time LBM is discussed in this chapter.

The theory and applications of developed LB solver for laminar particle-laden flows is presented in Chapter 3. The immersed boundary method (IBM), which takes the particle-fluid interactions into account is explained and the equations are given. Afterwards, particle position update method, collision models, the influence of force term in LB equations and numerical algorithms are presented. Finally, the code is validated for numerous applications of single and multiple solid rigid particles against the results from experiments and other numerical models. Both 2D and 3D cases are modeled and the effect of particle shape is tested as well.

Since many multiphase flows occur in a non-isothermal state, the heat transfer effect on particle motion needs a careful and complete study. This issue is covered in Chapter 4. The formulation of the non-isothermal model and treatment of heat source term are first presented. For numerical validation, stationary and moving particles with constant or varying temperature are modeled. Again, both circular and spherical particles are taken into account. Finally, various applications of the model are introduced in which heat transfer to/from particles can significantly alter the behavior of the particles. This effects depend on many parameters including Grashof number, Prandtl number and fluid/particle properties.

Flow in porous media is covered in Chapter 5. Different configurations including a face-centered and a body-centered cube together with a real geometry reconstructed from CT images are successfully modeled and the effect of multi-relaxation time LBM on the permeability is investigated.

Chapter 6 is devoted to the simulation of particle-laden turbulent channel flows with spherical particles. In this respect, turbulent flow in a straight channel is seeded with multiple spherical particles. It is shown that particles can change the characteristics of the flow. Particles concentration belongs to the dense regime. It is checked how mean flow velocity, its rms and particle distribution vary with the distance from the wall. Vortex structures change noticeably in the presence of particles.

In many practical applications, particle shape is not spherical. Therefore, Chapter 7 concerns the simulation of spheroidal particles in both laminar and turbulent flows. It includes introducing a new method for distribution of Lagrangian points on particle surface and using quaternions for updating particle rotational velocity. A validation case for rotation of an ellipsoid in a Couette flow is given. The influence of multiple particles on a turbulent channel flow is investigated and compared to the results of spherical particles.

This dissertation is concluded with a summary, recommendations, and outlook which are presented in Chapter 8. The main contributions and novelties contained in this work are listed below:

Highlights and main contributions:

- Development of a new LBM tool that can accurately handle different laminar and turbulent two-phase flows;
- Using LBM to simulate the motion of circular, elliptical, spherical and spheroidal particles in laminar flows;
- Developing a non-isothermal LBM tool to model the motion of fully-resolved particles by considering complete particle-particle and particle-fluid interactions;
- Presenting the immersed boundary-lattice Boltzmann simulation of turbulent particle-laden pressure-driven flows;
- Extending a model to investigate the behavior of ellipsoid particles based on IB-LBM;

Keywords: Lattice Boltzmann method, Immersed boundary method, Particle-laden flow, Porous media; Direct numerical simulation

Zusammenfassung

Mehrphasenströmungen finden in vielen natürlichen und industriellen Prozessen statt, einschließlich Filtration, Verschmutzungssteuerung, pharmazeutischen Anwendungen, Nahrungsmittelherstellung und Wirbelschichtreaktoren. Die experimentelle Untersuchung solcher Strömungen wird angestrebt, sie ist jedoch oft mit vielen Schwierigkeiten bei der Konstruktion und Durchführung verbunden. Hohe Investitionskosten sind ein weiteres Problem experimenteller Studien. In den letzten Jahren ist die Rechenleistung von Computern kontinuierlich und exponentiell gestiegen. Dies bietet eine gute Grundlage für die numerische Untersuchung von Mehrphasenströmungen. In der numerischen Simulationen können mehrere Geometrien mit unterschiedlichen Konfigurationen untersucht werden. Neben der Bedeutung der mehrphasigen Strömungsmodellierung bestand eine weitere Motivation für diese Dissertation darin, eine Alternative für klassische Navier-Stokes-basierte Löser zu verwenden. Die Lattice-Boltzmann-Methode (LBM) ist seit ihrer Einführung vor drei Jahrzehnten ein vielversprechender und robuster Ansatz.

Diese Dissertation zielt auf die Entwicklung eines Lattice-Boltzmann-Lösers (ALBORZ) für verschiedene Partikel-Fluid-Zweiphasenströme ab. Der Schwerpunkt liegt dabei auf den Partikelströmungen und dem Fluidstrom innerhalb von porösen Strukturen. In dieser Hinsicht werden sowohl laminare als auch turbulente Strömungen betrachtet und auch nicht-isotherme Anwendungen untersucht. Die Dissertation enthält sieben Kapitel, die sich wie folgt gliedern.

In Kapitel 1 wird die Bedeutung der LBM für Mehrphasenströme vorgestellt. Ein kurzer Überblick über den Stand der Technik wird ebenfalls gegeben. Die vollständige Zielstellung dieser Dissertation ist im letzten Teil dieses Kapitels zusammengefasst.

Kapitel 2 prüft die Grundlagen und die Gleichungen der LBM, beginnend mit einem kurzen historischen Hintergrund des Modells, und erklärt ferner die Weiterentwicklungen in den letzten Jahren. Danach werden die Boltzmann-Transportgleichung sowie das *single relaxation time* (SRT) Modell dargestellt. Der Vergleich von SRT-LBM mit klassischen Navier-Stokes-basierten Lösers ist ein weiteres Thema in diesem Kapitel. Die Vor- und Nachteile dieses Modells werden sorgfältig überprüft. Schließlich wird die *multi-relaxation time* (MRT)-LBM in diesem Kapitel diskutiert.

Die Theorie und Anwendungen des entwickelten LB-Lösers für laminare partikelbeladene Strömungen werden in Kapitel 3 ausführlich dargestellt. Die Immersed-Boundary-Methode, die die Partikel-Fluid-Wechselwirkungen berücksichtigt, wird erläutert und die Gleichungen aufgelistet. Anschließend werden das Verfahren zur Aktualisierung der Partikelposition, das Kollisionsmodell, der Einfluss des Kraftterms in den LB-Gleichungen und der numerische Algorithmus behandelt. Schließlich wird der Code für zahlreiche Anwendungen einzelner und mehrerer Partikel mit den Ergebnissen von Experimenten und anderen numerischen Modellen validiert. Sowohl 2D als auch 3D-Fälle werden modelliert und die Wirkung der Partikelform wird ebenfalls untersucht.

Da viele Mehrphasenströmungen in nicht-isothermen Prozessen auftreten, erfordert die Auswirkung der Wärmeübertragung auf die Partikelbewegung eine sorgfältige und umfassende Untersuchung. Dieses Problem wird in Kapitel 4 behandelt. Die Formulierung des nicht-isothermen Modells für den Wärmequellen-Term werden vorgestellt. Zur numerischen Validierung werden stationäre und sich bewegende Partikel mit konstanten oder variablen Temperaturen modelliert. Auch hier werden sowohl kreisförmige als auch sphärische Partikel berücksichtigt. Schließlich werden verschiedene Anwendungen des Modells eingeführt, bei denen der Wärmeübergang zu/von Partikeln deren Verhalten signifikant verändern kann. Diese Effekte hängen von vielen Parametern ab, z.B. der Grashof-Zahl, der Prandtl-Zahl und den Fluid- und

Partikeleigenschaften.

Die Durchströmung poröser Medien ist in Kapitel 5 enthalten. Es werden verschiedene Konfigurationen, einschließlich eines flächenzentrierten und eines körperzentrierten Würfels zusammen mit einer aus CT-Bildern rekonstruierten, realen Geometrie, erfolgreich modelliert und der Effekt der MRT-LBM auf die Permeabilität untersucht.

Kapitel 6 befasst sich mit der Simulation partikelbeladener turbulenter Kanalströme. Hier werden in die turbulente Strömung eines Kanals mehrere sphärische Partikel eingebracht. Es zeigt sich, dass die Partikel die Eigenschaften der Strömung verändern können. Die Partikelkonzentration ist hoch und gehört zum dichten Regime. Die mittlere Strömungsgeschwindigkeit, deren mittlere Quadratwurzel und die Partikelverteilung hängen vom vertikalen Abstand zur Wand ab. Die Wirbelstruktur zeigt große Veränderungen, wenn Partikel vorhanden sind.

In vielen praktischen Anwendungen ist die Partikelform nicht sphärisch. Daher behandelt Kapitel 7 die Simulation von Ellipsoidpartikeln sowohl in laminaren als auch in turbulenten Strömungen. Es beinhaltet die Einführung einer neuen Methode für die Verteilung der Lagrange-Punkte auf der Partikeloberfläche und die Verwendung von Quaternionen für die Aktualisierung der Rotationsgeschwindigkeit der Partikel. Ein Validierungsfall für die Rotation eines Ellipsoids in einer Couette-Strömung ist gegeben. Der Einfluss mehrerer Partikel auf einen turbulenten Kanalfluss wird untersucht und mit den Ergebnissen von sphärischen Partikeln verglichen.

Diese Dissertation schließt mit einer Zusammenfassung, Empfehlungen und einem Ausblick in Kapitel 8. Die wichtigsten Beiträge und Neuheiten in dieser Arbeit sind nachfolgend aufgelistet:

Wesentliche Inhalte und Neuerungen:

- Entwicklung eines neuen LBM-Lösers (ALBORZ), welcher verschiedene laminare, turbulente und zweiphasige Strömungen modellieren kann;
- Verwendung der LBM zur Simulation der Bewegung von kreisförmigen, elliptischen und sphärischen Partikeln in laminaren Strömungen;
- Entwicklung eines nicht-isothermen LBM-Lösers zur Modellierung der Bewegung voll aufgelöster Partikel unter Berücksichtigung vollständiger Partikel-Partikel- und Partikel-Fluid-Wechselwirkungen;
- Einführung der IB-LBM Simulation turbulenter Druckströmung mit Partikeln;
- Modellerweiterung zur Untersuchung des Verhaltens von Ellipsoidpartikeln auf Basis von IB-LBM;

Schlüsselwörter: Lattice-Boltzmann-Methode, Immersed-Boundary-Methode, Partikel, Poröses Medium, Direkte-Numerische-Simulation

Contents

List of Tables

List of Figures

Nomenclature

Roman Symbols

a	particle (major) radius	[m]
B	blockage ratio	[-]
b	particle minor radius	[m]
b_f	body force	[N/m^3]
c_0	Kozeny-Carman factor	[-]
$\boldsymbol{c}_i$	lattice speed in direction i	[m/s]
c_{ij}	force scale of collision	[N]
cir_factor	parameter for point distribution on spheroid	[-]
$C_{p,f}$	specific heat of fluid	[J/(kg.K)]
$C_{p,p}$	specific heat of particle	[J/(kg.K)]
$C_{p,r}$	specific heat ratio	[-]
c_s	sound speed	[m/s]
D	diameter	[m]
$D(x)$	delta function at x	[-]
D_f	degree of freedom	[-]
d'_i	distance of i^{th} particle to an imaginary particle	[m]
d_{ij}	distance between i^{th} and j^{th} particle	[m]
d_p	particle diameter	[m]
D_s	dimension of the space	[-]
E	total energy	[J]
e	internal energy	[J]
E_p	second stiffness factor for particle-particle collision	[-]
E_w	second stiffness factor for particle-wall collision	[-]
$\mathbf{f}$	tensor of distribution function in MRT	[-]
$\boldsymbol{F}$	force vector	[N]
$\boldsymbol{f}$	force density vector	[N/m^3]
f	particle distribution function	[-]
f'	post-collision distribution function	[-]
$\boldsymbol{F}_B$	buoyancy force	[N]
$\boldsymbol{F}^c$	collision force	[N]
$\boldsymbol{f}_f$	force vector in MRT	[N/m^3]

f_i	distribution function in direction i	[-]
F_s	reduced form of distribution function	[-]
$\boldsymbol{g}$	gravity	[m/s^2]
G	channel flow driving force	[N/m^3]
G	shear rate	[1/s]
g	temperature distribution function	[-]
$\mathcal{H}$	Hamiltonian	[-]
H	channel half-height	[m]
I	mass moment of inertia	[kg.m^2]
k	permeability	[m^2]
k_B	Boltzmann constant	[J/K]
L	domain length	[m]
L_{ch}	characteristic length	[m]
L_e	fluid travel path length	[m]
$\mathbf{M}$	transformation matrix in MRT	[-]
$\mathbf{m}$	moment tensor in MRT	[-]
M	mass	[kg]
M	transformation matrix from inertial to body-fixed frame	[-]
N	number of particles	[-]
n	n^{th} time step	[-]
N_A	Avogadro's number	[-]
N_l	number of Lagrangian points	[-]
nps	number of points per each strip of spheroid	[-]
$\boldsymbol{p}$	linear momentum	[kg.m/s]
p	pressure	[Pa]
$\boldsymbol{q}$	molecule position vector	[m]
Q	Q-criterion	[1/s^2]
Q	exchanged heat	[J]
q_0, q_1, q_2, q_3	quaternions	[-]
R	ideal gas constant	[J/(mol.K)]
R	radius	[m]
$\mathbf{S}$	diagonal matrix of relaxation times in MRT	[-]
$\boldsymbol{S}$	surface control	[-]
S	surface area	[m^2]
s	strain rate	[-]
$\boldsymbol{T}$	Torque	[N.m]
T	temperature	[C]
T	tortuosity	[-]
t	time	[s]
t^*	non-dimensional time	[-]

T_r	rotation period	[s]
$\boldsymbol{U}$	velocity	[m/s]
$\boldsymbol{u}$	velocity vector	[m/s]
$\overline{U}$	mean velocity in porous media	[m/s]
U	particle settling velocity value	[m/s]
$\boldsymbol{U}^d$	desired velocity	[m/s]
u_{mag}	velocity magnitude	[m/s]
$\boldsymbol{v}$	peculiar velocity	[m/s]
$\boldsymbol{v}$	shifted velocity vector in Shan-Chen model	[m/s]
V	volume	[m^3]
V_s	normalization vector	[-]
W	width	[m]
W_i	weight coefficient in direction i	[-]
$\boldsymbol{x}$	position vector	[m]
X	main flow direction in porous media	[-]
$\boldsymbol{X}$	position vector	[m]

Greek Symbols

α	parameter for point distribution on spheroid	[-]
α	thermal diffusivity	[m^2/s]
β	thermal expansion coefficient	[1/K]
δ	Kronecker delta	[-]
Δh	grid size	[m]
$\Delta\rho$	particle and fluid density difference	[kg/m^3]
ΔT	temperature difference	[C]
Δt	time step	[s]
ΔS_l	length or area of particle segment	[m, m^2]
Δx	grid size in x direction	[m]
ε_p	stiffness factor for particle-particle collision	[-]
ε_w	stiffness factor for particle-wall collision	[-]
$\boldsymbol{\zeta}$	lattice particle velocity	[m/s]
ζ	repulsive force range	[m]
θ	Euler angle	[rad]
θ	orientation angle of particle	[rad]
θ	parameter for point distribution on spheroid	[-]
κ	von Kármán constant	[-]
λ	particle aspect ratio	[-]
λ	relaxation time	[s]
μ	fluid dynamic viscosity	[Pa·s]
μ'	bulk viscosity	[Pa·s]

ν	fluid kinematic viscosity	[m^2/s]
$\boldsymbol{\xi}$	microscopic particle velocity	[m/s]
ρ	density	[kg/m^3]
ρ_r	density ratio	[-]
$\boldsymbol{\sigma}$	fluid stress tensor	[Pa]
σ'	deviatoric stress	[Pa]
τ	relaxation time	[-]
τ	stress	[Pa]
τ_P	particle-induced stress	[Pa]
τ_p	particle response time	[s]
ϕ	Euler angle	[rad]
ϕ	porosity	[-]
ϕ	solid phase volume fraction	[-]
$\boldsymbol{\Phi}$	mass loading	[-]
ψ	Euler angle	[rad]
$\boldsymbol{\Omega}$	rotational speed	[rad/s]
Ω	collision operator	[-]
ω_i	vorticity field	[1/s]
ω_i	non-dimensional weight coefficient in direction i	[-]

Non-dimensional Parameters

Ga	Galileo number
Gr	Grashof number
Ma	Mach number
Nu	Nusselt number
Pr	Prandtl number
Ra	Rayleigh number
Re	Reynolds number
St	Stokes number

Subscripts and Superscripts

B	Boussinesq
b	bulk
c	center
c	cold
c	collision
ch	characteristic
cyl	cylinder
d	desired
eq	equilibrium
f	fluid

g	temperature field LB property
h	hot
i	i^{th} discrete velocity
K	Kolmogorov
l	Lagrangian
maj	major
N	number of particles
n	time step
noF	no force
noH	no heat
p	particle
R	Reynolds
r	particle to fluid property ratio
ref	reference value
T	terminal value
V	viscous
w	wall
x, y, z	Cartesian coordinate system directions
τ	friction

Abbreviations

ALE	Arbitrary Lagrangian-Eulerian
BBGKY	Bogoliubov, Born, Green, Kirkwood, Yvon
BCC	Body-centered cube
BGK	Bhatnagar, Gross, Krook
CFD	Computational Fluid Dynamics
CT	Computed tomography
DDF	Double distribution function
DEM	Discrete element method
DF	Direct forcing
DKT	Drafting, kissing, tumbling
DLM	Distributed Lagrange multiplier
DNS	Direct numerical simulation
EDF	Equilibrium distribution function
FCC	Face-centered cube
FDM	Fictitious domain method
FHP	Frisch, d'Humières, Hasslacher
HSB	Higuera, Succi, Benzi
IBM	Immersed boundary method
LB	Lattice Boltzmann

LBE	Lattice Boltzmann equation
LBM	Lattice Boltzmann method
LES	Large eddy simulation
LGA	Lattice gas automata
LGCA	Lattice gas cellular automata
LH	Lower half
LHS	Left hand side
MKM	Moser, Kim, Mansour
MPI	Message passing interface
MRT	Multi-relaxation time
NS	Navier-Stokes
PDF	Particle distribution function
PDF	Probability density function
RHS	Right hand side
rms	root mean square
SRT	Single relaxation time
TKE	Turbulent kinetic energy
UH	Upper half
VK	Vreman, Kuerten

Chapter 1

Introduction

1.1 Motivation and objective

Multiphase flows are common in a wide range of industrial applications and environmental processes. Examples include sediment transport, aerosols, pulp and paper industry, crystallization and pharmaceutical processes. Multiphase flows can be classified according to the state of different phases or components. Hence, gas/solids flows, liquid/solids flows, or bubbly flows can be identified. Exact prediction of fluid flow behavior is central to the efficiency of these processes. Three approaches are usually used in this respect: 1) experimental studies, which need laboratory equipment, 2) theoretical modeling, based on mathematical equations and models for the flow, 3) computational studies, using the computing power of modern computers to explore the problem. Experimental studies are often expensive and may need special equipment. Theoretical studies are mainly limited to very simple geometries. For complex geometries or turbulent regimes, an analytical formulation is almost impossible to achieve. Due to enhanced computational power, numerical simulation is getting more and more important.

With respect to numerical studies, multiphase flows are first classified based on the interface of two phases, like *dispersed* or *separated* flows. In dispersed flows, particles or droplets are distributed in a connected volume of the continuous phase. Separated flows include two or more continuous streams of different fluids which are separated by interfaces; like those happen in free-surface flows. Two main types of dispersed phase models are usually identified: *trajectory models* and *two-fluid models*. In trajectory models, the motion of the dispersed phase is modeled by following the motion of particles. This type of modeling is also called the Lagrangian approach. If solid particles are used, each particle can be a *point* or a *fully-resolved* particle. Different terms for drag, lift and moment forces are either accurately calculated or appropriate correlations are used. On the other hand, in two-fluid models (the Eulerian approach), the dispersed phase is treated as a second continuous phase that is interacting with the first, continuous phase. Relevant equations of mass, momentum, and energy are written for the flow. The discrete nature of the disperse phase is neglected in this case [1].

Due to the wide and straightforward application of the trajectory model for finite-size particles, it is used in this thesis for the simulation of particle-laden flows; with the emphasis on solid particles dispersed in a fluid flow. In this regard, the volume fraction of the dispersed phase, ϕ, and its mass loading Φ are the two main parameters that determine the level of interaction between the phases. When both values are small, the carrier flow has the dominant effect on the dynamics of the dispersed phase (i.e., one-way coupled). When the mass of the dispersed phase is comparable with that of the carrier phase, the back-influence of the dispersed phase on the carrier-phase dynamics cannot be ignored (i.e., two-way coupled). By a further increase of ϕ, the interactions between particles (such as collisions) cannot be neglected and this regime is described as four-way coupling [2, 3].

This study was started after completion of several experimental projects considering the possibility of drag reduction in a turbulent flow by addition of elongated particles. Therefore, a solver was needed to take into account large non-spherical particles in a turbulent flow. For this purpose, the lattice Boltzmann method (LBM) appeared to be attractive. On the way toward understanding ultimately drag reduction- an objective not reached yet in this thesis and left for future studies- a variety of challenges were encountered and successfully solved. Additional applications, even if slightly out of focus, become possible, and have been considered as well in this study.

Numerical simulation of finite-size particles in four-way coupled regimes is often very challenging and demands high computational time and power even at small fractions of solid phase. Most of the studies in this regard are based on Navier-Stokes (NS) solvers. During the last three decades, the lattice Boltzmann method has evolved as a robust alternative for classical Navier-Stokes equations. The LBM was originally developed as an automaton for fluid systems. It has been later obtained from the Boltzmann transport equation with a single relaxation time collision operator. At the macroscopic level, it has been shown to recover the Navier-Stokes equations in the limit of weakly compressible flow. In LBM, the data are only exchanged with the first neighbors. Thus, LBM is highly adequate for parallel computing. This has increased LBM applications in different flow regimes and configurations. Therefore, LBM is used here to simulate finite-size particles in fluid flows. In addition to particle-laden flows, fluid flow in porous structures and complex geometries is modeled here by LBM.

1.2 Thesis outline

This thesis describes some contributions in the simulation of laminar and turbulent two-phase flows using LBM. All studies are performed with an in-house LB solver (ALBORZ) developed by myself since 2013 at the Laboratory of Fluid Dynamics and Technical Flows (LSS), University of Magdeburg. High-efficiency computations in terms of CPU time and memory have been conducted with ALBORZ. The code can model both 2D and 3D configurations on a parallel architecture. Most of the simulations of porous structures and turbulent particulate flows could not be achieved without the parallelized structure of the code. After this *Introduction*, the thesis continues with a description of the lattice Boltzmann approach.

Chapter 2 (*Lattice Boltzmann Method*) contains an introduction into lattice Boltzmann method. The chapter encompasses the historical background of the model, its importance, advantages and disadvantages, governing equations and description of single- and multi-relaxation time models. This chapter also justifies the reason behind using a specific type of LB configuration in the following chapters.

Chapter 3 (*Laminar Particulate Flows*) deals with the simulation of fully-resolved rigid particles in laminar fluid flows. The study includes both circular and elliptical particles in 2D, and spherical particles in 3D configurations. The immersed boundary method (IBM) handles fluid-particle interactions. Newton's equation of motion, particles' collision approach and LBM with force term are the other topics covered in this chapter. It ends with multiple validation and application cases.

Chapter 4 (*Non-isothermal Particulate Flows*) presents the extension of our LB tool to non-isothermal applications. Heat exchange between particles and the fluid is modeled in this chapter. This extension is another contribution of this thesis that is of great importance to many practical applications, like the motion of catalyst particles. This chapter includes the formulation of thermal IB-LBM, the method of updating particle temperature for both equal and unequal particle and fluid heat capacities. Different particle shapes are modeled, where particles have constant or varying temperature.

Chapter 5 (*Porous Media Flow*) aims to develop and demonstrate the robustness of LBM for complex geometries like porous structures. Locality of calculations is the main feature that makes the LBM suitable for these type of geometries. This chapter will use three different schemes to predict the permeability. Simulations include structured and unstructured packings and the influence of force scheme, relaxation time and domain size will be studied. Furthermore, some correlations for the prediction of permeability and tortuosity in faced- and body-centered cube packings will be provided.

Chapter 6 (*Turbulent Channel Flow with Resolved Spherical Particles*) presents simulation results of spherical particles motion in turbulent channel flows. Up to now, all simulations were in laminar regime at relatively low Reynolds number. Simulation of turbulent flow is inherently complex because of wide range of time and length scales involved. Particles make the problem even more complex. To do so, multiple fully-resolved spherical particles are released in a turbulent channel flow. Effect of particles on mean and fluctuating flow parameters will be studied and compared to those of single-phase flow. The simulation is carried out for different concentrations, particle densities and sizes.

Chapter 7 (*Two-Phase Flows with Prolate Spheroidal Particles*) covers the simulation of laminar and turbulent flows with spheroidal particles. The chapter starts with an introduction, followed by the governing equations of spheroid rotation. The method of quaternions is explained and validated for the rotation of a spheroid in a Couette flow. The next part extends the study to turbulent flows with suspended spheroidal particles, to investigate the effect of particle shape on turbulent flow properties. Effect of spheroidal particles on turbulence is compared to that with spherical ones.

Chapter 8 (*Conclusions and Outlook*) closes this thesis with a summary and discussion of the presented research topics and results. Some perspectives regarding future LBM applications will be stated. In particular, the importance and novelty of LBM for other multiphase flows will be discussed. Future topics on the simulation of other types of particle-laden flows will be covered as well.

1.3 ALBORZ Features

In this section, the features applied in the developed LB code (ALBORZ) are listed. These include:

- 2D and 3D simulations of laminar and turbulent flows
- Single- and multi-relaxation time schemes
- Particle-fluid interaction by immersed boundary method
- Reading geometry of the computational domain from the file
- Simulation of circular and elliptical particles in 2D and spherical and spheroidal particles in 3D studies
- Curved boundary treatment in 2D simulations
- Code parallelization by message passing interface (MPI)
- Non-isothermal studies using a double distribution function
- Particle-particle and particle-wall interaction by spring force and lubrication models

Chapter 2

Lattice Boltzmann Method

2.1 Historical background

Fluid mechanics is a branch of physics that involves the study of fluids and forces on them. Generally, there are three approaches to simulate the transport equations of the fluid. These mathematical models can be categorized based on the available time and length scales of the physical problem. The first one is the *continuum* (top-down) approach, which involves a continuum description of macroscopic phenomena, by deriving partial or ordinary differential equations for conservation of mass, momentum and energy in the system. The Navier-Stokes equations for a continuum, e.g., an incompressible fluid flow are often used in this respect to represent the conservation of momentum. Given the complexity of real phenomena, it is very difficult to solve analytically these differential equations. Therefore, alternative methods like finite difference, finite volume or finite element are employed to convert the differential equations into a system of algebraic equations. The algebraic equations are solved iteratively by applying the boundary and initial conditions. The simulation can continue until reaching a convergence criteria in case of steady problems. Conventional computational fluid dynamic (CFD) techniques follow this methodology.

On the other side, the fluid is composed of a large number of atoms or molecules that collide with each other and have a random motion. This scale of study of single atoms is called *microscopic* (bottom-up) approach. In this regard, the inter-particle forces are identified and each particle position is updated by solving an ordinary differential equation. The multi-scale expansion of statistical mechanics is used to relate the molecular and the macroscopic properties. For instance, temperature and pressure are related to the kinetic energy of the particles and frequency of particles collisions with the walls, respectively. Transport properties of the fluid (viscosity, thermal conductivity, etc.) can also be measured from linear response theory using Einstein expression or the Green-Kubo relation. Because of the large number of particles present in a small portion of the fluid, this method is only applicable to very small volumes, usually of sub-micrometer size. This makes the analysis of large systems almost impossible.

The lattice Boltzmann method (LBM) locates at the middle of both mentioned techniques. Boltzmann aimed to connect micro- and macro-scales by not considering each single particle behavior but the behavior of a collection of particles instead. The distribution function acts as the single variable that represents the collection of particles in contrast to the traditional CFD methods where the macroscopic variables are solved through conservation equations. LBM is able to recover the Navier-Stokes equations in the limit of nearly incompressible fluid flows. The scale of LBM is the so-called *meso-scale*.

The LBM was originally developed from lattice gas automata (LGA) in the late 1980's. LGA tracks the motion of discrete gas particles residing on a regular lattice where particles can stream and collide. It assumes that fluid behavior at macroscale is based on the statistical collective behavior of fluid molecules. It follows certain rules to assure that mass, momentum and energy are conserved during collision and streaming. The first LGA model was introduced by Hardy *et al.* [4] and is known as HPP model after the names of the authors. In this model which is based on a square lattice, velocity of particles change when they encounter head-on collision. This model lacks sufficient symmetry and does not lead to the Navier-Stokes equations in the macroscopic limit. This issue was relieved by the introduction of FHP model, which has hexagonal symmetry [5]. This model was able to model different 2D geometries, such as fluidized beds [6]. However, development of both FHP and HPP models to 3D studies was a tedious task. This issue was addressed later by Frisch *et al.* [7]. The FHP model still has some major limitations. A fundamental one is the statistical noise due to its Boolean nature. The second one is the non-Galilean invariance property due to the density dependence of the convection coefficient of the Navier-Stokes equation. Finally, the pressure that is given via an equation of state has an explicit and unphysical velocity dependence [8, 9]. Therefore, the Boolean variable of LGA was later replaced with a real-valued distribution function that can take a real value between 0 and 1, instead of only 0 or 1 [10]. McNamara and Zanetti were the first to propose using the lattice Boltzmann equation (LBE) as a separate numerical method. To overcome the problem of excessive memory and computational cost associated with nonlinear LB equation a linear collision operator was proposed by Higuera and Jimenez [11]. Higuera *et al.* [12], who used a linearized expression for the collision term, suggested the enhanced collisions model (HSB model) to remove the LBE limitation to low Reynolds number flows and to make the LB collision operator independent of any LGA model. The equilibrium distribution function still came from LGA. Moreover, the problems of density-dependent convection coefficient (lack of Galilean invariance) and velocity-dependent pressure were still unsolved because the authors used Fermi gases. This issue was solved by using a Maxwell-type distribution [8, 13]. Thus, they obtained noise-free models with Galileian invariance and a velocity-independent pressure. Koelman [14] and Chen *et al.* [15] further simplified the collision operator by using a constant value known as relaxation parameter. This form of LBM is the well-known single relaxation time (SRT)-LBM with BGK operator [16]. The choice of the BGK collision operator should conserve mass, momentum and energy and satisfies H-theorem as well. He and Luo [17] later derived LBM directly from the Boltzmann equation.

Thus, LBM is proven as a robust method that is free from both the statistical noise of LGA and the complexity of solving the exact Boltzmann equation and is widely used in various research fields including multiphase and multi-component flows [18, 19], porous media [20, 21], non-Newtonian fluids [22, 23], heat transfer [24, 25], suspended particles [26, 27], turbulent flows [28, 29], microfluidics [30, 31], and blood flow [32, 33], to cite a few.

2.2 LBM description

2.2.1 Boltzmann transport equation

Considering only mono-atomic gases, a given particle state depends on its position and velocity. Therefore, instead of a 3D physical space, at any given time the particle state can be defined in a 6D space composed of 3 physical dimensions and 3 phase dimensions. Based on this and starting from the microscopic representation of the system one can choose either the Newton or Hamilton equations to describe the motion of the fluid. Governing Newton equations are written as

$$\frac{\mathrm{d}\boldsymbol{x}_i}{\mathrm{d}t} = \frac{\boldsymbol{p}_i}{m}, \tag{2.1}$$

$$\frac{\mathrm{d}\boldsymbol{p}_i}{\mathrm{d}t} = \boldsymbol{F}_i, \tag{2.2}$$

where $i = 1, \cdots, N$, denotes particle index, $\boldsymbol{x}_i$ is the position of the i^{th} molecule, $\boldsymbol{p}_i = m\boldsymbol{\xi}$ the linear momentum of molecule and $\boldsymbol{F}_i$ the external force due to intermolecular interactions or external fields such as gravity or magnetic field.

The Hamiltonian of the system ($\mathcal{H}$) represents the total energy of the system including the kinetic and potential energy due to molecular interactions. Using $\mathcal{H}$, the motion of fluid molecules can be expressed as

$$\dot{\boldsymbol{x}}_i = \frac{\partial \mathcal{H}}{\partial \boldsymbol{p}_i}, \qquad \dot{\boldsymbol{p}}_i = -\frac{\partial \mathcal{H}}{\partial \boldsymbol{x}_i}, \qquad i = 1, 2, \cdots, N. \tag{2.3}$$

These equations are helpful but limited to very small systems because of the large number of molecules present in real configurations. For example, 1 cm^3 of ideal gas contains 2.69×10^{19} molecules at standard pressure and temperature.

The next level of description of such systems in a higher level is known as the mesoscopic description. For a system of N particles, where N is much smaller than the real number of molecules, the state of the system is represented by the distribution function $f_N(\boldsymbol{p}_1, \boldsymbol{q}_1, ..., \boldsymbol{p}_N, \boldsymbol{q}_N)$ where $\boldsymbol{q}$ and $\boldsymbol{p}$ are the generalized position and momentum vectors, respectively. $f_N(\boldsymbol{x}_1, \boldsymbol{p}_1, ..\boldsymbol{x}_N, \boldsymbol{p}_N, t)d\boldsymbol{x}_1, d\boldsymbol{p}_1...d\boldsymbol{x}_N, d\boldsymbol{p}_N$ is the probability of finding particle N in the interval $[\boldsymbol{x}_1, \boldsymbol{x}_1 + d\boldsymbol{x}_1] \times [\boldsymbol{p}_1, \boldsymbol{p}_1 + d\boldsymbol{p}_1] \times \cdots \times [\boldsymbol{x}_N, \boldsymbol{x}_N + d\boldsymbol{x}_N] \times [\boldsymbol{p}_N, \boldsymbol{p}_N + d\boldsymbol{p}_N]$. The distribution function is a function of all particle coordinates in the phase space and contains various correlations between particles. f_N obeys the Liouville equation [34]:

$$\frac{\partial f_N}{\partial t} - \sum_{j=1}^{3N} \left(\frac{\partial \mathcal{H}}{\partial x_j} \frac{\partial f_N}{\partial p_j} - \frac{\partial \mathcal{H}}{\partial p_j} \frac{\partial f_N}{\partial x_j} \right) = 0. \tag{2.4}$$

The reduced form of the distribution function (F_s) is obtained by integrating over part of the phase space:

$$F_s(\boldsymbol{x}_1, \boldsymbol{p}_1, ..., , \boldsymbol{x}_s, \boldsymbol{p}_s) = V^s \int f_N(\boldsymbol{x}_1, \boldsymbol{p}_1, ..., \boldsymbol{x}_N, \boldsymbol{p}_N) \prod_{j=s+1}^{N} \mathrm{d}\boldsymbol{x}_j \mathrm{d}\boldsymbol{p}_j. \tag{2.5}$$

where V_s is a normalization factor. Bogoliubov, Born, Green, Kirkwood and Yvon showed that a coupled system of differential equations for reduced density distributions (F_s) is equivalent to Eq. (2.4) [35]. This system of equations is known as the BBGKY hierarchy.

In Eq. (2.5), the single particle distribution function time evolution equation has one term defined by the two-particle distribution function. Iterating over all levels of description up to the N-particle distribution function one would see that each level has a collision term defined through the next-level distribution function. Therefore the BBGKY hierarchy has to be truncated at some point to get approximate solutions. The famous Boltzmann equation has been derived through such a truncation of the BBGKY hierarchy by the assumption of two-particle local collisions with uncorrelated velocities before collision and free of external forces.

Under such assumptions, the BBGKY hierarchy can be truncated to the single particle distribution function $f(\boldsymbol{x}, \boldsymbol{\xi}, t) \propto F_1(\boldsymbol{x}_1, \boldsymbol{p}_1, t)$ giving the Boltzmann transport equation:

$$\frac{\partial f}{\partial t} + \boldsymbol{\xi} \cdot \nabla_x f + \frac{\boldsymbol{F}}{m} \cdot \nabla_\xi f = \Omega(f, f), \tag{2.6}$$

where $\Omega(f, f)$ is the two-body collision term and $\dfrac{\boldsymbol{F}}{m}$ is the acceleration depending only on space and time. Thus, the Boltzmann equation describes the evolution of the particle distribution function.

Density ρ and velocity $\boldsymbol{u}$ are the moments of the distribution function that can be calculated by integrating over the phase space:

$$\rho = \int f(\boldsymbol{x}, \boldsymbol{\xi}, t) d\boldsymbol{\xi}, \tag{2.7}$$

$$\rho \boldsymbol{u} = \int \boldsymbol{\xi} f(\boldsymbol{x}, \boldsymbol{\xi}, t) \mathrm{d}\boldsymbol{\xi}. \tag{2.8}$$

Similar to Eqs. (2.7), (2.8), the energy density can be defined as a second-order moment of the distribution function:

$$\rho(\boldsymbol{x}, t) E(\boldsymbol{x}, t) = \int \frac{1}{2} \boldsymbol{\xi}^2 f(\boldsymbol{x}, \boldsymbol{\xi}, t) \mathrm{d}\boldsymbol{\xi}, \tag{2.9}$$

where $E(\boldsymbol{x}, t)$ is the total energy. It is worth mentioning that Eq. (2.9) is only valid for mono-atomic components as we have assumed that translational movement is the only source of kinetic energy. For poly-atomic gases there would also be contributions from rotational and vibrational movement. By introducing the relative velocity $\boldsymbol{u}$ which is the deviation of the particle velocity from the local mean velocity ($\boldsymbol{v} = \boldsymbol{\xi} - \boldsymbol{u}$) we get:

$$\rho(\boldsymbol{x}, t) e(\boldsymbol{x}, t) = \int \frac{1}{2} |\boldsymbol{v}|^2 f(\boldsymbol{x}, \boldsymbol{\xi}, t) \mathrm{d}\boldsymbol{\xi}, \tag{2.10}$$

where $e(\boldsymbol{x}, t)$ is the internal energy. Therefore, the total and internal energy densities are related by $\rho e = \rho E - \dfrac{1}{2} \rho |\boldsymbol{u}|^2$. In kinetic theory, the internal energy can also be expressed as,

$$e = \frac{D_f}{2} RT = \frac{D_f}{2} N_A k_B T, \tag{2.11}$$

where D_f , N_A , and k_B are the number of degrees of freedom of a particle, Avogadro's number, and the Boltzmann constant, respectively. The pressure (or stress tensor) can also be defined through the following second-order moment:

$$p = \int (\boldsymbol{\xi} - \boldsymbol{u}) \otimes (\boldsymbol{\xi} - \boldsymbol{u}) f(\boldsymbol{x}, \boldsymbol{\xi}, t) \mathrm{d}\boldsymbol{\xi}. \tag{2.12}$$

$(\boldsymbol{\xi} - \boldsymbol{u}) \otimes (\boldsymbol{\xi} - \boldsymbol{u})$ represents the tensor product such that for example $(\boldsymbol{cc})_{ij} = c_i c_j$.

2.2.2 Collision term

The collision operator in the Boltzmann equation has a number of properties. One of these properties is that it conserves the three first moments of the distribution function. These conserved quantities are also known as collision invariants ($\psi_k(\boldsymbol{\xi})$). Mathematically, the preceding is expressed as:

$$\int \Omega(f, f) \psi_k(\boldsymbol{\xi}) \mathrm{d}\boldsymbol{\xi} = 0, \tag{2.13}$$

where $\psi_0 = 1$, $(\psi_1, \psi_2, \psi_3) = \boldsymbol{\xi}$ and $(\psi_4) = \boldsymbol{\xi}^2$. In terms of macroscopic quantities, this means that the collision operator conserves mass, momentum and energy. Another fundamental property of this collision operator was shown in 1872 by Boltzmann. This property, known as H-theorem states that for any distribution function, $f(\boldsymbol{x}, \boldsymbol{\xi}, t)$, the H-function, defined by $H(t) = \int f \ln f \mathrm{d}\boldsymbol{x} \mathrm{d}\boldsymbol{\xi}$, should decrease with time , i.e.,

$$\frac{\mathrm{d}H}{\mathrm{d}t} \leq 0. \tag{2.14}$$

This condition is satisfied only and if only the system moves toward the equilibrium state, which is the Maxwell-Boltzmann equilibrium distribution. The H-theorem states that entropy never decreases spontaneously.

Due to the complicated nature of the collision operator of Boltzmann transport equation, a number of simpler alternatives have been proposed. Simpler collision operators should respect two constraints of conserving the collision invariants, and shifting the system towards a Maxwellian distribution (H-theorem). Both of these constraints are fulfilled by a model known as the BGK approximation, proposed by Bhatnagar, Gross and Krook in 1954 [16]. In the context of this approximation, the collision operator is expressed as:

$$\Omega(f,f) = -\frac{1}{\lambda}[f(\boldsymbol{x},\boldsymbol{\xi},t) - f^{(eq)}(\boldsymbol{x},\boldsymbol{\xi},t)], \tag{2.15}$$

where λ is the relaxation time due to collision and $f^{eq}(\boldsymbol{x},\boldsymbol{\xi},t)$ is the equilibrium distribution function (EDF). Based on this model the system relaxes to the equilibrium state as a result of collisions. This model is known as single relaxation time (SRT) BGK model; it conserves mass, momentum and energy equations and satisfies the H-theorem.

2.3 Single relaxation time model

As we have seen, the Boltzmann equation is the starting point of the LBM. This equation is used to find the statistical distribution of particles within a fluid ($f(\boldsymbol{x},\boldsymbol{\xi},t)$) instead of tracing each single particle. The Boltzmann equation with BGK approximation (without external force term) is written as

$$\frac{\partial f(\boldsymbol{x},\boldsymbol{\xi},t)}{\partial t} + \boldsymbol{\xi}\cdot\nabla f(\boldsymbol{x},\boldsymbol{\xi},t) = -\frac{1}{\lambda}\left[f(\boldsymbol{x},\boldsymbol{\xi},t) - f^{eq}(\boldsymbol{x},\boldsymbol{\xi},t)\right]. \tag{2.16}$$

The BGK model considers only two-body collisions without introducing significant error in the results. The equilibrium distribution function in the above equation is the Maxwell-Boltzmann distribution function because it minimizes the Boltzmann entropy (H),

$$f^{eq} = \frac{\rho}{(2\pi RT)^{(D_s/2)}}\exp\left(-\frac{(\boldsymbol{\xi}-\boldsymbol{u})^2}{2RT}\right), \tag{2.17}$$

where $R = k_B/m$ is the ideal gas constant with k_B the Boltzmann constant, m the molecular mass of gas particles, D_s the dimension of the space, and ρ, $\boldsymbol{u}$, T the macroscopic density of mass, velocity, and temperature, respectively. The macroscopic variables, ρ, $\boldsymbol{u}$, T are the microscopic velocity moments of the distribution function, f. The Taylor series expansion of f^{eq} up to second order of velocity (to recover the Navier-Stokes equation) reads [14]

$$f^{eq}(\boldsymbol{x},\boldsymbol{\xi},t) = \frac{\rho}{(2\pi RT)^{(D_s/2)}}\exp\left(-\frac{\boldsymbol{\xi}^2}{2RT}\right)\left[1 + \frac{\boldsymbol{\xi}\cdot\boldsymbol{u}}{RT} + \frac{(\boldsymbol{\xi}\cdot\boldsymbol{u})^2}{2(RT)^2} - \frac{|\boldsymbol{u}|^2}{2RT}\right] + \mathcal{O}(\boldsymbol{u}^3). \tag{2.18}$$

In the next step, Eq. (2.16) is discretized in phase space. Thus, instead of an infinite number of velocity directions, a finite number of velocities $\{\boldsymbol{c}_i\}$ is used. To do so, equilibrium distribution function is represented as $f_i^{eq}(\boldsymbol{x},t) = W_i f^{eq}(\boldsymbol{x},\boldsymbol{c}_i,t)$. Then, following Gaussian-type quadrature of the expanded EDF approximates:

$$\int \boldsymbol{\xi}^k f^{eq} d\boldsymbol{\xi} = \sum_i W_i \boldsymbol{c}_i^k f^{eq}(\boldsymbol{c}_i), \quad 0 \leq k \leq 3, \tag{2.19}$$

where $\boldsymbol{c}_i$ is the discrete velocity set and W_i is the weight associated with the velocity $\boldsymbol{c}_i$. In order to calculate the hydrodynamic moments of the distribution function, an approximation by quadratures is needed:

$$\int \Phi(\boldsymbol{\xi}) f^{eq} d\boldsymbol{\xi} = \sum_i W_i \Phi(\boldsymbol{c}_i) f_i(\boldsymbol{x}, t), \tag{2.20}$$

where $\Phi(\boldsymbol{\xi})$ is a polynomial of $\boldsymbol{\xi}$ [36]. Using an effective discrete distribution function of $f_i(\boldsymbol{x}, t) = W_i f(\boldsymbol{x}, \boldsymbol{c}_i, t)$ also satisfies the conservation relations (Eqs. (2.7), (2.8)) and leads to

$$\frac{\partial f_i}{\partial t} + \boldsymbol{c}_i \cdot \nabla f_i = -\frac{1}{\lambda} \left[f_i(\boldsymbol{x}, t) - f_i^{eq}(\boldsymbol{x}, t) \right]. \tag{2.21}$$

A discretization of the Boltzmann equation in time and space, and the conversion of the space of velocities $\boldsymbol{\xi}$ into a finite set of velocities $\{\boldsymbol{c}_i\}$ within which the particles are allowed to move in the lattice and integrating Eq. (2.21) from t to $t + \Delta t$ with the assumption of constant collision term in this interval, finally leads to the well-known lattice Boltzmann discretized SRT-BGK model [17]:

$$\boxed{f_i(\boldsymbol{x} + \boldsymbol{c}_i \Delta t, t + \Delta t) - f_i(\boldsymbol{x}, t) = -\frac{1}{\tau} \left[f_i(\boldsymbol{x}, t) - f_i^{eq}(\boldsymbol{x}, t) \right],} \tag{2.22}$$

where f_i is the distribution function of particles moving with speed $\{\boldsymbol{c}_i\}$ and the right-hand side accounts for the SRT collision term with $\tau \equiv \lambda / \Delta t$ being the non-dimensional relaxation time. Incorporating the bracket coefficients of Eq. (2.18) into weight coefficients leads to the following form of equilibrium distribution function in the isothermal case:

$$\boxed{f_i^{eq} = \omega_i \rho \left[1 + \frac{\boldsymbol{c_i} \cdot \boldsymbol{u}}{c_s^2} + \frac{(\boldsymbol{c_i} \cdot \boldsymbol{u})^2}{2 c_s^4} - \frac{|\boldsymbol{u}|^2}{2 c_s^2} \right],} \tag{2.23}$$

with

$$\omega_i = \frac{W_i \exp\left(-\frac{c_i^2}{2 c_s^2} \right)}{(2 \pi c_s^2)^{(D_s/2)}}, \tag{2.24}$$

and sound speed $c_s = \sqrt{RT}$ is model-dependent. For isothermal models, RT is constant, and hence, c_s is constant as well. The weight coefficients and c_s values depend on the space dimension and number of discrete velocities (Sec. 2.4). The macroscopic velocity $\boldsymbol{u}$ in Eq. (2.23) must satisfy the requirement for low Mach number, i.e. $|\boldsymbol{u}| / c_s = \mathrm{Ma} \ll 1$. Under condition of low Mach and Knudsen number, LBM recovers the NS equation for a weakly compressible flow by means of a Chapman-Enskog analysis [5, 37].

Macroscopic quantities including density and velocity are defined by the 0$^{\text{th}}$, and 1$^{\text{st}}$ moments of the probability distribution function, respectively:

$$\rho = \sum_i f_i, \tag{2.25}$$

$$\rho \boldsymbol{u} = \sum_i \boldsymbol{c}_i f_i. \tag{2.26}$$

Conceptually, the SRT-LBM algorithm is implemented in two steps: first, the collision of particles, which controls the relaxation toward equilibrium; and in the second step, the streaming of particles in which distribution functions are shifted along the lattice directions to the neighboring lattice cells.

$$\text{collision}: f_i^{'}(\boldsymbol{x}, t) = f_i(\boldsymbol{x}, t) - \frac{1}{\tau}\left[f_i(\boldsymbol{x}, t) - f_i^{eq}(\boldsymbol{x}, t)\right], \tag{2.27}$$

$$\text{streaming}: f_i(\boldsymbol{x} + \boldsymbol{c}_i \Delta t, t + \Delta t) = f_i^{'}(\boldsymbol{x}, t), \tag{2.28}$$

where the relaxation parameter (τ) in Eq. (2.27) is related to the kinematic lattice viscosity, ν, through:

$$\nu = \left(\tau - \frac{1}{2}\right) c_s^2 \Delta t, \tag{2.29}$$

and pressure is related to density via the equation of state:

$$p = \rho c_s^2. \tag{2.30}$$

2.4 Two- and three-dimensional stencils

It was shown in Sec. 2.3 that a continuous equilibrium distribution function can be represented by a discrete one in which weight coefficients must be selected. Determination of weight factors is based on a third-order Hermite formula [17, 38].

In the final discretized form of LB equation, the physical space is covered by regular lattices that are populated by discrete particles. Particles jump from one lattice node to another with discrete particle velocities $\boldsymbol{c}_i$, and collide with each other at these nodes. The set of discrete velocities is often denoted by DmQn, where m and n are the spatial dimension and the total number of the lattice velocities, respectively. Among different available stencils, in this thesis the 9-velocity model on a 2D square lattice, known as the D2Q9 model, and the 19-velocity model on a 3D cubic lattice, denoted as the D3Q19 model are used. These two discrete velocity models are depicted in Fig. 2.1.

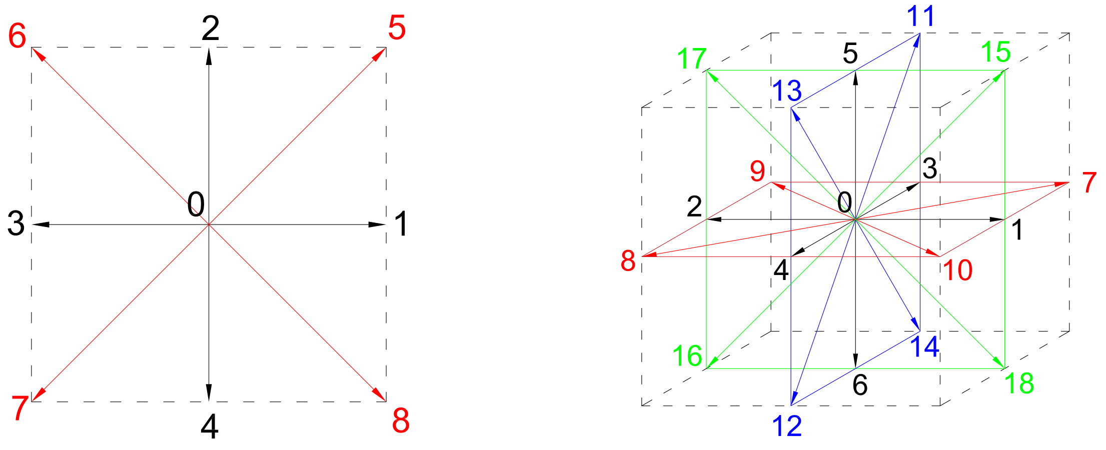

(a) (b)

Figure 2.1: Velocity direction vectors of (a) D2Q9 structure; (b) D3Q19 structure

The velocity vectors for D2Q9 model $\boldsymbol{c_i} = [c_{ix}, c_{iy}]$ are given by

$$\boldsymbol{c}_i = \begin{cases} (0,0), & i = 0 \\ (\pm 1, 0), (0, \pm 1), & i = 1, \cdots, 4 \\ (\pm 1, \pm 1). & i = 5, \cdots, 8 \end{cases} \tag{2.31}$$

The corresponding weight coefficients are

$$\omega_i = \begin{cases} 4/9, & i = 0 \\ 1/9, & i = 1, \cdots, 4 \\ 1/36. & i = 5, \cdots, 8 \end{cases} \tag{2.32}$$

The D3Q19 model has the velocity vectors $\boldsymbol{c_i} = [c_{ix}, c_{iy}, c_{iz}]$ where

$$\boldsymbol{c}_i = \begin{cases} (0,0,0), & i = 0 \\ (\pm 1, 0, 0), (0, \pm 1, 0), (0, 0, \pm 1), & i = 1, \cdots, 6 \\ (\pm 1, \pm 1, 0), (\pm 1, 0, \pm 1), (0, \pm 1, \pm 1). & i = 7, \cdots, 18 \end{cases} \tag{2.33}$$

The weight coefficients for this model are:

$$\omega_i = \begin{cases} 1/3, & i = 0 \\ 1/18, & i = 1, \cdots, 6 \\ 1/36. & i = 7, \cdots, 18 \end{cases} \tag{2.34}$$

The sound speed for both stencils is equal to $c_s = \Delta x / (\sqrt{3} \Delta t)$.

2.4.1 The Chapman-Enskog expansion

In order to use LBM for modeling fluid flow, it is necessary to show that the LB equation recovers the NS equation in the limit of low Mach and Knudsen numbers. To do so, a multi-scale analysis is carried out. In this type of analysis, known as Chapman-Enskog multi-scale expansion, different terms in the LB equation are written as power series with a small coefficient (ϵ) related to the Knudsen number. Using a Taylor series expansion of the distribution function together with the Chapman-Enskog analysis lead to terms with different powers of ϵ. By regrouping and equating the terms of the same order of ϵ and calculating the moments of distribution functions, mass conservation and NS equation are preserved. The Chapman-Enskog expansion of SRT-LBM is presented in Appendix A.

2.4.2 SRT-LBM advantages and limitations

In this part, the advantages and limitations of LBM will be discussed in more detail. The advantages of LBM can be explained as follows:

- The advection term (streaming) is linear compared to the non-linear operator in NS equations;
- Pressure is simply calculated through an equation of state, while NS-based solvers rely on a Poisson equation that cannot be solved efficiently on parallel computers;
- In LBM, the distribution function at each node depends only on its own PDF and those of the adjacent nodes. Hence, LBM can be used to solve the fluid flow in complex structures such as porous media. Parallelization would be then quite straightforward for LB solvers. For large domains of porous media or direct numerical simulation of turbulent flows parallelization is unavoidable but is very efficient for LBM;
- LBM is a mesoscopic approach and thus more suitable to incorporate the microscopic physics. It is based on the Boltzmann equation, which is one of the fundamental equations in statistical physics;
- According to Guo and Shu [39], due to better rotational symetry of LBM compared to classical second order finite-difference and finite-volume schemes, LBM may result in more accurate results.

On the other side, there are some limitations using LBM:

- LBM is inherently an unsteady flow solver and therefore steady-state computations are not possible. For these cases, one should wait until the initial conditions converge to the final steady solution which might be time-consuming;

- The standard LBM is not suitable for body-fitted coordinates due to using only square or cubic lattices. In this case, the curved boundary treatment [40–42] or using immersed boundary method [43] is recommended. The methods of curved boundary interpolate distribution function at the real location of the wall. The immersed boundary methods rely on the Cartesian grids but use some mapping points on the surface of solid walls. Force and velocity data are exchanged between fluid and solid nodes using discrete delta functions;

- The next point that must be noticed is that, in case of D2Q9 and D3Q19 models, the SRT-LBM can only handle isothermal flows. Treating non-isothermal flows requires using a separate distribution function that solves the advection-diffusion equation of energy transfer. The method is usually recognized as double distribution function (DDF) model [44–46]. An alternative would be using the so-called multi-speed approach [47–49] with higher number of discrete velocities, for example D2Q21 stencil. Higher-order velocity terms are also kept in the equilibrium distribution function to recover the energy equation at the macroscopic level. Boundary condition implementation and parallelization of multi-speed methods are not as straightforward and as efficient as common stencils. The Prandtl number is also fixed and numerical instability may occur when only one distribution function is used. Hybrid models are another option [50, 51], in which temperature field is solved through an external solver rather than LBM, such as with a finite-difference method;

- The Prandtl number in SRT-LBM (regardless of number of discretized velocities) is fixed at 1 because all moments relax at the same rate. This issue can be circumvented using an ellipsoidal statistical BGK model [52] or again using a separate distribution function for energy transfer (DDF). So, the energy equation has a separate relaxation parameter which is linked with the thermal diffusivity of the fluid. Using a multi relaxation time (MRT) model together with multi-speed approach and an equilibrium distribution function with $\boldsymbol{u}^3$ terms is another alternative for treating non-unity Prandtl numbers when only one distribution function is utilized. But using only one of these methods without others cannot solve unity Prandtl number issue [53];

- Another issue with LBM is the compressibility error due to ignoring the change of density in the continuity equation and in the momentum equation, since the density variation is proportional to Ma^2, i.e., $\rho(\boldsymbol{x}, t) = \rho_0 + \mathcal{O}(\mathrm{Ma}^2)$. Therefore, LBM can be viewed as a compressible solver for incompressible Navier-Stokes equations. In this regard, keeping the velocity in the range of $\mathrm{Ma} = u/c_s \ll 1$ is of great importance for incompressible regimes. To reduce the compressibility error for incompressible flows, some models have been introduced so far. They mostly change the equilibrium distribution function so that instead of $\nabla \cdot (\rho \boldsymbol{u})$, only $\nabla \cdot (\boldsymbol{u})$ will appear in the continuity equation, as in an incompressible flow [54, 55]. Some others try to decrease the effect of this error by keeping $\mathcal{O}(u^3)$ terms in equilibrium distribution function and using a more complex lattice. However, there is still one error of $\mathcal{O}(\mathrm{Ma}^2)$ due to bulk viscosity term [56];

- LBM is generally limited to low Mach number flows. Low velocity assumption is used in the expansion of equilibrium distribution function and in the Chapman-Enskog expansion. In the formulation of equilibrium distribution function (Eq. (2.23)) only velocity terms up to $\boldsymbol{u}^2$ are kept and the truncation error of $\boldsymbol{u}^3$ terms grows as macroscopic velocity increases. Therefore, modeling high speed compressible flows in shock waves and detonation phenomena is challenging. During recent years some compressible LB approaches are proposed using either a flexible sound speed [57], variable lattice velocity [58], combination of DDF and multi-speed approaches [59], introducing additional viscosity [60] or using entropic LBM [61];

- In LBM, bulk viscosity (also known as the volume viscosity or second viscosity) is fixed and has a non-zero value. It must be noted that bulk viscosity has different definitions among different people. Some name the total combination of $(\mu' - \frac{2}{3}\mu)$ the bulk viscosity. Here, we only refer to bulk viscosity by term μ'. The general (compressible) Navier-Stokes equations is written in the form:

$$\partial_t \rho + \nabla \cdot (\rho \boldsymbol{u}) = 0, \tag{2.35}$$

$$\partial_t (\rho \boldsymbol{u}) + \nabla \cdot (p\mathbf{I} + \rho \boldsymbol{u}\boldsymbol{u}) = \nabla \cdot \boldsymbol{\sigma'}. \tag{2.36}$$

The deviatoric stress has the generic form

$$\sigma'_{ab} = \mu \left(\partial_\alpha u_\beta + \partial_\beta u_\alpha - \frac{2}{3}\delta_{\alpha\beta} \nabla \cdot \boldsymbol{u} \right) + \mu' \delta_{\alpha\beta} \nabla \cdot \boldsymbol{u}. \tag{2.37}$$

In incompressible Navier-Stokes equation, the effect of bulk viscosity is automatically eliminated because $\nabla \cdot \boldsymbol{u}$ is zero based on the continuity equation. Therefore, the real value of bulk viscosity is not important for an incompressible Navier-Stokes solver. In LBM, however, Eq. (2.35) is solved for mass conservation. This equation can be written as

$$(\partial_t + \boldsymbol{u} \cdot \nabla)\rho + \rho \nabla \cdot \boldsymbol{u} = 0, \tag{2.38}$$

where the terms proportional to $\nabla \cdot \boldsymbol{u}$ are $\mathcal{O}(\mathrm{Ma}^2)$. Therefore, in SRT-LBM neither $\nabla \cdot \boldsymbol{u}$ nor μ' are zero. Dellar [56] showed that in LBM, $\mu' = 2\mu/3$, that eliminates the last two terms of Eq. (2.37). This result is satisfactory for isothermal flows. For non-isothermal cases with large density variations or in compressible regimes, the term $(\mu' - \frac{2}{3}\mu)\nabla \cdot \boldsymbol{u}$ should be kept in the equations. Dellar [56] proposed an extra term in the equilibrium distribution function to solve the issue;

- SRT-BGK model faces numerical instability at zero-viscosity limit. It would be thus difficult to model very high Reynolds number or turbulent flows. To improve the numerical stability and reach high Reynolds numbers, several methods have been proposed. Among them, the MRT collision operator [62, 63], cascaded LB method [64], entropic [65] and the cumulant model [66] are widely used;

- The no-slip boundary condition in LBM is usually implemented by getting the missing populations from the post-collision ones of the opposite direction (half-way bounce-back). Luo *et al.* [67] showed that wall location depends on the value of relaxation time and wall locates at $\Delta = 0.5$ if and only if $\nu = 1/(2\sqrt{6})$ (or $\tau = 1.1123$). Ginzbourg and Adler [68] expressed that the exact location of the wall is one-half lattice between the fluid and the solid wall if and only if the relaxation times are different and properly selected. Use of different relaxation times is not possible in SRT. MRT eases the problem. This issue is more important when the interaction of solid wall and the fluid is handled by momentum exchange method which is based on the bounce-back principle or when flow in porous media is simulated. For straight walls, the effect is negligible and SRT model would be the right choice.

In spite of above mentioned limitations, SRT-LBM is still the most popular LB approach for a variety of flow regimes and conditions and will be used throughout this thesis unless otherwise stated.

2.5 Multi-relaxation time model (MRT)

In MRT model, different moments of the distribution function relax at different rates, while in SRT model, all moments relax at the same rate. MRT allows us to choose lower relaxation times for non-hydrodynamic moments, providing the maximum degrees of freedom to optimize LBM stability. Proper selection of relaxation parameters solves the issue of instability at low relaxation times, or of reduced accuracy at high relaxation times occurring for SRT-LBM.

For this purpose, in MRT, the evolution takes place in a moment space instead of the velocity space. The MRT-LBM equation without a force term is written as:

$$\mathbf{f}(\boldsymbol{x} + \boldsymbol{c}_i \Delta t, t + \Delta t) = \mathbf{f}(\boldsymbol{x}, t) - \mathbf{M}^{-1} \left(\mathbf{S} \left[\mathbf{m} - \mathbf{m}^{eq} \right] \right), \tag{2.39}$$

with $\mathbf{m} = \mathbf{M}\mathbf{f}$ and $\mathbf{m}^{eq} = \mathbf{M}\mathbf{f}^{eq}$. Here, $\mathbf{M}$ is the transformation matrix, $\mathbf{f}$ is the matrix of moments, and $\mathbf{S}$ is a diagonal matrix in the moment space, which contains relaxation time of each moment. In this thesis, MRT is used for 3D porous media simulation and turbulent flow initialization. The corresponding relaxation matrix in 3D is:

$$\mathbf{S} = \mathrm{diag}\left[0, s_1, s_2, 0, s_4, 0, s_4, 0, s_4, s_9, s_{10}, s_9, s_{10}, s_{13}, s_{13}, s_{13}, s_{16}, s_{16}, s_{16}\right], \tag{2.40}$$

where $s_1 = 1.19$, $s_2 = s_{10} = 1.4$, $s_4 = 1.2$, $s_9 = s_{13} = 1/\tau$, and $s_{16} = 1.98$ [63]. In SRT all elements of this matrix are $1/\tau$. The transformation matrix $\mathbf{M}$ in D3Q19 model is given by

$$\begin{bmatrix}
1 & 1 & 1 & 1 & 1 & 1 & 1 & 1 & 1 & 1 & 1 & 1 & 1 & 1 & 1 & 1 & 1 & 1 & 1 \\
-30 & -11 & -11 & -11 & -11 & -11 & -11 & 8 & 8 & 8 & 8 & 8 & 8 & 8 & 8 & 8 & 8 & 8 & 8 \\
12 & -4 & -4 & -4 & -4 & -4 & -4 & 1 & 1 & 1 & 1 & 1 & 1 & 1 & 1 & 1 & 1 & 1 & 1 \\
0 & 1 & -1 & 0 & 0 & 0 & 0 & 1 & -1 & 1 & -1 & 1 & -1 & 1 & -1 & 0 & 0 & 0 & 0 \\
0 & -4 & 4 & 0 & 0 & 0 & 0 & 1 & -1 & 1 & -1 & 1 & -1 & 1 & -1 & 0 & 0 & 0 & 0 \\
0 & 0 & 0 & 1 & -1 & 0 & 0 & 1 & 1 & -1 & -1 & 0 & 0 & 0 & 0 & 1 & -1 & 1 & -1 \\
0 & 0 & 0 & -4 & 4 & 0 & 0 & 1 & 1 & -1 & -1 & 0 & 0 & 0 & 0 & 1 & -1 & 1 & -1 \\
0 & 0 & 0 & 0 & 0 & 1 & -1 & 0 & 0 & 0 & 0 & 1 & 1 & -1 & -1 & 1 & 1 & -1 & -1 \\
0 & 0 & 0 & 0 & 0 & -4 & 4 & 0 & 0 & 0 & 0 & 1 & 1 & -1 & -1 & 1 & 1 & -1 & -1 \\
0 & 2 & 2 & -1 & -1 & -1 & -1 & 1 & 1 & 1 & 1 & 1 & 1 & 1 & 1 & -2 & -2 & -2 & -2 \\
0 & -4 & -4 & 2 & 2 & 2 & 2 & 1 & 1 & 1 & 1 & 1 & 1 & 1 & 1 & -2 & -2 & -2 & -2 \\
0 & 0 & 0 & 1 & 1 & -1 & -1 & 1 & 1 & 1 & 1 & -1 & -1 & -1 & -1 & 0 & 0 & 0 & 0 \\
0 & 0 & 0 & -2 & -2 & 2 & 2 & 1 & 1 & 1 & 1 & -1 & -1 & -1 & -1 & 0 & 0 & 0 & 0 \\
0 & 0 & 0 & 0 & 0 & 0 & 0 & 1 & -1 & -1 & 1 & 0 & 0 & 0 & 0 & 0 & 0 & 0 & 0 \\
0 & 0 & 0 & 0 & 0 & 0 & 0 & 0 & 0 & 0 & 0 & 0 & 0 & 0 & 0 & 1 & -1 & -1 & 1 \\
0 & 0 & 0 & 0 & 0 & 0 & 0 & 0 & 0 & 0 & 0 & 1 & -1 & -1 & 1 & 0 & 0 & 0 & 0 \\
0 & 0 & 0 & 0 & 0 & 0 & 0 & 1 & -1 & 1 & -1 & -1 & 1 & -1 & 1 & 0 & 0 & 0 & 0 \\
0 & 0 & 0 & 0 & 0 & 0 & 0 & -1 & -1 & 1 & 1 & 0 & 0 & 0 & 0 & 1 & -1 & 1 & -1 \\
0 & 0 & 0 & 0 & 0 & 0 & 0 & 0 & 0 & 0 & 0 & 1 & 1 & -1 & -1 & -1 & -1 & 1 & 1
\end{bmatrix} \tag{2.41}$$

In 3D studies, four components of $\mathbf{m}$ are density and momentum in x, y and z directions. For zeroth moment, for example, $m_0 = \sum_i M_{0,i} f_i$. Other components of matrix $\mathbf{m}$ are specified by using Hermite polynomials or Gram-Schmidt procedure. This procedure ensures that rows of matrix $\mathbf{M}$ are orthogonal vectors and, therefore, they are unique. Hence, moments can relax to equilibrium ones independently of each other. The 19 orthogonal moments in the D3Q19 stencil are:

$$\mathbf{m} = (\rho, e, \varepsilon, j_x, q_x, j_y, q_y, j_z, q_z, 3p_{xx}, 3\pi_{xx}, p_{ww}, \pi_{ww}, p_{xy}, p_{yz}, p_{xz}, m_x, m_y, m_z). \tag{2.42}$$

The equilibrium moments are defined as

$$\rho^{eq} = \rho, \tag{2.43}$$

$$e^{eq} = -11\rho + 19(j_x^2 + j_y^2 + j_z^2), \tag{2.44}$$

$$\varepsilon^{eq} = w_\varepsilon \rho + \frac{w_{\varepsilon j}}{\rho_0}(j_x^2 + j_y^2 + j_z^2), \tag{2.45}$$

$$q_x^{eq} = -\frac{2}{3} j_x, \quad q_y^{eq} = -\frac{2}{3} j_y, \quad q_z^{eq} = -\frac{2}{3} j_z \tag{2.46}$$

$$p_{xx}^{eq} = \frac{1}{3\rho_0}\left[2j_x^2 - (j_y^2 + j_z^2)\right], \quad p_{ww}^{eq} = \frac{1}{\rho_0}\left[2j_y^2 - j_z^2\right], \tag{2.47}$$

$$p_{xy}^{eq} = \frac{1}{\rho_0} j_x j_y, \quad p_{yz}^{eq} = \frac{1}{\rho_0} j_y j_z \quad p_{xz}^{eq} = \frac{1}{\rho_0} j_x j_z \tag{2.48}$$

$$\pi_{xx}^{eq} = w_{xx} p_{xx}^{eq}, \quad \pi_{ww}^{eq} = w_{xx} p_{ww}^{eq}, \tag{2.49}$$

$$m_x^{eq} = m_y^{eq} = m_z^{eq} = 0, \tag{2.50}$$

where w_ε, $w_{\varepsilon j}$ and w_{xx} are free parameters in the D3Q19 model. d'Humières *et al.* [63] suggested using $w_\varepsilon = 3$, $w_{\varepsilon j} = -11/2$ and $w_{xx} = -1/2$.

2.6 Summary

In this chapter, the lattice Boltzmann method was introduced, including its history, formulation, advantages and shortcomings. Moreover, different architectures of LBM consisting of SRT and MRT were explained. In the rest of this dissertation, multiphase flows will be modeled. To do so, LBM will be used as the flow solver because of numerous advantages. In particular, linear convective term, locality of calculations and high parallel efficiency are fascinating. In our simulations, we only deal with incompressible regimes of low Mach number and small temperature variations. Thus, standard SRT-LBM is satisfactory and is utilized unless otherwise stated. For non-isothermal cases (Chapter 4), DDT model will be implemented to have freedom on the choice of Prandtl number at a reasonable computational cost. For high Reynolds flows (Chapter 6), MRT will be used to increase the stability for the initialization of turbulence. After turbulence establishment, SRT will be utilized.

Next chapter will go deeper into the modeling of laminar particulate flows by means of LBM. Fluid-particle interaction forces are taken into account by IBM, which will be explained with validation and application cases.

Chapter 3

Laminar Particulate Flows

3.1 Introduction

Particulate flows are present in many natural and industrial applications such as filtration, pollution control, blood clogging, fluidized bed, crystallization, or chemical reactors involving catalyst particles. For many years, the study and design of particle systems were limited to empirical and experimental research. During the past decades and as a result of increased computational capability and advanced modeling techniques, the numerical analysis of particulate flows has attracted the attention of many research groups. Three major numerical approaches can be identified in this regard. The first approach is the *two-fluid* model (as special case of the multi-fluid model) in which the properties of the particles are assumed to be continuous, like those of a pure fluid. Thus, conservation equations of mass, momentum and energy are developed through an averaging process and the constitutive relations for the solid phase are usually closed using the kinetic theory of granular flow. These equations are discretized at each computational node and solved through a procedure similar to that used for the fluid [3, 69]. The interaction between the two phases is described by drag force correlations. This model is an Eulerian-Eulerian approach that does not properly model all details of particle-particle and particle-fluid interactions.

The second approach is the *Lagrangian point-particle* model. This method is appropriate for sufficiently small particles in dilute regimes. This method fails to give an accurate prediction of the flow behavior when these conditions are not met. In this model, each particle is treated as a point and its position is determined via Newton's equations of motion. This model is an Eulerian-Lagrangian approach and estimates the force acting on each particle by an empirical drag force.

The third approach of handling particles, is the so called *fully-resolved simulation*, which is the most accurate method. Here, the Eulerian grid is typically an order of magnitude smaller than the size of the particles, so that the fluid flow behavior around and between particles is also computed. In this case, no correlation is required and both particle-particle and particle-fluid interactions can be modeled in a realistic way [70].

The fully-resolved simulation methods fall into two categories: boundary-fitted and non-boundary fitted. In the boundary-fitted techniques, the generated computational grid fits the particle surface. This type of mesh is usually unstructured for complex surface geometries. This implies that mesh generation is computationally expensive and troublesome, especially when treating moving objects. The arbitrary Lagrangian-Eulerian (ALE) approach locates in this group [71]. This method loses its efficiency in case of 3D geometry or in the presence of numerous particles. Non-boundary fitted approaches are then easier to implement. The main methods in this category are: the distributed Lagrange multiplier or fictitious domain method (DLM/FDM, see [72]) and the immersed boundary method (IBM). IBM was first introduced by Peskin [43, 73] in order to model blood flow in the heart. In IBM, the fluid equations are discretized on a fixed Eulerian grid over the entire domain and the immersed boundary is discretized on a moving Lagrangian mesh.

In this chapter, the lattice Boltzmann method is employed to simulate different laminar particulate flows with solid rigid particles. The first popular way to calculate the interaction force between the particle and the fluid in LBM is the so-called momentum exchange method. This method is based on balancing the momentum of the fluid at the obstacle surface using bounce-back technique. It has been widely used in the literature [74–77]. One other promising approach is the IBM, where the boundary shape is taken into account. Since both IBM and LBM are based on a Cartesian grid, a combination can be readily applied to simulations of moving boundary problems. This combination is denoted as IB-LBM in what follows. In IBM the force density is evaluated at each Lagrangian point using either the penalty method [43], the momentum exchange method [78] or the direct forcing (DF) method [79, 80].

Feng and Michaelides [81] first developed an IB-LBM coupled model and applied it to simulate the sedimentation of a large number of particles in an enclosure. In their approach (penalty method) the particle boundary was treated as a deformable medium with high stiffness. This method has the drawback that it requires a priori selection of the stiffness parameter, based on the specific problem to be solved. One year later they developed the direct IB-LBM model [82] based on what was originally proposed by Mohd-Yusof [79] for fixed complex boundaries. In the direct forcing method, the force density term is naturally determined in the calculation process and there is therefore no need to use a free parameter for the stiffness coefficient. Niu *et al.* [78] proposed an IB-LBM approach called the momentum-exchange-based IB-LBM. Dupuis *et al.* [83] proposed a direct-forcing IB-LBM without solving the Navier-Stokes equations for the evaluation of boundary force density. Their method is considered as a pure direct-forcing IB-LBM.

IB-LBM has been applied in recent years to an increasing variety of flow conditions. Kang and Hassan [84] used a DF IB-LBM based on the split-forcing LBM with various interface schemes for flow problems with stationary complex boundaries. They suggested using the IB-LBM with a sharp interface scheme for stationary boundary problems but stated that for moving boundary cases, the diffuse interface scheme is more suitable because it produces a smooth evolution of forcing points. In the diffuse interface scheme, forcing points are located on the immersed object boundary.

Suzuki and Inamuro [85] investigated the internal mass effect for various particle Reynolds numbers through the IB-LBM simulations of a moving body in a fluid. They found that the internal mass effect is fairly small for Reynolds numbers about 1, but grows as the Reynolds number increases. The effect becomes distinct for a Reynolds number over 10. Later, the authors proposed a LBM combined with a higher-order IBM using a smooth velocity field near boundaries, to expand the velocity field smoothly into the body domain across the boundary [86].

The chapter is organized as follows. First, the governing equations of DF-IBM together with the discretized equations are presented. Then, simulation results of moving rigid particles for different 2D and 3D flows of increasing complexity are discussed. Results of this chapter have been partly published in [87, 88].

3.2 Numerical formulation

3.2.1 Immersed boundary method

Here the direct-forcing IBM is used to couple the fluid and particle phases. In IBM, the fluid equations are discretized on a fixed Eulerian grid over the entire domain and the immersed boundary is discretized on a moving Lagrangian mesh [43, 79].

The momentum equation for an incompressible viscous flow field reads

$$\frac{\partial \boldsymbol{u}}{\partial t} + \boldsymbol{u} \cdot \nabla \boldsymbol{u} = -\frac{1}{\rho_f} \nabla p + \nu_f \nabla^2 \boldsymbol{u} + \boldsymbol{f}, \tag{3.1}$$

where $\boldsymbol{u}$, ρ_f , and ν_f are the fluid velocity, density, and kinematic viscosity, respectively. Parameters p and $\boldsymbol{f}$ are the pressure and a force density due to presence of particles.

In order to use the direct-forcing IBM, the discretized form of Eq. (3.1) is rewritten as:

$$\frac{\boldsymbol{u}^{n+1} - \boldsymbol{u}^n}{\Delta t} = \boldsymbol{RHS}^n + \boldsymbol{f}^n, \tag{3.2}$$

where Δt is the time step, n and $n+1$ are the present and next time steps, and $\boldsymbol{RHS}^n$ includes convective, viscous and pressure terms. Following the method proposed by Uhlmann [80], the force density term at any Lagrangian point ($\boldsymbol{X}_l$) is evaluated from the desired velocity ($\boldsymbol{U}^d$)

$$\boldsymbol{f}_l^n = \frac{\boldsymbol{U}^d - \boldsymbol{u}^{noF}}{\Delta t}, \tag{3.3}$$

where $\boldsymbol{u}^{noF}$ means the velocity at step $n+1$ without being forced and is calculated regardless of the existence of any forcing term. It is calculated in 3D simulations by Eq. (3.4) based on the velocity at the Eulerian nodes ($\boldsymbol{u}_{i,j,k}$):

$$\boldsymbol{u}^{noF} = \sum_{i,j,k} \boldsymbol{u}_{i,j,k} D(\boldsymbol{x}_{i,j,k} - \boldsymbol{X}_l)(\Delta h)^3, \tag{3.4}$$

where Δh is the lattice size ($= 1$) and $\boldsymbol{X}_l$ denotes the location of the Lagrangian point. The desired velocity at each Lagrangian point reads

$$\boldsymbol{U}^d = \boldsymbol{U}_p + \boldsymbol{\Omega}_p \times (\boldsymbol{X}_l - \boldsymbol{X}_c), \tag{3.5}$$

where $\boldsymbol{U}_p$ and $\boldsymbol{\Omega}_p$ are the translational and angular velocity of the particle, respectively, and $\boldsymbol{X}_c$ is the location of the particle center. The discrete Dirac delta function in Eq. (3.4) is defined for 3D cases as follows (2D formulation is similarly derived):

$$D(\boldsymbol{x}_{i,j,k} - \boldsymbol{X}_l) = \frac{1}{(\Delta h)^3} d_h\left(\frac{x - x_l}{\Delta h}\right) d_h\left(\frac{y - y_l}{\Delta h}\right) d_h\left(\frac{z - z_l}{\Delta h}\right), \tag{3.6}$$

and the following 4-point delta function is used to estimate $d_h(r)$ in the present study [89]:

$$d_h(r) = \begin{cases} \frac{1}{8}\left(3 - 2\,|r| + \sqrt{1 + 4|r| - 4r^2}\right) & 0 \le |r| < 1 \\ \frac{1}{8}\left(5 - 2\,|r| - \sqrt{-7 + 12|r| - 4r^2}\right) & 1 \le |r| < 2 \\ 0 & |r| \ge 2 \end{cases}, \tag{3.7}$$

Finally, the force term that is exerted on each Eulerian point is calculated by spreading the Lagrangian force term:

$$\boldsymbol{f}_{i,j,k} = \sum_{i,j,k} \boldsymbol{f}_l D(\boldsymbol{x}_{i,j,k} - \boldsymbol{X}_l) \Delta S_l \Delta h, \tag{3.8}$$

where ΔS_l is the area (in 3D) of the of the surface boundary at a Lagrangian point l.

3.2.2 Newton's equations of motion

For the simulation of a moving particle, the equations of motion for each particle must be considered. Newton's equation of particle translational velocity ($\boldsymbol{U}_p$) reads:

$$M_p \frac{d\boldsymbol{U}_p}{dt} = -\int_S \boldsymbol{\sigma} \cdot d\boldsymbol{S} + (\rho_p - \rho_f) V_p \boldsymbol{g} + \boldsymbol{F}^c, \tag{3.9}$$

where, ρ_p, V_p and M_p are the particle density, volume and mass respectively, $\boldsymbol{\sigma}$ is the fluid stress tensor and $\boldsymbol{U}_p$ is the translational velocity of particle. Subscripts f and p indicate the fluid and the particle, respectively. Here, $\boldsymbol{S}$ denotes the control surface. The first term on the right-hand side of Eq. (3.9) is the interaction force between the particle and the surrounding fluid, the second term is the buoyancy force and the third term ($\boldsymbol{F}^c$) includes particle-particle and particle-wall collision forces. The first term on the RHS consists of stationary surface force and internal fluid mass term:

$$-\int_S \boldsymbol{\sigma} . d\boldsymbol{S} = -\rho_p \int \boldsymbol{f}_l dV + M_f \frac{d\boldsymbol{U}_p}{dt}. \tag{3.10}$$

In the present study the approach already suggested by Feng and Michaelides [90] is adopted to evaluate internal fluid mass effect wherever this effect is considered. This method is useful when fluid and particle have the same density. Therefore, the particle velocity can be updated at each iteration via the following equation:

$$M_p \frac{d\boldsymbol{U}_p}{dt} = -\rho_p \sum_{l=1}^{N_l} \boldsymbol{f}_l \Delta V_l + M_f \frac{d\boldsymbol{U}_p}{dt} + (\rho_p - \rho_f) V_p \boldsymbol{g} + \boldsymbol{F}^c, \tag{3.11}$$

Above equation is discretized as:

$$\boldsymbol{U}_p^{n+1} = \boldsymbol{U}_p^n + \frac{1}{M_p}\left(-\rho_p \sum_b \boldsymbol{f}_l^n \Delta V_l\right)\Delta t + \frac{M_f}{M_p}\left(\boldsymbol{U}_p^n - \boldsymbol{U}_p^{n-1}\right) + \frac{1}{M_p}\left(M_p - M_f\right)\boldsymbol{g}\Delta t + \frac{1}{M_p}\boldsymbol{F}^c \Delta t, \tag{3.12}$$

where $M_f = M_p \rho_f / \rho_f$. Newton's equation of angular particle motion reads

$$\boldsymbol{T} = I_p \cdot \frac{d\boldsymbol{\Omega}_p}{dt} + \boldsymbol{\Omega}_p \times (I \cdot \boldsymbol{\Omega}), \tag{3.13}$$

where $\boldsymbol{\Omega}_p$ is the angular velocity of the particle, $\boldsymbol{T}$ is the total torque exerted on particle center and I_p is the mass moment of inertia of particle. In case of circular, elliptical and spherical particles, I is constant and is equal to $0.5 M_p R^2$, $0.25 M_p (R_1^2 + R_2^2)$ and $0.4 M_p R^2$, respectively. Here, R denotes the radius of circle or sphere and R_1 and R_2 are the radii of an ellipse. Therefore, the second term on the right hand side of Eq. (3.13) can be omitted and this equation can be rearranged as:

$$-\int_S (\boldsymbol{X}_l - \boldsymbol{X}_c) \times \boldsymbol{\sigma} \cdot d\boldsymbol{S} = I_p \frac{d\boldsymbol{\Omega}_p}{dt}. \tag{3.14}$$

In the above equation $\boldsymbol{X}_l$ and $\boldsymbol{X}_c$ are the position vectors of a Lagrangian boundary surface point and the center of particle, respectively. Equation (3.14) can be discretized as:

$$\boldsymbol{\Omega}_p^{n+1} = \boldsymbol{\Omega}_p^n + (\frac{1}{I_p})\left[-\sum_l (\boldsymbol{X}_l - \boldsymbol{X}_c) \times \boldsymbol{f}_l^n \Delta V_l\right]\Delta t + \left(\frac{I_f}{I_p}\right)\left(\boldsymbol{\Omega}_p^n - \boldsymbol{\Omega}_p^{n-1}\right). \tag{3.15}$$

For spheroidal particles the second term on the right hand side of Eq. (3.13) must be maintained. For this case, the concept of quaternions is used to solve this equation, as will be described later in Chapter 7. After calculating the particle translational velocity at $n+1$, one can update the particle new center position:

$$\boldsymbol{X}_c^{n+1} = \boldsymbol{X}_c^n + 0.5\left(\boldsymbol{U}_p^{n+1} + \boldsymbol{U}_p^n\right)\Delta t. \tag{3.16}$$

The particle orientation is updated by using the appropriate 2D or 3D rotation matrix. The value of $\boldsymbol{U}^d$ for each Lagrangian point is then determined by:

$$\boldsymbol{U}^d(X_l) = \boldsymbol{U}_p + \boldsymbol{\Omega}_p \times (\boldsymbol{X}_l - \boldsymbol{X}_c). \tag{3.17}$$

3.2.3 Collision model

When simulating particles in the fluid, collision models are required to prevent particles from penetrating into other particles or walls. In this thesis the well-known repulsive force model of Glowinski [72] and Feng and Michaelides [82] is adopted. For circular and spherical particles, the repulsive force on the i^{th} particle from the j^{th} particle reads

$$\boldsymbol{F}_{i,j}^{p-p} = \begin{cases} 0, & d_{ij} > R_i + R_j + \zeta \\ \frac{c_{ij}}{\varepsilon_p}\left(\frac{d_{ij}-R_i-R_j-\zeta}{\zeta}\right)^2\left(\frac{\boldsymbol{x}_i-\boldsymbol{x}_j}{d_{ij}}\right), & R_i + R_j < d_{ij} \leq R_i + R_j + \zeta \\ \left(\begin{array}{c} \frac{c_{ij}}{\varepsilon_p}\left(\frac{d_{ij}-R_i-R_j-\zeta}{\zeta}\right)^2 \\ +\frac{c_{ij}}{E_p}\left(\frac{R_i+R_j-d_{ij}}{\zeta}\right) \end{array}\right)\left(\frac{\boldsymbol{x}_i-\boldsymbol{x}_j}{d_{ij}}\right), & d_{ij} \leq R_i + R_j \end{cases} \tag{3.18}$$

where $\boldsymbol{x}_i$ and $\boldsymbol{x}_j$ are the particles center position vector; the parameter c_{ij} is the force scale that is chosen to be the buoyancy force on the body for the case of particle sedimentation; ε_p is the stiffness parameter for particle-particle collisions; E_p is also a stiffness parameter but has a lower value than ε_p to ensure a larger repulsive force in order to avoid unphysical behavior during particle overlap; R_i and R_j are the radii of the particles, ζ is the range of the repulsive force and $d_{ij} = |\boldsymbol{x}_i - \boldsymbol{x}_j|$ is the distance between particle centers. A similar formula is used for particle-wall collision:

$$\boldsymbol{F}_{i}^{p-w} = \begin{cases} 0, & d'_i > 2R_i + \zeta \\ \frac{c_{ij}}{\varepsilon_w}\left(\frac{d'_i-2R_i-\zeta}{\zeta}\right)^2\left(\frac{\boldsymbol{x}_i-\boldsymbol{x}'_i}{d'_i}\right), & 2R_i < d'_i \leq 2R_i + \zeta \\ \left(\begin{array}{c} \frac{c_{ij}}{\varepsilon_w}\left(\frac{d'_i-2R_i-\zeta}{\zeta}\right)^2 \\ +\frac{c_{ij}}{E_w}\left(\frac{2R_i-d'_i}{\zeta}\right) \end{array}\right)\left(\frac{\boldsymbol{x}_i-\boldsymbol{x}'_i}{d'_i}\right), & 2R_i < d'_i \leq 2R_i + \zeta \end{cases} \tag{3.19}$$

where $\boldsymbol{x}'_i$ is the coordinate vector of the center of the nearest imaginary particle located on the other side of the wall boundary and $d'_i = |\boldsymbol{x}_i - \boldsymbol{x}'_i|$ is the distance to this imaginary particle. As previously, ε_w is the stiffness parameter for particle-wall collisions and E_w is another stiffness parameter with a lower value than ε_w.

3.2.4 LBM with force term

In order to take into account fluid-particle interactions, a force term needs to be added to the flow solver part. The regular formulation of SRT-LBM without a force term is given by

$$\text{collision} : f_i^{'}(\boldsymbol{x}, t) = f_i(\boldsymbol{x}, t) - \frac{1}{\tau}\left[f_i(\boldsymbol{x}, t) - f_i^{eq}(\boldsymbol{x}, t)\right], \tag{3.20}$$

$$\text{streaming} : f_i(\boldsymbol{x} + \boldsymbol{c}_i\Delta t, t + \Delta t) = f_i^{'}(\boldsymbol{x}, t), \tag{3.21}$$

where f_i is the distribution function of particles moving with speed $\{\boldsymbol{c}_i\}$, τ is the non-dimensional relaxation time and Δt is the time step. The equilibrium distribution function f_i^{eq} is defined as:

$$f_i^{eq} = \omega_i \rho_f \left[1 + \frac{\boldsymbol{c_i} \cdot \boldsymbol{u}}{c_s^2} + \frac{(\boldsymbol{c_i} \cdot \boldsymbol{u})^2}{2c_s^4} - \frac{|\boldsymbol{u}|^2}{2c_s^2} \right], \tag{3.22}$$

where ω_i is the weight coefficient and macroscopic quantities including density and velocity are defined by the 0^{th} and 1^{st} moments of the probability distribution function, respectively:

$$\rho_f = \sum_i f_i, \tag{3.23}$$

$$\rho_f \boldsymbol{u} = \sum_i \boldsymbol{c}_i f_i. \tag{3.24}$$

In the present study three schemes will be considered to describe the force term in the simulations. **Scheme 1.** Guo *et al.* [91] proposed the split-forcing LBM, which enables the LBM to recover the NSE (mass and momentum conservation equations) with second-order accuracy (compared with lumped forcing). In this formulation, the force term is first added to LBM collision step:

$$f_i'(\boldsymbol{x}, t) = f_i(\boldsymbol{x}, t) - \frac{1}{\tau} \left[f_i(\boldsymbol{x}, t) - f_i^{eq}(\boldsymbol{x}, t) \right] + F_i(\boldsymbol{x}, t) \Delta t, \tag{3.25}$$

where $F_i(\boldsymbol{x}, t)$ is defined by

$$F_i(\boldsymbol{x}, t) = \left(1 - \frac{1}{2\tau} \right) \omega_i \left[3 \frac{\boldsymbol{c}_i - \boldsymbol{u}(\boldsymbol{x}, t)}{c_s^2} + 9 \frac{\boldsymbol{c}_i \cdot \boldsymbol{u}(\boldsymbol{x}, t)}{c_s^4} \boldsymbol{c}_i \right] \cdot \boldsymbol{F}(\boldsymbol{x}, t). \tag{3.26}$$

In the second step (after streaming), the macroscopic velocity is calculated through

$$\rho_f \boldsymbol{u} = \sum_i \boldsymbol{c}_i f_i + \frac{\Delta t}{2} \boldsymbol{F}. \tag{3.27}$$

Scheme 2. As suggested by Shan and Chen [18], Eq. (3.20) is used but the equilibrium velocity in Eq. (3.22) is shifted using $\boldsymbol{v}$ instead of $\boldsymbol{u}$:

$$\boldsymbol{v} = \boldsymbol{u} + \frac{\tau}{\rho_f} \boldsymbol{F}. \tag{3.28}$$

Scheme 3. Originating from the lattice gas automata [7, 92], a force term is introduced into Eq. (3.25) with the following form

$$F_i(\boldsymbol{x}, t) = 3 \Delta \boldsymbol{x} \omega_i \boldsymbol{c}_i \cdot \boldsymbol{F}(\boldsymbol{x}, t). \tag{3.29}$$

3.2.5 Numerical approach

In order to be able to implement the numerical schemes discussed previously, the following computation algorithm is used, involving 8 steps:

1. Set the initial value of $\boldsymbol{u}(\boldsymbol{x},0)$, $\boldsymbol{F}(\boldsymbol{x},0)$ and $\rho_f(\boldsymbol{x},0)$ and compute the initial values of $f_i(\boldsymbol{x},0)$ by Eq. (3.22). Assign $\boldsymbol{U}_p(0)$ and $\boldsymbol{\Omega}_p(0)$.
2. Perform LBM calculations (sequence for scheme 1: Eqs. (3.26), (3.25), (3.21), (3.23), (3.27); scheme 2: Eqs. (3.28), (3.20), (3.21), (3.23), (3.24); scheme 3: Eqs. (3.29), (3.25), (3.21), (3.23), (3.24).
3. Calculate the Lagrangian velocity $\boldsymbol{u}^{noF}(\boldsymbol{X}_l,t)$ by interpolation from $\boldsymbol{u}(\boldsymbol{x},t)$ using Eq. (3.4).
4. Calculate collision forces by Eqs. (3.18) and (3.19) for all particles.
5. Compute Lagrangian force $\boldsymbol{f}(\boldsymbol{X}_l,t)$ by Eq. (3.3).
6. Spread forces of step 5 from Lagrangian to Eulerian nodes by Eq. (3.8).
7. Use equations of motion to update particle center position and orientation as well as translational and angular velocities (see Section 3.2.2).
8. Loop back to step 2 until end of simulation.

3.3 Simulation results

In this section, simulation results for different particle shapes and geometries are presented for problems of increasing complexity. The accuracy of the developed numerical tool is checked by comparison with benchmarks, involving both numerical and experimental results from other groups.

3.3.1 Sedimentation of a single circular particle in 2D

The first validation case is the sedimentation of a single circular particle under gravity in a vertical channel, following the configuration described in [93]. The domain size is 2×6 cm^2 and the particle radius is 0.25 cm. The fluid density (ρ_f) and dynamic viscosity (μ_f) are 1000 kg/m^3 and 0.01 Pa·s, respectively, and the particle density (ρ_p) is 1250 kg/m^3. The fluid and the particle are initially at rest. The particle starts its motion at the location [1.0, 4.0] cm from the bottom left corner of the domain. For this test case a lattice size of 50 μm is employed (400×1200 grid points) and the relaxation parameter is set to $\tau = 0.53$. Figure 3.1 depicts the results obtained with different schemes for the vertical particle velocity versus time, when considering the internal fluid mass effect. It can be observed that our results are identical to that obtained by Kang [93] using the IB–LBM. This is a first confirmation of the accuracy of

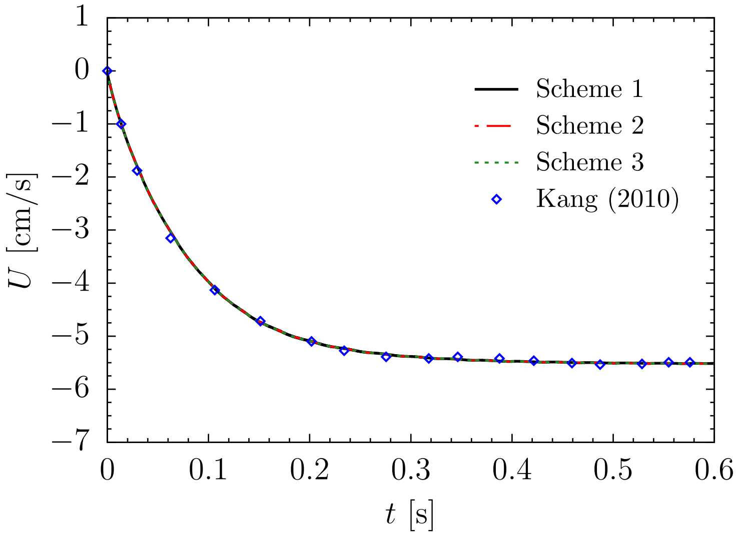

Figure 3.1: Time evolution of a single 2D circular particle vertical velocity computed with three force schemes and compared to those of Kang for settling in a closed square under gravity (Sec. 3.3.1)

the direct–forcing IB–LBM for moving particles. Furthermore, the results of the three schemes cannot be distinguished, showing that all three can be equally employed for this particular configuration. By comparing the computational time for the three cases on a standard desktop PC (Core i5, 3.3 GHz CPU, 16 GB RAM) it was observed that scheme 2 [18] is slightly faster than scheme 3, while scheme 1 is the slowest one.

3.3.2 Sedimentation of two circular particles in 2D

In this section, we investigate the sedimentation of two circular particles in a viscous fluid, considering the well–known case of "drafting, kissing, and tumbling" (DKT) motion [94]. Physical conditions and numerical parameters are summarized in Tables 3.1 and 3.2, respectively, and follow the setup considered in [93]. Particle positions are relative to an origin set at the left-bottom corner of the computational domain. Initially, the first particle is 10 μm off the channel center and the second particle is -10 μm off the channel center, 0.5 cm below the first particle. Both particles and the fluid have zero initial velocities. Figure 3.2 shows the variation in the vertical velocity of the two particles with time, compared with the results of Uhlmann [80] obtained by an explicit diffuse DF scheme applied on the NS equation. Before the collision of the particles (∼0.17 s), all results are identical. The slightly different vertical velocity variations observed after particle kissing for different schemes can be attributed to differences in the numerical approach and the particle collision models employed. Considering now the three different schemes used, Fig. 3.2 shows that the results of Scheme 3 indicate a noticeable and increasing deviation for the second particle compared with the two other schemes at the end of the process. Figure 3.3 depicts the vertical fluid velocity contour in the domain. Note that the leading particle creates a wake of low pressure. The trailing particle is caught in this wake

Table 3.1: Physical conditions for the sedimentation of two circular particles in 2D

Channel size [cm]	Particles diameter [cm]	Particle density [kg/m^3]	Initial position [cm]	Fluid density [kg/m^3]	Fluid viscosity [Pa·s]
6×2	0.25	1500	1: (5, 1.001) 2: (4.5, 0.999)	1000	0.001

Table 3.2: Numerical parameters for the sedimentation of two circular particles in 2D domain

Lattice size [μm]	Time step [μs]	Domain size	Relaxation time	Collision threshold (ζ)	Collision stiffness (ε_p, E_p)
50	25	1200×400	0.53	2	0.1, 0.05

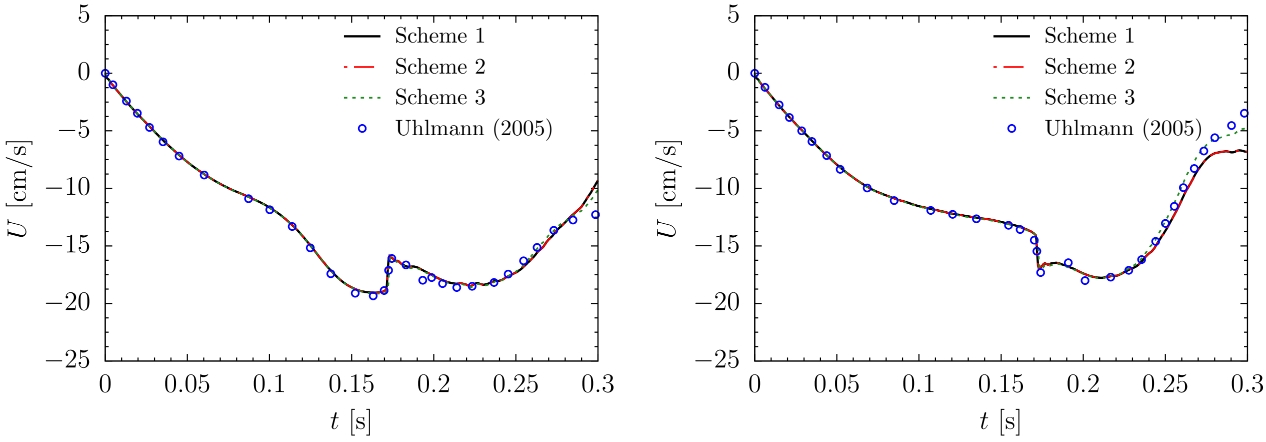

(a) (b)

Figure 3.2: Settling velocity U of (a) particle 1, and (b) particle 2 as a function of time t for the DKT test case of two circular particles computed by three force schemes and validated by NS based simulations of Uhlmann (2005) (Sec. 3.3.2)

and therefore falls faster than the leading one (drafting). The increased velocity of the trailing particle creates a kissing contact with the leading particle. During contact, the two particles form an elongated body along the streaming direction. This state is unstable, and as a result, the particles tumble under the influence of a coupling force that brings them into a stable state.

3.3.3 Sedimentation of an elliptical particle in 2D

In this section, the sedimentation of an elliptical particle is considered in a 2D flow, as previously studied in [85], [95], and [96]. The configuration is depicted in Fig. 3.4, where a and b are the lengths of the major and minor axes, respectively. In physical units, a and b are 0.1 and 0.05 cm, respectively, the gravitational constant is 9.8 m/s^2, acting along the x-axis, and H the width of the channel (here set to 0.4 cm). The variable θ represents the orientation of the particle, which is initially equal to 45°. The kinematic viscosity of the fluid is 10^{-6} m^2/s. Three density

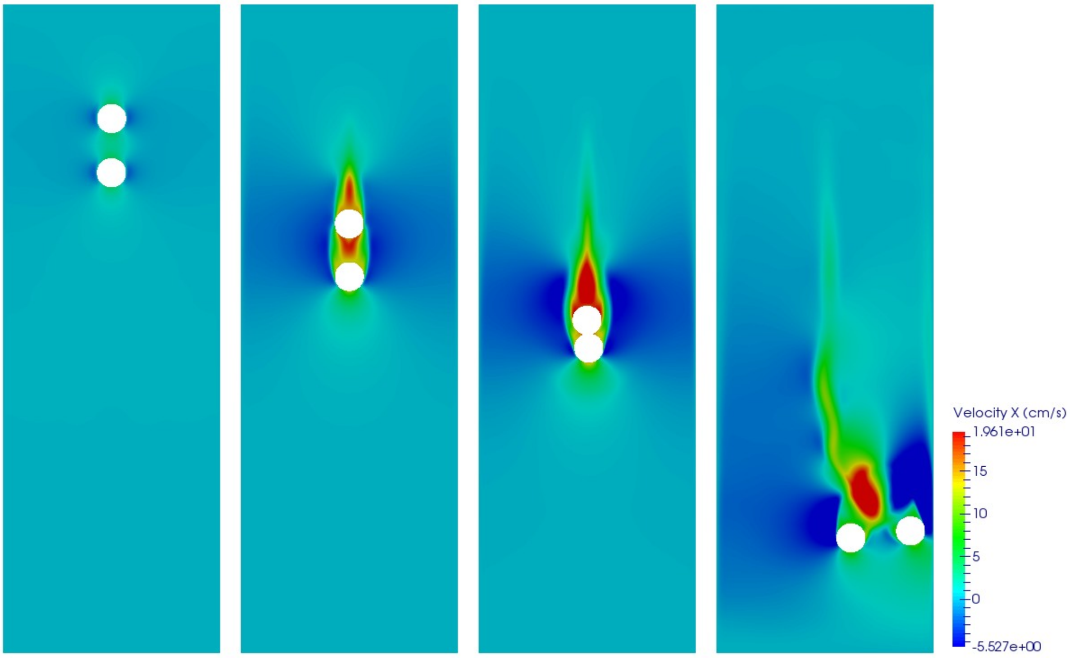

Figure 3.3: Contours of vertical velocity and particles position at $t = 0.025$, 0.125, 0.175, and 0.3 s (from left to right) for a 2D-DKT simulation in a closed box (Sec. 3.3.2)

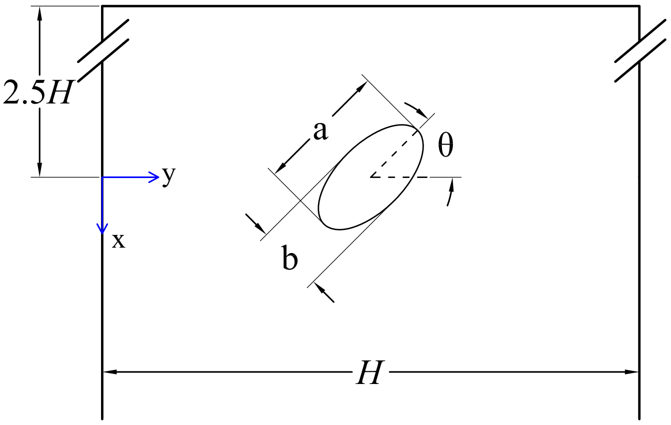

Figure 3.4: Schematic of an elliptical particle settling under gravity in a channel with particle initial inclination angle θ and aspect ratio a/b

ratios (particle to fluid) of $\rho_r = 1.01$, 1.1, and 1.5 are considered. The computational domain is 3500×200 and τ is set to 0.6364 for all three cases. The center of the elliptical particle starts its motion at the initial position of $(x_c, y_c) = (0, 0.5H)$, where the origin of coordinates is located at distance $2.5H$ from the upper wall of the channel. Halfway bounce-back boundary condition is applied to the channel walls. On the boundary of the ellipse, 250 Lagrangian nodes are placed. In Figs. 3.5–3.7, comparisons are shown concerning particle trajectory and orientation using Scheme 1. Clearly, the results obtained are in excellent agreement with other published numerical results. For a density ratio of $\rho_r = 1.5$, the elliptical particle shows oscillations around the centerline; for lower density ratios, the particle angle rapidly goes to zero.

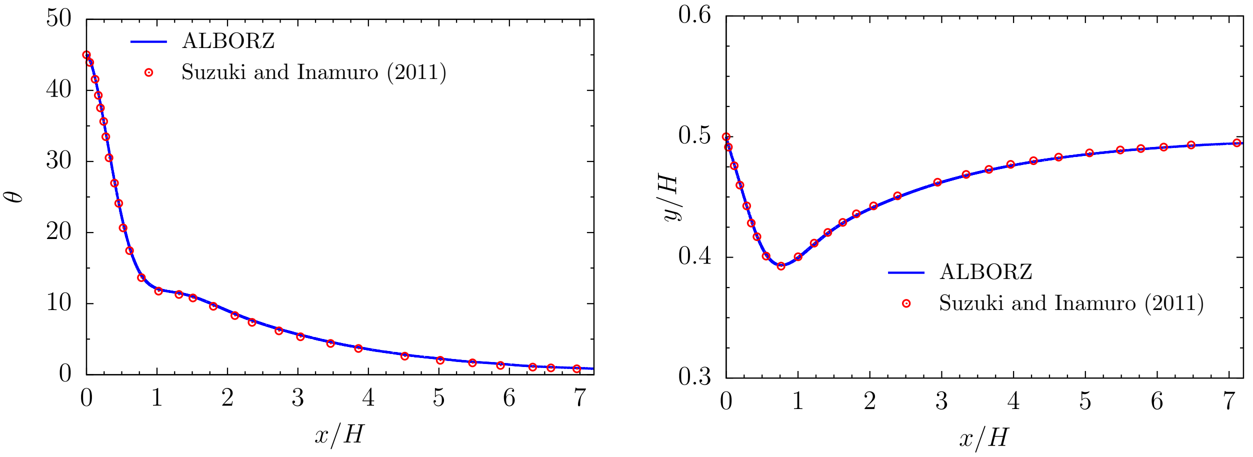

(a) (b)

Figure 3.5: (a) Orientation angle θ with respect to the horizontal axis, and (b) location of an elliptical particle settling under gravity in a long channel as a function of particle center x–position ($\rho_r = 1.01$) compared to simulation results of Suzuki and Inamuro (2011) (Sec. 3.3.3)

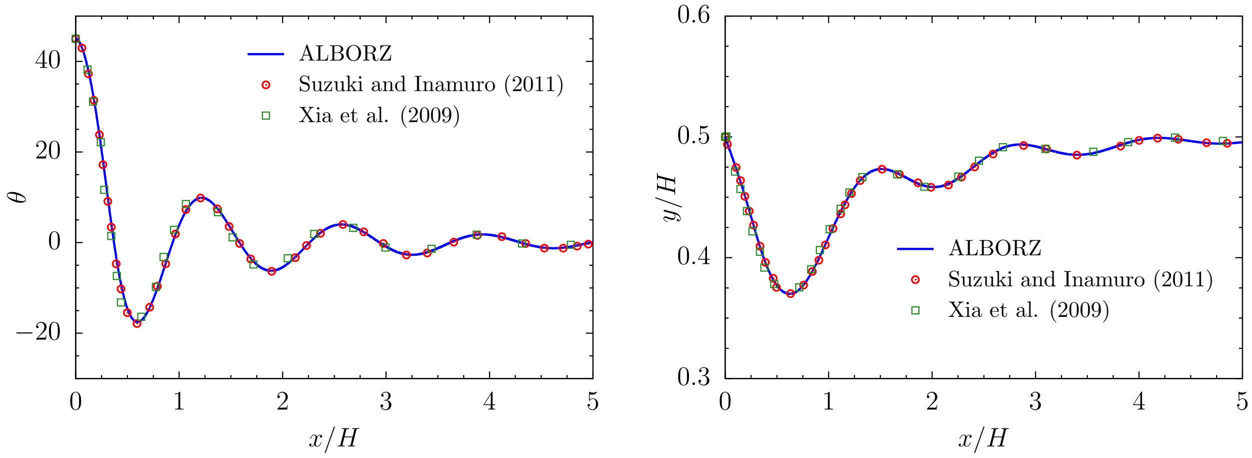

(a) (b)

Figure 3.6: (a) Orientation angle θ with respect to the horizontal axis, and (b) location of an elliptical particle settling under gravity in a long channel as a function of particle center x–position ($\rho_r = 1.1$) compared to simulation results of Suzuki and Inamuro (2011) (Sec. 3.3.3)

3.3.4 Sedimentation of a single sphere

After successful comparisons of 2D flows, 3D flows were then considered. First, the sedimentation of a sphere in an enclosure was modeled, comparing the results obtained with the available experimental data of Ten Cate *et al.* [97]. The test case (see Fig. 3.8) involves a box of size $10 \times 10 \times 16$ cm^3, and a spherical particle of diameter $D_p = 1.5$ cm and density $\rho_p = 1120$ kg/m^3. The fluid is initially at rest and the particle is released at a height of 12 cm from the bottom of the enclosure, before falling under gravity ($g = 9.8$ m/s^2). For this simulation, the domain is divided into a $200 \times 200 \times 320$ lattice grid. The number of Lagrangian force points on the sphere is $N_l = 2828$ and the area allocated to each Lagrangian point is calculated using the

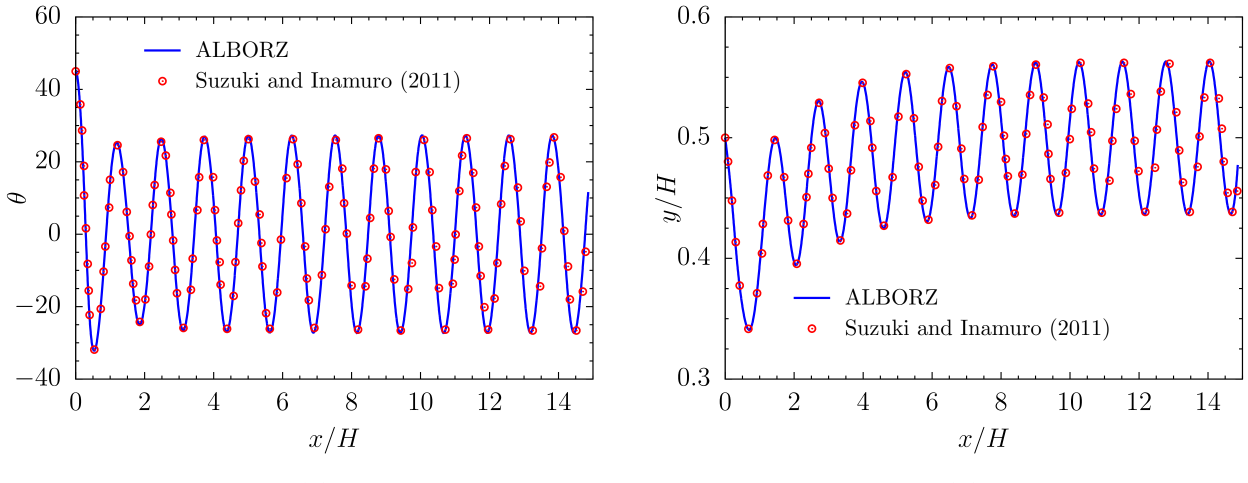

(a) (b)

Figure 3.7: (a) Orientation angle θ with respect to the horizontal axis, and (b) location of an elliptical particle settling under gravity in a long channel as a function of particle center x–position ($\rho_r = 1.5$) compared to simulation results of Suzuki and Inamuro (2011) (Sec. 3.3.3)

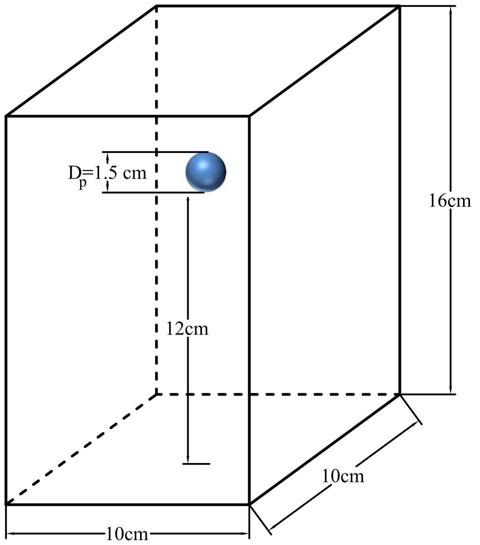

Figure 3.8: Schematic of the simulation domain for spherical particle sedimentation (Sec. 3.3.4)

method of Uhlmann [80]:

$$\Delta V_l = \frac{\pi \Delta x}{3N_l}\left(12\left(\frac{D_p}{2}\right)^2 + (\Delta x)^2\right). \tag{3.30}$$

A uniform distribution of the Lagrangian points on the spherical surface of the particles is established using the explicit spiral set proposed by Saff and Kuijlaars [98]. Based on the particle sedimentation velocity in an infinite domain, four particle Reynolds numbers are considered. The fluid density varies in these cases from 960 to 970 kg/m^3 and its dynamic viscosity ranges from 0.058 to 0.373 Pa·s. Particle collisions with the walls are determined using Eq. (3.19) with $\varepsilon_p = 0.1$, $E_p = 0.01$ and $\zeta = 1$. Physical and numerical conditions for this simulation are listed in Table 3.3. Internal fluid mass has been included in our simulations. The notion of

Table 3.3: Fluid properties in the experiment and simulation for sedimentation of a single sphere ($D_p = 1.5$ cm) in a closed box

Case	Re	ρ_f [kg/m^3]	$\mu_f \times 10^3$ [Pa·s]	τ
1	1.5	970	373	1.1
2	4.1	965	212	0.8
3	11.6	962	113	0.6
4	32.2	960	58	0.6

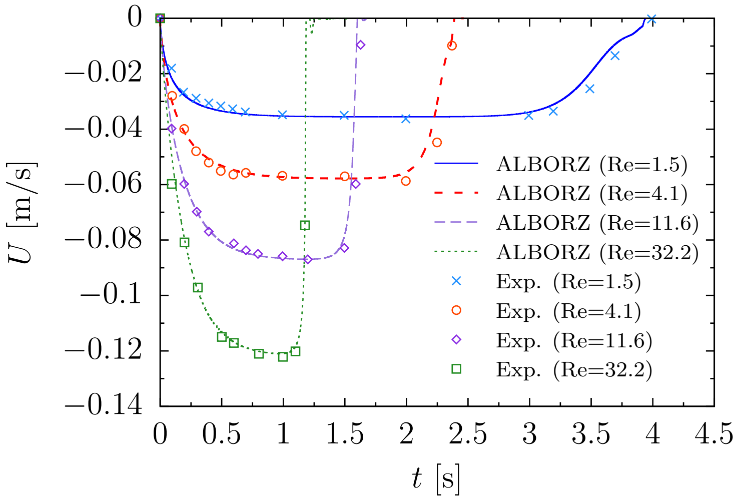

Figure 3.9: Settling velocity of a single spherical particle vs. time computed for different Reynolds numbers and compared to the experimental data of Ten Cate et *al.* (2002) (Sec. 3.3.4)

Table 3.4: Comparison of the computational time for single sphere sedimentation

Scheme	Scheme 1	Scheme 2	Scheme 3
Duration of 50 iterations (s)	146	84	108

corrected radius is used as well. The forcing points then reside on a spherical surface of radius $r_b = \sqrt[3]{\frac{r^3+(r-\Delta x)^3}{2}}$.

Figure 3.9 depicts our results for the particle vertical velocity, compared with the experimental data. Obtained results agree almost perfectly with the experimental measurements, highlighting again the validity of the numerical procedure. Finally, with Re = 32.2, Table 3.4 compares the computational times for each of the three schemes; Scheme 2 is again the fastest and Scheme 1 the slowest.

3.3.5 DKT motion in 3D

To further assess the performance of the developed IB-LBM approach, the case of two spheres falling in a closed container is considered using the configuration considered in [99, 100]. A DKT motion similar to that described in 2D case is observed. The same configuration was also studied by Breugem [101] using IBM combined with NS equations. The author investigated the effect of

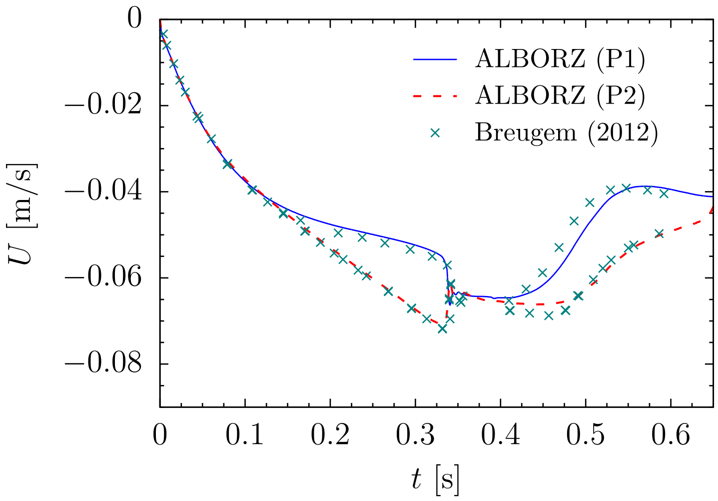

Figure 3.10: Vertical velocity U of two particles vs. time for a 3D DKT motion compared to the available NS simulations of Breugem (2012) (Sec. 3.3.5)

internal fluid mass and corrected radius using multi–DF. For our test, the container dimension is 0.04 m × 0.01 m × 0.01 m in the x-, y- and z–direction, respectively. Gravity acts in the x-direction ($g = 9.8$ m/s^2). Both particles have a diameter of $D_p = 1.67 \times 10^{-3}$ m and density of $\rho_p = 1140$ kg/m^3. The density of the fluid is $\rho_f = 1000$ kg/m^3 and its kinematic viscosity is $\nu = 10^{-6}$ m^2/s. At $t = 0$ s, the two spheres are placed in the container above each other at a distance $x_c = 0.035$ and $x_c = 0.0316$ m from the container bottom wall, respectively. To initiate the DKT motion, the particles are again placed slightly off center. Therefore, the upper sphere is positioned at $y_c = z_c = 0.505$ cm, whereas the lower sphere is placed at $y_c = z_c = 0.495$ cm. The fluid and the spheres are initially at rest. For the simulation, a computational domain of 384 × 96 × 96 lattice units is used and a relaxation parameter of $\tau = 0.6$ is retained. To model collisions, the parameters $\varepsilon_p = 2$, $E_p = 0.1$, and $\zeta = 1$ are used.

In Fig. 3.10, DF IB-LBM results for the particle sedimentation velocity are compared with those of Breugem [101]. In both cases, internal fluid mass and corrected radius are taken into account. Our simulation reproduces correctly the DKT behavior, and in particular, before collision, an excellent agreement is found. After kissing, different behaviors are expected and indeed observed in consequence of the different collision models and collision factors employed in both studies. Figure 3.11 compares the results obtained for the settling velocity of the upper particle with and without internal fluid mass, as well as with and without corrected radius. When either internal fluid mass or corrected radius is neglected, the particle falls more slowly. For the same reason, the kissing time (first collision time) shifts to later times if internal fluid mass and/or corrected radius are not included in the simulation. This effect of internal fluid mass has been previously observed in the simulations of Kang [93]. Having found that for a single particle these two effects must be included to reproduce the experimental results, there is a strong inference that internal fluid mass and corrected radius must also be taken into account for 3D simulations of multiple particles.

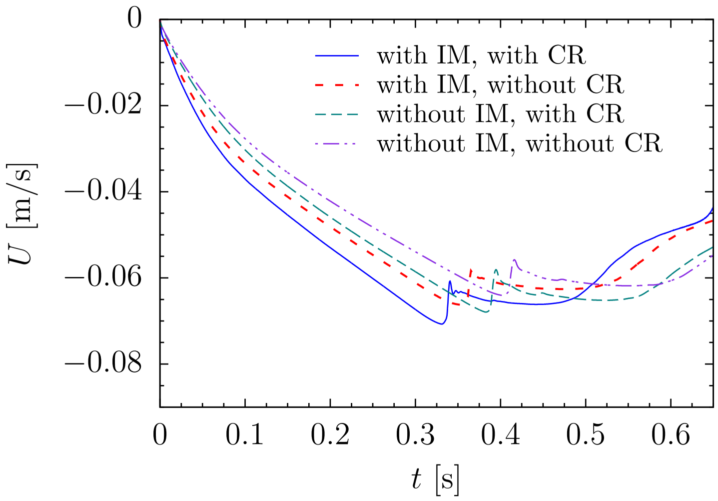

Figure 3.11: Effect of internal fluid mass (IM) and corrected radius (CR) on settling velocity U of the initially upper particle in DKT motion of two spherical particles versus physical time of simulation (Sec. 3.3.5)

3.4 Summary

In this chapter, the DF IB-LBM approach has been implemented and successfully applied to different cases of increasing complexity involving 2D and 3D flows. The LBM was used for the fluid and the IBM used to take into account particles in the fluid. In the DF-IBM, the force density term was naturally determined as part of the calculation. To transfer the force term from the Lagrangian to the Eulerian nodes, discrete delta functions are used. By comparison with published reference data, the motion of circular and elliptical (in 2D), and spherical particles (in 3D) can be accurately computed with the resulting code, ALBORZ. Three different force schemes have been considered in the LBM, for which computational speed and accuracy were compared. Shan-Chen model was found to be faster than others. Also both internal fluid mass and corrected radius (i.e., retraction of the Lagrangian grid from the surface toward the interior of the particles) lead to significant changes in the predicted particle velocity, and should therefore be taken into account. The internal fluid mass should have even more impact at higher density ratios. Further tests show that the corrected radius has less impact at very fine grid resolution.

Up to now, the flow regime in all cases was laminar and isothermal. After this successful validation, the current code can be used for more complicated applications by including heat transfer or turbulence in the computations. The simulation of non-isothermal and turbulent particle-laden flows is the subject of Chapters 4 and 6, respectively. Next chapter concerns particulate flows with heat transfer to/from particles. The topic is important and relevant to many chemical and natural processes.

Chapter 4

Non-isothermal Particulate Flows

4.1 Introduction

The main goal of this chapter is the extension of the developed LB solver to different non-isothermal flows with the main focus on two-phase flows with suspended particles. The numerical simulation of particulate flows is already quite complex. This complexity increases even further when heat transfer must be taken into account. Although there has been an increasing interest for corresponding studies in recent years, only few publications can be found. Gan *et al.* [102] used the ALE-finite element method to model the motion of particles having heat transfer with surrounding fluid; however, this method was computationally expensive. Yu *et al.* [103] extended the DLM/FDM to simulate two dimensional (2D) particulate flows with heat transfer. They considered particles of constant or varying temperature. Kim and Choi [104] and Pacheco [105] applied IBM to heat transfer between a fluid and stationary objects. Feng and Michaelides [106] developed an IB finite-volume technique and applied this approach to heat transfer in particle-laden flows, where particles were moving. They verified their results by comparison with those of Yu *et al.* [103]. They were also able to use this approach at $\rho_r C_{p,r} = 1$ (ρ_r: particle to fluid density ratio; $C_{p,r}$: particle to fluid specific heat ratio) and tackle the instability problems appearing around this threshold. However, they assumed a uniform temperature inside the particle, which is only valid for high thermal conductivities of the solid particle. Dan and Wachs [107] used the DLM method to model heat transfer problems in 3D with constant particle temperature. Kang and Hassan [108] applied two types of thermal IB-LBM, a hybrid model and a simplified double-population method to simulate heat transfer between particles and the fluid. However, the simulation was limited to 2D and particles had a fixed temperature. Wachs [109] studied the rising of 3D catalyst particles using a parallelized DNS-IBM with a fictitious domain method. Deen [110] implemented DNS-IBM to study the heat transfer in both stationary beds and fluidized beds. Ström and Sasic [111] used volume of fluid approach and modeled the motion of solid stationary and moving particles in the presence of heat transfer effects in both 2D and 3D domains. Weiwei [112] developed a novel IBM under the framework of NS solver and applied it to non-isothermal flows in the presence of solid particles. Xia *et al.* [113] modeled heat transfer from 3D moving spheres using a ghost-cell based

IBM. Recently, Zhang *et al.* [114] proposed a combined thermal LBM-IBM-DEM and simulated heat transfer between single and multiple particles with carrier fluid.

Therefore, the combination of thermal IBM with LBM is an interesting topic. In this work we aim to extend this approach to 3D cases in which fully-resolved spherical particles are moving while having heat exchange with surrounding fluid flow; the issue that has not been addressed by above mentioned articles. The case of variable particle temperature will be studied as well; both in two- and three dimensional simulations. For this purpose, a force density and an energy density term are introduced into the LBM equations. These force and energy terms are evaluated through a direct-forcing and direct-heating IBM, respectively. Part of the results of this chapter have been published in [115].

4.2 Model formulation

4.2.1 Thermal LBM

The formulation of LBM for isothermal flows has been presented in Chapters 2, 3. In this chapter, the flow hydrodynamics will be described by the same formulation

$$f_i(\boldsymbol{x}+\boldsymbol{c}_i\Delta t, t+\Delta t) - f_i(\boldsymbol{x}, t) = -\frac{1}{\tau_f}\left[f_i(\boldsymbol{x}, t) - f_i^{eq}(\boldsymbol{x}, t)\right], \tag{4.1}$$

where f_i is the distribution function of particles moving with speed $\{\boldsymbol{c}_i\}$, τ_f is the non-dimensional relaxation time and Δt is the time step. The equilibrium distribution function f_i^{eq} is defined as:

$$f_i^{eq} = \omega_i \rho_f \left[1 + \frac{\boldsymbol{c_i}\cdot\boldsymbol{u}}{c_s^2} + \frac{(\boldsymbol{c_i}\cdot\boldsymbol{u})^2}{2c_s^4} - \frac{|\boldsymbol{u}|^2}{2c_s^2}\right], \tag{4.2}$$

where ω_i is the weight coefficient and macroscopic quantities including density and velocity are defined by the 0^{th} and 1^{st} moments of the probability distribution function, respectively:

$$\rho_f = \sum_i f_i, \tag{4.3}$$

$$\rho_f \boldsymbol{u} = \sum_i \boldsymbol{c}_i f_i. \tag{4.4}$$

There are generally two types of thermal LBM to model heat transfer. One approach is to use a double-distribution function; the second one is a hybrid model. In the former one two distribution functions are considered, one for the momentum transport and one for energy transport. Different methodologies have been proposed in this regard including passive scalar model [25], internal energy distribution function [45, 46] , and total energy distribution function [44]. In the hybrid scheme one has to add another numerical method like finite difference to compute the temperature field while a hydrodynamic LBM model is used for the flow field. In the present study, the model proposed by Peng *et al.* [45] is used. It relies on a simplified form of the internal energy distribution function model. Therefore, in a similar way to the flow field, the temperature field can be described using a separate distribution function (g) and its relevant relaxation time τ_g:

$$g_i(\boldsymbol{x} + \boldsymbol{c}_i \Delta t, t + \Delta t) - g_i(\boldsymbol{x}, t) = -\frac{1}{\tau_g}\left[g_i(\boldsymbol{x}, t) - g_i^{eq}(\boldsymbol{x}, t)\right]. \tag{4.5}$$

The equilibrium distribution function for the temperature field is defined as [116]:

$$g_i^{eq} = \omega_i \rho_f T \left[1 + \frac{\boldsymbol{c_i} \cdot \boldsymbol{u}}{c_s^2} + \frac{(\boldsymbol{c_i} \cdot \boldsymbol{u})^2}{2c_s^4} - \frac{|\boldsymbol{u}|^2}{2c_s^2}\right], \tag{4.6}$$

Thermal diffusivity, α, is defined in terms of its relaxation times:

$$\alpha = \left(\tau_g - \frac{1}{2}\right)\frac{(\Delta x)^2}{\Delta t}. \tag{4.7}$$

After evaluation of each distribution function at lattice nodes, temperature is calculated via:

$$\rho_f T = \sum_i g_i \tag{4.8}$$

When the effects of compression work and the viscous heat dissipation are negligible, the above formulation recovers the energy equation. In this study, the Boussinesq approximation is applied to calculate the buoyancy force term ($\boldsymbol{F}_B$) for the flow field equation. It assumes the buoyancy term to depend linearly on the temperature difference with the bulk flow, which leads to the coupling of the energy and momentum equations as:

$$\boldsymbol{F}_B = \rho_{f,ref}\boldsymbol{g}\beta(T - T_{ref}), \tag{4.9}$$

where β is the coefficient of thermal expansion, $\boldsymbol{g}$ is the acceleration due to gravity, T_{ref} is the reference (bulk) temperature and $\rho_{f,ref}$ is the fluid density at T_{ref}. In this chapter, we use the Shan–Chen approach [18] to apply the buoyancy force, $\boldsymbol{F}_B$, and volume force due to particle-fluid interactions, $\boldsymbol{F}$, into Eq. (4.1). Thus, the equilibrium velocity in Eq. (4.2) is shifted by using $\boldsymbol{v}$ instead of $\boldsymbol{u}$:

$$\boldsymbol{v} = \boldsymbol{u} + \frac{\tau_f}{\rho_f}(\boldsymbol{F}_B + \boldsymbol{F}). \tag{4.10}$$

In the rest of this chapter, following non-dimensional parameters are used to discuss hydrodynamic or thermal properties. Prandtl number (Pr) relates kinematic viscosity (ν) and thermal diffusivity (α)

$$\mathrm{Pr} = \frac{\nu}{\alpha}, \tag{4.11}$$

Grashof and Rayleigh numbers are defined respectively via Eqs. (4.12) and (4.13).

$$\mathrm{Gr} = \frac{g\beta\Delta T L_{ch}^3}{\nu^2}, \tag{4.12}$$

$$\mathrm{Ra} = \mathrm{Gr}\cdot\mathrm{Pr}, \tag{4.13}$$

where L_{ch} is the characteristic length and ΔT is the temperature difference. Wherever density (or heat capacity) ratio is discussed, it denotes particle density (or heat capacity) divided by the corresponding fluid property. The Reynolds number (Re) reflects the flow regime based on the characteristic length, L_{ch}, and velocity, U_{ch}, and reads

$$\mathrm{Re} = \frac{U_{ch}L_{ch}}{\nu}. \tag{4.14}$$

4.2.2 IBM for heat source term

Details of the immersed boundary method for hydrodynamic force interaction between particle and fluid can be found in Sec. 3.2.1. Similarly, IBM for heat exchange is applied. Energy transfer in an incompressible fluid with constant properties is given by:

$$\frac{\partial T}{\partial t} + \boldsymbol{u}\cdot\nabla T = \alpha\nabla^2 T + q, \tag{4.15}$$

where $q = Q/(\rho_f C_{p,f})$ is the heat source due to heat exchange with particles. In order to calculate the heat source term at each Lagrangian node of particle, one can write:

$$q_l^n = \frac{T^d - T^{noH}}{\Delta t}, \tag{4.16}$$

with T^{noH} defined in a 3D study by

$$T^{noH} = \sum_{i,j,k} T_{i,j,k} D(\boldsymbol{x}_{i,j,k} - \boldsymbol{X}_l)(\Delta h)^3. \tag{4.17}$$

Thus, the heat source on the Eulerian nodes would be

$$q_{i,j,k} = \sum_{i,j,k} q_l D(\boldsymbol{x}_{i,j,k} - \boldsymbol{X}_l)\Delta S_l \Delta x. \tag{4.18}$$

The Eulerian heat source term is applied into LBM after modifying Eq. (4.5) by the method of Seta [117]:

$$g_i(\boldsymbol{x} + \boldsymbol{c}_i\Delta t, t + \Delta t) - g_i(\boldsymbol{x}, t) = -\frac{1}{\tau_g}\left[g_i(\boldsymbol{x}, t) - g_i^{eq}(\boldsymbol{x}, t)\right] + w_i\rho_f q(\boldsymbol{x}, t)\Delta t. \tag{4.19}$$

Finally, in case of particles with varying temperature, the particle transient temperature is updated by solving the following differential equation, which is obtained from the energy balance for the particle

$$(\rho_p C_{p,p} - \rho_f C_{p,f}) V_p \frac{dT_p}{dt} = \int Q_p dV - \int Q_l dV, \tag{4.20}$$

where C_p stands for the specific heat, Q_p is the heat source inside the particle (e.g., due to chemical reaction) and Q_l is the exchanged heat between the particle and fluid. In order to avoid difficulties associated with the case of $\rho_f C_{p,f} \simeq \rho_p C_{p,p}$ that may lead to a wrong estimation of particle temperature in Eq. (4.20), the approach suggested by Feng and Michaelides [106] is used, which results in the following discretized form of the evolution equation for the particle temperature:

$$\rho_p C_{p,p} V_p \frac{T_p^{n+1} - T_p^n}{\Delta t} = \rho_f C_{p,f} V_p \frac{T_p^n - T_p^{n-1}}{\Delta t} + \int Q_p dV - \int Q_l dV. \tag{4.21}$$

In this study relying on thermal IBM, no points are distributed inside the particles. This means that each particle has a uniform temperature. This approximation holds for high thermal conductivity ratio between the particle and the fluid. In other words, the Biot number ($\mathrm{Bi} = \frac{hD_p}{k_p}$) must be sufficiently small.

4.3 Numerical validation

In order to verify the robustness of the developed thermal IB-LBM, different two- and three-dimensional simulations have been conducted, considering either particles of constant or varying temperature. In 2D conditions, the natural convection from an eccentrically located cylinder in a square box is first studied. In the second case, the sedimentation of a cold particle in a hot fluid is investigated. The third case considers the motion of a circular catalyst particle of variable temperature in a closed box. In 3D, the developed method is validated for the motion of a single spherical catalyst particle with heat generation inside the particle.

4.3.1 Eccentrically located cylinder in a square enclosure

First, natural convection from a hot cylinder, eccentrically located in a square box, is simulated. A schematic representation of the problem is shown in Fig. 4.1. Enclosure sides are of an equal length L and the cylinder diameter is $D = 0.4L$. Half-way bounce-back boundary condition is applied on the solid walls for this and the following test cases. The cylinder is off-center in y direction and the eccentric distance is $m = 0.1L$. A no-slip condition is considered on the walls. Adiabatic boundary condition is imposed on the top and bottom walls while the side walls are kept at constant non-dimensional temperature of $T_w = 0$. In D2Q9 model the unknown temperature distribution functions on side walls are obtained similar to the bounce back method for momentum transport distribution functions [45, 118]. For instance, unknown distribution

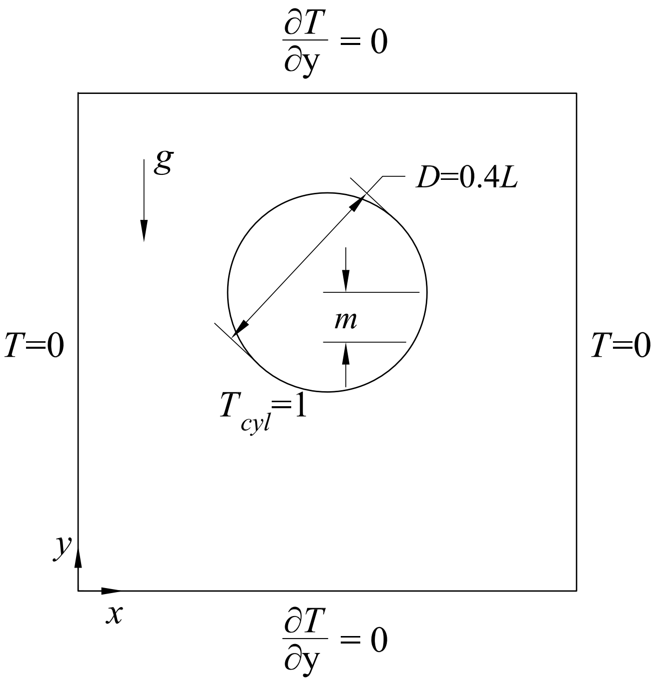

Figure 4.1: Schematic diagram of the simulation domain for heat transfer from an eccentric hot cylinder ($D = 0.4L$) in a closed box with adiabatic and zero-temperature walls (wall length $= L$) under the effect of gravity (g) (Sec. 4.3.1)

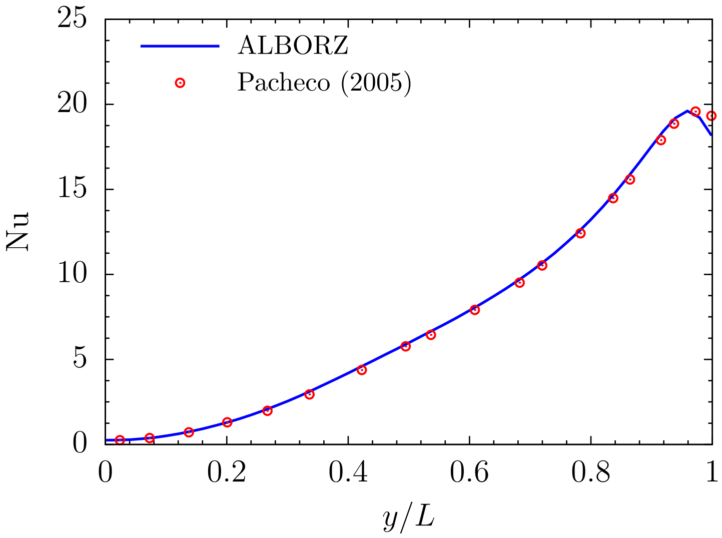

Figure 4.2: Local Nusselt number Nu along the side wall for a 400 × 400 domain of Fig. 4.1 compared to the data of Pacheco et *al.* (2005) (Sec. 4.3.1)

functions on the west wall are evaluated as:

$$\begin{aligned} g_1 &= T_w(w_1 + w_3) - g_3, \\ g_5 &= T_w(w_5 + w_7) - g_7, \\ g_8 &= T_w(w_8 + w_6) - g_6. \end{aligned} \tag{4.22}$$

A first-order extrapolation scheme is used to obtain the values of unknown thermal

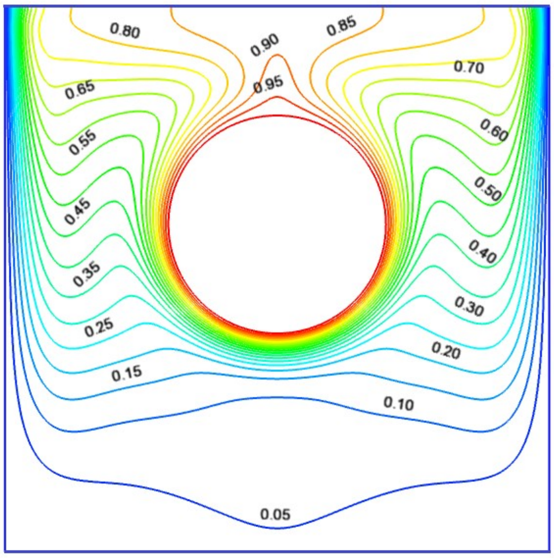

Figure 4.3: Isotherms distribution (colored by temperature) for heat transfer from a hot stationary eccentric cylinder in a 2D box to the surrounding fluid under the effect of natural convection (Sec. 4.3.1)

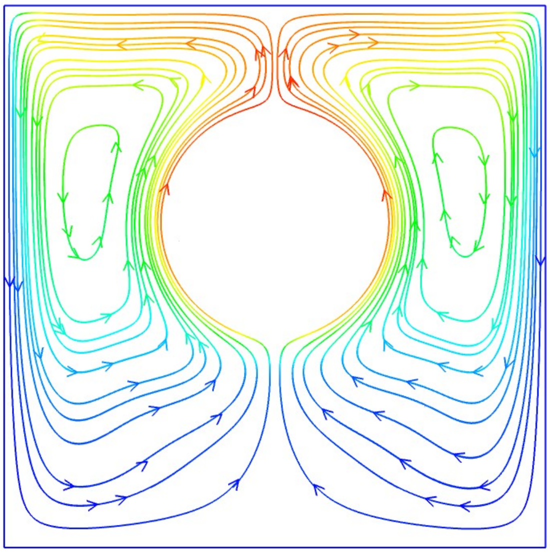

Figure 4.4: Streamlines (colored by temperature) for heat transfer from a hot stationary eccentric cylinder in a 2D box to the surrounding fluid under the effect of natural convection (Sec. 4.3.1)

distribution functions for the upper and lower walls. The non-dimensional flow numbers are: Prandtl number, $\mathrm{Pr} = 10$, Grashof number, $\mathrm{Gr} = 10^5$. The cylinder is stationary during the simulation and holds a constant non-dimensional temperature of $T_{cyl} = 1$. The surrounding fluid is initially at $T = 0$. This temperature difference results in the onset of natural convection. As the fluid near the cylinder gradually gets warm, it moves upward and the cold fluid near the side walls moves downward.

For the thermal IB-LBM simulation, a domain size of 400×400 is selected. Preliminary tests have shown that this is fine enough to capture the flow field. The flow relaxation parameter in LBM is $\tau_f = 0.53$ and 1500 surface nodes are placed on the perimeter of the cylinder. Note that $g\beta$ value is set to zero for the nodes that are located inside the cylinder. This is valid as well for all the following test cases. Here, the obtained results are compared to those from Pacheco *et al.* [105] who used a 250 × 250 domain. Figure 4.2 compares the local Nusselt number along the side walls, which is defined as

$$\mathrm{Nu} = -\frac{L_c}{T_h - T_c} \frac{\partial T}{\partial x}\bigg|_{x=0} . \tag{4.23}$$

It is seen that the present study yields good agreement with those of Pacheco *et al.* [105]. Slight differences are observed near $y = L$, probably due to the superior resolution used in the present study, since our tests did not deliver grid independence for a coarser, 250 × 250 grid.

Figures 4.3 and 4.4 illustrate the isotherms and streamlines in the domain, respectively. It is clear from Fig. 4.3 that isotherms show a higher concentration on the lower side of the cylinder and also in the region close to the upper corners, denoting fast changes in temperature, as expected in this test case. Figure 4.4 illustrates the streamlines in the domain. Around the hot cylinder, fluid is heated and therefore moves upwards while near the walls it is cooled down and tends to move downward.

4.3.2 Cold 2D particle sedimentation in a long channel

In this section, sedimentation of a cold particle with constant temperature in a long wall-bounded vertical channel is computed. This test case was first investigated by Gan *et al.* [102] using a boundary-fitted ALE method, considering a particle starting its motion from the channel center. Later, Yu *et al.* [103] investigated the problem by means of a fictitious domain method and assumed the particle being initially located off channel centerline. This case has been revisited by other researchers in recent years [106, 108, 109, 112, 119]. These studies have shown that particle behavior and its sedimentation pattern depend strongly on the Grashof number.

A particle with diameter D_p is located in a channel of width $4D_p$. The channel is long enough so that the lateral equilibrium position of the particle can be observed. The Reynolds number based on the reference velocity (U_{ref}) is 40.5, with:

$$\mathrm{Re} = \frac{U_{ref} D}{\nu}, \tag{4.24}$$

$$U_{ref} = \sqrt{\pi \left(\frac{D_p}{2}\right) g(\rho_r - 1)}. \tag{4.25}$$

In LBM, the gravitational force is calculated from Eq. (4.25) based on the selected relaxation parameter and Reynolds number. In the current study $D_p = 60\Delta h$ (with Δh: lattice size) and $\tau_f = 0.53$ are considered. A total of 350 Lagrangian nodes are distributed over the particle perimeter. Particle temperature is constant and equal to $T = 0$ during the simulation. A constant hot temperature condition of $T = 1$ (non-dimensional value) is applied on the side walls. The fluid inside the channel is initially at rest at the same hot temperature of 1. A no-slip boundary condition is applied on the walls. Prandtl number and particle to fluid density ratio

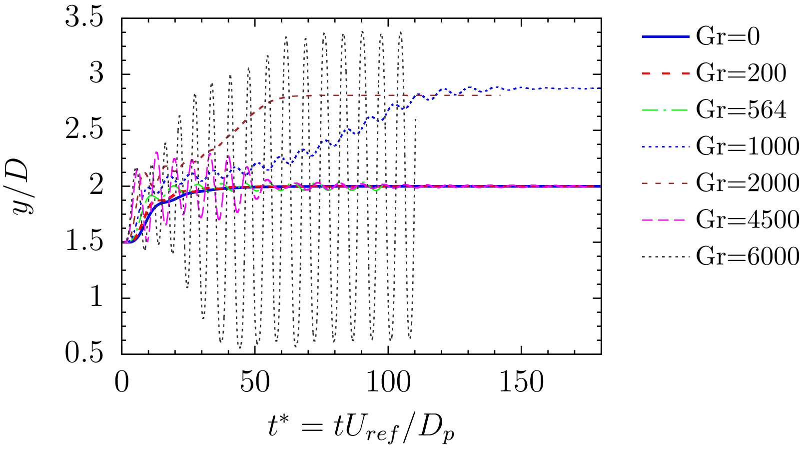

Figure 4.5: Lateral position of a cold particle vs time for particle settling under gravity in hot fluid computed for different Grashof numbers demonstrating different settling regimes (Sec. 4.3.2)

are respectively: Pr=0.7 (corresponding to air), $\rho_r = \rho_p/\rho_f = 1.00232$. The particle is initially placed a half-diameter away from the centerline. For the isothermal case (i.e., Gr $= 0$) the Reynolds number (based on the terminal settling velocity) is $\mathrm{Re}_T = \frac{u_T D_p}{\nu} = 20.92$, which shows very good agreement with the value of 21 reported in [102], and 21.2 in [103]. Yu *et al.* [103] identified six different regimes for particle lateral equilibrium positions and wake structure behind the particle depending on the Grashof number:

- Regime A ($0 <$ Gr < 500): particle settles steadily along the centerline and the flow and temperature fields are steady and symmetric;
- Regime B ($500 <$ Gr < 810): particle oscillates periodically about the centerline and vortex shedding occurs behind the particle;
- Regime C ($810 <$ Gr < 2150): particle first exhibits an oscillating behavior but the oscillation gradually dies out and particle reaches finally a steady-state sedimentation close to one of the walls;
- Regime D ($2150 <$ Gr < 3500): particle sediments steadily along the centerline and symmetric wake vortices are observed behind the particle, but vortex shedding disappears;
- Regime E ($3500 <$ Gr < 4300): particle moves periodically around the centerline with low-amplitude oscillations and vortex shedding is observed;
- Regime F (Gr > 4500): particle shows regular oscillations with a large amplitude around the centerline.

Figure 4.5 depicts the time history of the particle lateral position for various Grashof numbers. The obtained results confirm as a whole the flow regimes previously discussed. However, similar

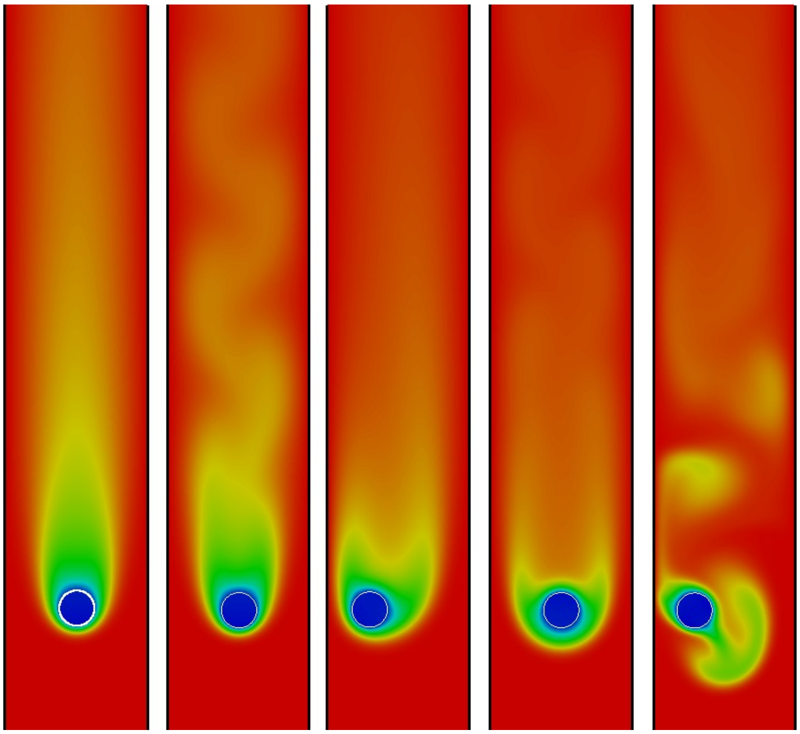

Figure 4.6: Instantaneous temperature field of a settling cold cylinder in a hot fluid for different Grashof numbers; From left to right: Gr = 200, 564, 2000, 4500, 6000 (Sec. 4.3.2)

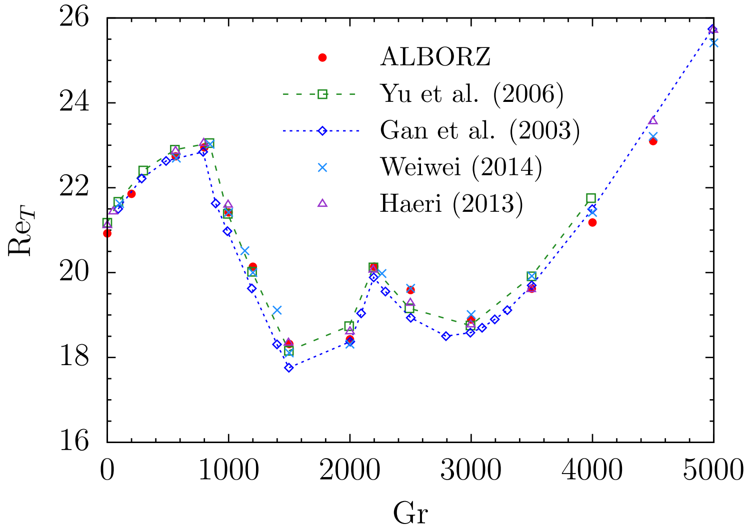

Figure 4.7: Reynolds number (based on the terminal settling velocity) plotted as a function of Grashof number Gr and compared to other simulations for the case of single cold particle settlement in a hot vertical channel (Sec. 4.3.2)

to the observations of Wachs [109] and Haeri and Shrimpton [119] and in contrary to those of Yu *et al.* [103], it is found that at Gr = 4500 the particle does not experience large-amplitude oscillations yet. In our simulations, the turbulent-like flow in which the particle oscillates strongly (Regime F) does not occur at Gr = 4500 but at noticeably larger values.

Figure 4.6 presents the temperature field for Grashof numbers ranging from 200 to 6000. Different flow patterns can be seen. The particle does not contact the wall for any of the

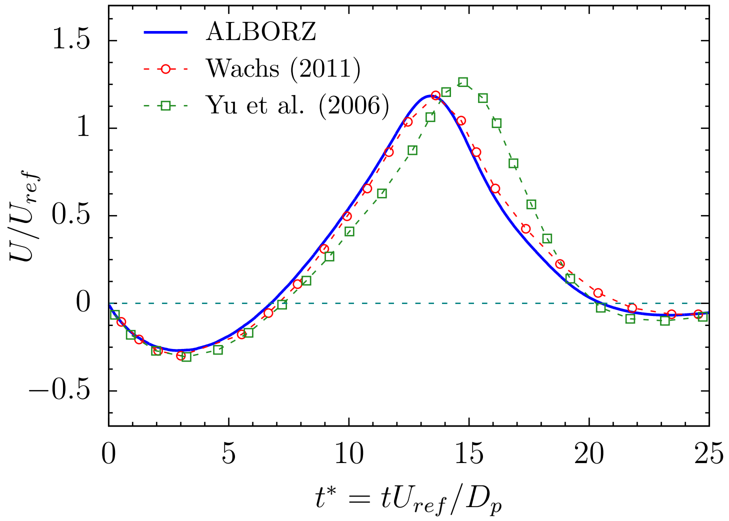

Figure 4.8: Normalized vertical velocity U/U_{ref} of a 2D catalyst particle with non-constant temperature in a closed box plotted against dimensionless time t^* for $C_{p,r} = 1.0$ (Sec. 4.3.3)

considered situations. Figure 4.7 shows a comparison of the Reynolds numbers (Re_T) obtained here with those discussed in previous publications. One can see that the obtained results are in good agreement with other studies. The observed small differences can be attributed to slightly different computational algorithms.

4.3.3 Single 2D catalyst with a freely varying temperature

In this test case, a single catalyst particle with a time-dependent temperature is placed in an enclosure. Remember that, in the current simulations, the whole particle has a uniform temperature, which is valid for high particle thermal conductivities. Heat is generated inside the particle at a constant rate, mimicking the effect of an exothermic reaction. The computational domain is taken to be of size $8D_p \times 16D_p$ where D_p is the catalyst particle diameter. Initially, the particle is located at the center of the enclosure and all velocities as well as the temperature are set to zero. Walls are also kept at $T_w = 0$ during the simulation. The simulation parameters are: $\mathrm{Re}_{ref} = 40$; $\rho_r = 1.1$; $\mathrm{Gr} = 1000$; $\mathrm{Pr} = 0.7$; $C_{p,r} = C_{p,p}/C_{p,f} = 1.0$; $\overline{Q}_p = 1$. The Reynolds number is defined by Eq. (4.24) and the normalized heat generation (per particle unit area) reads

$$\overline{Q}_p = \frac{Q_p D_p}{\rho_f C_{p,f} U_{ref}(T_m - T_0)}. \tag{4.26}$$

It must be noted that the non-dimensional temperature T_m is set to 1 in Eq. (4.26) and in the definition of the Grashof number as well. In the present LBM study, $D_p = 90\Delta h$ is employed. The obtained results are compared to those of Yu *et al.* [103] and Wachs [109]. Wachs [109] assumed a unique temperature over the particle surface, while in the simulations of Yu *et al.* [103], the temperature distribution within the particle area is calculated based on the particle thermal conductivity. Figure 4.8 depicts the time evolution of the particle vertical velocity. As the particle is released in the domain, it is initially cold and settles down under gravity.

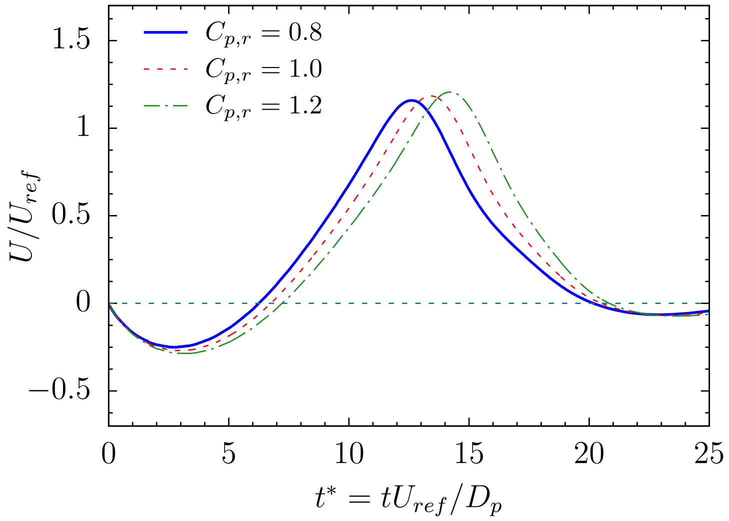

Figure 4.9: Effect of heat capacity ratio $C_{p,r}$ on normalized vertical velocity U/U_{ref} of a 2D catalyst with variant temperature due to heat generation inside the particle for different dimensionless times t^* (Sec. 4.3.3)

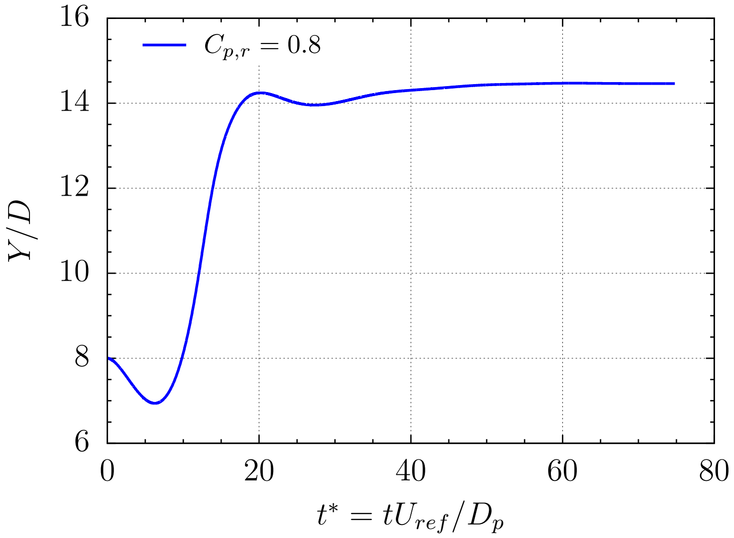

Figure 4.10: Normalized catalyst particle vertical position Y/D versus dimensionless time t^* for $C_{p,r} = 0.8$ during the heat transfer from the particle to the surrounding fluid due to heat generation inside the particle (Sec. 4.3.3)

The temperature inside the particle gradually increases due to heat generation, so that the surrounding fluid becomes warmer as well, leading to the onset of natural convection. Thus, while still moving in downward direction, its acceleration gets to zero at $t^* = 2.84$. It continues its motion in negative direction (downward) until $t^* = 6.74$. At this point, natural convection acting upward finally overcomes gravity and the particle moves in the upward direction until it experiences resistance by the upper wall. At $t^* = 20.51$ the particle moves again toward the bottom. It can be concluded from the comparisons plotted in Fig. 4.8 that the obtained results correctly predict the particle behavior. They are very close to the data of Wachs [109].

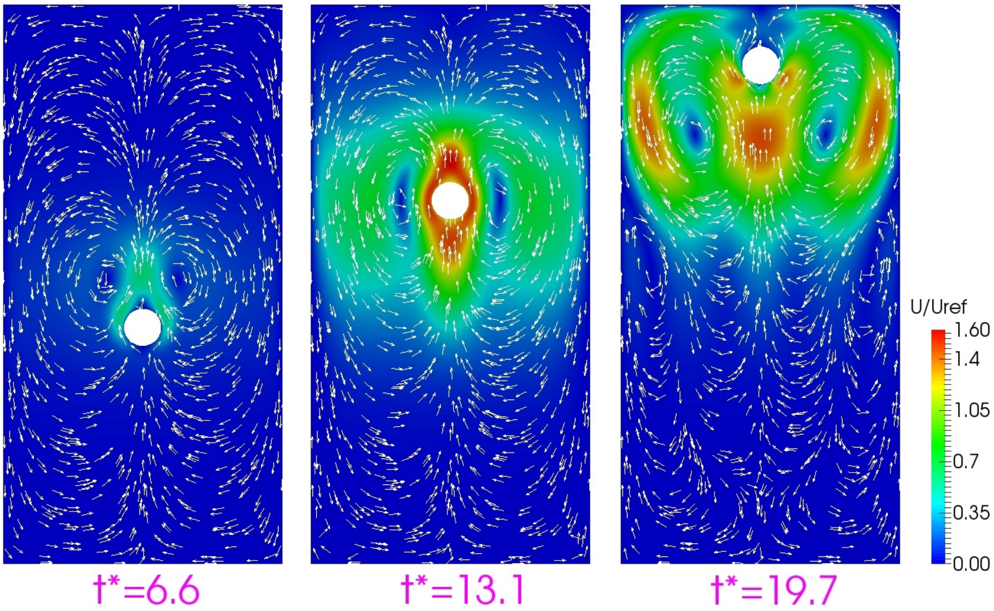

Figure 4.11: Velocity field and velocity vectors at different time steps $t^* = tU_{ref}/D$ for the vertical motion of a single catalyst particle in a fluid considering heat generation inside the particle (Sec. 4.3.3)

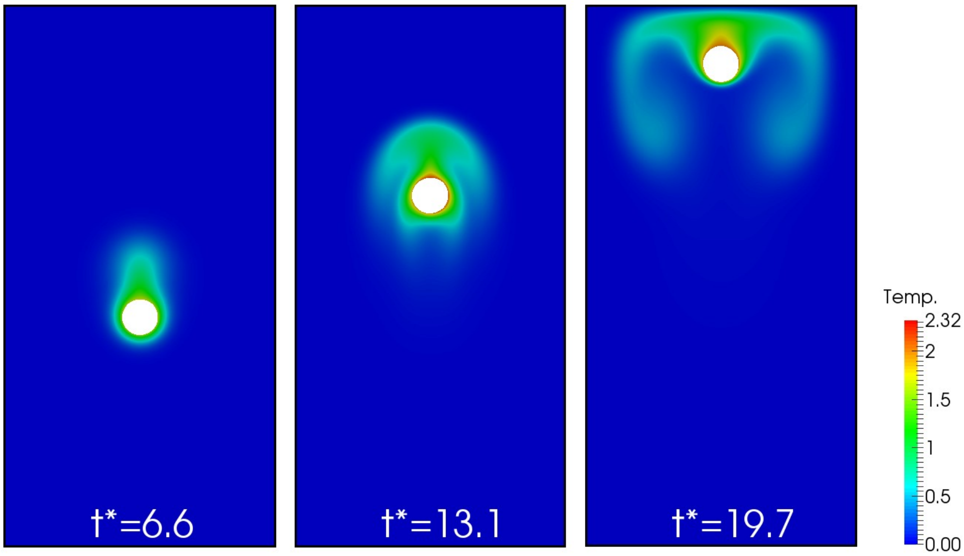

Figure 4.12: Temperature field at different time steps $t^* = tU_{ref}/D$ for the vertical motion of a single catalyst particle in a fluid considering heat generation inside the particle (Sec. 4.3.3)

However, as in [109], the present study predicts the maximum velocity with a slight shift, which is justified by the assumption of uniform particle temperature.

The influence of the heat capacity ratio on particle behavior is investigated in Fig. 4.9. As expected, the lower the heat capacity of the particle, the sooner the particle reaches its maximum velocity. This is justified by the faster increase of the particle temperature. On the other hand, for $C_{p,r} = 1.2$ the process is slower and the particle reaches its maximum velocity later. Furthermore, the maximum particle velocity is slightly higher at larger heat capacity ratios.

Figure 4.10 illustrates the particle vertical position versus time for $C_{p,r} = 0.8$; the interesting particle levitation motion can be seen there. It can be observed that the particle reaches a stationary state near the upper wall where the lift and drag forces are in equilibrium; the particle never touches the upper wall.

Figures 4.11 and 4.12 represent the velocity and temperature fields at three non-dimensional time steps, respectively, where the particle behavior at different stages can be better observed. Velocity vectors are also shown in Fig. 4.11. These results demonstrate that the thermal IBM in conjunction with LBM can be accurately applied to physical cases where non-isothermal effects are dominant. Moreover, the effect of differing thermophysical properties and varying particle temperature can be taken into account.

4.3.4 Motion of a spherical catalyst in an enclosure

In this part, the heat and fluid flow fields around a spherical catalyst particle in a box are considered. The particle has diameter D_p and is located in a box of $8D_p \times 8D_p \times 16D_p$. Similar to the 2D case (see Sec. 4.3.3) particle and fluid are initially at $T = 0$. A constant cold temperature is imposed on the surrounding walls. The particle is located at domain center at $t = 0$. Heat is gradually generated inside the particle, mimicking the effect of a chemical reaction. Non-dimensional parameters are set to (Re_{ref}, Pr, Gr, $C_{p,r}$, $\rho_r, \overline{Q}_p$)= (40, 0.7, 1000, 1.0, 1.1, 1.0). The non-dimensional heat source in the particle is 1 and the reference velocity in 3D reads

$$U_{ref} = \sqrt{\frac{4}{3} D_p g(\rho_r - 1)}. \tag{4.27}$$

The particle is resolved with 24 nodes along its diameter in the simulations. The obtained results are compared with those of Wachs [109], Störm and Sasic [111] and Xia *et al.* [113] in Figs. 4.13, 4.14.

It is observed that all simulations are qualitatively identical and lie quantitatively close to each other. The slight quantitative differences observed between the results are probably the consequence of slightly different numerical algorithms. Since no experimental data and no “golden truth” solution are available, it is unclear which result might be closer to reality. Qualitatively, the particle behaves similar to the 2D case. Considering the particle velocity and position it can be seen that in the 3D simulation the particle zero velocity is induced by the collision with the upper wall (at $t^* \simeq 22$), while in the 2D case the particle reaches zero velocity when natural convection and gravity are in equilibrium, which occurs at a small distance below the upper wall. It is also clear from Fig. 4.13 that after experiencing the highest velocity, the spherical particle decelerates suddenly due to collision with the wall while in 2D, the deceleration is slower and is not followed by a wall collision. Obviously, the influence of the wall on the particle movement is stronger in 2D than in 3D. For the 3D case, after colliding with the wall, the particle separates again and finally reaches a stable position close to the upper wall. Comparing to Fig. 4.10, this stable position lies even closer to the wall in 3D.

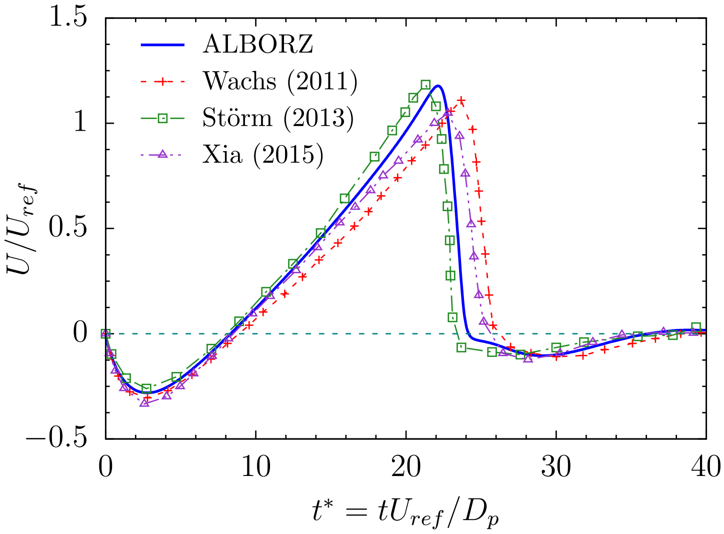

Figure 4.13: Vertical velocity U/U_{ref} of a spherical catalyst particle over time t^* where heat is constantly generated inside the particle (Sec. 4.3.4)

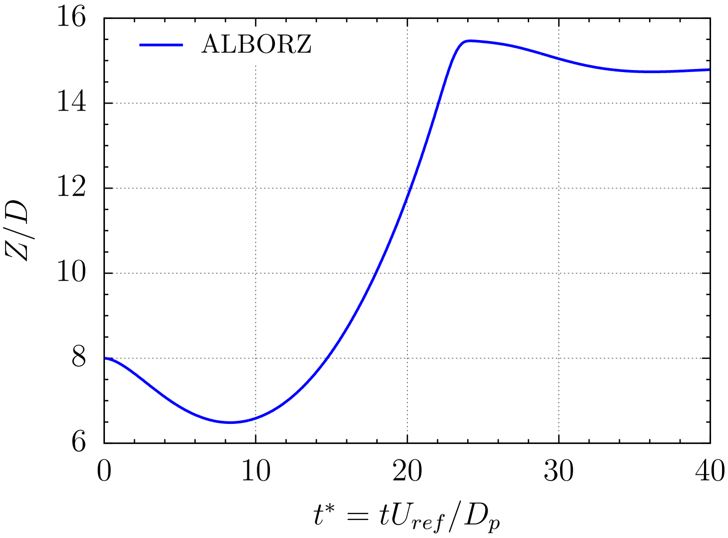

Figure 4.14: Vertical position Z/D of a spherical catalyst particle over time t^* where heat is constantly generated inside the particle (Sec. 4.3.4)

4.4 Applications

In this section, thermal IB-LBM approach is first applied to the well-known drafting, kissing and tumbling (DKT) case with heat transfer effects. Next, the motion of single and multiple spherical particles is modeled and finally 60 catalyst particles that are moving and interacting with each other are taken into account in 3D simulation.

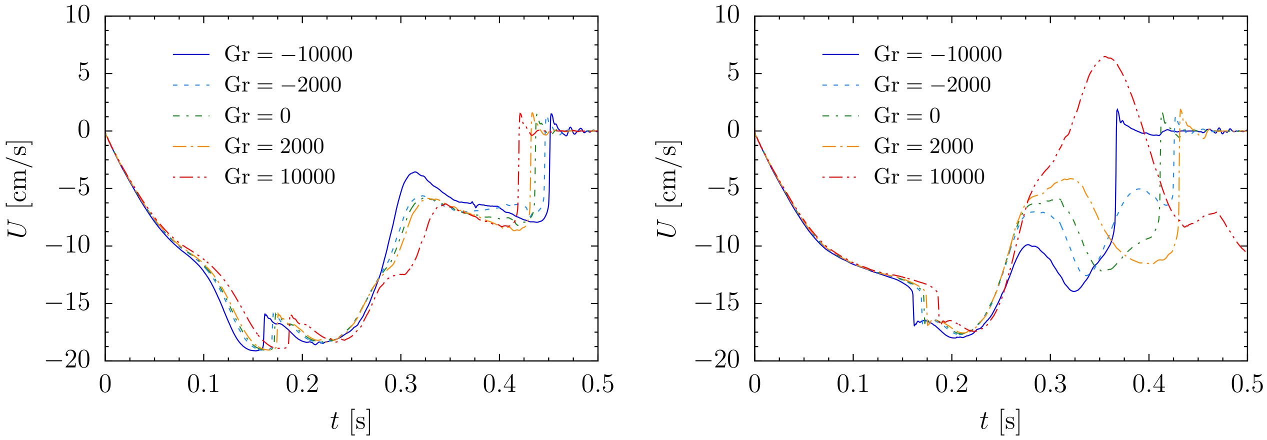

(a) P1 (b) P2

Figure 4.15: Effect of Grashof number on the sedimentation velocity of two cylindrical particles (P1, P2) over time for non-isothermal DKT test case (Sec. 4.4.1)

4.4.1 DKT motion with heat transfer

Now, 2D simulations are extended to consider circumstances where more than one particle is present. This allows investigations involving relative particle motion and particle-particle collisions. The classical benchmark of DKT motion is considered here. Two circular particles ($D_p = 0.25$ cm) are located in an enclosure (2 cm×6 cm) with solid walls on all boundaries.

The isothermal case was simulated by Uhlmann [80]. The upper particle (P1) is initially 10 μm off the channel center while the lower one (P2) is -10 μm off the channel center and 0.5 cm below the first particle. Flow density and dynamic viscosity are 1000 kg/m^3 and 0.001 Pa·s, respectively. Particle density is constant and equal to 1500 kg/m^3. Particles and fluid are initially at zero velocity. In the current LBM study the particle diameter is discretized by 50 lattices. Different Grashof numbers, as defined using the particle diameter as the reference length scale, are considered: a) isothermal particles (Gr=0); b) hot particles with Gr = 2000, 10000; and c) cold particles with Gr = -2000, -10000. Particles are assumed to have constant temperature during sedimentation. In case of positive or negative Grashof numbers, the walls are kept at a normalized temperature of $T_w = 0$ and $T_w = 1$, respectively. The Prandtl number in non-isothermal cases is 1.0. The time evolution of the particles settling velocity is plotted in Fig. 4.15. It is obvious that after the collision stage, thermal convection is more dominant for particle P2 (initially lower) compared to P1. The reason is that this particle shows a stronger lateral movement toward the wall. It is also observed that natural convection effect is strongest after $t = 0.26$ s. Before this time, the two particles are nearly aligned, resulting in a lower projected frontal area. After this point the two particles separate and the structure of the flow behind them changes completely.

It is also clear that a colder particle generally settles down faster than a hot particle. This is particularly true at low Re numbers, because the fluid around a cold particle is heavier than the bulk fluid and therefore tends to settle down by itself. This results in a lower drag force and

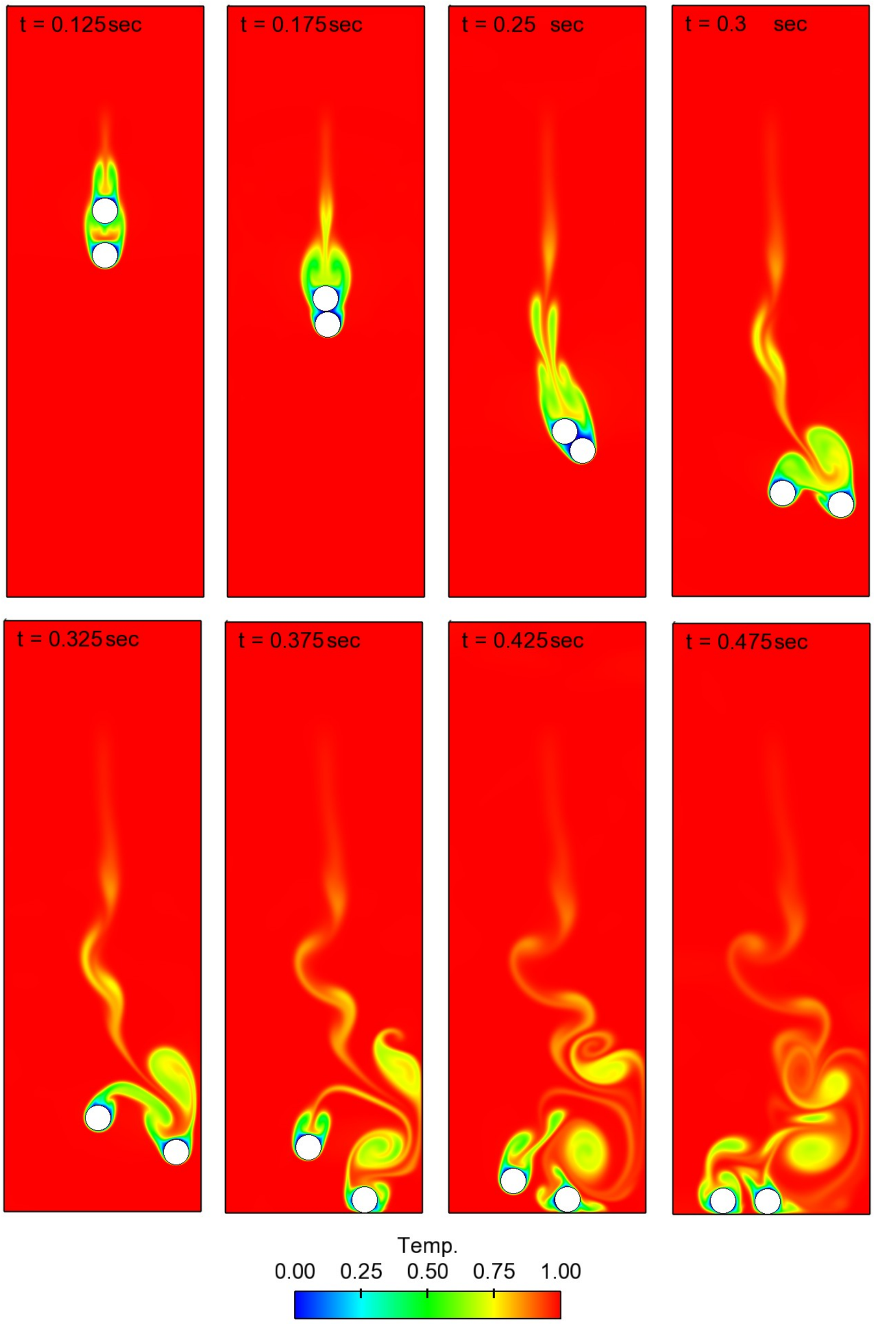

Figure 4.16: Temperature field evolution during a non-isothermal DKT case for Gr = −10000 (Sec. 4.4.1)

consequently a higher settling particle velocity. This phenomenon is seen for the pre-collision stage in Fig. 4.15 and is more evident for Gr = −10000. However, the flow structure of this case involving two particles is far more complex, since hydrodynamics and particles are affected by collisions and by wake effects, which strongly modify the particulate flow after collision. Moreover, the figure shows that positive values of Gr postpone particles collision. Figure 4.16 shows the particles position and temperature field for the case of cold particles at Gr = −10000 where drafting, kissing and tumbling stages are illustrated.

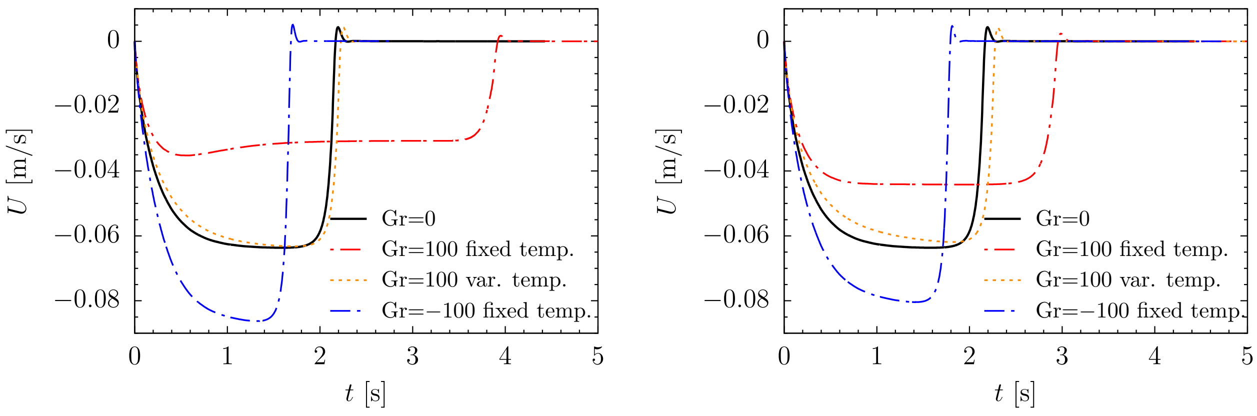

(a) Pr = 1 (b) Pr = 5

Figure 4.17: Effect of Grashof and Prandtl number on settling velocity U of a spherical particle in a closed box versus time t (Sec. 4.4.2)

4.4.2 Effect of heat transfer on single sphere sedimentation

The motion of spherical particles in closed enclosures is an interesting phenomenon to investigate particle/fluid interaction. This section investigates the influence of various factors including Grashof number, constant or varying temperature and Prandtl number on the sedimentation behavior of spheres. A vertical box is considered, in which a solid sphere is released and settles down under gravity. Domain size is $16 \times 10 \times 10$ cm^3. Particle diameter is 1.5 cm and its density is $1.1\rho_f$. Fluid density is 1000 kg/m^3 and its dynamic viscosity is equal to 0.1 Pa·s. The particle and fluid have equal heat capacities. Domain is discretized by $160 \times 100 \times 100$ grid cells. Different flow regimes based on heat transfer effects will be studied: a) Gr = 0 (no heat transfer); b) Gr = 100 (hot particle with constant temperature); c) Gr = −100 (cold particle with constant temperature; d) Gr = 100 (hot particle with non-constant temperature). Moreover, the effect of Prandtl number (Pr = 1 or 5) will be checked. Temperature of the walls is constant in all cases ($T_w = 0$ for positive Grashof numbers and $T_w = 1$ for negative Grashof numbers).

Figure 4.17 represents particle velocity versus time for Pr = 1 and Pr = 5. First, it is seen that hot particle with constant temperature (Gr = 100) settles at a lower speed compared to the other cases. Heat transfer from the hot particle makes the surrounding fluid warmer. As a result, this fluid zone will have a lower density and tends to move upward. This increases the drag on the particle and consequently lowers the particle velocity and increases the settling time. On the other hand, fluid around cold particle has a higher density and tends to move downwards, which eases particle downward motion. When a hot particle has a varying temperature, its behavior is located between those of isothermal and hot temperature cases. However, the velocity profile of variable temperature particle is much closer to isothermal case rather than to the profile of hot, constant-temperature particle. This proves that the heat exchange between solid particle and the fluid plays an important role even at low or moderate Grashof values.

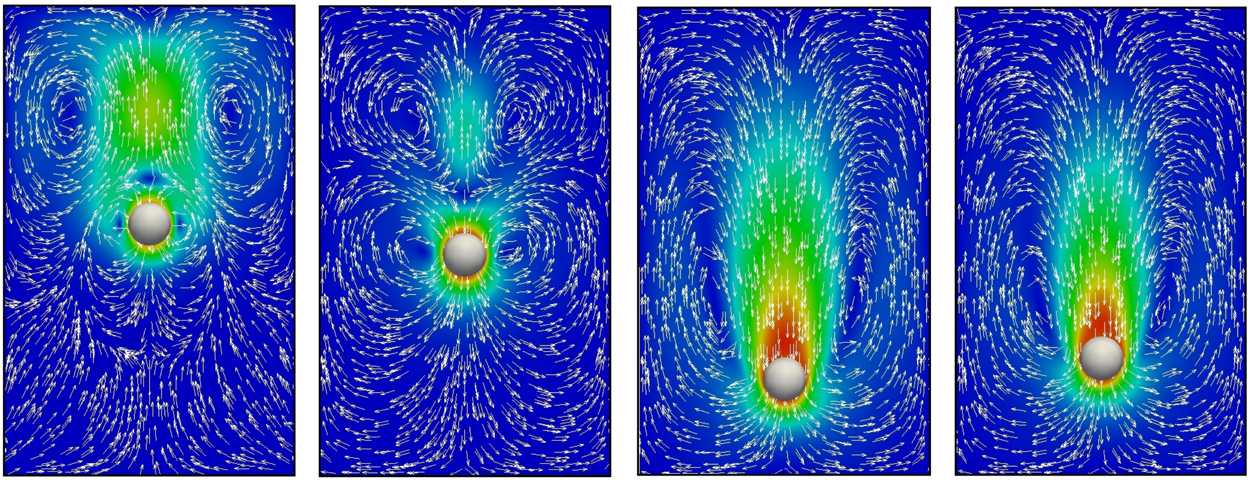

Figure 4.18: Velocity field and particle position at $t = 1.33$ s for (from left to right) a) $\mathrm{Pr} = 1$, $\mathrm{Gr} = 100$, b) $\mathrm{Pr} = 5$, $\mathrm{Gr} = 100$, c) $\mathrm{Pr} = 1$, $\mathrm{Gr} = -100$, d) $\mathrm{Pr} = 5$, $\mathrm{Gr} = -100$; during the motion of a single spherical particle in a box with heat transfer effects (Sec. 4.4.2)

Effect of Prandtl number on particle velocity can be seen by comparing Fig. 4.17 (a) and (b). It is seen that a hot particle moves downward slower in a fluid of lower Prandtl number ($\mathrm{Pr} = 1$). A cold particle ($\mathrm{Gr} = -100$), on the other hand, settles faster in lower Prandtl number fluid. In case of non-constant particle temperature, the final particle velocities are very close before they hit the lower wall. Figure 4.18 depicts velocity fields for four different regimes. It is seen that positive Grashof regimes show a more complex flow structure, with more vortices. In this state, normally two vortices are formed behind the particle. Depending on time and Prandtl number two other large vortices can be observed at the side of the particle. For negative Grashof values, there exist only two main vortices on the two sides of the particle. For $\mathrm{Gr} = 100$ and $\mathrm{Pr} = 1$ a smaller portion of the fluid, limited to the vicinity of the particle is affected. Below the particle, part of the fluid tends to move downward while other regions show positive velocity. These interactions hinder particle motion and therefore lowers particle settling velocity. For negative Grashof values heat transfer from the fluid to the particle promotes particle downward motion, increasingly so at lower Prandtl values.

4.4.3 Three spheres in an enclosure with heat exchange effects

In order to conduct further investigation on the effect of heat transfer on the particle behavior, three spherical particles have been released in a box. Domain size and particle and fluid properties are similar to previous simulation. Prandtl number is assumed equal to 1. Three spherical particles are initially located on the corners of a triangle. The length of each triangle side is 2.795 cm. Upper particle (P1) has initially a vertical distance of 12.75 cm from the bottom wall. Two other particles (P2, P3) are 2.5 cm below this particle, being symmetrically located on two sides of P1. Three cases are considered, namely: $\mathrm{Gr} = 0, -100, 100$ corresponding to isothermal, cold and hot particles.

Figures 4.19 and 4.20 depict respectively the variation of particles vertical velocity and

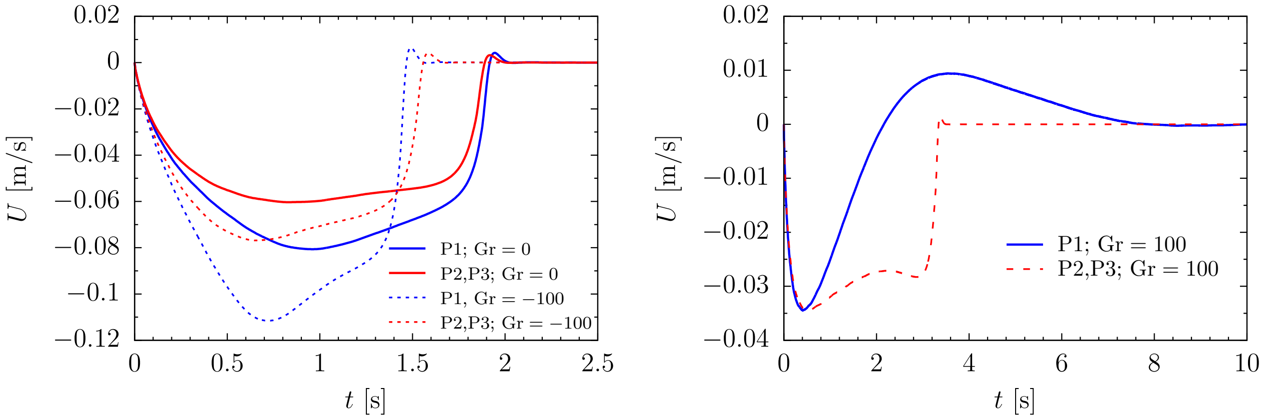

(a) Gr = 0, Gr = −100 (b) Gr = 100

Figure 4.19: Settling velocity U of three spherical particles in a box as a function of time t for different Grashof numbers (Sec. 4.4.3)

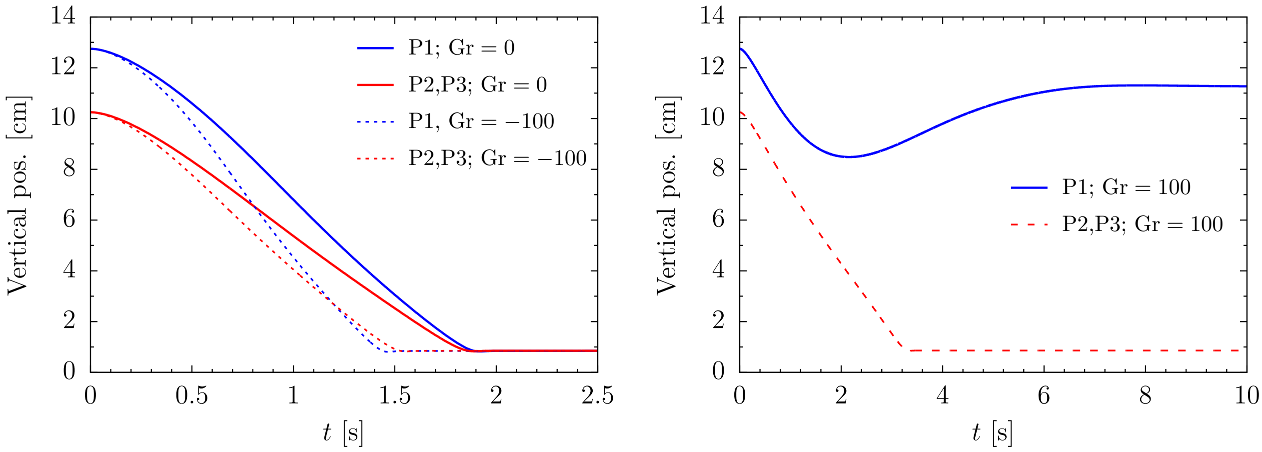

(a) Gr = 0, Gr = −100 (b) Gr = 100

Figure 4.20: Vertical position of three spherical particles in a box measured from the bottom wall as a function of time t for different Grashof numbers (Sec. 4.4.3)

their distance from the bottom wall with time. First comparing subfigures (a) and (b), one can observe that, as expected, cold particles have higher velocity and reach the bottom of the enclosure faster. It is also seen that in isothermal and cold particle simulations, all particles tend to reach the lower wall almost together. This means that, the initial vertical distance between P1 and the two other particles decreases gradually and the three particles hit the bottom wall almost simultaneously. This is explained by the lateral motion of P2 and P3 compared to only vertical motion of P1. For Gr = −100, it is interesting to see that P1 can even overtake P2 and P3 and hit the wall sooner i.e., the effect of negative Grashof value on particle velocity is more dominant for P1. In case of Gr = 100 (subfigures b), P2 and P3 reach the bottom wall after 3.45 s, which is much larger time than the required time for their counterparts at Gr = 0 or Gr = −100. The behavior of P1 at Gr = 100 is quite noticeable. This particle never hits the bottom wall. It first moves downward with nearly the same velocity as the two other

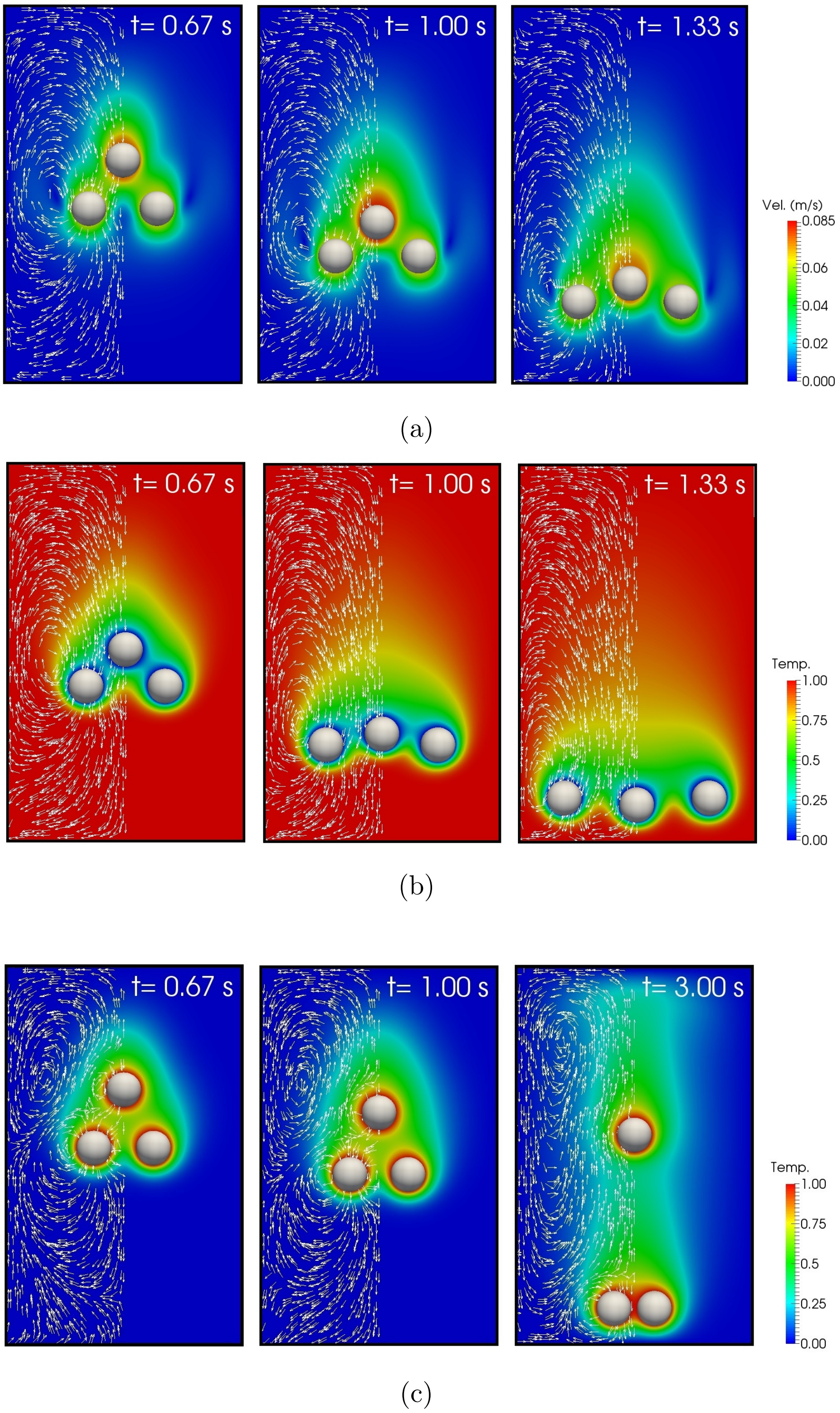

(a)

(b)

(c)

Figure 4.21: Particles position and distribution of (a) velocity at Gr = 0 (b) temperature at Gr = −100 and (c) temperature at Gr = 100; during the motion of three spherical particles in a closed box shown on the middle plane (Sec. 4.4.3)

particles and its velocity magnitude reaches a maximum value at $t = 0.41$ s. From this point and because of strong upward flow around P1, particle velocity approaches zero ($t = 2.15$ s). Then it starts an upward motion before being stopped close to the top wall as a result of near-wall flow structures. For the rest of the simulation, the upward buoyancy force keeps the particle at a fixed position (around $H = 11.3$ cm).

Evolution of velocity and temperature fields with time is presented in Fig. 4.21 along the central plane. Velocity vectors are shown as well. Due to symmetry, velocity vectors are only depicted on half the central plane. In isothermal case, the motion of upper particle pushes the two other particles away. However, the height of the box is not long enough so that P1 cannot overtake P2 and P3. At $\mathrm{Gr} = -100$, the lateral motion of P2 and P3 is greater compared to $\mathrm{Gr} = 0$. This allows P1 to reach the bottom wall sooner. For $\mathrm{Gr} = 100$ two vortices beside the center part of the box push P2 and P3 to the center. The strong temperature field formed above P2 and P3 is clearly seen in Fig. 4.21 at $t = 3$ s.

4.4.4 Considering 60 spherical catalyst particles in an enclosure

Finally, the developed methodology is used to simulate the movement of 60 spherical catalyst particles in an enclosure. The size of the enclosure is $8D \times 8D \times 19D$ and particles are initially randomly placed in the lower section of the box. However, it is ensured that all particles have initially a minimum distance of $3\Delta h$ from the wall or from any other particle. During the simulation, the particles experience a repulsive force represented by a spring–force model when they have a distance of Δh or less from another particle or from the wall. The simulation parameters are set to $(\mathrm{Re}_{ref}, \mathrm{Pr}, \mathrm{Gr}, C_{p,r}, \rho_r, \overline{Q}_p)$= (40, 0.7, 1000, 1.0, 1.1, 3.88). The fluid is initially at the cold temperature and the walls are always maintained at the cold temperature of $T = 0$. A mesh size of $\Delta h = D/24$ is considered, leading to a grid number of $192 \times 192 \times 456$.

Figure 4.22 depicts the isotherms in the center plane and the distribution of particles in the domain at four different time steps. It is seen that, similar to the single particle case (Subsec. 4.3.4), the particles tend to move upward due to strong natural convection. However, because of the movements of the relatively large number of particles in the domain, strong hydrodynamic modifications and vortical structures appear. Sometimes, individual particles are trapped into these structures. As a result they may move upward even faster than the single particle, or on the contrary be convected back toward the bottom wall. As a result, the arrival time of the particles at the upper wall now shows a broad distribution.

The average vertical position of 60 particles is depicted in Fig. 4.23. Particles initially show for a short time a downward motion, then rapidly accelerate towards the upper wall. They finally reside at a position close to the upper wall while being separated from the upper and side walls and from other particles by the implemented repulsive force. The curves concerning maximum and minimum location of particles illustrate that the particles experience a vast range of location before getting stable near the upper wall. This test case demonstrates that the developed thermal IB–LBM tool can simulate the motion of multiple particles involving heat transfer, as found in many configurations of practical interest. This simulation required 1304 seconds for every 100 iterations (11.8 h for the whole process) and 12.1 GB RAM using a standard desktop PC (Core i5, 3.3 GHz CPU, 16 GB RAM).

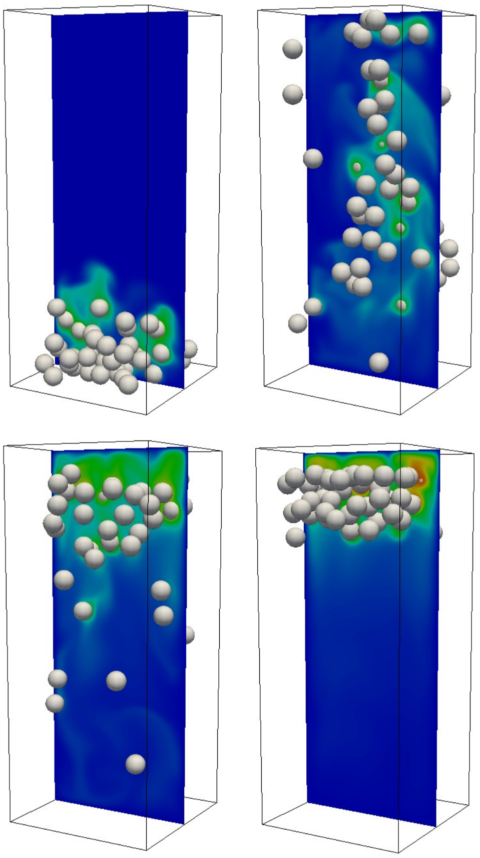

Figure 4.22: Temperature distribution in the center plane and time evolution of particles position at t^* =6.9, 18.5, 30.1 and 47.4, from left to right and top to bottom for the motion of 60 non-isothermal spherical particles in a closed box (Sec. 4.4.4)

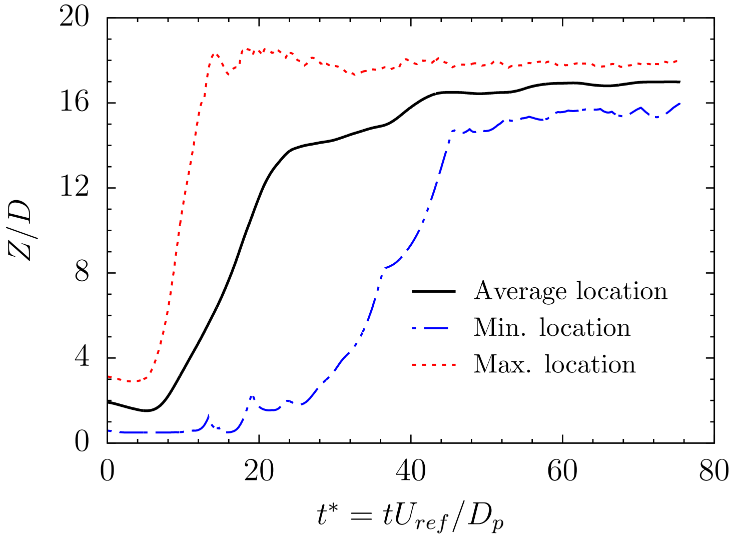

Figure 4.23: Average vertical position of the 60 particles (black), together with the position of the highest (red) and lowest (blue) particle in the box, illustrating the disparity of the instantaneous positions (Sec. 4.4.4)

4.5 Summary

A thermal immersed boundary lattice Boltzmann method has been presented and implemented in the in-house LB solver. It allows resolving the motion of solid particles in the fluid, even in presence of large heat transfer effects. The continuous fluid is discretized on an Eulerian frame while particle motion is modeled based on the Lagrangian approach. The force (resp. heat) density in the LB equation is calculated using a direct-forcing (resp. direct-heating) approach. The effect of temperature variation on the flow field is taken into account through the Boussinesq approximation. Particle translational and angular velocity is updated at each time step using Newton's equation of motion, assuming a homogeneous temperature inside each particle in this study. Different configurations of increasing complexity have been considered both in 2D and 3D geometries. The accuracy of the simulations has been first validated by comparing the obtained results to previously published studies. A very good agreement has been observed, both for stationary and moving particles. In addition to particles at constant temperature, the developed approach is also able to take into account flows involving particles with varying temperature. Finally, it has been shown that many interacting particles can be considered using the same approach with acceptable computational requirements. Thus, thermal IB-LBM can now be used to investigate a variety of practical configurations, for instance chemical reactors and reactive fluidized beds. In the next chapter, fluid flow in complex geometries is considered. For this purpose, flow in porous structures will be modeled and the effect of SRT and MRT models will be studied.

Chapter 5

Porous Media Flow

5.1 Introduction

Flow through porous media is a very attracting engineering subject due to wide practical applications, ranging from aquifers and mineral rocks to catalysts, biomedical and filter simulations. This has led in the last years to an increasing number of investigations on this subject in chemical, environmental and biological engineering.

Permeability is perhaps the most important property in the study of porous media. It is a measure of the ability of the structure to transmit fluids, and has been considered in many experimental studies [e.g., 120–122]. Because of the high cost and long duration of such experiments it is attractive to determine the permeability by analytical or numerical simulations. However, analytical approaches are limited to very simple geometries and low Reynolds numbers. They are usually based on the Stokes equation (only valid for creeping fluid) for simple boundary conditions. Progress in meshing and also increasing computational power have paved the way for numerical methods to emerge as a reliable tool concerning many fluid dynamic conditions. However, standard Navier-Stokes codes fail in many cases to represent the flow behavior in porous media, due to poor convergence and instability problems. Additionally, sophisticated meshing strategies are needed for this type of complex geometry. As we discussed before, LBM has emerged in the recent decades as a promising alternative to the Navier-Stokes equations [10, 123].

LBM was shown to be equivalent to an explicit, second-order accurate approximation of the NS equation [124]. Locality of calculations, easy implementation of a no-slip boundary condition in complex geometries and efficient parallelization make LBM very attractive for flows in complex geometries [39], like porous media. Using imaging techniques, such as computed tomography (CT), the structure of the porous media can be captured and directly represented in the LBM.

One of the first applications of LBM in porous media simulation can be traced back to the work of Succi *et al.* [125]. They checked the validity of the lattice Boltzmann model for flow simulation in complex 3D geometries. From 1989 onwards, many researchers have relied on the LBM for different cases of single or multiphase porous media flows. For instance, Pan *et al.* [126]

investigated the effect of single or multiple relaxation time (SRT/MRT). They also studied the influence of different bounce-back implementations on the accuracy for different packings. Degruyter *et al.* [127] combined X-ray microtomography and LBM to study flow characteristics in samples from different silicic volcanic deposits.

Chukwudozie and Tyagi [128] modeled fluid flow in periodic arrays of sphere packs using LBM; macroscopic flow parameters such as permeability, tortuosity, and β-factor were calculated. They also studied the test case of an irregular pack of uniform-diameter spheres constructed from CT images. Cho *et al.* [129] investigated the permeability of microscale fibrous porous media. They concluded that the permeability shows a strong dependence on porosity and a lower dependence on the fiber arrangement.

Parallel computing allows for a drastically faster simulation of complex phenomena as compared to serial computing; it is now unavoidable in many cases. In this respect, LBM is an ideal candidate, since it only requires nearest-neighbor information during computations. This led to a growing number of studies based on shared or distributed parallel computing during the last years [e.g., 130, 131].

In the present study, LBM is adopted to calculate the permeability of three-dimensional porous media. The effect of force scheme, domain resolution and relaxation time will be discussed for three cases; 1) face-centered cube; 2) body-centered cube; 3) a real geometry constructed from CT images. Results of this chapter have been partly published in International Journal of Heat and Fluid Flow [132].

Throughout this chapter SRT or MRT models will be used. MRT model without a force term has been discussed in Sec. 2.5. In MRT model, different moments of the distribution function relax at different rates, while in SRT model, all moments relax at the same rate. MRT allows defining individual relaxation times for all the variables by construction of a collision matrix, providing the maximal number of degrees of freedom to optimize LBM stability. The MRT-LBM equation with a force term can now be written as:

$$\mathbf{f}(\mathbf{x}+\mathbf{c}_i\Delta t, t+\Delta t) = \mathbf{f}(\mathbf{x},t) - \mathbf{M}^{-1}\left(\mathbf{S}\left[\mathbf{m}-\mathbf{m}^{eq}\right] - \left(\mathbf{I}-\frac{1}{2}\mathbf{S}\right)\mathbf{m}_F\right), \tag{5.1}$$

with $\mathbf{m} = \mathbf{M}\mathbf{f}$, $\mathbf{m}_F = \mathbf{M}\mathbf{f}_F$ and $\mathbf{f}_F = \{F_i\}_{i=0,\cdots,18} = (F_0, F_1, \cdots, F_{18})^T$ in D3Q19 model. Each forcing term (F_i) has the same form as Eq. (3.26) following Guo's scheme.

5.2 Parallelization

The current study relies again on the in-house LBM code ALBORZ. It uses in 3D a D3Q19 stencil. The code is parallelized by using message passing interface (MPI), in order to exploit efficiently the computational power of a large number of processors. Domain decomposition is carried out in the main flow direction. Each subdomain is then assigned to a unique core. Each processor core performs the computation within its own subdomain. Distribution functions are then exchanged between two neighbor subdomains after each LBM streaming step, and before applying the boundary conditions.

The parallel speedup of the code has been evaluated for a three-dimensional Poiseuille flow in a channel discretized with 400 × 100 × 20 nodes. Using a parallel cluster with AMD opteron 2.1 GHz processors and 16 GB main memory, a simulation involving 100 processors is 4.8 times faster than when using 20 processors, which corresponds to 96% parallel efficiency.

5.3 Results

In this section, the simulation results obtained for FCC and BCC cubes as well as for a real porous media described by a set of CT images will be presented to calculate permeability and tortuosity. The permeability of a porous medium, k, can be calculated from Darcy's law [133] in the limit of low Reynolds numbers. It is related to the mean flow velocity and applied pressure gradient:

$$k = -\frac{\mu \overline{U}}{\left(\dfrac{dp}{dx}\right)}. \tag{5.2}$$

In Eq. (5.2), $\overline{U}$ is the mean velocity in the entire flow domain including solid lattices and dp/dx is the applied pressure gradient. In LBM, a uniform body force b_f can be used instead of a pressure gradient, which produces the same flow rate as the pressure-driven flow. One should note that Darcy's law is only valid in the limit of very low Reynolds numbers, typically $\text{Re} < 1$. Under this condition, permeability is independent of fluid properties like density, viscosity and pressure gradient. At high Reynolds numbers the contribution of fluid inertia to pressure drop becomes significant and the permeability varies with flow conditions. In such a case, non-Darcy effects must be taken into account, which leads to an extra term (Forchheimer drag) in Eq. (5.2).

5.3.1 Case I: Face-centered cube (FCC) structure

First, a FCC cube is considered. As in all further computations, two node types can be distinguished in the geometry: fluid nodes (index 1) and solid nodes (index 0). In this academic configuration, solid nodes are automatically set in the LBM code using standard equations of spheres and half-way bounce back boundary condition is applied on solid walls. The geometry of the test case is shown in Fig. 5.1. The relation of each cube side size to the sphere diameter is given in the same figure.

Porosity as defined by the fraction of void space to total space is $\phi = 0.25952$. The permeability in this FCC cube has been previously determined by solving unsteady Stokes equations for the microscopic flow by Chapman and Higdon [134]. They have reported a dimensionless permeability, k^*/D^2, of 1.736×10^{-4} (the symbol "*" indicates the reference permeability).

Initial conditions for the flow simulations are zero velocity and uniform lattice density of 1 throughout the domain. A constant body force is applied along the X direction. The applied

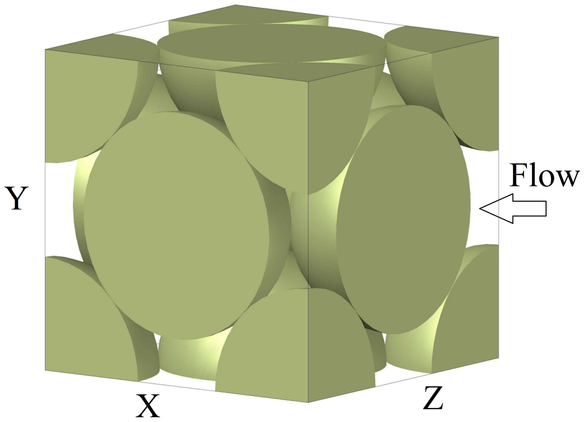

Figure 5.1: FCC packing structure (domain: $\sqrt{2}D \times \sqrt{2}D \times \sqrt{2}D$) (Sec. 5.3.1)

Table 5.1: FCC packing results

D	$k/D^2 \times 10^4$	Error (%)	Re
14.14	1.496	−13.81	1.0×10^{-6}
70.71	1.699	−2.11	1.1×10^{-4}
141.42	1.708	−1.61	8.9×10^{-4}
212.13	1.712	−1.36	3.0×10^{-3}

boundary condition on solid nodes is the half-way bounce back condition, while a periodic boundary condition is applied on all cube faces. The simulation continues until reaching steady-state, defined considering the permeability value between two time steps n and $n-1$ using:

$$\text{steady state}: \left|\frac{k^n - k^{n-1}}{k^{n-1}}\right| < 1 \times 10^{-8}. \tag{5.3}$$

Table 5.1 reports the calculated permeability for different sphere diameters, corresponding to different domain resolutions using SRT-LBM. It can be seen that as the domain resolution increases, dimensionless permeability gets closer to the reference value, $k^*/D^2 = 1.736 \times 10^{-4}$. The result at coarse resolution ($D = 14.14$) is found to be far from the expected value. However, the results of $D = 141.42$, and even more for $D = 212.13$ are very good, with less than 2% difference from the reference. Figure 5.2 shows the flow field in the FCC geometry. It should be noticed that to ensure Darcy's law validity for these calculations, only small body force values are considered, leading to low Reynolds numbers, defined based on the mean flow velocity, sphere diameter, D, and kinematic viscosity, ν:

$$\text{Re} = \frac{\overline{U}D}{\nu}. \tag{5.4}$$

By changing the structure of the cube and arrangement of spheres another packing is created as shown in Fig. 5.3. The porosity is the same as in the former FCC packing ($\phi = 0.25952$). The permeability value in this structure is calculated and given in Table 5.2, which confirms the

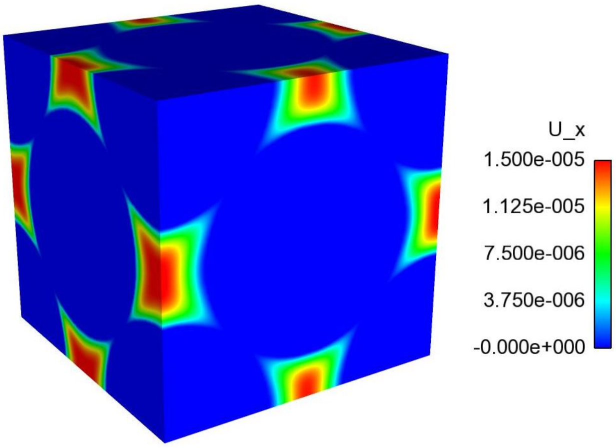

Figure 5.2: Velocity field in FCC packing

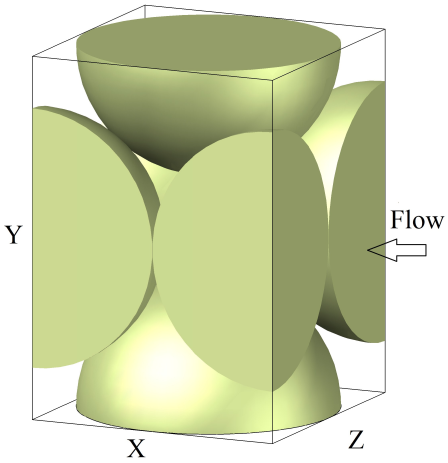

Figure 5.3: Sphere packing (domain: $D \times \sqrt{2}D \times D$) (Sec. 5.3.1)

Table 5.2: Results corresponding to Fig. 5.3 (Sec. 5.3.1)

D	$k/D^2 \times 10^4$	Re
20	1.468	1.2×10^{-5}
50	1.798	2.25×10^{-4}
100	1.704	1.68×10^{-3}
200	1.738	1.39×10^{-2}

importance of domain resolution on the final results. The permeability of this structure is close to that discussed for FCC packing because both have the same porosity and the same sphere diameter of D. Also, in both cases the distance of each sphere center to neighboring spheres is either D or $\sqrt{2}D$ which leads to similar flow paths.

Figure 5.4 depicts the steady-state velocity field for $D = 100$ of this geometry, where the velocity distribution on the cube sides can be observed. The reported velocity is in LB units and along X direction. Figure 5.5 illustrates the flow field on a 2D slice at the middle Z-direction of Fig. 5.4. It is clear that the center of the domain shows a lower velocity compared to the area between the spheres, where constriction locally leads to flow acceleration.

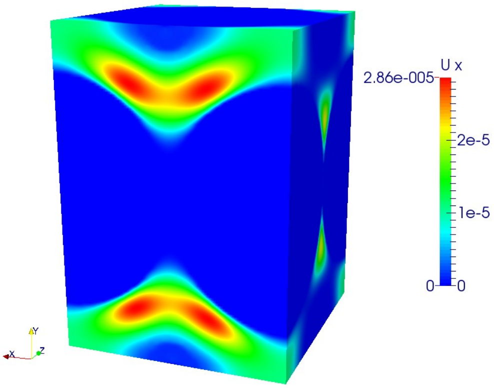

Figure 5.4: Flow field detail in the sphere packing of Fig. 5.3

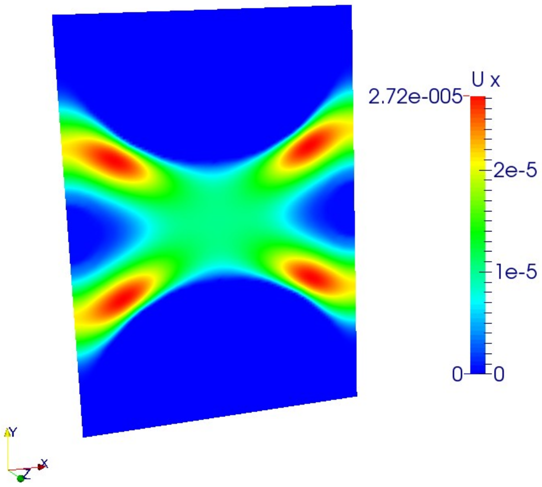

Figure 5.5: Central horizontal slice through Fig. 5.3 (Sec. 5.3.1)

5.3.2 Case II: Body-centered cube (BCC) structure

The second case that is studied here is a BCC structure, as seen in Fig. 5.6. The sphere diameter is D and the cube length in each direction is $\frac{2\sqrt{3}}{3}D$, which results in a porosity of $\phi = 0.31983$. Initial conditions of the flow field are similar to Case I and the fluid flows through the sphere pack along X direction due to a small body force. Chapman and Higdon [134] reported dimensionless permeability value of $k^*/D^2 = 5.023 \times 10^{-4}$. Tables 5.3-5.6 report the calculated permeability using three approaches: Shan-Chen SRT (SC-SRT), Guo-SRT (G-SRT) and Guo-MRT (G-MRT) for 60 different cases. The results are presented for various relaxation times and domain resolutions.

Figures 5.7-5.11 are plotted using the data of Tables 5.3-5.6 and represent k/k^* vs. sphere diameter for different relaxation times. One can see immediately that as the domain resolution increases, the results get much closer to the reference value. For example the predicted permeability with G-MRT approach at $\tau = 1.4$ and $D = 173.21$ shows less than 0.7% error; while for the coarsest domain (corresponding to $D = 17.32$) the difference was 10.5%. It is seen in Figs. 5.7 and 5.8 that for $\tau = 0.6$ and $\tau = 0.8$, the G-SRT model has the highest accuracy compared to SC-SRT and G-MRT for all domain resolutions. At $\tau = 1.0$, the SC-SRT model is

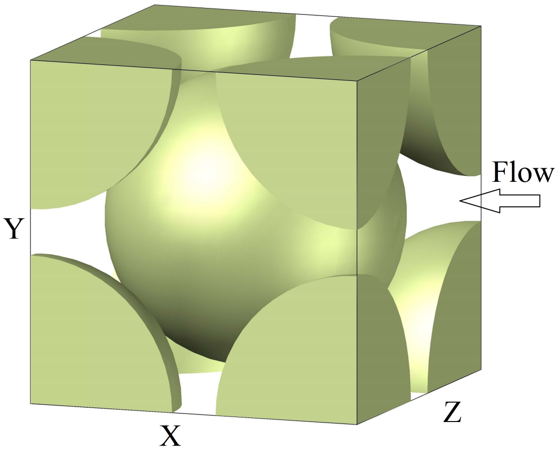

Figure 5.6: BCC packing structure ($2\frac{\sqrt{3}}{3}D \times 2\frac{\sqrt{3}}{3}D \times 2\frac{\sqrt{3}}{3}D$) (Sec. 5.3.2)

Table 5.3: BCC packing results ($D = 17.32$)

Case	τ	Method	$k/D^2 \times 10^4$	k/k^*	Error (%)	Re
1	0.6	G-SRT	3.793	0.755	-24.49	1.8×10^{-4}
2	0.8	G-SRT	4.893	0.974	-2.59	2.5×10^{-5}
3	1	G-SRT	5.826	1.160	15.98	1.1×10^{-5}
4	1.2	G-SRT	6.741	1.342	34.21	6.0×10^{-6}
5	1.4	G-SRT	7.647	1.522	52.25	4.0×10^{-6}
6	0.6	G-MRT	3.466	0.690	-31.00	1.6×10^{-4}
7	0.8	G-MRT	3.966	0.790	-21.05	2.1×10^{-5}
8	1	G-MRT	4.197	0.836	-16.44	8.0×10^{-6}
9	1.2	G-MRT	4.361	0.868	-13.19	4.0×10^{-6}
10	1.4	G-MRT	4.493	0.894	-10.55	3.0×10^{-6}
11	0.6	SC-SRT	3.612	0.719	-28.09	1.69×10^{-4}
12	0.8	SC-SRT	4.349	0.866	-13.41	2.3×10^{-5}
13	1	SC-SRT	4.918	0.979	-2.08	9.0×10^{-6}
14	1.2	SC-SRT	5.470	1.089	8.89	5.0×10^{-6}
15	1.4	SC-SRT	6.011	1.197	19.67	3.0×10^{-6}

briefly the most accurate one. However, for $\tau = 1.2$ and $\tau = 1.4$, the G-MRT approach shows its superiority, especially at higher resolutions, while G-SRT shows the poorest results. Overall, for the current configuration, a relaxation time of $\tau = 0.8 - 0.9$ is found appropriate for SRT models. However, it is clear that all schemes approach each other and converge toward the reference value as resolution increases.

It can also be concluded from Figs. 5.7 and 5.8 that G-SRT and SC-SRT tend to underpredict permeability at $\tau = 0.6$ and $\tau = 0.8$, while at higher τ values, the results of these two models lead to an overpredicted value. G-MRT model shows underpredicted results for all relaxation times.

At higher relaxation times, all schemes converge to a steady state solution at a lower number of iterations. For example, case 55 ($\tau = 1.4$) requires only 7500 time steps to reach the steady state (Eq. (5.3)), while case 51 ($\tau = 0.6$) needs 55500 iterations. Both cases have less than 3%

Table 5.4: BCC packing results ($D = 43.30$)

Case	τ	Method	$k/D^2 \times 10^4$	k/k^*	Error (%)	Re
16	0.6	G-SRT	4.672	0.930	-7.00	3.4×10^{-3}
17	0.8	G-SRT	5.012	0.998	-0.22	4.1×10^{-4}
18	1	G-SRT	5.257	1.047	4.66	1.5×10^{-4}
19	1.2	G-SRT	5.491	1.093	9.31	8.2×10^{-5}
20	1.4	G-SRT	5.730	1.141	14.08	5.2×10^{-5}
21	0.6	G-MRT	4.562	0.908	-9.18	3.3×10^{-3}
22	0.8	G-MRT	4.743	0.944	-5.58	3.8×10^{-4}
23	1	G-MRT	4.818	0.959	-4.08	1.4×10^{-4}
24	1.2	G-MRT	4.868	0.969	-3.09	7.3×10^{-5}
25	1.4	G-MRT	4.906	0.977	-2.33	4.4×10^{-5}
26	0.6	SC-SRT	4.643	0.924	-7.57	3.4×10^{-3}
27	0.8	SC-SRT	4.925	0.981	-1.95	3.9×10^{-4}
28	1	SC-SRT	5.113	1.018	1.79	1.5×10^{-4}
29	1.2	SC-SRT	5.289	1.053	5.29	7.8×10^{-5}
30	1.4	SC-SRT	5.471	1.089	8.91	4.9×10^{-5}

Table 5.5: BCC packing results ($D = 86.60$)

Case	τ	Method	$k/D^2 \times 10^4$	k/k^*	Error (%)	Re
31	0.6	G-SRT	4.839	0.963	-3.66	2.8×10^{-2}
32	0.8	G-SRT	5.003	0.996	-0.41	3.2×10^{-3}
33	1	G-SRT	5.103	1.016	1.59	1.2×10^{-3}
34	1.2	G-SRT	5.188	1.033	3.28	6.2×10^{-4}
35	1.4	G-SRT	5.271	1.049	4.94	3.8×10^{-4}
36	0.6	G-MRT	4.778	0.951	-4.88	2.8×10^{-2}
37	0.8	G-MRT	4.868	0.969	-3.08	3.2×10^{-3}
38	1	G-MRT	4.906	0.977	-2.34	1.1×10^{-3}
39	1.2	G-MRT	4.929	0.981	-1.88	5.9×10^{-4}
40	1.4	G-MRT	4.946	0.985	-1.53	3.6×10^{-4}
41	0.6	SC-SRT	4.832	0.962	-3.81	2.8×10^{-2}
42	0.8	SC-SRT	4.981	0.992	-0.84	3.2×10^{-3}
43	1	SC-SRT	5.067	1.009	0.87	1.2×10^{-3}
44	1.2	SC-SRT	5.138	1.023	2.28	6.1×10^{-4}
45	1.4	SC-SRT	5.207	1.037	3.66	3.7×10^{-4}

error but there is a large difference between the total number of iterations and consequently total computational time.

Figures 5.12-5.15 represent k/k^* versus relaxation time for different D values. It is obvious that the numerically predicted permeability value increases when increasing the relaxation time for all three schemes. It can be also seen that for all diameters, G-SRT model shows the highest difference between the permeability values predicted at $\tau = 0.6$ and at $\tau = 1.4$. In contrast, the G-MRT model shows the lowest dependence on viscosity at all resolutions, and delivers

Table 5.6: BCC packing results ($D = 173.21$)

Case	τ	Method	$k/D^2 \times 10^4$	k/k^*	Error (%)	Re
46	0.6	G-SRT	4.936	0.983	-1.73	2.3×10^{-2}
47	0.8	G-SRT	5.016	0.999	-0.15	2.6×10^{-3}
48	1	G-SRT	5.058	1.007	0.70	9.4×10^{-4}
49	1.2	G-SRT	5.090	1.013	1.34	4.8×10^{-4}
50	1.4	G-SRT	5.119	1.019	1.91	2.9×10^{-4}
51	0.6	G-MRT	4.905	0.976	-2.35	2.3×10^{-2}
52	0.8	G-MRT	4.951	0.986	-1.43	2.5×10^{-3}
53	1	G-MRT	4.969	0.989	-1.07	9.3×10^{-4}
54	1.2	G-MRT	4.980	0.991	-0.85	4.7×10^{-4}
55	1.4	G-MRT	4.988	0.993	-0.69	2.9×10^{-4}
56	0.6	SC-SRT	4.934	0.982	-1.77	2.3×10^{-2}
57	0.8	SC-SRT	5.010	0.997	-0.25	2.6×10^{-3}
58	1	SC-SRT	5.049	1.005	0.53	9.4×10^{-4}
59	1.2	SC-SRT	5.078	1.011	1.09	4.8×10^{-4}
60	1.4	SC-SRT	5.103	1.016	1.59	2.9×10^{-4}

Table 5.7: Computational time for BCC structure

Method	Wall clock time (s)
G-SRT	14.4
G-MRT	21.4
SC-SRT	12.8

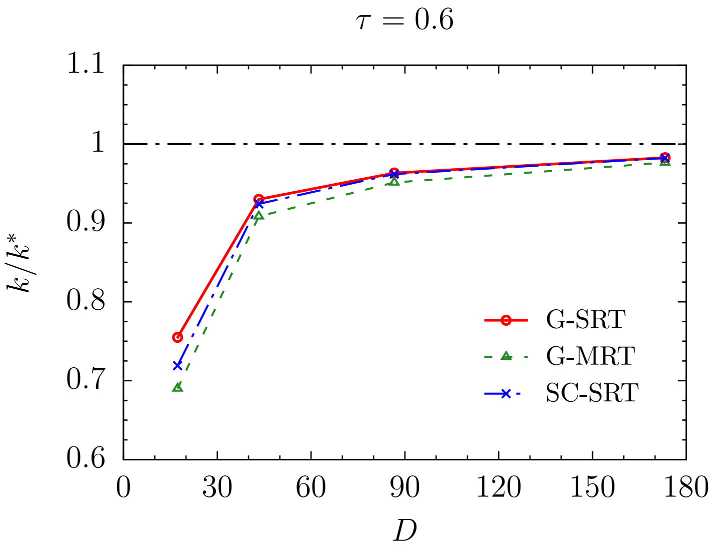

Figure 5.7: Dimensionless permeability k/k^* vs. sphere diameter D for $\tau = 0.6$ based on different force schemes (Guo-SRT, Guo-MRT, Shan-Chen-SRT) for the BCC packing (Sec. 5.3.2)

therefore the most robust estimate. SC-SRT always locates between the other two schemes. SC-SRT and G-SRT schemes tend to coincide at fine domains. Furthermore, the results are more sensitive to relaxation time value for coarser domains; for all three schemes, each curve in

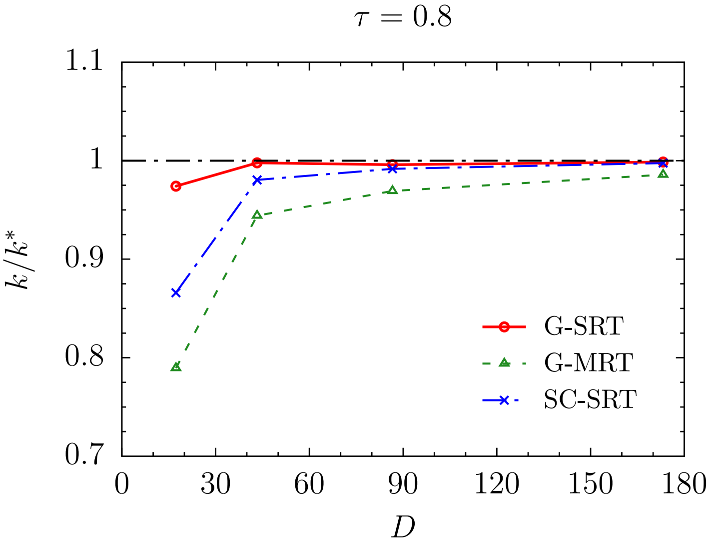

Figure 5.8: Dimensionless permeability k/k^* vs. sphere diameter D for $\tau = 0.8$ based on different force schemes (Guo-SRT, Guo-MRT, Shan-Chen-SRT) for the BCC packing (Sec. 5.3.2)

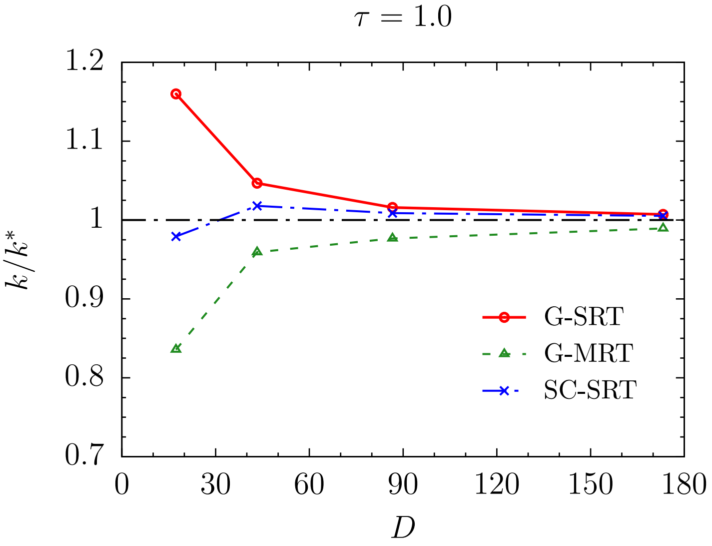

Figure 5.9: Dimensionless permeability k/k^* vs. sphere diameter D for $\tau = 1.0$ based on different force schemes (Guo-SRT, Guo-MRT, Shan-Chen-SRT) for the BCC packing (Sec. 5.3.2)

Fig. 5.12 has a much higher slope compared to its counterpart from Fig. 5.15 (note the different scales on the vertical axis).

It is also interesting to compare the computational cost of these methods. For this purpose, the case with $D = 86.6$ and $\tau = 1.0$ was selected. Table 5.7 shows the wall clock time for 100 iterations on 20 cores. It can be observed that SC-SRT is 12% and 67% faster than G-SRT and G-MRT models, respectively. The G-MRT model is almost 50% slower than G-SRT, because the G-MRT approach includes an additional force term in the calculations and larger matrix computations are present.

Generally speaking, it is seen that, for the examined BCC configuration, each force scheme (G-SRT, G-MRT and SC-SRT) may lead to better results in some regions. But when considering

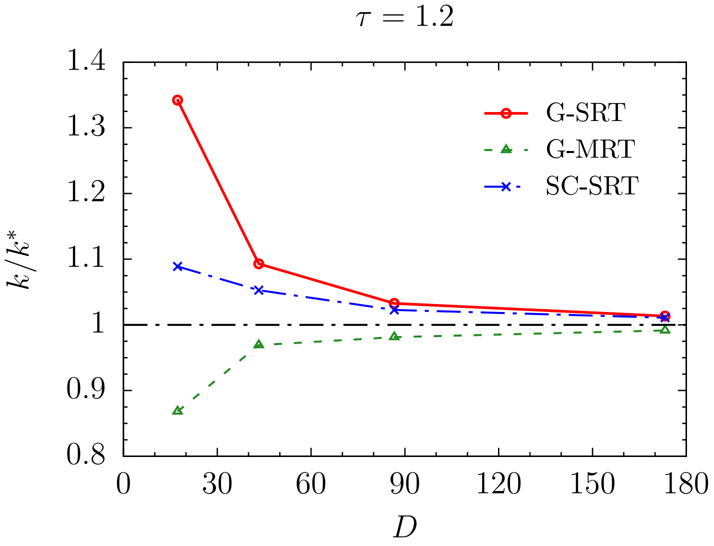

Figure 5.10: Dimensionless permeability k/k^* vs. sphere diameter D for $\tau = 1.2$ based on different force schemes (Guo-SRT, Guo-MRT, Shan-Chen-SRT) for the BCC packing (Sec. 5.3.2)

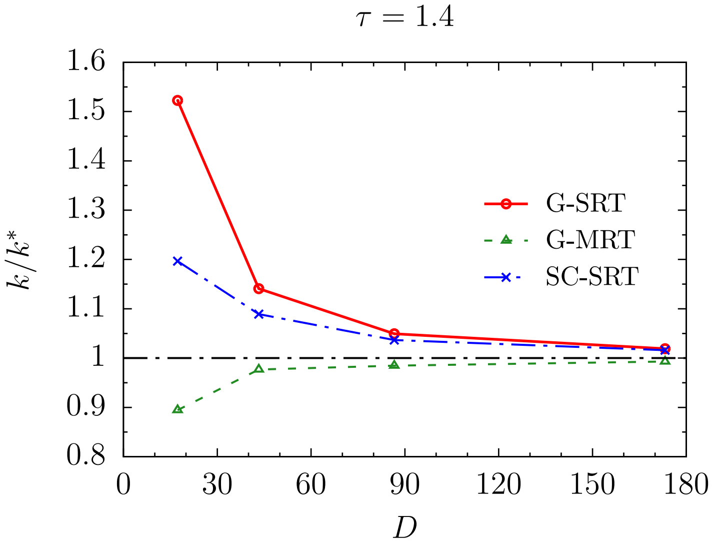

Figure 5.11: Dimensionless permeability k/k^* vs. sphere diameter D for $\tau = 1.4$ based on different force schemes (Guo-SRT, Guo-MRT, Shan-Chen-SRT)

the strong dependency of SRT models on the relaxation time it can be concluded that the proper choice of the force scheme, relaxation time and domain resolution is a trade-off between the required accuracy and computational cost. From one side, higher resolutions lead to more accurate results. Also, for higher resolutions a lower dependency of the results on the relaxation time was observed. But they demand more computational time. On the other hand, higher relaxation times result in a lower number of iterations to reach the steady state but they may lead to higher Mach numbers and ultimately violate the validity of LBM beyond a certain point. The MRT model shows the lowest viscosity dependence in comparison with SRT models but is slower than SRT.

Flow field detail is shown in Fig. 5.16 for case 42 of Table 5.5. Figure 5.17 depicts the

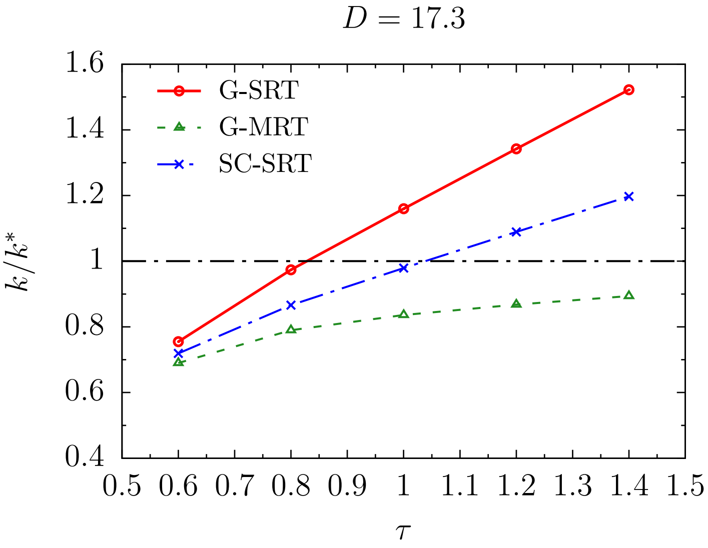

Figure 5.12: Dimensionless permeability k/k^* vs. relaxation time τ for sphere diameter $D = 17.3$ for the BCC packing (Sec. 5.3.2)

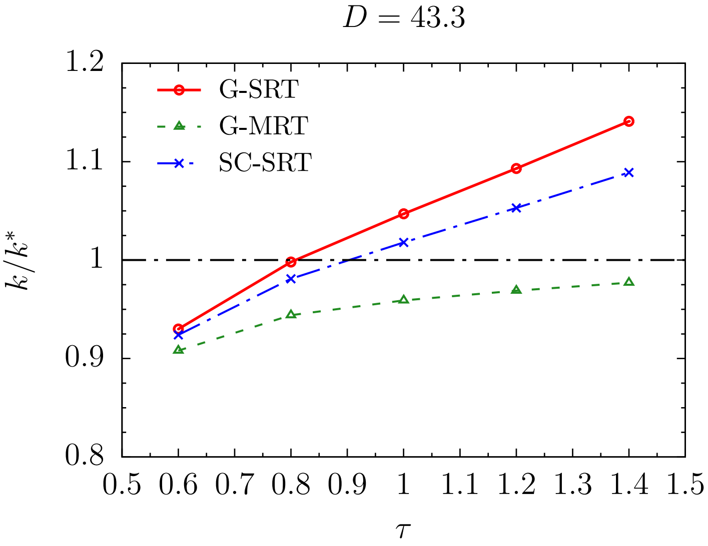

Figure 5.13: Dimensionless permeability k/k^* vs. relaxation time τ for sphere diameter $D = 43.3$ for the BCC packing (Sec. 5.3.2)

streamlines for this case, highlighting the flow topology within the structured packing.

5.3.3 Effect of porosity

In this part, the effect of porosity on the permeability and tortuosity will be investigated. For this purpose, the permeability over a range of porosity values in both BCC and FCC structure is calculated. MRT-LBM approach with a domain size of 200 × 200 × 200 will be used. The spheres location remains unchanged (Figs. 5.1, 5.6) but the diameter varies to get different porosities. Overall, 16 geometries are simulated, including 8 BCC and 8 FCC structures.

Tortuosity is a measure of how much the fluid flows on an indirect path as it passes along a porous medium; it can also be considered as an average elongation of fluid paths. It is defined

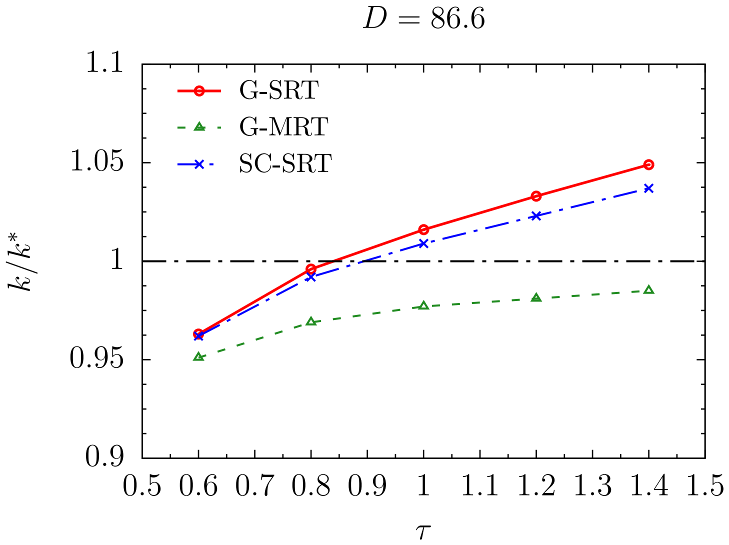

Figure 5.14: Dimensionless permeability k/k^* vs. relaxation time τ for sphere diameter $D = 86.6$ for the BCC packing (Sec. 5.3.2)

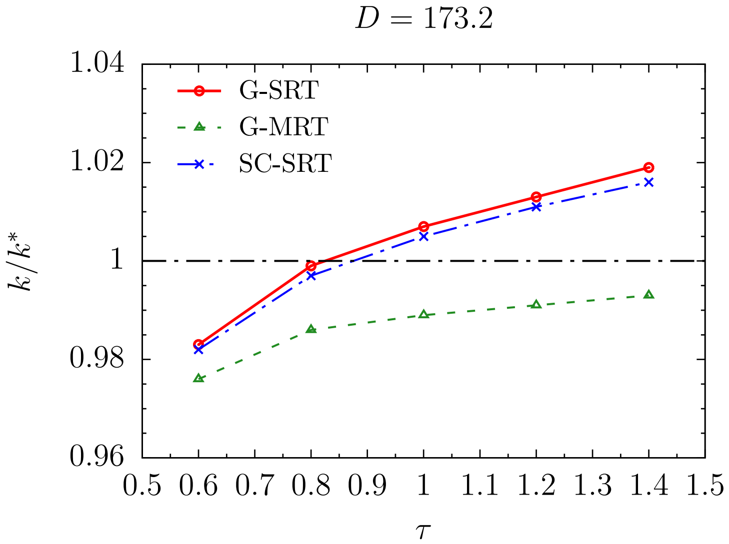

Figure 5.15: Dimensionless permeability k/k^* vs. relaxation time τ for sphere diameter $D = 173.2$ for the BCC packing (Sec. 5.3.2)

as the ratio of the actual distance that fluid travels in the domain (L_e) to the straight length along the major flow direction (L):

$$T = L_e/L. \tag{5.5}$$

Here, we use the following equation to calculate the tortuosity (T) of the porous medium [135]:

$$T = \frac{\sum_{i,j,k} u_{mag}(i,j,k)}{\sum_{i,j,k} |u_x(i,j,k)|}. \tag{5.6}$$

Results are illustrated in Figs. 5.18, 5.19. It is first seen that the permeability is less influenced by the type of geometry. Results of both BCC and FCC geometries follow similar

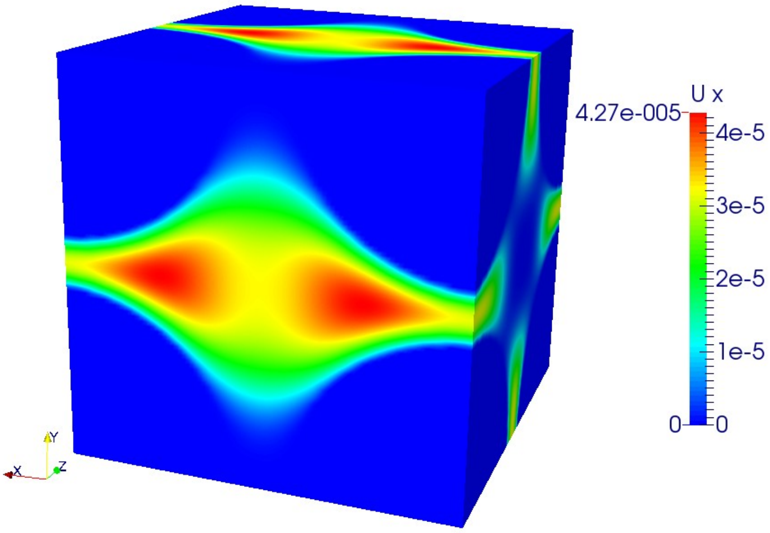

Figure 5.16: Flow field detail of BCC packing colored by x-velocity (Case 42) (Sec. 5.3.2)

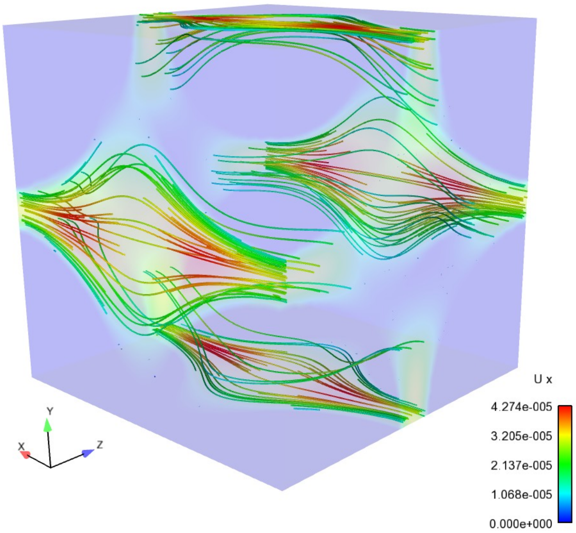

Figure 5.17: Streamlines through a BCC packing colored by x-velocity (case 42) (Sec. 5.3.2)

trends. Permeability shows a major increase by the increase of porosity, which demonstrates the importance of porosity. The permeability of FCC structure is lower than BCC one at low porosities but both are very close at higher porosity values. On the other hand, Fig. 5.19 shows that tortuosity is significantly influenced by the geometry. FCC packing has generally a higher tortuosity. This can be attributed to more spherical sections being located in the cube, which divert the fluid from the straight direction. The graph of the FCC packing is steeper but the difference between the tortuosity of the two geometries decreases at higher porosity values, because streamlines get straight. From Fig. 5.18 the Kozeny-Carman (KC) factor (c_0) [136, 137] can be determined as well [138, 139]:

$$k = \frac{\phi^3}{c_0(1-\phi^2)S^2}, \tag{5.7}$$

where S is the specific surface per unit volume of solid material ($= \pi D^2/(\pi D^3/6) = 6/D$).

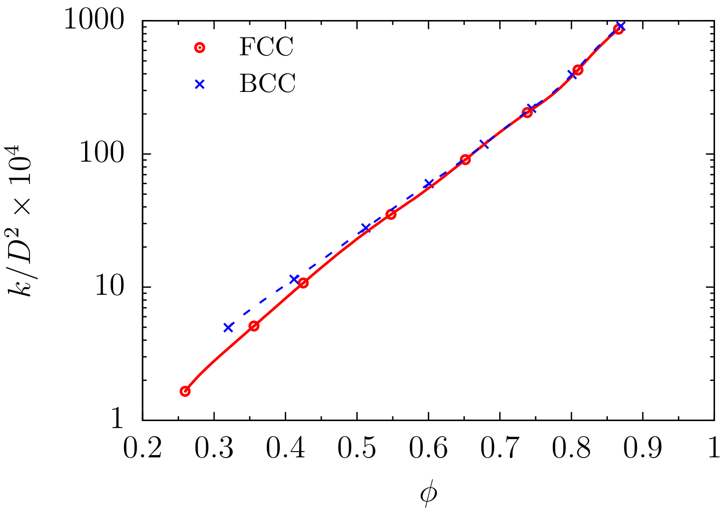

Figure 5.18: Permeability of FCC and BCC geometries at different porosities ϕ (Sec. 5.3.3)

Equation (5.7) gives a relation between permeability and porosity. Thus,

$$k = \frac{\phi^3 D^2}{36c_0(1-\phi^2)} \Rightarrow \frac{k}{D^2} = \frac{\phi^3}{36c_0(1-\phi^2)}. \tag{5.8}$$

Values of c_0 versus porosity (ϕ) are shown in Fig. 5.20 based on the data of Fig. 5.18. A 4th-order polynomial fit of the KC factor is found from these simulations as

$$\text{BCC}: \ c_0 = 168.0847\phi^4 - 309.7246\phi^3 + 203.5196\phi^2 - 47.6256\phi + 6.7517, \tag{5.9}$$

$$\text{FCC}: \ c_0 = 92.9370\phi^4 - 136.2792\phi^3 + 67.1633\phi^2 - 8.8750\phi + 5.1214. \tag{5.10}$$

This equation can be used to estimate the KC factor knowing the porosity value, and then find the dimensionless permeability based on the porosity of these cubic structures occupied by spheres.

5.3.4 Case III: real geometry

In the last test case the real geometry of a 3D porous medium is reconstructed from a set of 2D images. Each image is captured by computed tomography technique. Combining LBM and CT technique may allow detailed flow simulations in such complex geometries. However, corresponding computations may require unrealistic resources. Therefore, an acceptable choice between image resolution and computational requirements must be found.

To investigate the effect of image resolution on the results, the permeability has been calculated with LBM at three image resolutions of the available geometry: 1151 × 1151, 500 × 500 and 200 × 200. The number of images for all three cases is chosen as 20, which leads finally to 26.5, 5.0 and 0.8 million grid cells in the LB simulation, respectively. The simulation process is as follows: The CT images are first read by an in-house MATLAB script and a

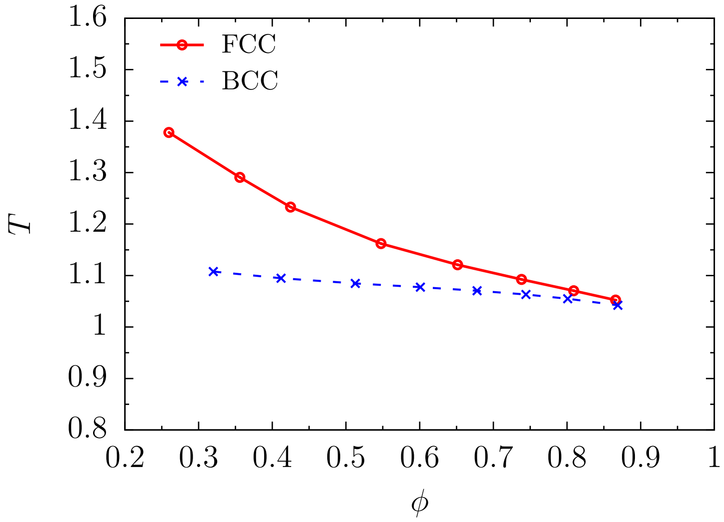

Figure 5.19: Tortuosity T of FCC and BCC geometries at different porosities ϕ (Sec. 5.3.3)

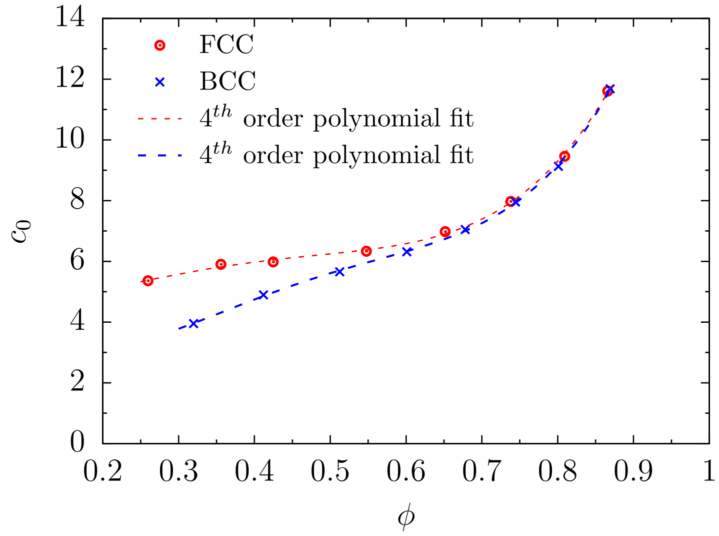

Figure 5.20: Kozeny-Carman factor c_0 of FCC and BCC packings versus porosity ϕ together with a 4th curve fit (Sec. 5.3.3)

geometry file (geometry.txt) is constructed over all images. This text file contains only 0 and 1, where 0 represents solid nodes (black in CT image) and 1 represents pore space (white in CT image). A sample of such CT images in high and low resolutions is shown in Fig. 5.21. The geometry text file is then read by the LBM code and the computational domain is created accordingly, before starting the calculation. Then, LBM proceeds until reaching the steady-state condition.

Table 5.8 shows the calculated permeability (in lattice units) and the error with respect to the result obtained with the highest resolution, since a theoretical prediction is not available for this case. The relaxation time was set to $\tau = 0.8$ for all resolutions. Considering the long computational time needed for this case, even when running on 50 cores of our computer cluster, the Shan-Chen scheme with a constant body force was finally employed, since it is the fastest one

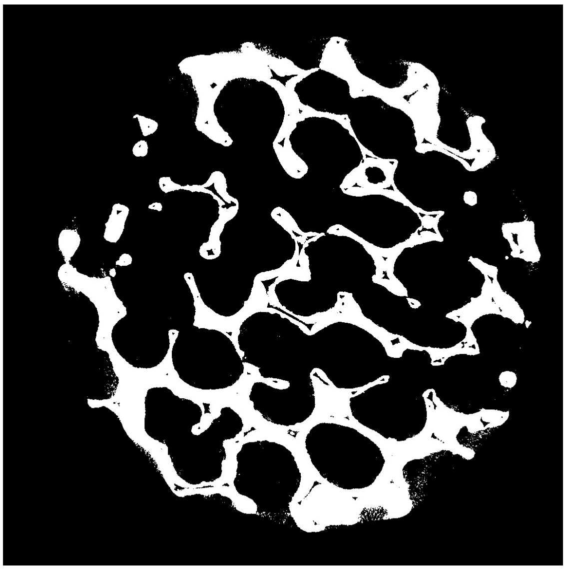

(a)

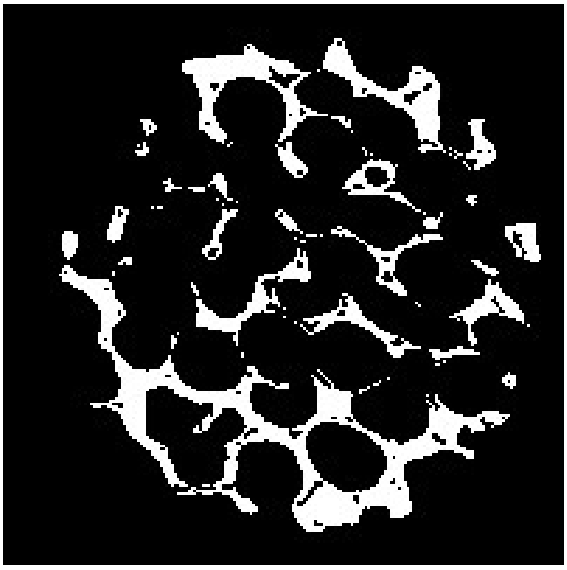

(b)

Figure 5.21: Sample image of a real porous media at high and low resolutions: (a) 1151 × 1151; (b) 200 × 200 (Sec. 5.3.4)

with good accuracy as shown previously. It can be observed that reducing the image resolution leads as expected to an increasing error, 4.2 and 19% error for 500 × 500 and 200 × 200 image sizes, respectively. Therefore, in similar situations, where the geometry is reconstructed from CT images, high enough image resolution is a critical factor.

Considering that an error below 5% is still acceptable, the intermediate resolution (500 × 500) has been kept for the final, three-dimensional simulation of the whole probe, using additionally a discretization of 200 in the direction of the CT cuts. Streamlines are shown in Fig. 5.22 as obtained by LBM in this 200 × 500 × 500 domain. On 50 cores, this 3D computation required 25 hours of computing time.

Table 5.8: Calculated permeability in Case III

Domain	Permeability (lu^2)	Permeability $\times \Delta x^2$	Error (%)
$20 \times 1151 \times 1151$	6.524	4.92×10^{-6}	–
$20 \times 500 \times 500$	1.282	5.13×10^{-6}	4.2
$20 \times 200 \times 200$	0.160	4.0×10^{-6}	−19

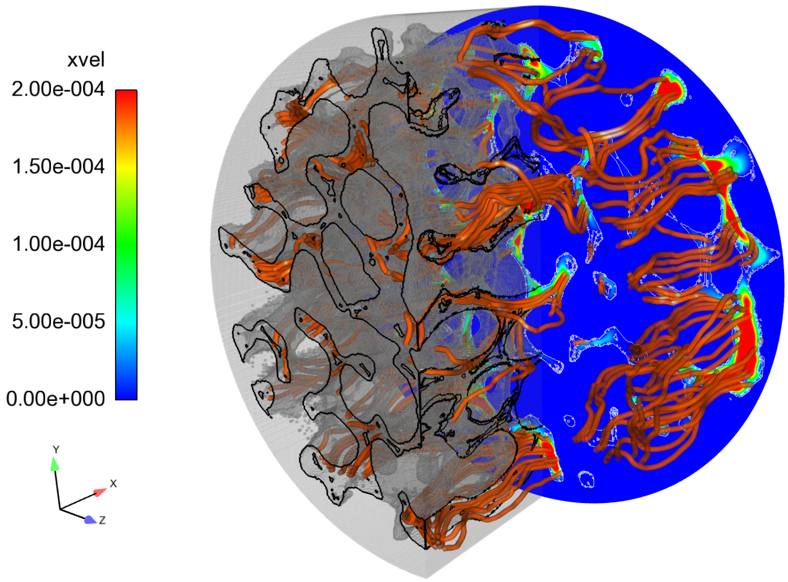

Figure 5.22: Streamlines and velocity field through a real porous medium colored by streamwise velocity (Sec. 5.3.4)

5.4 Summary

Lattice Boltzmann simulations of hydrodynamics in porous media have been used to predict the permeability value at low Reynolds numbers. Different test cases have been considered, including reference flow in FCC and BCC packings as well as a real porous media probe reconstructed from CT images. Two force schemes with single- or multiple relaxation times have been compared. The results show excellent agreement with analytically predicted value for FCC and BCC packings. For all three schemes (Guo-SRT, Guo-MRT and Shan-Chen-SRT), the accuracy of the predicted permeability depends strongly on the domain resolution. As expected, low resolutions lead to large errors. For a fixed domain size, the predicted permeability increases with the relaxation time for all studied approaches due to viscosity dependence of bounce-back boundary condition. As a whole, Guo-MRT shows a lower dependency on relaxation time, thus delivering a more robust estimate. However, it is also the approach leading to the longest simulations. Moreover, the impact of relaxation time is larger in coarser domains. Also, higher relaxation time models need lower number of iterations to reach the steady state solution. The influence of porosity on permeability and tortuosity was also examined. Permeability of both BCC and FCC structures follow similar trends when plotted against porosity, but tortuosities behave more differently. Finally, considering a real geometry, it was shown that LB simulations can indeed deliver numerical estimates of permeability in very complex configurations from a set of CT images when a sufficient resolution is used.

Chapter 6

Turbulent Channel Flow with Resolved Spherical Particles

6.1 Introduction

In many particulate flows, the flow regime is turbulent, which tremendously increases complexity compared to a laminar flow. In these cases, the inherent stochastic structure of the carrier-phase together with the random distribution of the particles result in complex particle-fluid interactions.

Addition of small amounts of particles to a turbulent flow can modify the turbulence characteristics significantly. Gore and Crowe [140] expressed that small particles suppress the turbulent intensity, whereas large particles enhance it. Small particles will attenuate fluid turbulence due to the lagging response of the particles with respect to the turbulent fluctuations. For larger particles, similar effects happen; however, a large particle will additionally cause wake shedding and, therefore, turbulence intensification was observed. Very small particles (microparticles) may increase the turbulence due to their fast response to changes in the fluid. However, high particle concentrations can lead to a completely different behaviour.

Many studies have considered experimental investigation of turbulent particulate flows [141–147]. Rashidi *et al.* [148] performed experiments with particles of different sizes in an open channel. They found that large particles (1100 μm) increase the turbulence intensities and Reynolds stresses. On the other hand, smaller particles (120 μm) decreased the measured intensities and Reynolds stresses. These effects were more pronounced by increasing the particle loading. Kussin and Sommerfeld [141] experimentally investigated a turbulent channel flow with a wide range of particle sizes. They stated that, large glass beads particles (0.625 and 1 mm) showed a turbulence augmentation in the core of the channel. However, in the near-wall regions of the channel, turbulence reduction was observed.

With respect to Lagrangian point-particles, Pan and Banerjee [149] considered a dilute particle-laden turbulent channel flow with a free surface ($\phi < 10^{-4}$). They used a pseudo-spectral method to solve the Navier-Stokes equations and point-particles were modeled in a Lagrangian framework. They observed that particles smaller than the dissipative length scale reduce turbulence intensities and Reynolds stress.

Mallouppas and van Wachem [150] carried out large eddy simulation (LES) of point-particles dispersed in a horizontal channel flow with the gravity acting perpendicular to the main flow. The results were in consistency with the experimental measurements of [141].

Most studies concerning turbulent particle-laden flows do not resolve individual particles. Another approach is based on *fully-resolved* simulations. In this case, interactions are modeled directly and the fluid motion around each moving particle is numerically resolved. Pan and Banerjee [151] modeled the presence of large particles in an open channel flow. Particles radius was $a = 0.05H$ or $0.1H$ with H being the half-channel height. Solid phase volume fraction was $\phi \sim 10^{-4}$, which still belongs to the dilute regime. They reported that, the presence of large particles alters the turbulence properties, particularly in the near-wall region. They found that particles increase turbulence intensities and Reynolds stress; this observation was more dominant for larger particles. Lashgari *et al.* [152] studied laminar to turbulent transition in a channel flow in the presence of small amounts of finite-size particles. They found that the critical Reynolds number beyond which laminar to turbulent flow transition occurs is reduced as compared to a single-phase flow. Kajishima *et al.* [153] simulated an upward turbulent flow in a vertical channel including solid particles ($d_p/H = 0.125$, $\phi \sim 10^{-3}$). They reported a strong modification of velocity and vorticity fluctuations. It was observed that, particles tend to move up mostly in the region close to the wall. It was also seen that the particles hinder the upward flow motion by reducing the mean velocity. On the other hand, velocity fluctuations showed an increase. Uhlmann [154] performed DNS of fully-resolved particles in a vertical channel flow ($\phi = 4.2 \times 10^{-3}$). Formation of large-scale elongated streak-like structures was reported. It was mentioned that turbulence intensity and the normal stress anisotropy were strongly increased with respect to the single-phase flow at the same bulk Reynolds number. This enhancement was attributed to an increase in the streamwise velocity fluctuations.

If the solid phase volume fraction is increased beyond the dilute regime, in the so-called dense regime, a four-way coupling model is required to accurately model all interactions. Corresponding studies are very challenging and, therefore, limited in number. Shao *et al.* [155] used a direct-forcing fictitious domain method (DF/FDM) and simulated a horizontal turbulent channel flow with finite-size solid particles at up to 7% solid-phase volume fraction. This method assumes that the interior of the particle is also filled with the fluid. They found that neutrally-buoyant particles decrease the maximum root mean square (rms) of the streamwise velocity fluctuation, while increasing it in the region very close to the wall and in the center region. The rms of normal and spanwise fluctuating velocities increased near the wall. Picano *et al.* [156] observed that overall drag reduction for very dense mixtures at high Reynolds number is probably due to a significant reduction of the turbulent drag that contributes to total shear stress. Recently, Fornari *et al.* [157] used immersed boundary method to investigate DNS of a particle-laden flows with spherical particles. The simulation was built on top of an incompressible Navier-Stokes equation solver and the effect of volume fraction and particle size was investigated.

In recent years, the lattice Boltzmann method has been successfully applied to various flow regimes including particulate flows, heat transfer phenomena, medical flows, porous media, etc. However, the application of LBM to DNS of particle-laden turbulent flows is quite new and limited. DNS is challenging, since it requires a proper resolution of all relevant scales in time and space [158]. Banari *et al.* [159] used LBM to model suspensions of rigid spherical point particles and observed changes in mean flow properties. Wang *et al.* [160] simulated a turbulent particle-laden flow, in which particle-fluid interactions were modeled by a Galilean-invariant momentum exchange method. The simulation was carried out for a single volume fraction and particle size, with neutrally-buoyant particles.

This chapter aims at numerically investigating the effects of fully-resolved particles in a turbulent channel flow concerning turbulence modulation, using four-way coupling. The LBM is used to resolve the fluid flow, while considering the effect of the particles by IBM. The influence of different parameters including particle size, volume fraction and density is investigated by varying these parameters. To the best of our knowledge, the current work is the first IBM-LBM publication concerning particle-laden pressure-driven turbulent channel flows. The rest of this chapter is organized as follows. First, the test case is described. It is followed by the validation of single-phase (unladen) turbulent channel flow against available DNS benchmarks. Then, the simulation results for fully-resolved particles interacting with the turbulent flow are presented. The effect of these particles on various turbulent flow characteristics is finally analyzed and discussed, before listing the most important observations. Results of this chapter have been partly published in [161].

6.2 Flow configuration

In this study, SRT-LBM based on the force scheme of Shan-Chen [18] is used to model the fluid flow and particle-fluid force and velocity interactions are modeled by IBM. Details of the model can be found in Chapters 2 and 3. A turbulent flow between two parallel flat walls is considered. A schematic of the computational domain is shown in Fig. 6.1. Domain size is $L_x = 4.6H$, $L_y = 2H$ and $L_z = 2H$, corresponding to the streamwise x, normal y, and spanwise z directions, respectively, and H is half the channel height. No-slip boundary condition is applied on the upper and lower walls, whereas the streamwise and spanwise directions correspond to periodic boundary conditions.

To accelerate the computations, the numerical domain is decomposed in x direction into several smaller blocks and the code is parallelized in this direction using the message-passing interface. Each processor core handles its own domain part and the particles whose center is located within the domain. After each time step, all the necessary fluid and particle data are exchanged between neighbouring processors.

In order to stick to the low Mach number requirement of the LBM, friction velocity (u_τ) is

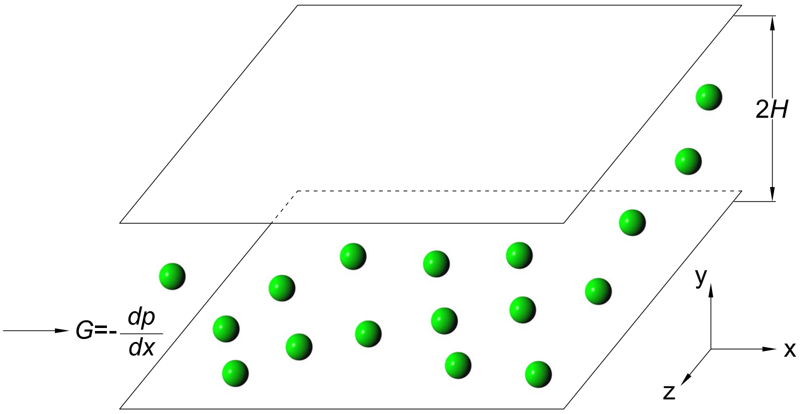

Figure 6.1: Schematic of the geometry of a turbulent channel flow with spherical particles, where G represents the flow-driving force (here, pressure gradient) (Sec. 6.2)

first calculated by:

$$u_\tau = \frac{U_0}{\kappa \ln \mathrm{Re}_\tau + B}, \tag{6.1}$$

where κ is the von Kármán constant and is equal to 0.4. Parameters $B = 5.5$ and $U_0 = 0.1$ are used in Eq. (6.1) to calculate the maximum probable flow velocity in the channel center [162]. Subsequently, a constant driving force is applied along the x direction, which is given by $G = \rho_f g = -dp/dx = \rho_f u_\tau^2/H$. The Reynolds number based on the friction velocity is defined by $\mathrm{Re}_\tau = u_\tau H/\nu = 180$, where ν is the kinematic viscosity and $u_\tau = (\tau_w/\rho_f)^{0.5}$. Here, τ_w is the shear stress at the wall. The corresponding bulk Reynolds number based on the bulk velocity (U_b) is equal to $\mathrm{Re}_b = U_b 2H/\nu = 5600$ and the domain is uniformly discretized by $600 \times 260 \times 260$ grid points along x, y and z directions. Based on this mesh size, the viscous length scale is equal to $l_\tau = \nu_f/u_\tau = 0.72$, which results in a non-dimensional mesh size $\Delta^+ = \Delta/l_\tau = 1.38$. The large-eddy turnover time is given by H/u_τ. Mean properties are calculated from the flow field and stored on disk every 0.04 large-eddy turnover time.

In order to avoid the long computational time required for transition from laminar to turbulent regime, the flow is initialized by one of our prior DNS results for a single phase flow. The results of the single-phase and particle-laden flows will be later compared at the same driving force. Another possible approach would be to keep the same flow rate, which is not used in the present study. In both particle-laden and particle-free cases, the data are collected when the turbulent flow is fully developed and statistically reaches the steady-state. For particle-laden flow, the particles are initially randomly positioned throughout the domain, avoiding any overlapping. The results will be presented in wall (inner) units, unless otherwise stated, and the velocity values are all scaled by u_τ. The root mean square of the velocity fluctuations is defined by $u_{rms} = \overline{u'u'}^{1/2}$ and is obtained by $u_{rms} = \sqrt{\overline{u^2} - \overline{u}^2}$. The other diagonal components, v_{rms} and w_{rms} are defined similarly. All fluid statistics are computed excluding the Eulerian nodes that are located inside the particles.

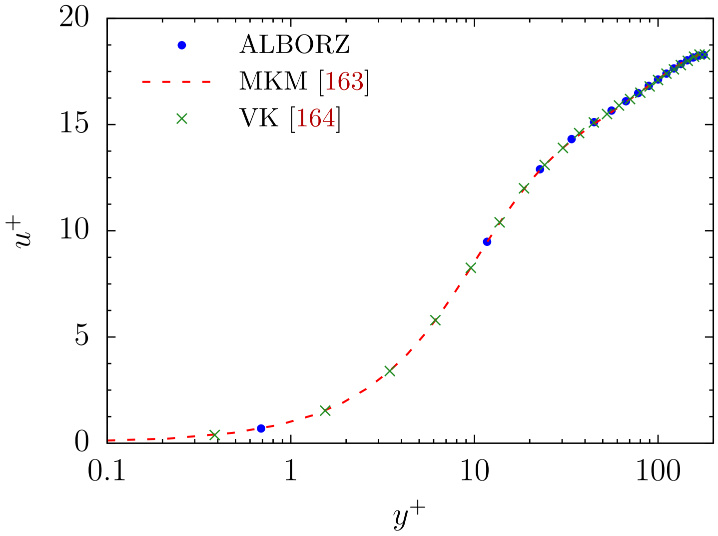

Figure 6.2: Comparison of normalized mean streamwise fluid velocity u^+ versus normalized distance from the wall y^+ for a turbulent single-phase channel flow with the benchmark data of Moser, Kim and Mansour (1999) and Vreman and Kuerten (2014) (Sec. 6.3.1)

In the case of particle-laden flow, considered particles are rigid and spherical, with a particle size of either $a/H = 0.06$ or 0.1, where a is the particle radius. This corresponds to 15.6 and 26 Eulerian grid points along particle diameter, respectively. Small and large particles are discretized by 765 and 2124 Lagrangian points on their surface, respectively. Two types of particles have been considered: neutrally-buoyant ($\rho_p = \rho_f$), and heavy ($\rho_p = 1.2\rho_f$). The solid phase volume fraction is either $\phi = 1.5$, 3, or 6%.

6.3 Results and discussion

As shown in previous chapters, the code has been already thoroughly validated concerning laminar particulate flows. Therefore, only the ability of the tool to describe turbulence must be validated. For this purpose, benchmark data for a single-phase turbulent flow is employed. The same code will then be used to simulate turbulent particulate flows.

6.3.1 Single-phase flow

A turbulent channel flow at a frictional Reynolds number of $\mathrm{Re}_\tau = 180$ is considered. The results of mean and fluctuating velocity components obtained by ALBORZ will be compared to the documented benchmark data of Moser, Kim and Mansour [163] (written MKM) and Vreman and Kuerten [164] (written VK).

The results of this comparison are presented in Figs. 6.2-6.4. The streamwise, normal, and spanwise velocity components are shown by u, v, and w, respectively. All have been normalized by friction velocity. The profile of the normalized mean streamwise velocity $u^+ = \overline{u}/u_\tau$ versus $y^+ = yu_\tau/\nu$ is depicted in Fig. 6.2. The mean value at each point y_1 is the average of mean

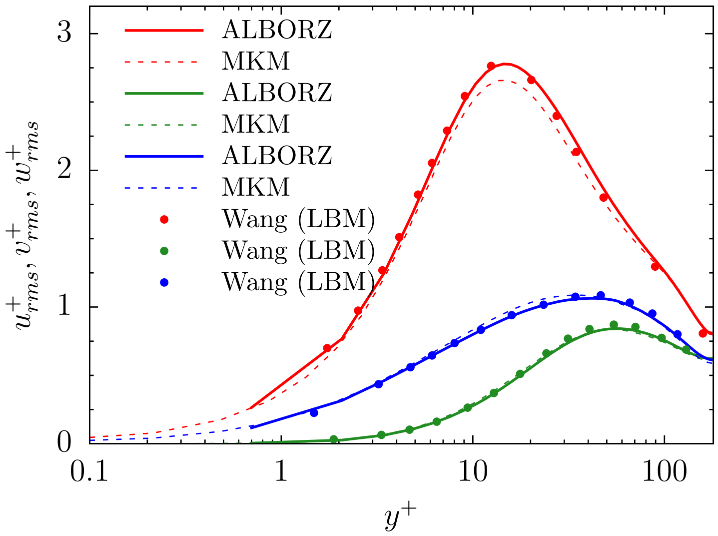

Figure 6.3: Comparison of rms of fluid velocity fluctuations as a function of distance from the wall in a single-phase turbulent channel flow with the data of Moser, Kim and Mansour (1999) and Wang et *al.* (2014)

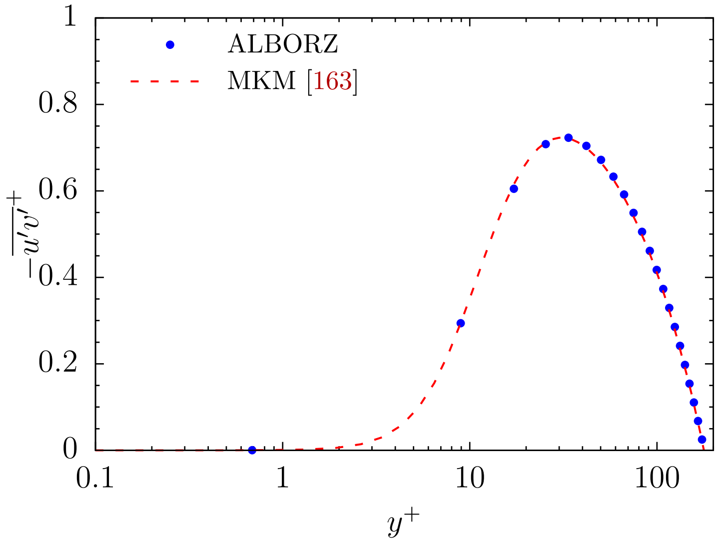

Figure 6.4: Comparison of normalized Reynolds shear stress as a function of distance from the wall in a single-phase turbulent channel flow with the data of Moser, Kim and Mansour (1999)

velocity at $y = y_1$ and $2H - y_1$. A very good consistency in terms of mean streamwise velocity along the whole channel height is observed.

Figure 6.3 shows the normalized rms of velocity fluctuations in all three directions, where $u^+_{rms} = u_{rms}/u_\tau$, $v^+_{rms} = v_{rms}/u_\tau$ and $w^+_{rms} = w_{rms}/u_\tau$. The results are in good agreement with those from MKM. However, slight deviations are observed, in particular concerning the peak value of u^+_{rms}. These differences are a direct result of the relatively low accuracy of LBM, which is only second-order in space [124]. It can be seen that our results are very close to those of Wang *et al.* [165], who also used a LBM solver for similar conditions and a similar resolution of $512 \times 256 \times 256$. At the same time, the agreement concerning the xy-component of the Reynolds

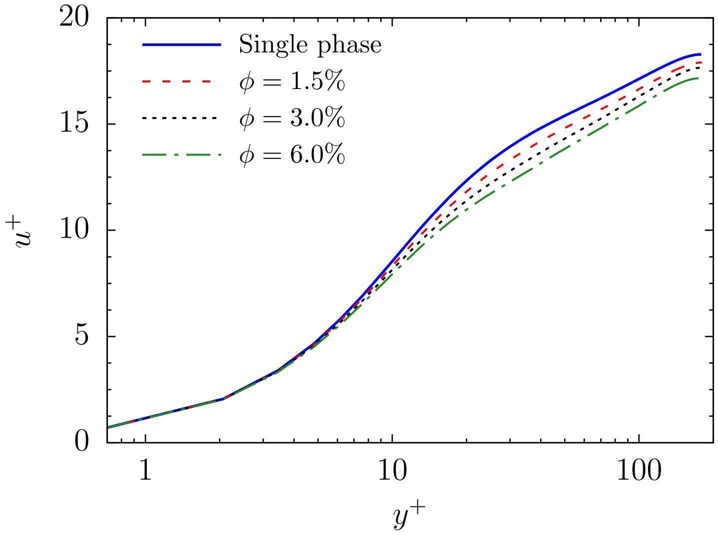

Figure 6.5: Mean streamwise velocity u^+ profile as a function of distance from the wall y^+ for single-phase and particle-laden flow for different solid-phase volume fractions ($a/H = 0.1$, $\rho_r = 1.0$)

shear stress is excellent, as demonstrated in Fig. 6.4. Considering that the focus is set here on comparisons between single-phase and two-phase flows more than on the absolute values, and keeping in mind that this single-phase simulation already takes 8 days of computing time using 150 processors (AMD opteron 2.1 GHz and 16 GB main memory), the employed resolution of $600 \times 260 \times 260$ will be kept, since it already leads to a good agreement with the reference data. From now on, the numerical setup remains always the same, and particles will be added to the flow, before comparing the results obtained for single-phase and particle-laden conditions.

6.3.2 Particle-laden flow

Now, the simulation results obtained for turbulent particle-laden flows under different conditions of concentration, particle size, and particle density will be discussed.

Effect of particle concentration

First, the influence of particle concentration on different flow parameters will be investigated. In this subsection, particle radius and density are always set at $a/H = 0.1$ (large particles) and $\rho_p = \rho_f$ (neutrally-buoyant), respectively. The mean streamwise velocity profile for various concentrations of solid phase is reported in Fig. 6.5. It can be seen immediately that mean velocity decreases by addition of particles and this effect is more pronounced at higher volume fractions. An average velocity reduction of 3.0, 5.0 and 7.9% for volume fractions of $\phi = 1.5$, 3 and 6% was observed respectively, in our simulations. It is interesting to see that, in all volume fractions, the maximum reduction of mean flow velocity occurs at $y^+ \approx 30$. It will be later shown that this point corresponds to the maximum local volume fraction of particles. At this location, the maximum velocity reduction stands at 4.3, 8.0 and 12.0% for $\phi = 1.5$, 3 and 6%,

Table 6.1: von Kármán constants for $u^+ = \kappa \ln y^+ + B$ as a function of particle volume fraction ϕ for $(a/H = 0.1,\ \rho_r = 1.0)$

Case	$\phi(\%)$	κ	B
1	0	2.5	5.6
2	1.5	2.65	4.5
3	3.0	2.79	3.45
4	6.0	2.9	2.5

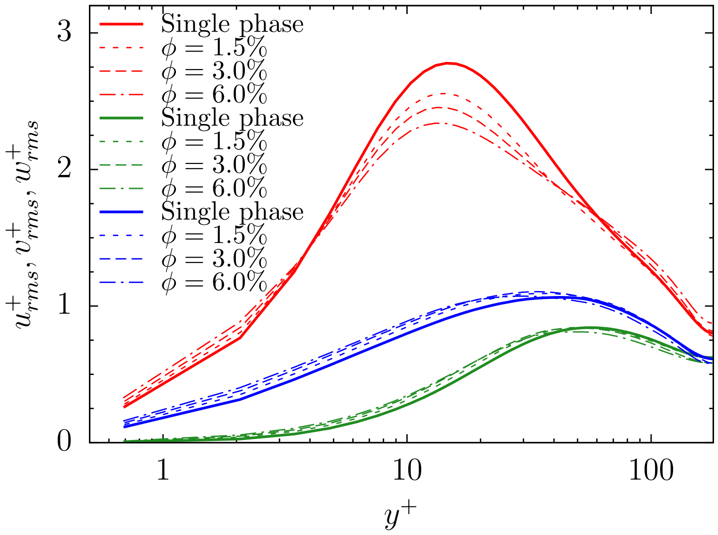

Figure 6.6: RMS of velocity fluctuations for single-phase and particle-laden flow for different solid-phase volume fractions $(a/H = 0.1,\ \rho_r = 1.0)$

respectively. It is also seen that, all profiles coincide in the region close to the wall due to using the same driving force. The particle-laden profiles are shifted downward. To interpret the data in terms of log-law profile, different von Kármán constants (κ, B) are reported in Table 6.1. The coefficient κ increases with volume fraction, but at a reducing rate from $\phi = 1.5\%$ to 3% and then to 6%. On the other hand, the coefficient B is decreasing rapidly when increasing ϕ.

Figure 6.6 shows the rms of velocity fluctuations. The maximum value of streamwise velocity fluctuations is significantly reduced when adding particles. Again, larger volume fractions lead to a stronger reduction. Shao *et al.* [155] attributed this reduction to a lower intensity of streamwise vortices. By increasing the volume fraction, the peak point is also shifted closer to the channel wall. At the same time, it is observed that streamwise velocity fluctuations increase in the near-wall region. In the core region, minor enhancement of u^+_{rms} value is observed again. Because of small vortices that are created close to the wall, both v^+_{rms} and w^+_{rms} increase at $y^+ < 40$. In the center region, normal and spanwise velocity fluctuations show little changes compared to a single-phase flow. Since the main motion of particles occurs in the streamwise direction, their influence is more pronounced in this direction compared to the other ones. It is also clear that the particle-laden cases are more isotropic than the single-phase one; velocity fluctuations become closer to each other in all three directions. Isotropy increases with increasing particle loading.

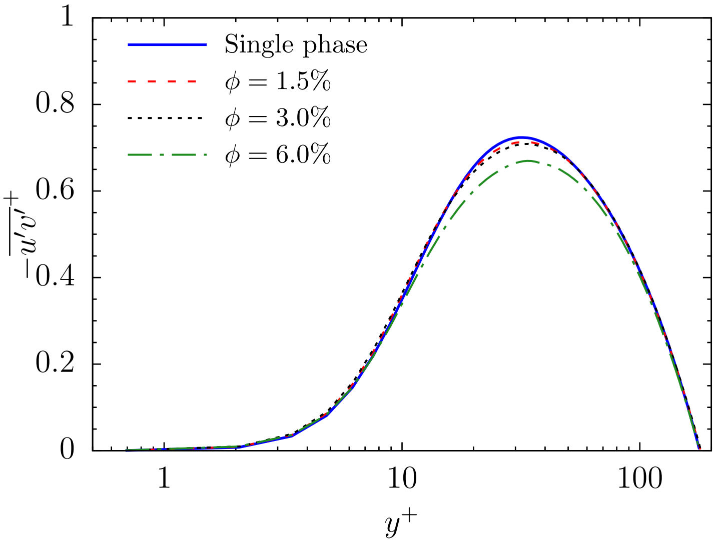

Figure 6.7: Reynolds stress profile for single-phase and particle-laden flow for different solid-phase volume fractions ($a/H = 0.1$, $\rho_r = 1.0$)

Figures 6.7 and 6.8 compare the results of Reynolds stress and turbulent kinetic energy (TKE), respectively. As expected from the previous velocity fluctuations, both parameters are generally reduced except for the near-wall region. Therefore, turbulence activity is overall reduced, mainly due to the change in streamwise velocity rms. Close to the channel center, xy-Reynolds stress and turbulent kinetic energy are almost identical to those of the single-phase flow. It is worth noting that a reduction of turbulence intensity does not necessarily mean that the flow rate increases because of the contribution from particle-induced stresses in the system.

Different components of streamwise momentum budgets (in wall units) are shown in Fig. 6.9, where $\tau = \tau_V + \tau_R + \tau_P$. Here, $\tau_V = du^+/dy^+$ is the viscous stress, $\tau_R = \overline{u'v'}^+$ is the xy-Reynolds stress and τ_P is particle-induced stress. The single-phase flow graph (Fig. 6.9a) shows that, the calculated total stress ($\tau = \tau_V + \tau_R$) follows almost exactly the analytical solution of $\tau^+ = 1 - y^+/\mathrm{Re}_\tau$ which is derived from streamwise momentum balance equation:

$$\frac{d}{dy}\left(\overline{u'v'} + \nu\frac{d\overline{u}}{dy}\right) = \frac{G}{\rho} = \frac{u_\tau^2}{H}, \tag{6.2}$$

which leads to

$$\overline{u'v'}^+ + \frac{du^+}{dy^+} = 1 - \frac{y}{H} = 1 - \frac{y^+}{\mathrm{Re}_\tau}. \tag{6.3}$$

This consistency proves again the accuracy of these calculations. Particle-laden data are shown in Fig. 6.9b for $\phi = 6\%$. It can be seen that, the xy-Reynolds shear stress is shifted downward. Viscous stress shows minor change. In this particle-laden case, particle stress (τ_P) is not negligible and it contributes to total stress. The effect of particle-induced stresses on total pressure drop was also observed by Picano *et al.* [156].

Next, the distribution of particles in different regions of the channel is investigated. The

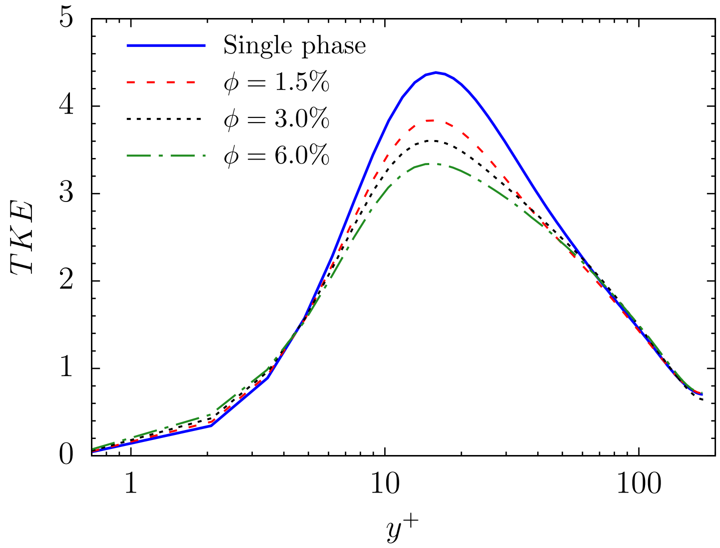

Figure 6.8: Distribution of turbulent kinetic energy for single-phase and particle-laden flow for different solid-phase volume fractions ($a/H = 0.1$, $\rho_r = 1.0$)

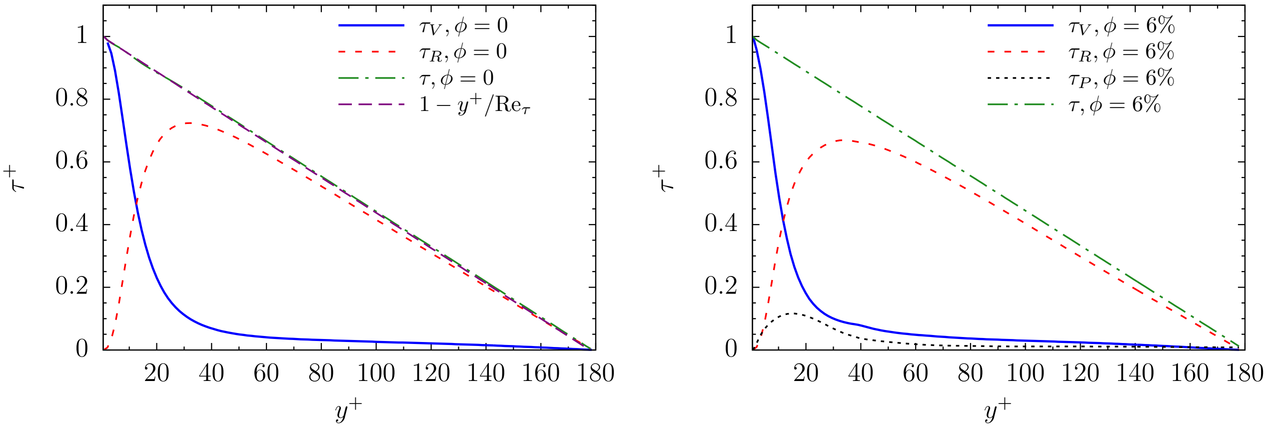

(a) (b)

Figure 6.9: Streamwise momentum budget for (a) single-phase flow; (b) particle-laden flow versus distance from the wall ($\rho_r = 1.0$, $\phi = 6\%$)

local volume fraction occupied by particles at each y position and each time step is computed as

$$\phi_j = \frac{\sum_{i=1}^{N_x} \sum_{k=1}^{N_z} \delta_{ik}(x_{ijk})}{N_x \times N_z}, \tag{6.4}$$

where $\delta_{ik}(x_{ijk})$ is 1 if the domain point is located inside the particle and is 0 if it is within the fluid region. This computation is carried out for all the 260 j-planes in y-direction. The resulting particle volume fraction is shown in Fig. 6.10. A clear peak is observed close to the wall at $y^+ \approx 30$, with the local peak value being quite close to the overall particle volume fraction, in particular at low particle concentration. Many particles thus appear to be trapped in the region close to the wall. As discussed before, this is also the point where maximum velocity

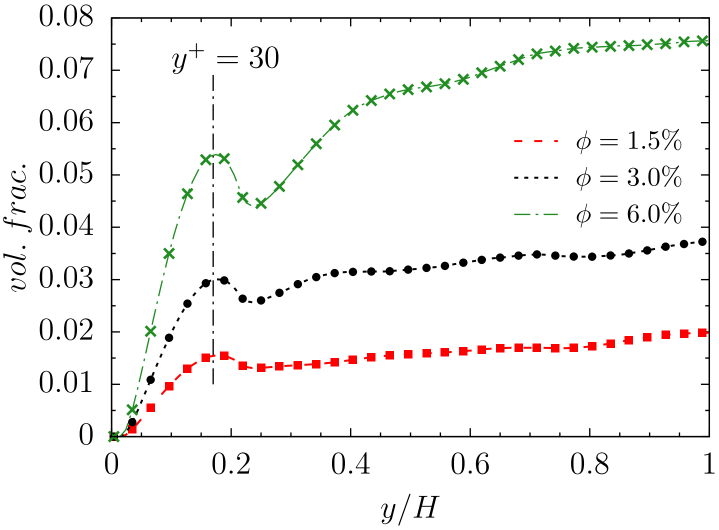

Figure 6.10: Distribution of local particle volume fraction as a function of distance from the wall y/H for different volume fractions ($a/H = 0.1$, $\rho_r = 1.0$)

reduction occurs. High concentration of particles near the wall leads to more particle-wall collisions. These collisions lead to higher rms of velocity fluctuations in Fig. 6.6. Therefore, at higher concentrations, the curve of rms of all velocity fluctuations is shifted upward.

If the local maximum value is normalized by the overall particle-phase volume fraction in each individual case, the lowest volume fraction ($\phi = 1.5\%$) shows the highest local peak of 103%, compared to only 90% for $\phi = 6\%$. It means that, when increasing volume fraction, more particles tend to move toward channel center, and the local peak around $y^+ \approx 30$ becomes less pronounced in relative manner. Based on Fig. 6.10, the local peak is followed by a minimum point before increasing again up to channel center. This accumulation of particles in the region close to the wall in wall-bounded flows was already observed in dilute regimes [see 154, 166, 167], although the peak was generally higher. At lower volume fractions, the path of the particles is mainly determined by the fluid. Therefore, a higher portion of particles are shifted from the channel center toward the wall. When increasing the volume fraction, particles penetrate in large-scale vortices and reduce their size and strength. Thus, such vortices have less energy and cannot carry the particles toward the wall as efficiently as before. Additionally, the importance of collisions redistributing the particles throughout the channel increases.

Figure 6.11 illustrates the average y-location of particles (averaged over both sides of the channel in y-direction) for $\phi = 6\%$. Since these particles are neutrally-buoyant, they tend to distribute symmetrically around channel center. Computing the average y-position of all particles over the total computational time, the obtained value is almost at channel center ($\overline{y_p}/H = 0.991$).

Figure 6.12 compares the mean streamwise velocity of particles and fluid. It is observed that the particles have a noticeably higher velocity than the fluid close to the wall. This phenomenon was also reported in experimental studies of Kiger and Pan [168] for the dilute regime. Near the channel center, fluid and particle have similar velocities. There is a small region between

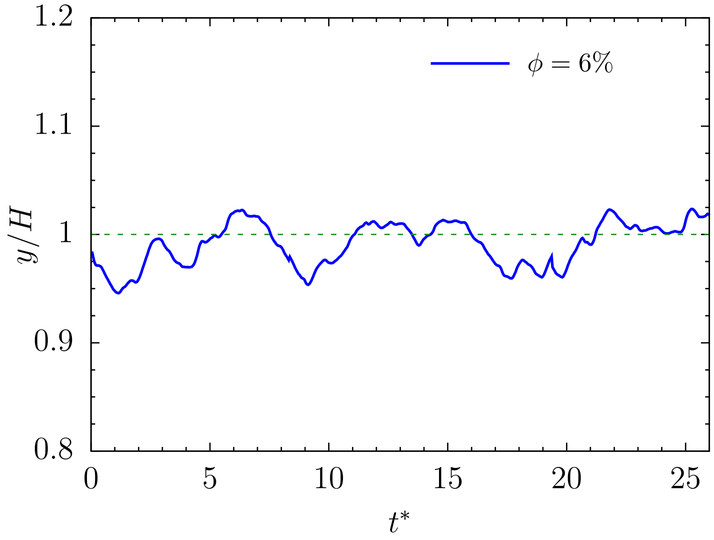

Figure 6.11: Average y-location of all particles during the simulation of a turbulent particle-laden flow with $a/H = 0.1$, $\rho_r = 1.0$

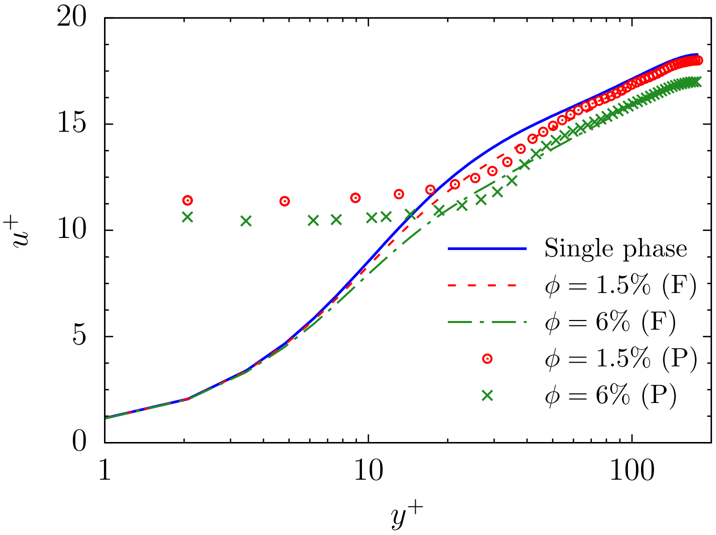

Figure 6.12: Mean velocity of particles (P) and of fluid (F) against distance from the wall for different particle concentration ($a/H = 0.1$, $\rho_r = 1.0$)

these two zones, again around $y^+ \approx 30$, where fluid velocity is slightly higher than particle velocity; local particle accumulation coincides with a particle velocity lower than that of the flow. The rms of particle and fluid velocity fluctuations for $\phi = 6\%$ is depicted in Fig. 6.13. Particle velocity fluctuations are in general much smaller than those found in the fluid. This is probably due to the lower tendency of the particles for motion, preventing fast changes in velocity. Exceptions are only observed very close to the wall.

Figure 6.14 shows an arbitrary snapshot with the distribution of all particles together with the streamwise velocity. Since these particles are neutrally-buoyant, particle distributions in the lower and upper half of the channel are similar.

Figure 6.15 depicts the side view of the iso-surfaces of the second invariant of the velocity

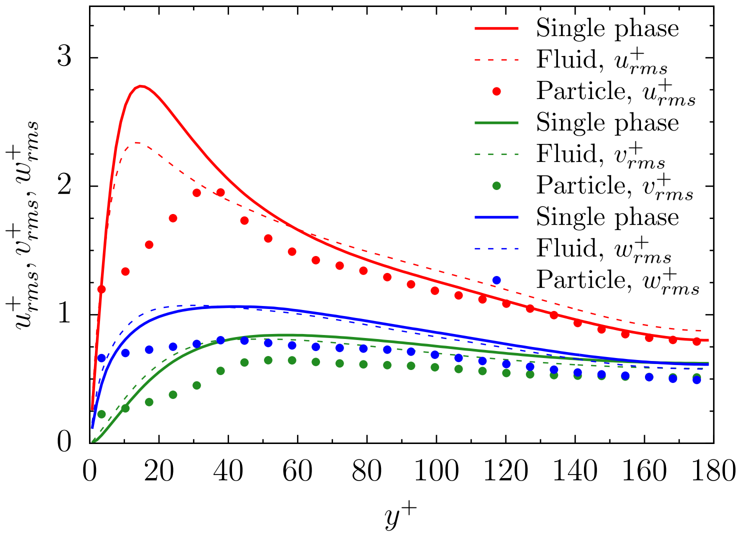

Figure 6.13: RMS of particles and of fluid velocity fluctuations against distance from the wall ($a/H = 0.1$, $\rho_r = 1.0$, $\phi = 6\%$)

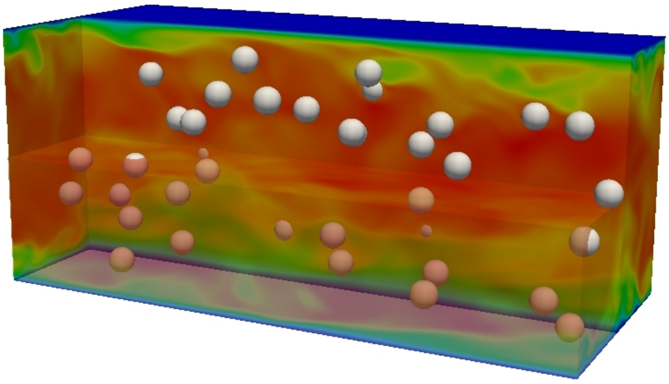

Figure 6.14: Instantaneous snapshot of particle distribution and turbulent flow structure, colored by streamwise velocity ($a/H = 0.1$, $\rho_r = 1.0$, $\phi = 1.5\%$)

gradient tensor, Q, which is classically used to visualize the vortices in the flow field [169]. The Q-criterion is defined using Einstein summation convention as

$$Q = \frac{1}{4}\left(\omega_i \omega_i - 2 s_{ij} s_{ji}\right), \tag{6.5}$$

where $\omega_i = \varepsilon_{ijk} \partial_j u_k$ is the vorticity field, s_{ij} is the strain rate of the velocity fluctuations and ε_{ijk} is the Levi-Civita symbol. Figure 6.16 shows the instantaneous snapshots of Q iso-surfaces on the lower-half of the channel, when removing the particles for an easier visualization. A visual analysis of both figures reveals that the presence of particles reduces the occurrence of large streamwise vortices, increasingly so at higher particle concentration. For all conditions, coherent flow structures and hairpin vortices can still be detected in the figures, though smaller-scale, nearly isotropic structures appear to play an increasing role at higher particle loading (see Fig. 6.16c).

It is interesting to examine the effect of particles based on particle Stokes number and volume

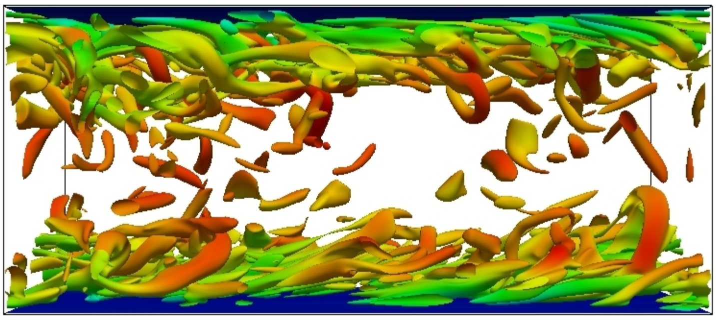

(a)

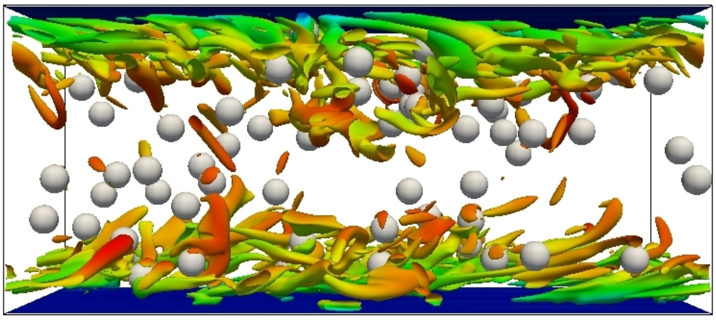

(b)

Figure 6.15: Iso-surface of $Q/\left(u_\tau^4/\nu^2\right) = 0.006$ colored by streamwise velocity; (a) without particles; (b) particle-laden flow ($a/H = 0.1$, $\rho_r = 1.0$, $\phi = 1.5\%$)

fraction. Particle Stokes number is defined as the particle response time to the fluid characteristic time scale. A particle with low Stokes number responds quickly to the flow. Characteristic time scale of the flow can be either the Kolmogorov ($\tau_K = \sqrt{\nu/\epsilon}$) or the near-wall scale ($\tau_\nu = \nu/u_\tau^2$). In this study, the latter approach is employed, considering the local accumulation of particles in the near-wall region around $y^+ \approx 30$.

Neutrally buoyant particles of density $\rho_r = 1.0$ and radius $a/H = 0.1$ have Stokes number larger than 10. Elghobashi [170, 171] presented a classification map of dilute particle-laden flows based on the particle volume fraction and Stokes number. This map shows whether the turbulent kinetic energy will increase or decrease. For dilute suspension of rigid particles ($10^{-6} < \phi < 10^{-3}$) he recognized two main zones based on the Kolmogorov Stokes number ($\mathrm{St}_K = \tau_p/\tau_K$). Normally, for very low Stokes numbers (i.e., microparticles) TKE increases. For $\mathrm{St}_K \gtrsim 1$ particles do not respond immediately to velocity fluctuations of the surrounding fluid. Thus, reduction of both TKE and dissipation relative to the single-phase flow is reported. For $\mathrm{St}_K \gtrsim 10$, due to vortex shedding behind the particle, TKE increases. The latter effect was confirmed in the simulations of Uhlmann [154]. However, it is helpful to discuss the dense regime as well, such as found in the test cases of the current study. In dense regime with particles of large Stokes number, the present results show that, in contrast to the observations of the dilute regime, TKE is reduced (see again Fig. 6.8). This is due to the strong impact of the particles on turbulent vortices, altering their structure and leading to increased dissipation.

In contrast to TKE, whose changes can be directly predicted based on the solid phase volume

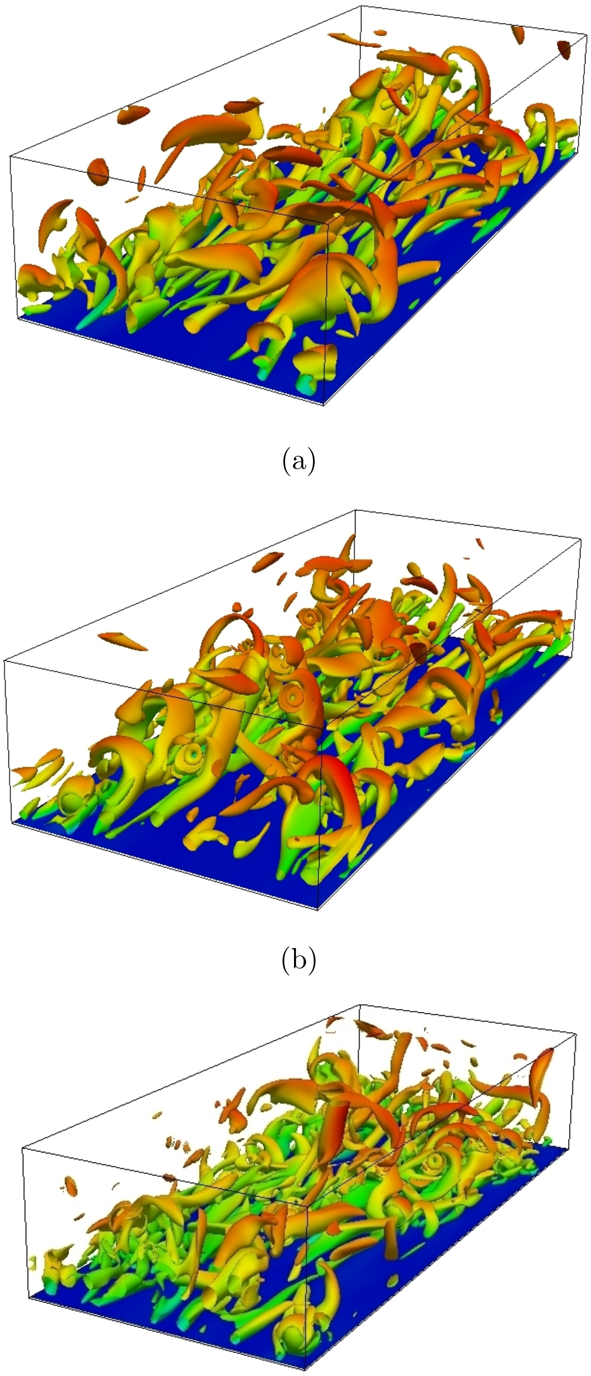

(a)

(b)

(c)

Figure 6.16: Iso-surface of $Q/\left(u_\tau^4/\nu^2\right) = 0.006$ on the lower-half of the channel colored by streamwise velocity; (a) Single-phase; (b) $a/H = 0.1$, $\rho_r = 1.0$, $\phi = 1.5\%$; (c) $a/H = 0.1$, $\rho_r = 1.0$, $\phi = 3\%$. For a better visualization, the particles are not shown.

fraction and Stokes number, the observed changes in pressure drop show strong dependency on particle shape and Reynolds number. Hence, a reduction of turbulence intensity does not necessarily lead to drag reduction; other parameters must be considered due to particle-induced stresses in the flow. In the present study, although TKE and Reynolds stress show a reduction when adding particles, a lower streamwise velocity is observed. Furthermore, it is possible that

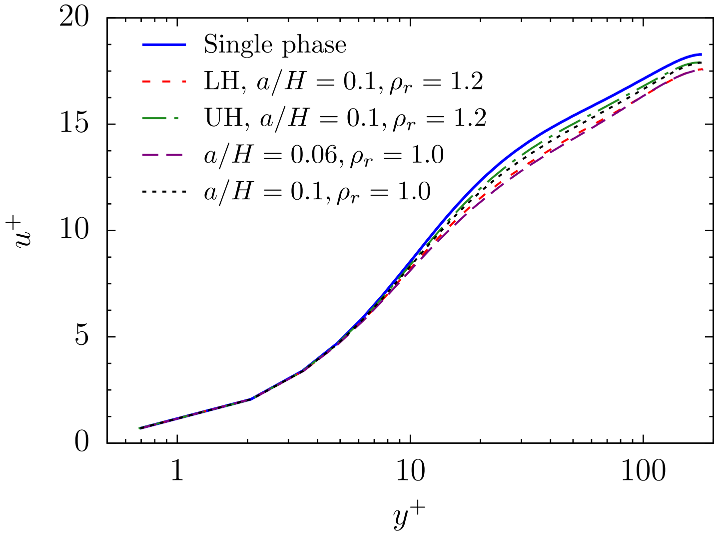

Figure 6.17: Effect of particle size and density on mean fluid velocity ($\phi = 1.5\%$) (LH: Lower-half, UH: Upper-half)

two particles of the same Stokes number and at the same volume fraction have different effects on the mean flow velocity due to different shapes, as will be discussed in the next chapter.

Effect of particle density and size

Now, the impact of using small or heavy particles at $\phi = 1.5\%$ is presented. The two effects are investigated separately. Small particles have a radius $a/H = 0.06$. Heavy particle density is set to $\rho_p/\rho_f = 1.2$; in that case, particle settling will occur, competing with particle redistribution by turbulence and collisions. The Galileo number quantifies the importance of gravity, as defined by

$$\mathrm{Ga} = \sqrt{\frac{\Delta\rho}{\rho_f}\frac{g d_p^3}{\nu^2}}. \tag{6.6}$$

where $\Delta\rho = \rho_p - \rho_f$. In this study, Ga = 28 and gravity (g) is acting in $-y$ direction. This Galileo number leads to gravity (g) in the same order of magnitude as applied driving force (G). First, we investigate the effect of particle size and density on mean and rms of velocity profile. The results are shown and compared in Fig. 6.17. It is seen that small particles reduce the mean flow velocity more than larger particles (by 5.0% compared to 3.0%, respectively), at the same overall volume fraction. Thus, small particles ($\mathrm{St}^+ = 26$) have a higher drag enhancement effect. The higher velocity reduction effect can be attributed to the larger total projected area of the smaller particles at the same volume fraction; the number of small particles in the domain at $\phi = 1.5\%$ is 305, which is considerably more than the 66 larger particles. The drag force on the particle is directly related to its projected area. Hence, smaller particles should have in general a stronger effect on vortices when keeping the volume fraction constant.

For the case of heavy particles, the velocity distribution on upper and lower half of the

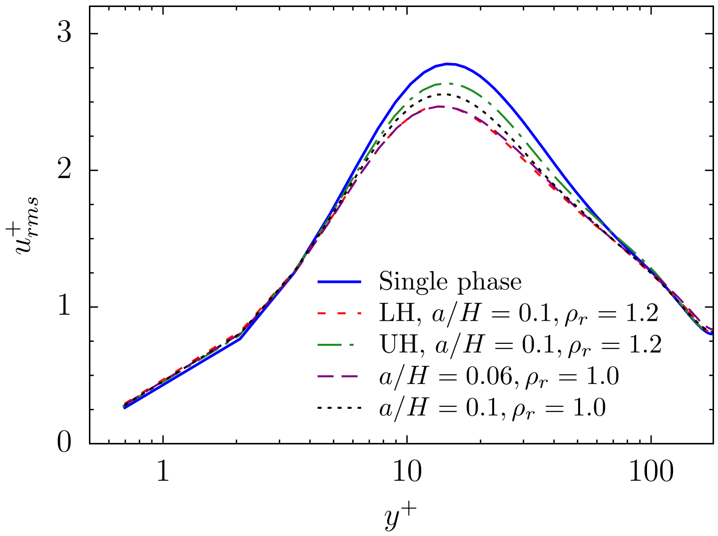

Figure 6.18: Effect of particle size and density on streamwise velocity fluctuations u^+_{rms} ($\phi = 1.5\%$) (LH: Lower-half, UH: Upper-half)

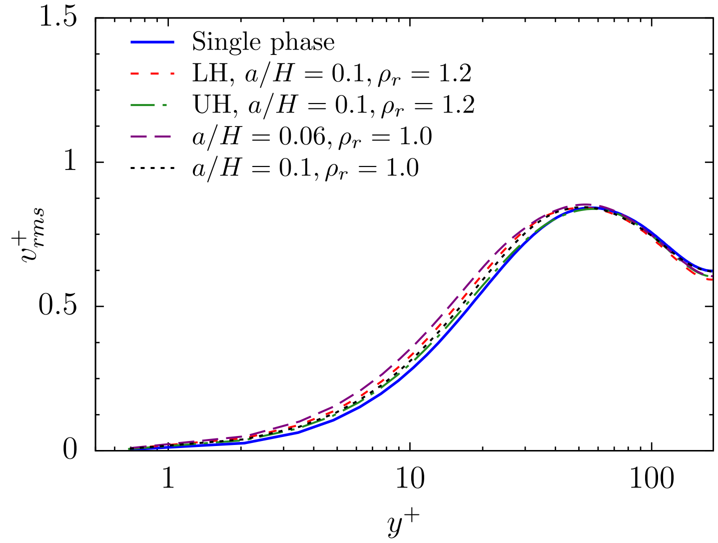

Figure 6.19: Effect of particle size and density on wall-normal velocity fluctuations v^+_{rms} ($\phi = 1.5\%$) (LH: Lower-half, UH: Upper-half)

channel are different. For representation, each one has been normalized by its relevant friction velocity. The mean streamwise velocity in the lower part of the channel is lower than for the upper part. An average velocity reduction of 4.8 and 2.3% is found for lower and upper parts, respectively, compared to the single-phase flow. In the upper part, far less particles are present and this brings all curves closer to their single-phase counterparts, while the high concentration of particles in the lower-half (due to settling) reduces mean velocity to a lower value.

Figures 6.18-6.20 depict the rms of fluid velocity fluctuations. Again, for heavy particles, the lower-half data show noticeably larger difference compared to single-phase data. Concerning the upper half, it is interesting to notice that w^+_{rms} becomes even slightly lower than the clear channel far away from the wall.

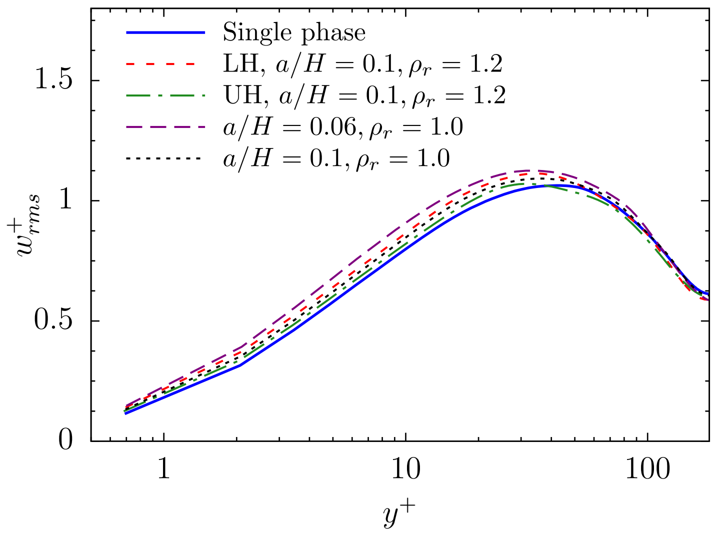

Figure 6.20: Effect of particle size and density on spanwise velocity fluctuations w^+_{rms} ($\phi = 1.5\%$) (LH: Lower-half, UH: Upper-half)

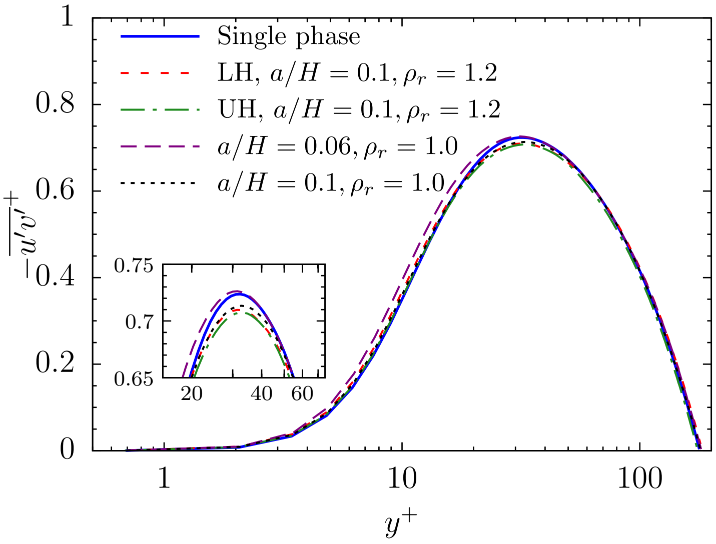

Figure 6.21: Effect of particle size and density on Reynolds shear stress ($\phi = 1.5\%$) (LH: Lower-half, UH: Upper-half)

When comparing now the results of two different particles sizes, the maximum streamwise velocity fluctuations of small particles is lower. For spanwise and normal directions, the curves for small particles locate above those of the larger particles close to the wall, i.e. $y^+ \lesssim 30$. Note, however, that the differences become less noticeable in the channel center region. Particle size effect on Reynolds shear stress is shown in Fig. 6.21. Looking closely around the peak region, it is seen that the small-particles profile has a slightly higher maximum value than the large-particles curve, showing that smaller particles enhance production of turbulent fluctuations compared to larger ones. It is expected that, choosing even smaller particles (still in the range of finite-size particles) would further increase the Reynolds shear stress. The peak value of Reynolds shear stress for heavy particles is slightly lower than for neutrally-buoyant particles,

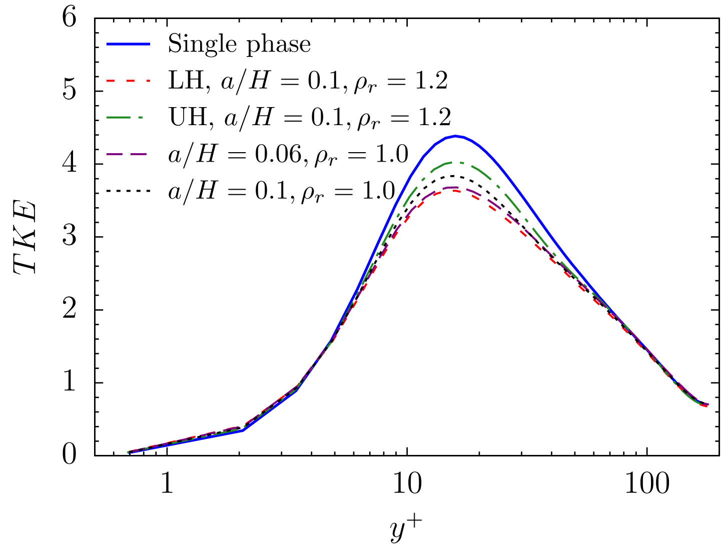

Figure 6.22: Effect of particle size and density on TKE in a turbulent channel flow ($\phi = 1.5\%$) (LH: Lower-half, UH: Upper-half)

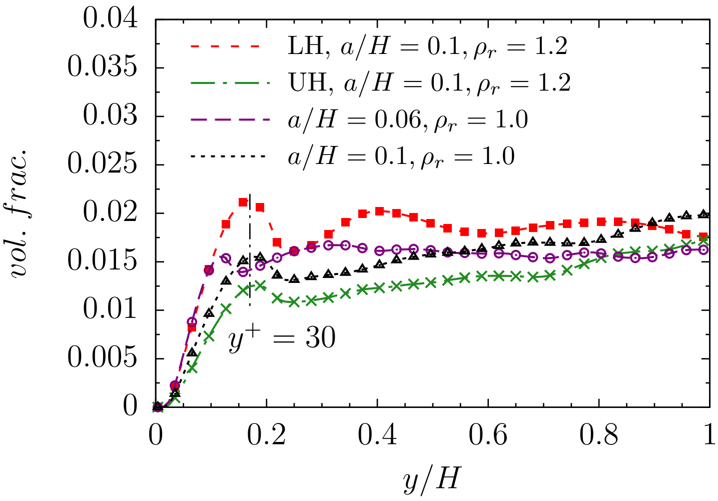

Figure 6.23: Local distribution of spherical particles along the channel height in a turbulent channel flow ($\phi = 1.5\%$) (LH: Lower-half, UH: Upper-half)

due to their higher Stokes number. Turbulent kinetic energy of small particles is again lower (Fig. 6.22). Moreover, heavy particles show as expected different curves on the lower and upper parts of the channel . For all cases, turbulent kinetic energy is reduced in the two-phase flow.

The distribution of particles is depicted in Fig. 6.23. When particle density is higher than fluid density, particle settlement leads to a very uneven distribution of particles in the lower and upper sections of the channel. Far more particles are present in the lower part; still, a peak in local particle concentration around $y^+ \approx 30$ is observed for both sections.

In the case of smaller, neutrally-buoyant particles, the local peak of particles distribution moves closer to the wall, at $y^+ \approx 22$. The maximum particle volume fraction occurs at $y \approx d_p$ for small particles and $y \approx 0.8d_p$ for larger ones. This is partly due to the weaker effect of particle-wall collisions due to the lower weight of small particles. Furthermore, it is observed that the volume fraction of smaller particles is more homogeneous. Small particles have less inertia to escape from the near-wall, low-velocity region. In contrary, larger particles lead to a steady increase of volume fraction beyond $y/H = 0.25$.

6.4 Summary

A systematic study of turbulent particulate flows has been performed using Immersed boundary-lattice Boltzmann Direct Numerical Simulation. The configuration is a straight channel at frictional Reynolds number of $\mathrm{Re}_\tau = 180$. After investigating the single-phase case, the resulting flow has been seeded with fully-resolved particles. Effect of particle concentration, size and density has been investigated. Based on the results, following conclusions can be drawn:

- IB-LBM is a robust method for the simulation of turbulent particulate flows in the dense regime. The combination of IBM and LBM captures the main characteristics of particle-laden flows.
- Addition of fully-resolved particles decreased mean velocity and consequently flow rate compared to the single-phase flow. Mean streamwise velocity is reduced by 3.0 and 7.9% for solid-phase volume fractions of $\phi = 1.5$ and 6%, respectively, when particle radius is set to $a/H = 0.1$.
- Maximum root mean square of streamwise velocity fluctuations is attenuated by addition of particles of $a/H = 0.1$. The peak is also slightly shifted toward the channel wall. On the other side, streamwise velocity fluctuations are increased in the region close to the wall and in the core zone. Enhancement of near-wall rms fluctuations is observed for normal and spanwise directions. Maximum Reynolds shear stress and turbulent kinetic energy are reduced.
- It was also observed that there is an equilibrium position close to the wall ($y^+ \approx 22 - 30$ depending on particle size) where local particle concentration shows a peak before experiencing some reduction and increasing again up to channel center. If the local peak value is normalized by particle volume fraction, lower mean volume fraction profile has a higher peak in comparison with higher volume fractions.
- By comparison of mean velocity of particles and fluid, a large lag of particle velocity close to the wall is observed. In the channel center, particle and fluid have approximately the same velocity. In the intermediate region, flow velocity is slightly higher than particles' velocity.
- Effect of particle density was investigated as well. Heavy particles ($\rho_r = 1.2$) show noticeably different velocity profiles in the upper and lower parts of the channel, breaking

the symmetry. Increase in particle density leads to sedimentation of many particles in the lower region.

- Smaller neutrally-buoyant particles ($a/H = 0.06$) reduced the mean velocity more than larger ones at the same concentration. It is thus expected that, further decreasing of particle size (but still in the scope of finite-size particles) would lead to more velocity reduction.
- It should be finally pointed out that, effect of fully-resolved particles on flow characteristics can be noticeably influenced by many parameters. Particle concentration and Stokes number play the main role in this regard. Based on the present simulations in the dense regimes, when particle Stokes number is large Reynolds shear stress is reduced; maximum streamwise velocity fluctuations and TKE reduce as well. By decreasing the Stokes number, Reynolds stress starts increasing and a stronger velocity reduction is observed. With respect to mean velocity variations, it would be advantageous to study now the effect of particle shape. In the dilute regimes, it is known that particles of the same Stokes number can have different effects on mean velocity [172]. Checking the impact of particle shape in the dense regime will be the topic of next chapter.

Chapter 7

Two-Phase Flows with Prolate Spheroidal Particles

7.1 Introduction

Although numerical simulations of particle-laden flows mainly consider spherical particles (because of easier treatment of particle motion), most particles have a non-spherical shape in practical cases. In this chapter, we study the effect of prolate spheroids on laminar and turbulent flow fields. A spheroid is an ellipsoid with two diameters being equal; and a prolate spheroid is obtained by rotating an ellipse about its major axis. With respect to non-spherical particles, most publications deal with laminar flows and a single suspended particle [173–176].

Jeffery [177] first derived an analytical solution for the rotation of an ellipsoid in simple shear flow at zero Reynolds number. Ding and Aidun [173] used lattice Boltzmann method (LBM) to investigate the effect of fluid inertia on the behavior of a single suspended ellipsoid in planar Couette flow with $\mathrm{Re} \leq 90$. Qi and Luo [174] modeled the rotation of a neutrally-buoyant spheroidal particle at moderate Reynolds numbers ($\mathrm{Re} < 467$). They identified different modes of particle rotation depending on the Reynolds number. Yu *et al.* [175] used the distributed Lagrangian multiplier based fictitious domain (DLM/FD) to test the rotation of oblate and prolate spheroids. They reported various rotation modes including Jeffery orbit, tumbling, quasi-Jeffery orbit, log rolling, and inclined rolling for a prolate spheroid by increasing particle Reynolds number. Huang *et al.* [176] extended the Reynolds number limit to 700. The effect of particle Reynolds number and its initial orientation on final mode of rotation was discussed. The simulations were based on a momentum exchange LBM. For a prolate spheroid, a motionless mode at $\mathrm{Re} > 445$ was reported. They later simulated sedimentation of an ellipsoid in narrow and infinitely long tubes [178].

The effect of finite-size particles on turbulence has been the subject of many studies [2, 155, 179, 180]. However, these studies are mostly concerned with spherical particles (see Chapter 6). The motion of non-spherical particles is inherently complex even in laminar flows. In turbulent regimes, the problem will be even more intriguing. During the last years, some researchers have modeled turbulent flows with non-spherical particles [181–183]. However, in most of these studies, particle size is smaller than the Kolmogorov length scale (the so-called *point particles*). Moreover, only one-way or two-way coupled simulations were performed, which only hold for low volume fractions of the solid phase. Thus, particle-particle interactions are mainly ignored. Zhang *et al.* [184] used DNS to compute the transport and deposition of ellipsoidal particles in dilute turbulent channel flows. The simulation was carried out by one-way coupling assumption. The accumulation of particles in the viscous sublayer and their alignment with the flow direction was reported in this work. Mortensen *et al.* [185] studied the distribution and orientation of small spheroids by means of DNS. The simulation was performed in an Eulerian-Lagrangian framework. Forces and torques were computed under creeping flow condition (Stokes flow) which is valid for low particle Reynolds number. A preferential orientation of elongated particles in the streamwise direction was reported. Later, Marchioli *et al.* [186] studied a turbulent channel flow with long particles and concluded that the aspect ratio has a minor effect on clustering, preferential distribution, and segregation of particles. Andersson *et al.* [187] showed drag reduction effect of point particles with an aspect ratio of 5. Zhao and van Wachem [188] investigated the behavior of elongated particles in a turbulent channel with frictional Reynolds number of $\mathrm{Re}_\tau = 150$. Particle-particle and particle-wall collisions were modeled in this work. However, the flow was in dilute regime and the particles were smaller than the Kolmogorov length scale. Drag enhancement by particles was reported. They later showed that, in dilute regimes, point particles of high aspect ratio and moderate Stokes number have minor drag reduction effect [172]. The only work that addresses the effect of finite-size non-spherical particles (cylindrical fibers) on turbulent flow was performed by Quang *et al.* [189]. They employed external boundary force method implemented by the lattice Boltzmann method to model the effect of rigid rods with a cylindrical shape for volume fractions up to 0.004.

DNS of fully-resolved spheroids in turbulent wall-bounded dense flows using LBM has not been performed yet to our knowledge. This issue is the purpose of this chapter. Modeled particles are larger than the Kolmogorov scale and their volume fraction corresponds to the dense regime. Moreover, particle-particle and particle-fluid interactions are taken into account (four-way coupled). The outline of this chapter is as follows: Sec. 7.2 describes particle dynamics. The validation is presented in Sec. 7.3. Section 7.4 presents laminar sedimentation of a spheroid in a long square tube, before considering a turbulent channel flow seeded with prolate spheroids. Finally, conclusions are driven in Sec. 7.5. Results of this chapter are partly published in [190].

7.2 Particle dynamics

A spheroid surface (Fig. 7.1) is described by the following equation

$$\frac{x'^2}{a^2} + \frac{y'^2}{b^2} + \frac{z'^2}{b^2} = 1, \tag{7.1}$$

where $(x',\ y',\ z')$ denotes a body-fixed coordinate system and a and b are the radii of the particle. In this study, a prolate spheroid is considered, i.e., $a > b$, with particle aspect ratio

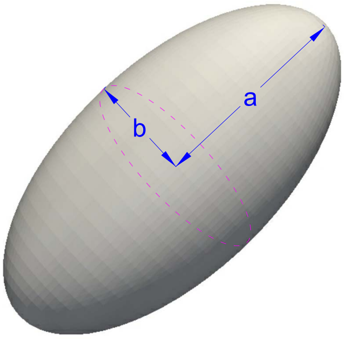

Figure 7.1: Spheroid geometry with semi major-axis a and semi minor-axes b

of $\lambda = a/b$. In order to use IBM, we need Lagrangian points that are distributed over particle surface. To distribute the points on the spheroid, a new procedure was implemented. The developed approach enables the exact surface of the ellipsoid to be retrieved; this avoids errors associated with methods that try to enforce a uniform distribution of points over the surface. For this purpose, the spheroid surface is first divided into a user-defined number of strips. These strips are placed along the particle major axis, such that their cross-section is always of circular shape. Using this property, it is possible to arrange a uniform distribution of points over each strip. Finally, assuming for instance that the particle major axis is initially parallel with the x–direction (the particle orientation can be changed through rotation after distributing the points), the location of each Lagrangian point is specified using procedure

```
$for\ i = 1 : ns$
  $\theta = i \times \pi / ns;$
  $nps\,[i] = [cir\_factor \times ns \times sin\theta];$
  $\alpha = 0;$
  $for\ j = 1 : nps\,[i]$
    $\alpha = \alpha + 2 \times \pi \,/\, nps\,[i]\,;$
    $Node\_y = y_c + b \times cos\alpha \times sin\theta;$
    $Node\_z = z_c + b \times sin\alpha \times sin\theta;$
    $Node\_x = x_c + a \times cos\theta;$
  $end;$
$end;$
```

where ns is the total number of strips, nps the number of points per each strip, and cir_factor is a parameter used to adjust the number of points on each strip and in practice is larger than 0.5. $Node\_x$, $Node\_y$, $Node\_z$ are the final coordinates of each Lagrangian point, and x_c, y_c, and z_c denote the location of particle center in inertial coordinate. The parameter θ is used to adjust each strip location and α to adjust each point location on the strip. In the above procedure, two parameters (cir_factor and ns) must be specified by the user, and nps is deduced from cir_factor. By fixing cir_factor, the number of points over all strips (nps) is automatically obtained. Higher cir_factor values result in a higher number of points on each strip.

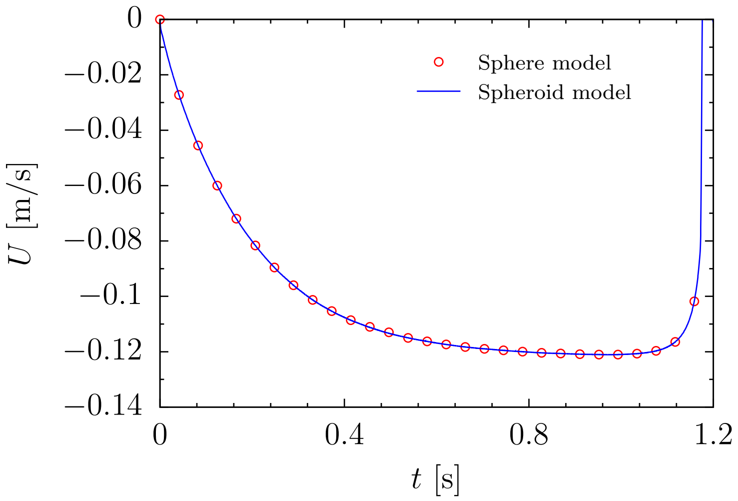

Figure 7.2: Settling velocity of a spherical particle at Re = 32.2 computed by two methods of points distribution on the surface

In order to calculate the surface area associated to each surface node, Eq. (7.2) is first used to obtain the surface area of the strip that lies between x_1 and x_2:

$$S = 2\pi b \int_{x_1}^{x_2} \sqrt{1 - \frac{(a-b)(a+b)\,x^2}{a^4}}dx = \frac{2\pi b}{s}\left[\frac{\arcsin(sx)}{2} + \frac{sx\sqrt{1-(sx)^2}}{2}\right]_{x_1}^{x_2}, \tag{7.2}$$

$$s = \sqrt{\frac{(a-b)(a+b)}{a^4}}. \tag{7.3}$$

If $x_1 = -a$ and $x_2 = a$ then S is the total surface area of the prolate spheroid. Finally, dividing S by the number of points on the corresponding strip, the area associated with each surface node of the prolate spheroid is obtained. Nevertheless, a and b cannot be the same and must be slightly different to prevent the integration from yielding a non-real result. For an initial check of this procedure, we employed it to recompute the results for the case of single sphere sedimentation. Using a relative difference of 0.001% between a and b, the new procedure gives a negligible difference with the results already discussed for sphere model, as can be seen from Fig. 7.2 for the test case of Sec. 3.3.4.

Let us now consider the general equations of motion of particles:

$$M_p\frac{d\boldsymbol{U}_p}{dt} = -\rho_p\sum_{l=1}^{N_l}\boldsymbol{f}_l\Delta V_l + M_f\frac{d\boldsymbol{U}_p}{dt} + (\rho_p-\rho_f)V_p\boldsymbol{g} + \boldsymbol{F}^c, \tag{7.4}$$

$$\boldsymbol{T} = I_p\frac{d\boldsymbol{\Omega}_p}{dt} + \boldsymbol{\Omega}_p \times (I_p\boldsymbol{\Omega}_p). \tag{7.5}$$

Equations (7.4) and (7.5) demonstrate the translational and rotational motion of the particle, respectively. Translational motion of the particle is updated by using the discretized form of

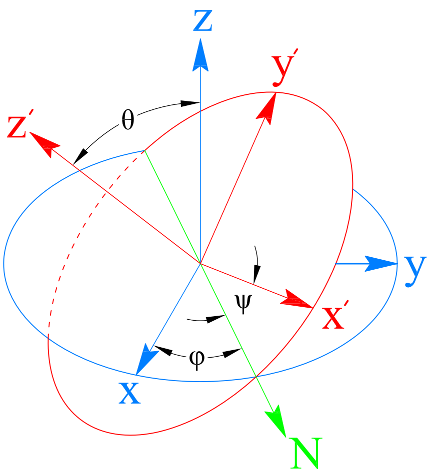

Figure 7.3: Euler angles

Eq. (7.4) (see Eq. (3.12)). To describe now the rotation of a prolate spheroid, two coordinate systems are employed: the inertial frame and the body-fixed frame. The inertial frame, $\boldsymbol{x} = \langle x, y, z \rangle$, is the frame that spans the computational domain (Eulerian framework). The particle frame, $\boldsymbol{x}' = \langle x', y', z' \rangle$, is attached to the particle with its origin at the particle mass center. The x'-axis of this coordinate is aligned with the principal axis of the particle. Equation (7.5) can be written in the body-fixed frame:

$$I'_{xx}\frac{d\Omega'_x}{dt} - \Omega'_y\Omega'_z(I'_{yy} - I'_{zz}) = T'_x, \tag{7.6}$$

$$I'_{yy}\frac{d\Omega'_y}{dt} - \Omega'_z\Omega'_x(I'_{zz} - I'_{xx}) = T'_y, \tag{7.7}$$

$$I'_{zz}\frac{d\Omega'_z}{dt} - \Omega'_x\Omega'_y(I'_{xx} - I'_{yy}) = T'_z. \tag{7.8}$$

In the above and next equations, all variables labeled with a prime are referenced with respect to the body-fixed coordinate. The principal moments of inertia in the body-fixed coordinate are $I'_{xx} = 2M_p b^2/5$, $I'_{yy} = M_p(a^2 + b^2)/5$ and $I'_{zz} = M_p(a^2 + b^2)/5$. To solve Eqs. (7.6)-(7.8), four quaternion variables are introduced:

$$q_0 = \cos(0.5\theta)\cos(0.5(\phi + \psi)), \tag{7.9}$$

$$q_1 = \sin(0.5\theta)\cos(0.5(\phi - \psi)), \tag{7.10}$$

$$q_2 = \sin(0.5\theta)\sin(0.5(\phi - \psi)), \tag{7.11}$$

$$q_3 = \cos(0.5\theta)\sin(0.5(\phi + \psi)), \tag{7.12}$$

where (θ, ϕ, ψ) are the Euler angles (see Fig. 7.3). The transformation from the inertial coordinate to the body-fixed frame is done by: first, a rotation by an angle ϕ about the z-axis; second, a rotation by an angle θ about the new x-axis (shown by N), and third, a rotation by an angle ψ about the z'-axis. The transformation matrix from the inertial to the body-fitted coordinate reads

$$M = \begin{bmatrix} q_0^2+q_1^2-q_2^2-q_3^2 & 2(q_1q_2+q_0q_3) & 2(q_1q_3-q_0q_2) \\ 2(q_1q_2-q_0q_3) & q_0^2-q_1^2+q_2^2-q_3^2 & 2(q_2q_3+q_0q_1) \\ 2(q_1q_3+q_0q_2) & 2(q_2q_3-q_0q_1) & q_0^2-q_1^2-q_2^2+q_3^2 \end{bmatrix}, \tag{7.13}$$

and therefore

$$T' = MT, \tag{7.14}$$

$$\Omega' = M\Omega. \tag{7.15}$$

These two relations are used to map the hydrodynamic moment vectors and the angular velocity vectors between the inertial and rotating (body-fixed) frames. The evolution of the quaternion parameters is governed by

$$\dot{q} = \begin{bmatrix} \dot{q}_0 \\ \dot{q}_1 \\ \dot{q}_2 \\ \dot{q}_3 \end{bmatrix} = \frac{1}{2} \begin{bmatrix} q_0 & -q_1 & -q_2 & -q_3 \\ q_1 & q_0 & -q_3 & q_2 \\ q_2 & q_3 & q_0 & -q_1 \\ q_3 & -q_2 & q_1 & q_0 \end{bmatrix} \begin{bmatrix} 0 \\ \Omega'_x \\ \Omega'_y \\ \Omega'_z \end{bmatrix}. \tag{7.16}$$

In our CFD code, the torques are first transformed from the inertial to the body-fixed coordinate using Eq. (7.14). Then, Eqs. (7.6)–(7.8) together with Eq. (7.16) (7 equations in total) are solved using a 4th-order Runge-Kutta integration algorithm to obtain each quaternion (q) and angular velocity (Ω') in the body-fixed coordinate system. Next, the angular rotation velocity in the inertial coordinate (Ω) is obtained by Eq. (7.15) using the inverse of matrix M. Quaternions are then normalized. Finally, the location of each Lagrangian point can be updated by $X = M^{-1}X'$.

7.3 Validation

In order to validate the correct rotation of a spheroid based on the equations presented in Sec. 7.2, comparison with analytical data for a single spheroid in Couette flow at small Reynolds numbers is provided (see Fig. 7.4). Then, higher Reynolds numbers will be tested as well. Both test cases concern a neutrally-buoyant spheroid suspended between two parallel plates. The spheroid particle is placed between these two parallel plates that are located at $y = 0$ and $y = N_y$, and move in opposite directions with velocities U and $-U$ along the x–direction. The resulting non-dimensional shear rate is $G = 2U/N_y$. Periodic boundary conditions are applied in the x– and z–directions. For the pure rotation of the particle around the z-axis, the Reynolds number is defined as:

$$\mathrm{Re}_p = \frac{4Ga^2}{\nu}. \tag{7.17}$$

Jeffery [177] showed that, the rotation angle, φ, and the angular rate of rotation, $\dot{\varphi}$, when one of the principal axes of the ellipsoid is kept parallel to the vorticity vector in a shear flow without

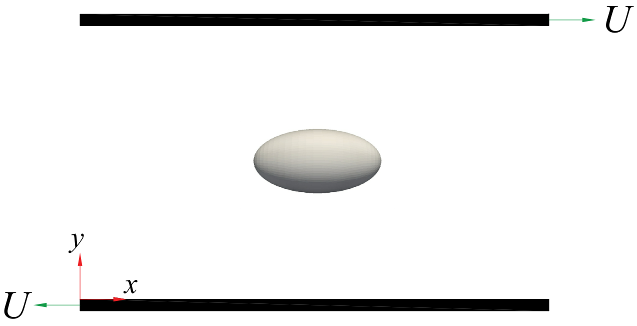

Figure 7.4: Schematic of a spheroid in Couette flow with moving walls (Sec. 7.3)

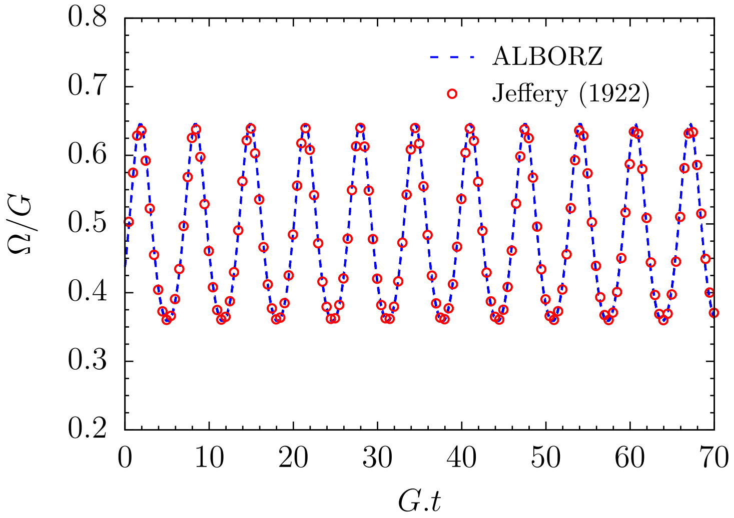

Figure 7.5: Rotational speed Ω/G vs. time for a single spheroid in a 3D Couette flow with small Reynolds number (Sec. 7.3)

inertia ($\mathrm{Re}_p = 0$) read

$$\cot\varphi = -\lambda\cot\left(\frac{\lambda\, G\, t}{\lambda^2+1}\right), \tag{7.18}$$

$$\dot{\varphi} = -\frac{G}{\lambda^2+1}\left(\lambda^2\sin^2\varphi + \cos^2\varphi\right). \tag{7.19}$$

For the first simulation set-up, the computational domain is discretized by 120 × 120 × 60 lattice nodes. The Reynolds number is $\mathrm{Re}_p = 0.5$ and the particle radii are $a = 6$ and $b = 4.5$, and the relaxation parameter is set to $\tau = 0.6$. The particle is located at the domain center. There is no constraint on particle translation and rotation but the simulation proved that the particle only rotates around z-axis without any translational motion. Results of the rotational speed of the particle are shown in Fig. 7.5. Our simulation results agree very closely with the analytical solution.

Now the accuracy of the results for higher Reynolds numbers is examined. Two domain resolutions are used: $(N_x, N_y, N_z)=(40, 40, 40)$ and $(80, 80, 80)$. Particle semi-major and semi-minor length are 12 and 3, respectively. The Reynolds number varies between 30 and 100

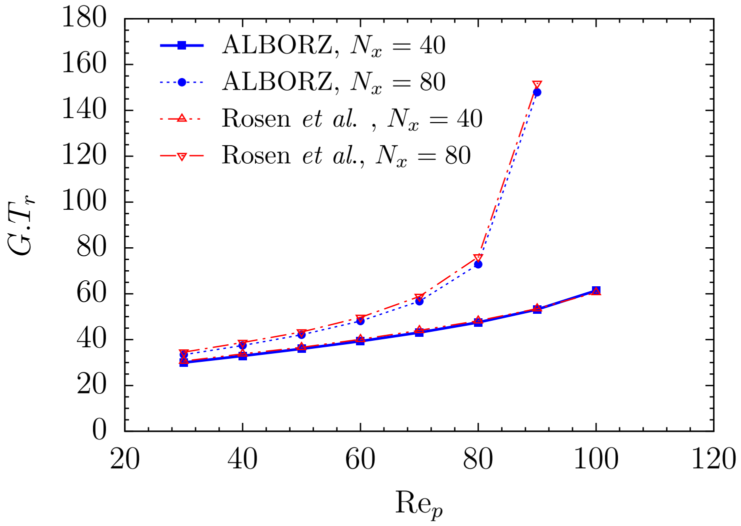

Figure 7.6: Comparison of rotation periods of a spheroid for different particle Reynolds numbers in two domain sizes ($N_x = 40$, 80) compared to the data of Rosén et *al.* (2014) (Sec. 7.3)

and the shear rate is $G = 1/600$. Figure 7.6 illustrates $G \cdot T_r$ values (T_r: period of a complete tumbling motion of the particle) versus Reynolds number. For both domain resolutions, our results are compared with the data of Rosén *et al.* [191]. The results are quite close and minor differences can be attributed to different numerical approaches since there is no golden truth in this case. Therefore, the developed direct forcing IB-LBM approach together with the technique implemented to distribute the Lagrangian points and calculate the surface area can be applied to spheroidal particles in next simulations.

7.4 Results

It this part the simulation results for both laminar and turbulent flows are presented.

7.4.1 Spheroid sedimentation in long narrow channels

Different sedimentation modes of a spheroid in a square tube are studied here. The geometry is shown in Fig. 7.7. A spheroid with particle radii of $a = 15$ and $b = 7.5$ is located in a long narrow square tube. Particle starts its motion with zero velocity and settles down under gravity. Galileo number is defined as

$$\mathrm{Ga} = \sqrt{\frac{\Delta\rho}{\rho_f}\frac{gD_{eq}^3}{\nu^2}}, \tag{7.20}$$

where D_{eq} is the equivalent diameter of a sphere of the same volume. The domain is assumed to be very long with stationary wall on top and zero gradient boundary condition at the bottom. All other sides are stationary walls. To prevent using a very long channel in numerical simulations, increasing the computational cost, we always keep the particle with a certain distance from upper and lower boundaries. During the simulations, when the particle moves one lattice downward,

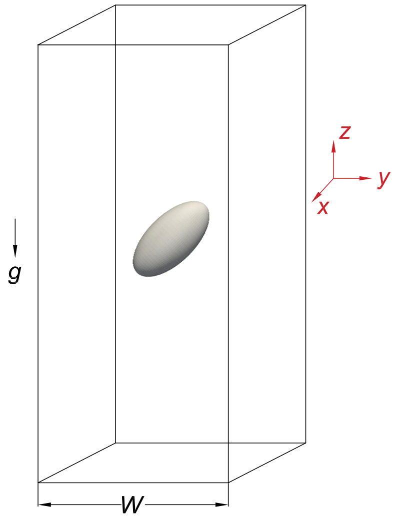

Figure 7.7: Single spheroid in a long tube settling under gravity g (Sec. 7.4.1)

Table 7.1: Sedimentation modes of spheroid

ρ_r	Ga	$B = 0.9$	1.16	1.33	1.5	1.67	2
1.16	6.9	OM	OM	IOO	IO	IO	HC
1.5	11.9	OM	IOO	IO	HC	HC	HC
3	23.8	OM	HC	HC	HC	HC	HC
4	29.1	OM	HCO	HC	HC	HC	HC

Table 7.2: Description of sedimentation modes

Type	Description
OM	Oscillatory Motion (beside the wall)
IOO	Inclined Off-center with Oscillations
HC	Horizontal at Center without oscillation
HCO	Horizontal at Center with Oscillation
IO	Inclined Off-Center without oscillation

one row is eliminated from the top and one row is added to the bottom of the domain. In all tests, the velocity field is initialized as zero in the whole domain.

Different sedimentation modes of the particle for different blockage ratios $B = \frac{W}{2a}$ are investigated. Density ratio changes between 1.16 to 4 and blockage ratio from 0.9 to 2. This leads to Galileo numbers of 6.9 to 29.1. Different sedimentation modes of the particle are reported in Table 7.1 with the definition of each term given in Table 7.2. It is interesting to note that, the particle gradually moves to the diagonal plane and all sedimentation modes are occurring there. Graphical representation of each mode is exemplified in Fig. 7.8.

At the lowest examined blockage ratio ($B = 0.9$), the particle shows an oscillatory motion around the centerline for all density ratios. For $B = 1.16$, four different regimes are observed. The particle has an OM at $\text{Ga} = 6.9$. By increasing density ratio, sedimentation regime varies from IOO at $\text{Ga} = 11.9$ to HC at $\text{Ga} = 23.8$ and finally to HCO at $\text{Ga} = 29.1$. When blockage ratio is increased to $B = 1.33$, the OM does not take place at all. HCO motion also disappears.

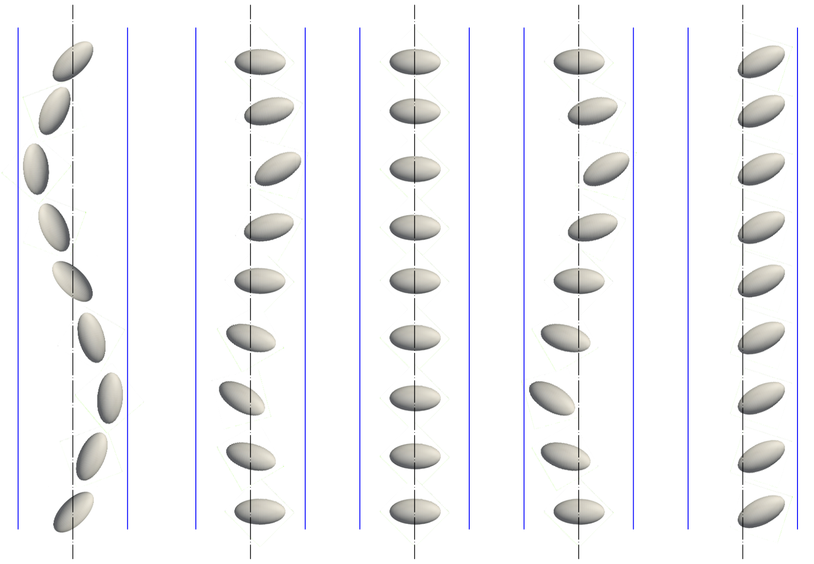

Figure 7.8: Different sedimentation modes of a single prolate spheroid in a long tube. From left to right: OM, IOO, HC, HCO, IO (dimensions not to scale) (Sec. 7.4.1)

Table 7.3: Characteristics of particles

Particle	Shape	$a/\Delta x$	$b/\Delta x$	$D_{eq}/\Delta x$	λ	ρ_p/ρ_f
P1	Spheroid	15.8	7.9	20.0	2.0	1.0
P2	Sphere	10.0	10.0	20.0	1.0	1.0

However, a new mode of sedimentation is introduced, IO; at $B = 1.33$ and $\mathrm{Ga} = 11.9$ particle settles down inclined at an off-center position without exhibiting any oscillation. By further enhancement of blockage ratio to $B = 1.5$, only two modes are observed. One is IO motion at $\mathrm{Ga} = 6.9$ and HC for all higher density ratios. For relatively wide channels ($B = 2$), the particle settles horizontally at center for all density ratios.

7.4.2 Turbulent channel flow with fully-resolved spheroids

In this part, the effect of fully-resolved spheroids on turbulent flow properties in a straight channel will be investigated, and comparison with spherical particles will be provided.

Simulation set-up

We use exactly the same configuration as in Sec. 6.2. In both particle-laden and particle-free cases, the data are collected when the turbulent flow is fully developed and statistically reaches steady-state. The results will be presented in wall (inner) units, unless otherwise stated, and the velocity values are all scaled by u_τ. All fluid statistics are computed excluding the Eulerian nodes that are located inside the particles.

In the case of particle-laden flow, particles are rigid. Two particle types are tested: one spheroidal (P1) and one spherical (P2). Particles size, aspect ratio are listed in Table 7.3.

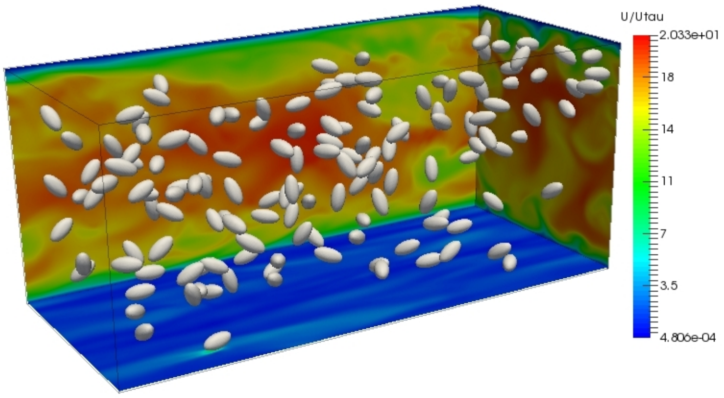

Figure 7.9: Snapshot of spheroidal particles in a turbulent channel at $\phi = 1.5\%$, colored by streamwise velocity (Sec. 7.4.2)

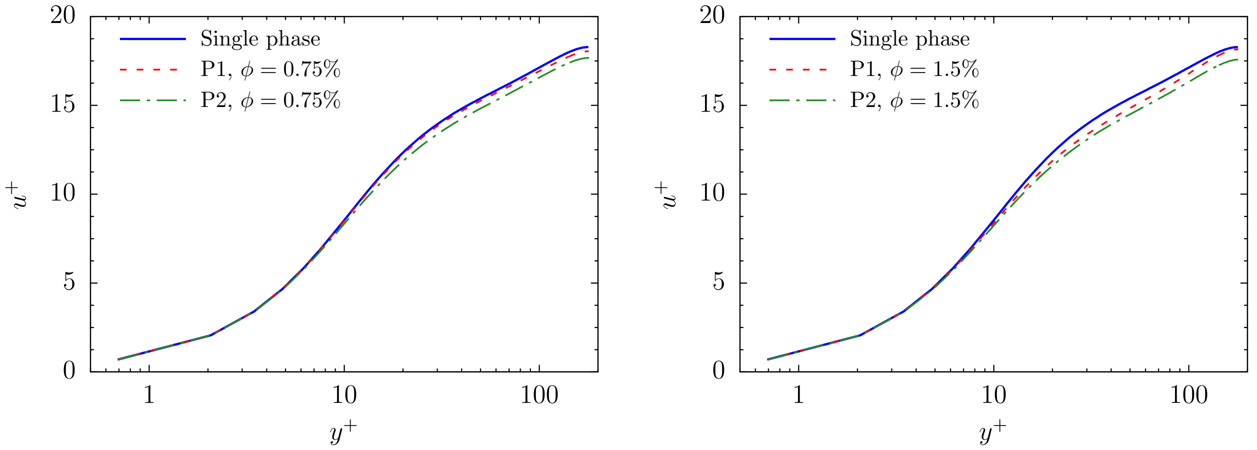

(a) (b)

Figure 7.10: Mean normalized streamwise fluid velocity u^+ versus normalized distance from the wall y^+ for turbulent flow laden with spheroidal (P1) and spherical (P2) particles; (a) $\phi = 0.75\%$; (b) $\phi = 1.5\%$ (Sec. 7.4.2)

Fluid statistics

Figure 7.9 shows a snapshot of P1 particles distribution together with the velocity field on three boundary planes for $\phi = 1.5\%$. The turbulent nature of the velocity field is seen in the figure. Particles are distributed in the whole channel. An accurate estimation of particles concentration in each part of the domain needs consideration of all simulation time steps and will be presented later.

To quantitatively investigate the effect of particles on turbulence, we start with fluid mean velocity along the channel height. Figure 7.10 compares the mean streamwise fluid velocity for two volume fractions of $\phi = 0.75$ and 1.5%. It is seen that both particle types decrease the mean streamwise velocity. However, velocity reduction by spheroids (P1) is less than that for spherical ones. At $\phi = 1.5\%$, P1 reduces the mean velocity by only 2% compared to 4.6% for P2. For volume fraction of $\phi = 0.75\%$, velocity reduction of 1.0% and 3.0% for P1 and P2 was

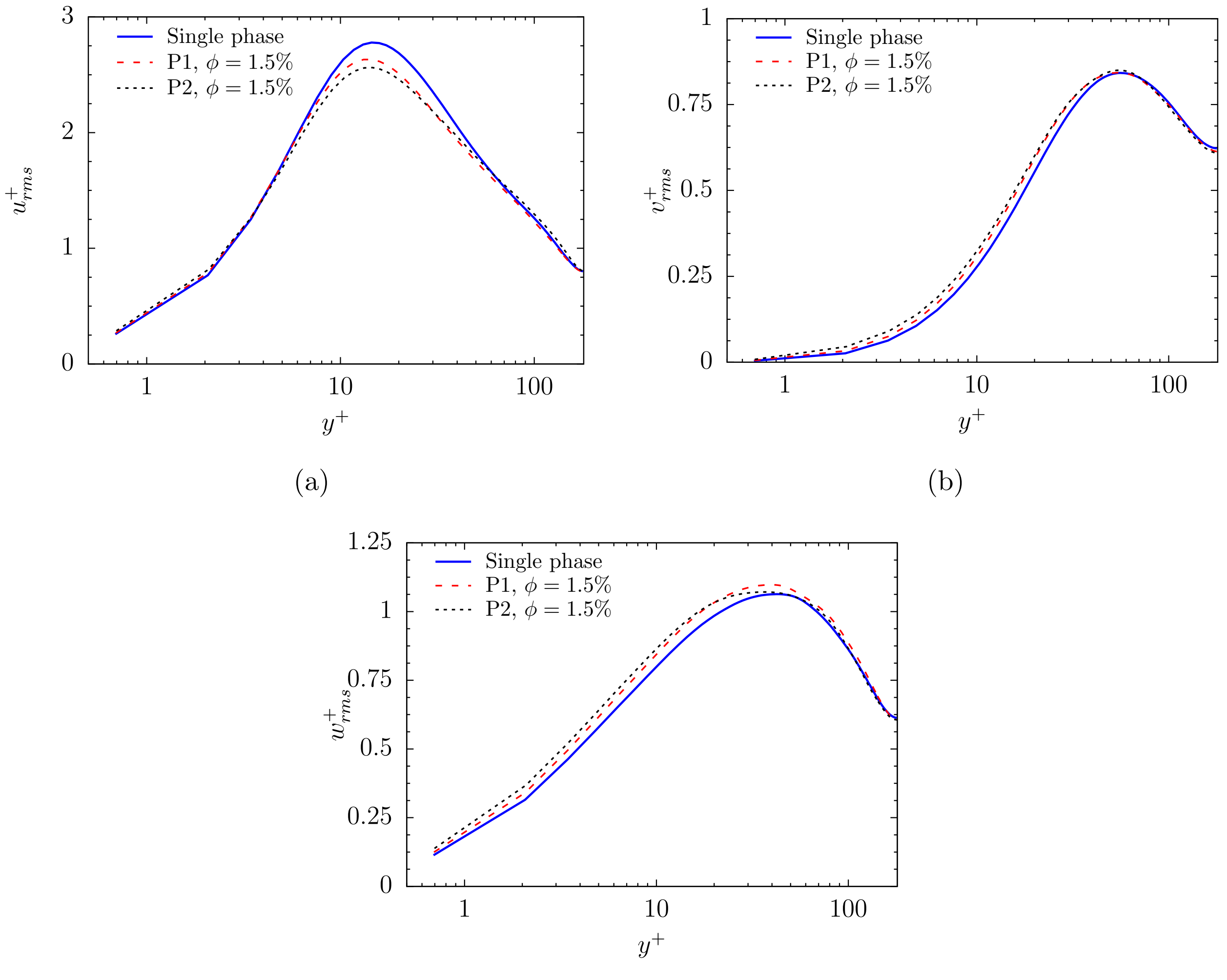

(a)

(b)

(c)

Figure 7.11: Rms of fluid velocity fluctuations based on the distance from the wall y^+ at $\phi = 1.5\%$ for turbulent flow laden with spheroidal (P1) and spherical (P2) particles; (a) u^+_{rms}; (b) v^+_{rms}; (c) w^+_{rms}

observed, respectively. This again proves that particle Stokes number (almost similar for P1 and P2) is not the only factor that contributes to pressure drop. Particle shape is another important parameter. In the region close to the wall all profiles coincide due to using the same driving force. Comparing the profile of P1 at $\phi = 0.75$ and 1.5% shows that by increasing the volume fractions, mean fluid velocity is reduced in the region of $15 < y^+ < 90$ but increases beyond this region toward the channel center ($90 < y^+ < 180$). For spherical particles, reduction in both areas is seen from the graph.

Particle effect on rms of velocity fluctuations for three different orthogonal directions at $\phi = 1.5\%$ is shown in Fig. 7.11. Adding the particles reduces the maximum streamwise velocity fluctuation for both particle types. However, the turbulence attenuation effect is more obvious for spherical particles. The profiles of spheroid particles (P1) are always closer to a single-phase flow. In the core region, P2 slightly increases streamwise velocity fluctuation while P1 has damping effect. With respect to normal (v^+_{rms}) and spanwise (w^+_{rms}) directions, behavior of

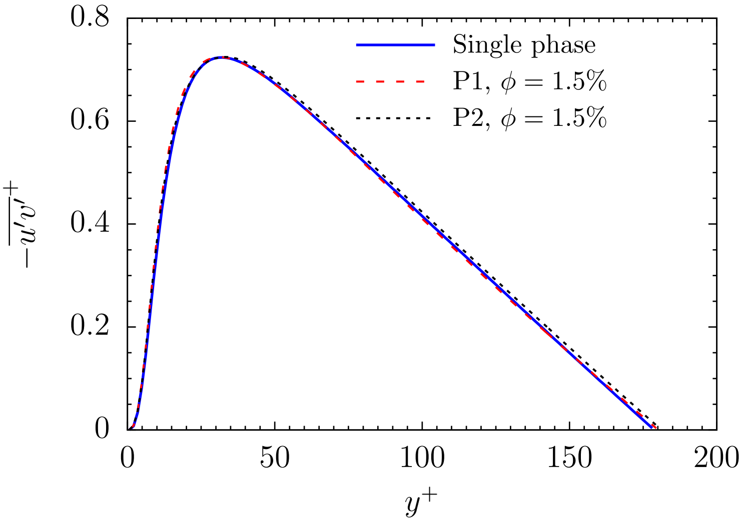

Figure 7.12: Reynolds stress of the fluid based on the distance from the wall y^+ for flow laden with spheroidal (P1) and spherical (P2) particles at $\phi = 1.5\%$

fluid-phase with spheroidal particles is again closer to a single-phase flow; however, the effect is less pronounced compared to streamwise direction. Enhancement of velocity fluctuations in the vicinity of the wall is observed for all directions due to small-scale vortices generated in this region. Furthermore, for all directions, the peak point of rms velocity is shifted toward the wall by adding the particles. This arises from local concentration of particles near the wall, in particular for spherical particles, as discussed later.

It must be noted that, the effect of finite-size particles on velocity fluctuations can be different in dilute and dense regimes. Uhlmann [154] reported enhancement of streamwise velocity fluctuations and reduction of normal and spanwise velocity fluctuations for finite-size spheres in dilute regimes. This phenomenon was attributed to vortex shedding behind the particles. In the dense regime, particles are able to change the structure of large vortices and generate small-scale vortices as well. This leads to a different behavior. Inertial point particles are also shown to augment streamwise intensity in numerical simulations of Zhao *et al.* [172] and Mortensen *et al.* [185].

The profile of Reynolds shear stress is not significantly influenced by particles for this volume fraction (Fig. 7.12). However, values of Reynolds shear stress for P1 are less than P2 far from the wall. By comparing these results to those of point spheroids from Zhao *et al.* [172], point particles are found to have a more obvious effect on velocity fluctuations and Reynolds shear stress, even at low volume fractions. In their study, spheroids of $\mathrm{St}^+ = 30$ at volume fraction of $\phi = 0.022\%$ shifted the profile of velocity fluctuation noticeably.

Turbulent kinetic energy for single- and multiphase cases are depicted in Fig. 7.13. Based on the definition of TKE ($k = \frac{1}{2}(u_x'^2 + u_y'^2 + u_z'^2)$) and Fig. 7.11, this quantity is mainly affected by streamwise velocity fluctuations. Therefore, its peak point is shifted downward for particle-laden cases. Again, the reduction for spheroidal particles is less than for spherical ones. Regions close to the wall and channel center remain almost unchanged.

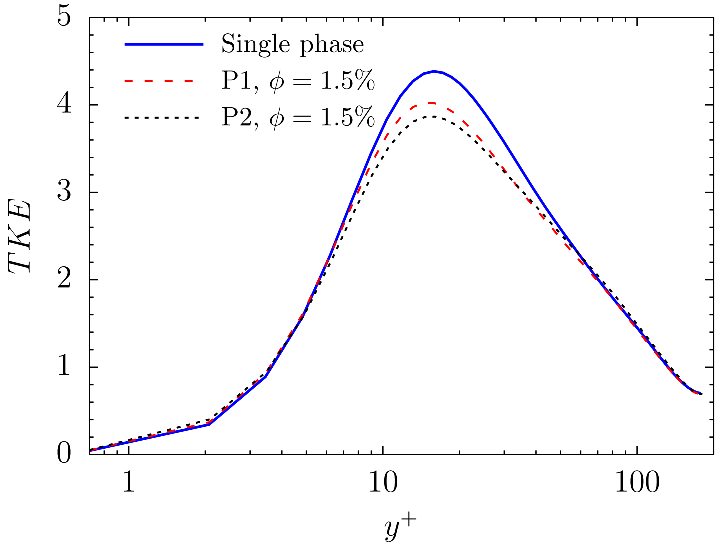

Figure 7.13: Turbulent kinetic energy of the fluid based on the distance from the wall y^+ for turbulent flow laden with spheroidal (P1) and spherical (P2) particles at $\phi = 1.5\%$

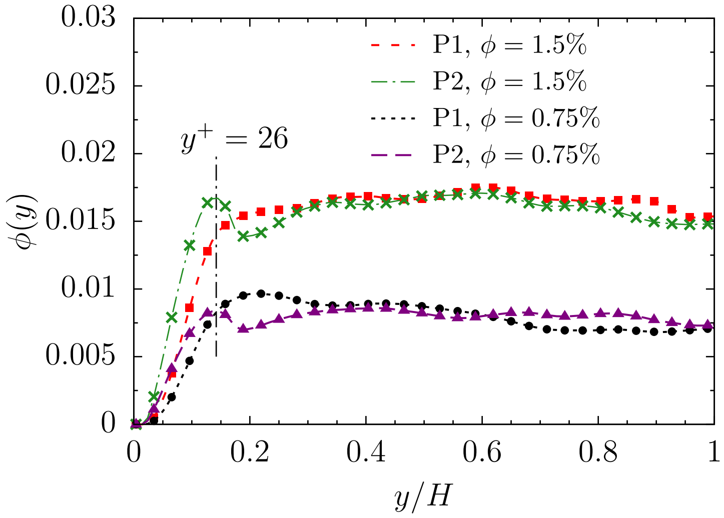

Figure 7.14: Local volume fraction of solid phase based on the distance from the wall for turbulent flow laden with spheroidal (P1) and spherical (P2) particles

Particle statistics

Now particles distribution, orientation and velocity statistics are considered. To do so, each Eulerian point, which is located inside a particle is treated with the relevant particle data such as its translational or rotational velocity.

Local volume fraction of particles for two volume fractions of $\phi = 0.75$ and 1.5% is shown in Fig. 7.14. As clearly seen in Chapter 6, spherical particles have a local peak of distribution close to the wall. The peak point corresponds to $y^+ = 26$ for P2. For spheroids, there is no clear local peak. Moreover, for both volume fractions, P2 has a higher volume fraction near the wall.

Particle P1, at $\phi = 0.75\%$, reaches a maximum volume fraction at $y/H \simeq 0.2$ before decreasing toward channel center. At $\phi = 1.5\%$, this particle reaches its maximum and then

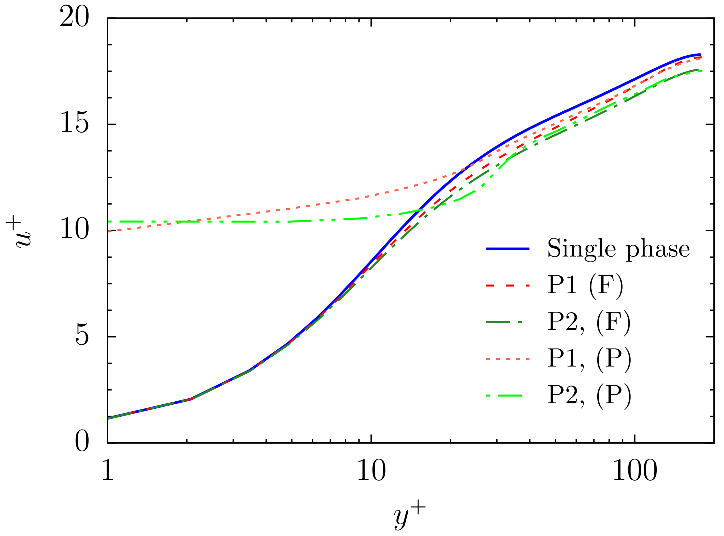

Figure 7.15: Velocity of particle phase (P) in comparison with fluid (F) based on the distance from the wall y^+ for turbulent flow laden with spheroidal (P1) and spherical (P2) particles for $\phi = 1.5\%$

shows a quite uniform volume fraction beyond $y/H = 0.2$. This point corresponds to about $0.8 l_{maj}$ with l_{maj} being particle major length ($= 2a$). This means that spheroidal particles do not have a preferential concentration near the wall, when volume fraction is sufficiently high. Spherical particles on the other hand stay mainly trapped close to the wall. Since the drag on spherical particles can be larger than that of spheroids, spherical particles cannot easily escape near wall streaks. Another factor that helps spheroids to move away from the wall is their collision with the wall, that generates a torque on the particle leading to particle rotation and changing near wall vortices.

Normalizing each profile of Fig. 7.14 by overall volume fraction, P1 at $\phi = 1.5\%$ shows $\phi(y)/\phi \approx 1$ far from channel wall. For volume fraction of $\phi = 0.75\%$, we observe $\phi(y)/\phi < 1$ close to the channel center. Thus, particles tend to move toward channel center when increasing volume fraction.

Figure 7.15 illustrates particles velocity in comparison with relevant fluid velocity for P1 and P2 at $\phi = 1.5\%$. In the viscous sublayer and part of the buffer layer ($y^+ \lesssim 20$), both particle types move faster than the fluid. In this area, fluid velocity is low. Since particles have finite size, part of the particles might be located in higher velocity regions. This results in higher average velocity of particles compared to local fluid layers. Moreover, P1 moves faster than P2 in this region due to its lower projected area. It is later shown that spheroids tend to align themselves in streamwise direction. Lower projected area and streamwise alignment lead to higher velocity of spheroids. In the center region, fluid and particles have the same velocity. Furthermore, it is seen that P1 always move faster than the fluid before reaching the same speed in the center. In contrast, P2 tends to move slower than the fluid in $18 < y^+ < 33$. This can be justified by the local maximum concentration of spheres around this limit, while spheroids have no preferential concentration at $\phi = 1.5\%$ (see Fig. 7.14). This effect is better seen in Fig. 7.16

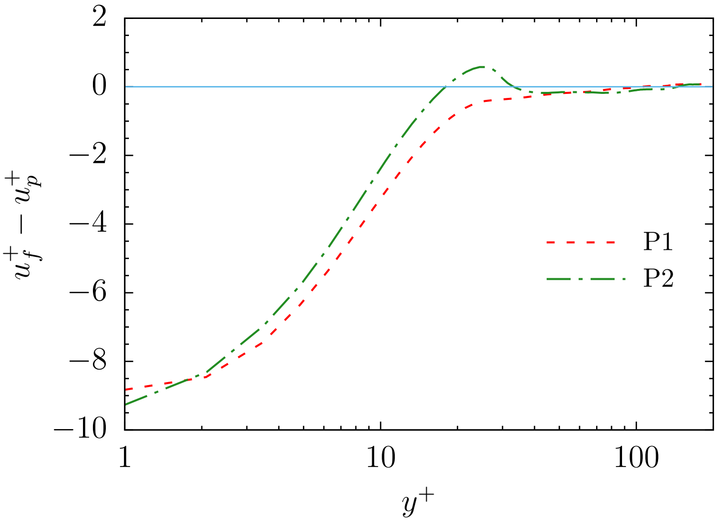

Figure 7.16: Mean streamwise relative velocity (= fluid velocity − particle velocity) based on the distance from the wall y^+ for turbulent flow laden with spheroidal (P1) and spherical (P2) particles for $\phi = 1.5\%$

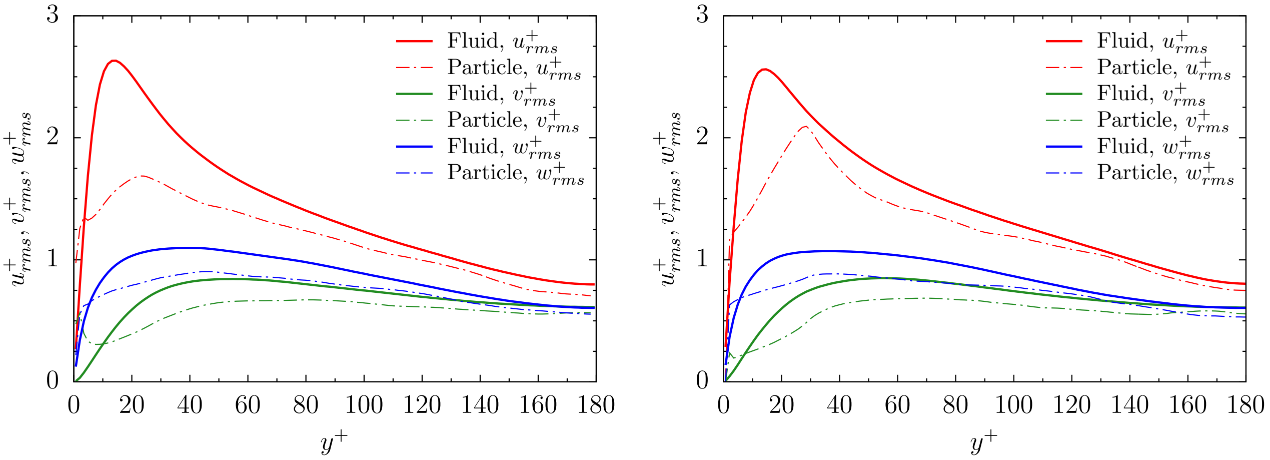

(a) (b)

Figure 7.17: Profiles of rms of velocity fluctuations versus distance from the wall for $\phi = 1.5\%$; (a) Spheroid (P1); (b) Spheric (P2)

where relative mean velocities are displayed and slip velocities are observed.

Figure 7.17 displays the rms of particle velocity fluctuations. Both P1 and P2 have generally lower velocity fluctuations than the relevant fluid due to their finite size, except for a small region very close to the wall. It is also observed by comparing Fig. 7.17a and b that spherical particles have higher streamwise fluctuations than spheroids. Normal and spanwise velocity fluctuations are less affected by particle shape. However, spheroids have higher wall-normal intensity near the wall compared to spheres. This is probably due to stronger effect of particle-wall collisions on spheroids.

Another important issue for spheroids is their orientation. Particle orientation has major influence on particle-fluid interactions. This issue has been investigated in the literature for

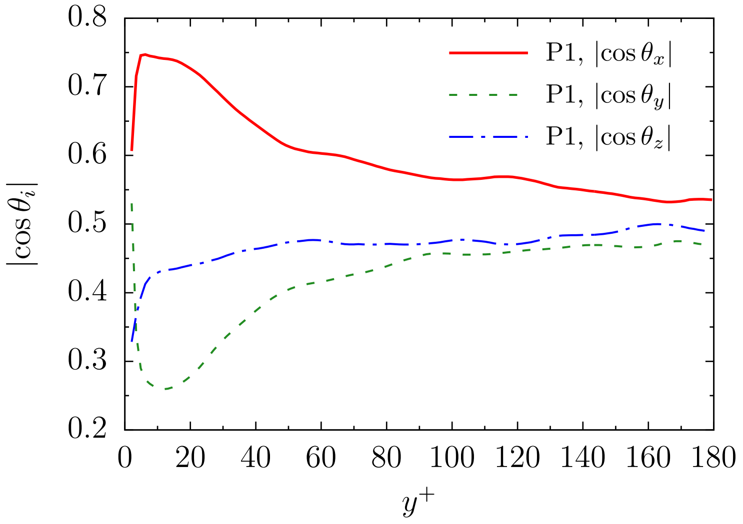

Figure 7.18: Mean absolute cosine of spheroidal particles (P1) orientation angle versus distance from the wall at $\phi = 1.5\%$

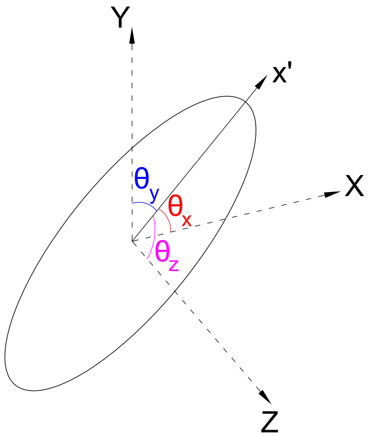

Figure 7.19: Angles between the major axis of the spheroid, x', and the inertial axes

point-size prolate and oblate spheroids [186, 188, 192–194]. It is generally found that the orientation of tracer and inertial spheroids is completely different near the wall. Tracer prolate spheroids (fibers) orient with their symmetry axis in the streamwise direction, whereas the symmetry axis of oblate spheroids (disks) align in the wall-normal direction. However, inertial point fibers demonstrate tumbling motion with the symmetry axis in the wall-normal/streamwise plane, while disks orient with their symmetry axis perpendicular to the wall-normal direction [194]. Orientation of finite-size prolates needs investigation.

Figure 7.18 depicts the absolute mean direction cosines $|\cos\theta_i|$ of P1 versus distance from the wall for x, y and z directions based on the definitions of Fig. 7.19, where θ_i is the angle between the symmetry axis of the spheroid and the relevant direction of the inertial reference frame. It can be immediately seen that finite-size spheroids tend to be aligned with their symmetry axis along streamwise direction, in particular close to the wall, where particles exhibit very strong preferential orientation in the streamwise direction (x). Higher velocity fluctuations might be

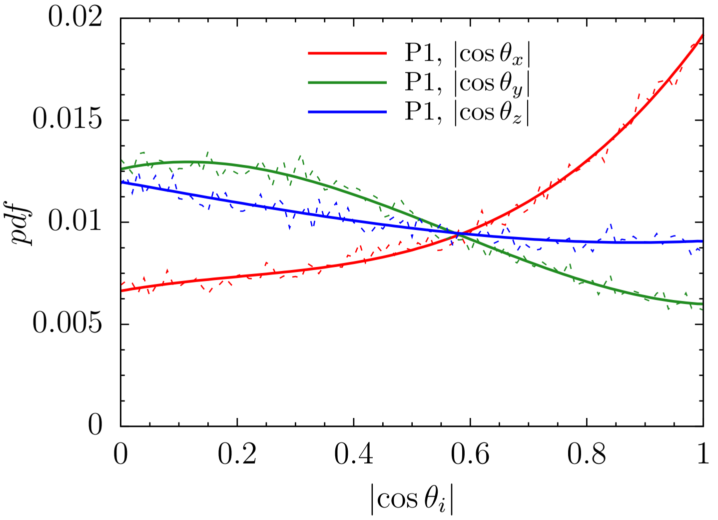

Figure 7.20: Pdf of the mean absolute cosine of particles orientation angle for spheroidal particles (P1) at $\phi = 1.5\%$

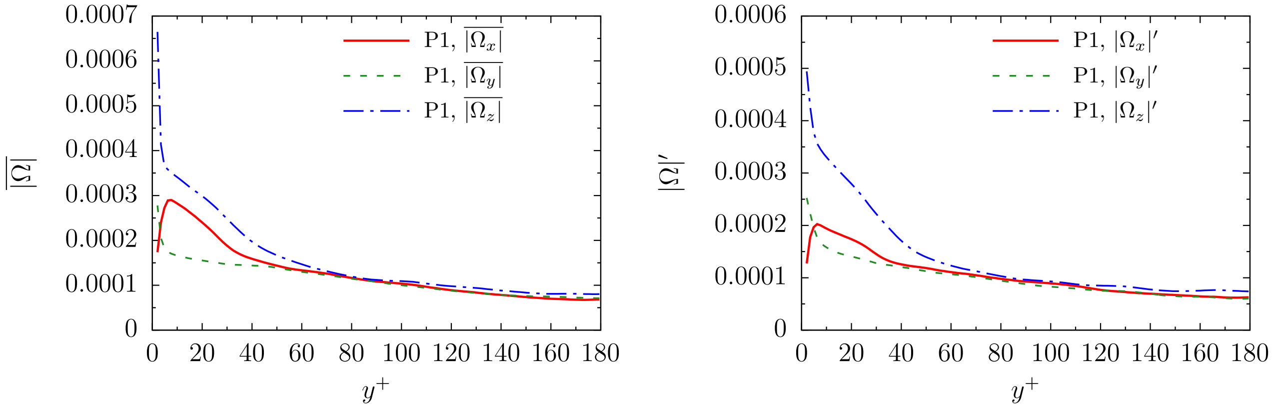

(a) (b)

Figure 7.21: (a) Mean and (b) rms of angular velocity of spheroidal particles (P1) versus distance from the wall for $\phi = 1.5\%$

responsible for particle alignment along x-direction [185, 195]. The peak point corresponds $\theta_x = 41°$ for P1. The probability of particles being oriented in spanwise and wall-normal directions is lower than in streamwise direction. Particle orientation along wall-normal direction (y) is the least probable one except for a very narrow region in the vicinity of the wall due to particle-wall collisions. Low values of $|\cos\theta_y|$ means that spheroids are mainly confined in x-z plane when they are near the walls. Orientation of spheroids in the spanwise direction (z) shows a plateau after $y^+ \simeq 40$.

In the core region, the orientations are more isotropic and random orientation is more probable. This effect is due to higher isotropy of the flow field fluctuations in channel center. However, the preferential orientation is still present, but is weaker. Alignment of finite-size spheroids is qualitatively similar to inertial point particles as reported in [186, 188].

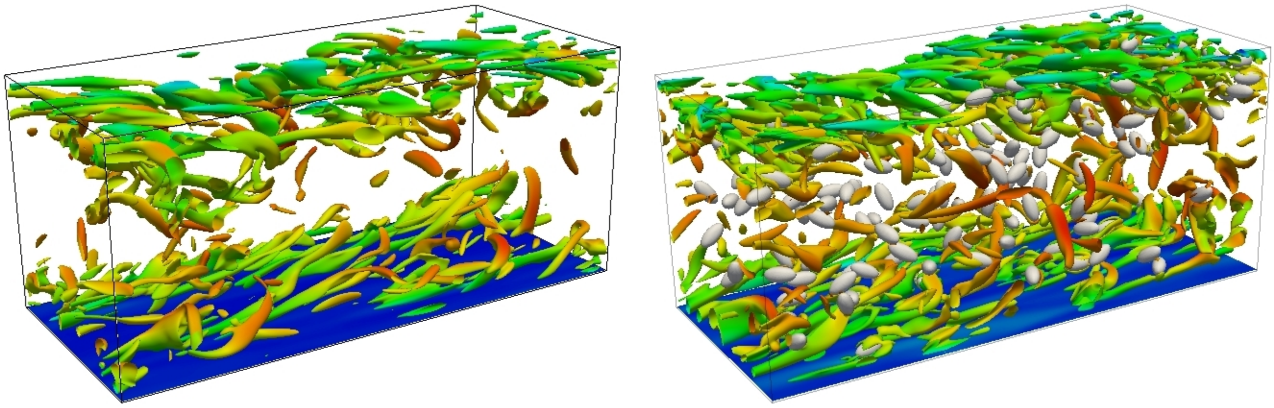

(a) (b)

Figure 7.22: Iso-surfaces of Q-criterion at $Q/(u^4/\nu^2) = 0.006$ for (a) single-phase and (b) particle-laden flow with spheroids (P1) at $\phi = 1.5\%$

The probability density functions of the direction cosine of the particle orientation angle, pdf($|\cos\theta_i|$), is shown in Fig. 7.20. Solid lines are a 3rd-order curve fit. This figure confirms the tendency of particles to be aligned in the streamwise direction. It is interesting to see that P1 has the same probability of alignment in all directions at $|\cos\theta| \approx 0.6$ or $\theta = 53°$. Before this point, pdf($|\cos\theta_y|$) is higher than the two other directions. Beyond this point, the probability of alignment along x-direction suddenly rises.

The mean and rms values of the absolute particle angular velocities are presented in Fig. 7.21. The rotation rate in spanwise direction is higher than streamwise and normal directions (Fig. 7.21a). This is mainly due to particle collisions with the walls and high shear rates near the walls. The rotation velocities are quite isotropic far from the wall. High rotation rate of P1 around z-direction together with particle alignment along x-direction implies that tumbling is the most frequent rotation mode of P1 near the wall. At the same time, particle has a kayaking rotation. Close to channel center, particle rotation is more complex and a unique rotation mode cannot be identified. Rms of spanwise angular velocity is still higher than the two other directions (Fig. 7.21b). The general behavior is similar to the mean component and isotropy is observed at channel center.

The structure of vortices in particle-free and particle-laden flows is illustrated in Fig. 7.22. Q-criterion is used to plot the iso-surfaces at $Q/(u^4/\nu^2) = 0.006$. It is seen that, addition of particles introduces many small-scale vortices.

7.5 Summary

IB-LBM has been used to simulate laminar and turbulent flows seeded with finite-size prolate spheroids. With respect to laminar flows, different particle behaviors were observed concerning rotation and sedimentation of particles. A turbulent channel flow at $\mathrm{Re}_\tau = 180$ with spheroids of aspect ratio of 2 has been modeled as well. Comparing the results with spherical particles it is found that:

- Finite-size spheroids have less drag enhancement effect compared to spheres. At volume fraction of $\phi = 1.5\%$, spheroids reduced mean velocity by only 2% compared to 4.6% for spheres with the same equivalent diameter.
- Streamwise turbulence attenuation occurs for both particle types. However, the effect is more pronounced for spherical ones.
- Although spheres show a local peak of volume fraction near the wall, it is not clearly the case for spheroids. Local volume fraction of spheroids increases gradually and reaches a plateau at increasing distance from the wall.
- Spheroids are mainly aligned along the streamwise direction. This preferential orientation is stronger close to the walls. Near channel center, particles show much less preferential orientation.

Chapter 8

Conclusions and Outlook

8.1 Conclusion

Numerical simulation of multiphase flows is inherently complex and challenging. Most published numerical studies are based on solving the Navier-Stokes equations. Lattice Boltzmann method has emerged and developed during the last three decades as an efficient mesoscopic solver of macroscopic phenomena. Despite recent advances in LBM, many questions are still unsolved. Efficient LB-simulations of laminar and turbulent particulate flows need further investigation.

The current thesis aimed to extend LBM applications to new, complex and state of the art test-cases. For this purpose, an efficient LB environment (ALBORZ) was developed during this work. First, immersed boundary method was combined with LBM to model laminar particulate flows. Both LBM and IBM are based on Eulerian grids; thus, their combination is quite advantageous. The fluid phase is discretized on an Eulerian frame, while particle motion is modeled based on the Lagrangian approach. For laminar particulate flows, different particle shapes (circle, ellipse, sphere and spheroid) can be modeled by the current code. A thorough validation involved a variety of configurations.

Then, non-isothermal flows were modeled. In this case, heat transfer to/from particles happen. Heat exchange is modeled in a similar way as particle-fluid force interaction, by the so-called direct-heating approach. The effect of temperature variation on the flow field was taken into account through the Boussinesq approximation. Simulation for stationary and moving particles as well as constant and variable particle temperatures was performed; leading to the first 3D thermal IB-LBM simulation of particulate flows. Catalyst reactors and reactive fluidized beds are possible applications for future studies.

LB simulations of hydrodynamics in porous media have been carried out to predict the permeability value at low Reynolds numbers. Permeability is the measure of flow velocity with respect to applied pressure gradient in porous media. Modeled test cases include FCC and BCC packings. Two force schemes with single- or multiple relaxation times have been compared. It was shown that low resolutions lead to large errors in permeability. Moreover, for a fixed domain size, the predicted permeability increased with the relaxation time for all approaches. Guo-MRT showed low dependency on relaxation time, thus delivering a more robust estimate. However, it is also the approach leading to the longest simulations. Finally, it was shown that permeability of both BCC and FCC structures follow similar trends when plotted against porosity, while tortuosities behave differently. A correlation was derived to predict the permeability in such structures when knowing porosity values.

The central aspect investigated in this work is the numerical simulation of turbulent particulate flows. The core configuration is a particle-laden flow between two parallel walls. After validation of the single-phase case, the flow was first seeded with fully-resolved spherical particles. Effect of particle concentration, size and density have been investigated. It was observed that, addition of fully resolved spheres decreased mean velocity compared to the single-phase flow. Also, rms of streamwise velocity fluctuations was overall attenuated by addition of particles, but it is increased in the region close to the wall and in the core zone. It is interesting to observe a point of local accumulation of particles near the wall. Finally, smaller neutrally-buoyant particles reduced the mean velocity more than larger ones at the same concentration, while heavy particles generated non-symmetrical distributions in the upper and lower part of the channel.

Finally, laminar and turbulent flows with finite-size spheroids have been simulated. In the laminar regime, particles showed different sedimentation modes when released in a vertical channel. Then, a turbulent particle-laden flow with spheroids of aspect ratio of 2 was computed. Finite-size spheroids have less drag enhancement effect compared to spheres. Streamwise turbulence attenuation occurred for spheroids as well. However, the effect was more pronounced for spherical ones. In contrast to spheres, spheroids did not show a clear local maximum concentration close to the wall; their local volume fraction increases gradually and reaches a plateau when increasing distance from the wall. Finally, spheroids were mainly aligned along the streamwise direction; the preferential orientation is even stronger close to the walls. Tumbling and kayaking motion were the most probable modes of particle rotation.

8.2 Highlights

Main novelties of current thesis can be summarized as:

- Development of a new LBM tool (ALBORZ) from scratch, that can accurately handle different laminar and turbulent two-phase flows;
- Using LBM to simulate the motion of circular, elliptical, spherical and spheroidal particles in laminar flows;
- Developing a non-isothermal LBM tool to model the motion of fully-resolved particles by considering complete particle-particle and particle-fluid interactions;
- Immersed boundary-lattice Boltzmann (IB-LB) simulation of turbulent particle-laden pressure-driven flows for spherical particles;
- First LBM computation of finite-size prolate spheroids in turbulent flows;

8.3 Outlook and recommendations

In future works, several developments can be carried out to extend applications of IB-LBM for particulate and multiphase flows. For:

Turbulent particulate flows:

- Test spheroidal and cylindrical particles of large aspect ratio and compare their influence on turbulent flow field. This, however, requires a fine enough resolution to capture the flow field. This would finally open the door to drag reduction studies;
- Use LES to reduce the computational cost of particulate flow simulations. In this manner, high Reynolds number regimes will be accessible which might change the nature of the interactions;

Laminar non-isothermal flows:

- Develop a method to account for non-uniform temperature distribution inside the particles, as found for non-negligible Biot numbers;
- Extend the non-isothermal applications to conduction in solid phase, which is relevant for conjugate heat transfer applications;
- Develop the model toward high Prandtl number regimes;

Laminar porous media flows:

- Extend the current code to account for curvature of solid boundaries, using relevant LBM curved-boundary treatments;
- Model heat transfer to/from solid surface, opening the door for modeling drying and evaporation phenomena.

References

[1] C. E. Brennen, *Fundamentals of Multiphase Flow.* Cambridge University Press, 2005.

[2] S. Balachandar and J. K. Eaton, "Turbulent dispersed multiphase flow," *Annual Review of Fluid Mechanics*, vol. 42, pp. 111–133, 2010.

[3] C. T. Crowe, J. D. Schwarzkopf, M. Sommerfeld, and Y. Tsuji, *Multiphase Flows with Droplets and Particles.* CRC press, 2011.

[4] J. Hardy, Y. Pomeau, and O. De Pazzis, "Time evolution of a two-dimensional classical lattice system," *Physical Review Letters*, vol. 31, p. 276, 1973.

[5] U. Frisch, B. Hasslacher, and Y. Pomeau, "Lattice-gas automata for the Navier-Stokes equation," *Physical Review Letters*, vol. 56, p. 1505, 1986.

[6] B. Van Wachem, A. Bakker, J. Schouten, M. Heemels, and S. De Leeuw, "Simulation of fluidized beds with lattice gas cellular automata," *Journal of Computational Physics*, vol. 135, pp. 1–7, 1997.

[7] U. Frisch, D. d'Humières, B. Hasslacher, P. Lallemand, Y. Pomeau, J.-P. Rivet, *et al.*, "Lattice gas hydrodynamics in two and three dimensions," *Complex Systems*, vol. 1, pp. 649–707, 1987.

[8] H. Chen, S. Chen, and W. H. Matthaeus, "Recovery of the Navier-Stokes equations using a lattice-gas Boltzmann method," *Physical Review A*, vol. 45, p. R5339, 1992.

[9] Y. Qian, D. d'Humières, and P. Lallemand, "Lattice BGK models for Navier-Stokes equation," *Europhysics Letters*, vol. 17, p. 479, 1992.

[10] G. R. McNamara and G. Zanetti, "Use of the Boltzmann equation to simulate lattice-gas automata," *Physical Review Letters*, vol. 61, no. 20, pp. 2332–2335, 1988.

[11] F. Higuera and J. Jimenez, "Boltzmann approach to lattice gas simulations," *Europhysics Letters*, vol. 9, pp. 663–668, 1989.

[12] F. Higuera, S. Succi, and R. Benzi, "Lattice gas dynamics with enhanced collisions," *Europhysics Letters*, vol. 9, p. 345, 1989.

[13] Y. Qian, D. d'Humières, and P. Lallemand, *Advances in Kinetic Theory and Continuum Mechanics*. Berlin: Springer Press, 1991.

[14] J. Koelman, "A simple lattice Boltzmann scheme for Navier-Stokes fluid flow," *Europhysics Letters*, vol. 15, p. 603, 1991.

[15] S. Chen, H. Chen, D. Martínez, and W. Matthaeus, "Lattice Boltzmann model for simulation of magnetohydrodynamics," *Physical Review Letters*, vol. 67, p. 3776, 1991.

[16] P. L. Bhatnagar, E. P. Gross, and M. Krook, "A model for collision processes in gases. I. Small amplitude processes in charged and neutral one-component systems," *Physical Review*, vol. 94, pp. 511–525, 1954.

[17] X. He and L.-S. Luo, "Theory of the lattice Boltzmann method: From the Boltzmann equation to the lattice Boltzmann equation," *Physical Review E*, vol. 56, p. 6811, 1997.

[18] X. Shan and H. Chen, "Lattice Boltzmann model for simulating flows with multiple phases and components," *Physical Review E*, vol. 47, pp. 1815–1819, 1993.

[19] X. Shan and H. Chen, "Simulation of nonideal gases and liquid-gas phase transitions by the lattice Boltzmann equation," *Physical Review E*, vol. 49, p. 2941, 1994.

[20] A. Cancelliere, C. Chang, E. Foti, D. H. Rothman, and S. Succi, "The permeability of a random medium: comparison of simulation with theory," *Physics of Fluids A*, vol. 2, pp. 2085–2088, 1990.

[21] R. S. Maier, D. Kroll, Y. Kutsovsky, H. Davis, and R. S. Bernard, "Simulation of flow through bead packs using the lattice Boltzmann method," *Physics of Fluids*, vol. 10, pp. 60–74, 1998.

[22] E. Aharonov and D. H. Rothman, "Non-newtonian flow (through porous media): a lattice-Boltzmann method," *Geophysical Research Letters*, vol. 20, pp. 679–682, 1993.

[23] L. Giraud, P. Lallemand, *et al.*, "A lattice Boltzmann model for Jeffreys viscoelastic fluid," *Europhysics Letters*, vol. 42, p. 625, 1998.

[24] Y. Qian, "Simulating thermohydrodynamics with lattice BGK models," *Journal of Scientific Computing*, vol. 8, pp. 231–242, 1993.

[25] X. Shan, "Simulation of Rayleigh-Bénard convection using a lattice Boltzmann method," *Physical Review E*, vol. 55, p. 2780, 1997.

[26] C. K. Aidun, Y. Lu, and E.-J. Ding, "Direct analysis of particulate suspensions with inertia using the discrete Boltzmann equation," *Journal of Fluid Mechanics*, vol. 373, pp. 287–311, 1998.

[27] A. J. Ladd, “Short-time motion of colloidal particles: Numerical simulation via a fluctuating lattice-Boltzmann equation,” *Physical Review Letters*, vol. 70, p. 1339, 1993.

[28] J. G. Eggels, “Direct and large-eddy simulation of turbulent fluid flow using the lattice-Boltzmann scheme,” *International Journal of Heat and Fluid Flow*, vol. 17, pp. 307–323, 1996.

[29] R. Benzi and S. Succi, “Two-dimensional turbulence with the lattice Boltzmann equation,” *Journal of Physics A: Mathematical and General*, vol. 23, p. L1, 1990.

[30] B. Li and D. Y. Kwok, “Discrete Boltzmann equation for microfluidics,” *Physical Review Letters*, vol. 90, p. 124502, 2003.

[31] D. Hlushkou, D. Kandhai, and U. Tallarek, “Coupled lattice-Boltzmann and finite-difference simulation of electroosmosis in microfluidic channels,” *International Journal for Numerical Methods in Fluids*, vol. 46, pp. 507–532, 2004.

[32] J. Zhang, P. C. Johnson, and A. S. Popel, “An immersed boundary lattice Boltzmann approach to simulate deformable liquid capsules and its application to microscopic blood flows,” *Physical Biology*, vol. 4, p. 285, 2007.

[33] T. Krüger, F. Varnik, and D. Raabe, “Efficient and accurate simulations of deformable particles immersed in a fluid using a combined immersed boundary lattice Boltzmann finite element method,” *Computers & Mathematics with Applications*, vol. 61, pp. 3485–3505, 2011.

[34] S. Harris, *An Introduction to the Theory of the Boltzmann Equation*. Courier Corporation, 1971.

[35] N. N. Bogoliubov, “Kinetic equations,” *Journal of Physics USSR*, vol. 10, pp. 265–274, 1946.

[36] L.-S. Luo, “Theory of the lattice Boltzmann method: Lattice Boltzmann models for nonideal gases,” *Physical Review E*, vol. 62, p. 4982, 2000.

[37] S. Chapman, “On the law of distribution of molecular velocities, and on the theory of viscosity and thermal conduction, in a non-uniform simple monatomic gas,” *Philosophical Transactions of the Royal Society of London. Series A, Containing Papers of a Mathematical or Physical Character*, vol. 216, pp. 279–348, 1916.

[38] T. Abe, “Derivation of the lattice Boltzmann method by means of the discrete ordinate method for the Boltzmann equation,” *Journal of Computational Physics*, vol. 131, pp. 241–246, 1997.

[39] Z. Guo and C. Shu, *Lattice Boltzmann Method and its Applications in Engineering (Advances in Computational Fluid Dynamics)*. World Scientific Publishing Company, 2013.

[40] O. Filippova and D. Hänel, "Grid refinement for lattice-BGK models," *Journal of Computational Physics*, vol. 147, pp. 219–228, 1998.

[41] M. Bouzidi, M. Firdaouss, and P. Lallemand, "Momentum transfer of a Boltzmann-lattice fluid with boundaries," *Physics of Fluids*, vol. 13, pp. 3452–3459, 2001.

[42] R. Mei, L.-S. Luo, and W. Shyy, "An accurate curved boundary treatment in the lattice Boltzmann method," *Journal of Computational Physics*, vol. 155, pp. 307–330, 1999.

[43] C. S. Peskin, "Numerical analysis of blood flow in the heart," *Journal of Computational Physics*, vol. 25, pp. 220–252, 1977.

[44] Z. Guo, C. Zheng, B. Shi, and T. Zhao, "Thermal lattice Boltzmann equation for low Mach number flows: decoupling model," *Physical Review E*, vol. 75, p. 036704, 2007.

[45] Y. Peng, C. Shu, and Y. Chew, "Simplified thermal lattice Boltzmann model for incompressible thermal flows," *Physical Review E*, vol. 68, p. 026701, 2003.

[46] X. He, S. Chen, and G. D. Doolen, "A novel thermal model for the lattice Boltzmann method in incompressible limit," *Journal of Computational Physics*, vol. 146, pp. 282–300, 1998.

[47] P. C. Philippi, L. A. Hegele Jr, L. O. Dos Santos, and R. Surmas, "From the continuous to the lattice Boltzmann equation: the discretization problem and thermal models," *Physical Review E*, vol. 73, p. 056702, 2006.

[48] F. Chen, A. Xu, G. Zhang, Y. Li, and S. Succi, "Multiple-relaxation-time lattice Boltzmann approach to compressible flows with flexible specific-heat ratio and Prandtl number," *Europhysics Letters*, vol. 90, p. 54003, 2010.

[49] F. J. Alexander, S. Chen, and J. Sterling, "Lattice Boltzmann thermohydrodynamics," *Physical Review E*, vol. 47, p. R2249, 1993.

[50] P. Lallemand and L.-S. Luo, "Hybrid finite-difference thermal lattice Boltzmann equation," *International Journal of Modern Physics B*, vol. 17, pp. 41–47, 2003.

[51] A. Mezrhab, M. Bouzidi, and P. Lallemand, "Hybrid lattice-Boltzmann finite-difference simulation of convective flows," *Computers & Fluids*, vol. 33, pp. 623–641, 2004.

[52] L. H. Holway Jr, "New statistical models for kinetic theory: methods of construction," *Physics of Fluids*, vol. 9, pp. 1658–1673, 1966.

[53] L. Zheng, B. Shi, and Z. Guo, “Multiple-relaxation-time model for the correct thermohydrodynamic equations,” *Physical Review E*, vol. 78, p. 026705, 2008.

[54] Q. Zou, S. Hou, S. Chen, and G. D. Doolen, “A improved incompressible lattice Boltzmann model for time-independent flows,” *Journal of Statistical Physics*, vol. 81, pp. 35–48, 1995.

[55] Z. Guo, B. Shi, and N. Wang, “Lattice BGK model for incompressible Navier–Stokes equation,” *Journal of Computational Physics*, vol. 165, pp. 288–306, 2000.

[56] P. J. Dellar, “Bulk and shear viscosities in lattice Boltzmann equations,” *Physical Review E*, vol. 64, p. 031203, 2001.

[57] F. J. Alexander, H. Chen, S. Chen, and G. Doolen, “Lattice Boltzmann model for compressible fluids,” *Physical Review A*, vol. 46, p. 1967, 1992.

[58] C. Sun, “Lattice-Boltzmann models for high speed flows,” *Physical Review E*, vol. 58, p. 7283, 1998.

[59] Q. Li, Y. He, Y. Wang, and W. Tao, “Coupled double-distribution-function lattice Boltzmann method for the compressible Navier-Stokes equations,” *Physical Review E*, vol. 76, p. 056705, 2007.

[60] Y. Gan, A. Xu, G. Zhang, X. Yu, and Y. Li, “Two-dimensional lattice Boltzmann model for compressible flows with high mach number,” *Physica A: Statistical Mechanics and its Applications*, vol. 387, pp. 1721–1732, 2008.

[61] N. I. Prasianakis and I. V. Karlin, “Lattice Boltzmann method for simulation of compressible flows on standard lattices,” *Physical Review E*, vol. 78, p. 016704, 2008.

[62] D. d’Humieres, “Generalized lattice-Boltzmann equations,” *Rarefied gas dynamics- Theory and simulations*, pp. 450–458, 1994.

[63] D. d’Humières, I. Ginzburg, M. Krafczyk, P. Lallemand, and L. Luo, “Multiple-relaxation-time lattice Boltzmann models in three dimensions.,” *Philosophical Transactions of the Royal Society of London, Series A*, vol. 360, no. 1792, pp. 437–451, 2002.

[64] M. Geier, A. Greiner, and J. G. Korvink, “Cascaded digital lattice Boltzmann automata for high Reynolds number flow,” *Physical Review E*, vol. 73, p. 066705, 2006.

[65] S. Ansumali and I. V. Karlin, “Single relaxation time model for entropic lattice Boltzmann methods,” *Physical Review E*, vol. 65, p. 056312, 2002.

[66] M. Geier, M. Schönherr, A. Pasquali, and M. Krafczyk, “The cumulant lattice Boltzmann equation in three dimensions: Theory and validation,” *Computers & Mathematics with Applications*, vol. 70, pp. 507–547, 2015.

[67] L.-S. Luo, W. Liao, X. Chen, Y. Peng, W. Zhang, *et al.*, “Numerics of the lattice Boltzmann method: Effects of collision models on the lattice Boltzmann simulations,” *Physical Review E*, vol. 83, p. 056710, 2011.

[68] I. Ginzbourg and P. Adler, “Boundary flow condition analysis for the three-dimensional lattice Boltzmann model,” *Journal de Physique II*, vol. 4, pp. 191–214, 1994.

[69] X. Chen and J. Wang, “A comparison of two-fluid model, dense discrete particle model and CFD-DEM method for modeling impinging gas-solid flows,” *Powder Technology*, vol. 254, pp. 94–102, 2014.

[70] M. Van der Hoef, M. van Sint Annaland, N. Deen, and J. Kuipers, “Numerical simulation of dense gas-solid fluidized beds: A multiscale modeling strategy,” *Annual Review of Fluid Mechanics*, vol. 40, pp. 47–70, 2008.

[71] H. H. Hu, N. A. Patankar, and M. Zhu, “Direct numerical simulations of fluid-solid systems using the arbitrary Lagrangian-Eulerian technique,” *Journal of Computational Physics*, vol. 169, pp. 427–462, 2001.

[72] R. Glowinski, T.-W. Pan, T. I. Hesla, and D. D. Joseph, “A distributed Lagrange multiplier/fictitious domain method for particulate flows,” *International Journal of Multiphase Flow*, vol. 25, pp. 755–794, 1999.

[73] C. S. Peskin, “Flow patterns around heart valves: a numerical method,” *Journal of Computational Physics*, vol. 10, pp. 252–271, 1972.

[74] A. J. Ladd, “Numerical simulations of particulate suspensions via a discretized Boltzmann equation. Part 1. theoretical foundation,” *Journal of Fluid Mechanics*, vol. 271, pp. 285–309, 1994.

[75] A. J. Ladd, “Numerical simulations of particulate suspensions via a discretized Boltzmann equation. Part 2. numerical results,” *Journal of Fluid Mechanics*, vol. 271, pp. 311–339, 1994.

[76] M. Dietzel, M. Ernst, and M. Sommerfeld, “Application of the lattice-Boltzmann method for particle-laden flows: Point-particles and fully resolved particles,” *Flow, Turbulence and Combustion*, vol. 97, pp. 539–570, 2016.

[77] M. Ernst, M. Dietzel, and M. Sommerfeld, “A lattice Boltzmann method for simulating transport and agglomeration of resolved particles,” *Acta Mechanica*, vol. 224, pp. 2425–2449, 2013.

[78] X. Niu, C. Shu, Y. Chew, and Y. Peng, “A momentum exchange-based immersed boundary-lattice Boltzmann method for simulating incompressible viscous flows,” *Physics Letters A*, vol. 354, pp. 173–182, 2006.

[79] J. Mohd-Yusof, “Combined immersed-boundary/B-spline methods for simulations of flow in complex geometries,” *Annual Research Briefs. NASA Ames Research Center, Stanford University Center of Turbulence Research: Stanford*, pp. 317–327, 1997.

[80] M. Uhlmann, “An immersed boundary method with direct forcing for the simulation of particulate flows,” *Journal of Computational Physics*, vol. 209, pp. 448–476, 2005.

[81] Z.-G. Feng and E. E. Michaelides, “The immersed boundary-lattice Boltzmann method for solving fluid-particles interaction problems,” *Journal of Computational Physics*, vol. 195, pp. 602–628, 2004.

[82] Z.-G. Feng and E. E. Michaelides, “Proteus: a direct forcing method in the simulations of particulate flows,” *Journal of Computational Physics*, vol. 202, pp. 20–51, 2005.

[83] A. Dupuis, P. Chatelain, and P. Koumoutsakos, “An immersed boundary lattice-Boltzmann method for the simulation of the flow past an impulsively started cylinder,” *Journal of Computational Physics*, vol. 227, pp. 4486–4498, 2008.

[84] S. K. Kang and Y. A. Hassan, “A direct-forcing immersed boundary method for the thermal lattice Boltzmann method,” *Computers & Fluids*, vol. 49, pp. 36–45, 2011.

[85] K. Suzuki and T. Inamuro, “Effect of internal mass in the simulation of a moving body by the immersed boundary method,” *Computers & Fluids*, vol. 49, pp. 173–187, 2011.

[86] K. Suzuki and T. Inamuro, “A higher-order immersed boundary-lattice Boltzmann method using a smooth velocity field near boundaries,” *Computers & Fluids*, vol. 76, pp. 105–115, 2013.

[87] A. Eshghinejadfard, A. Abdelsamie, G. Janiga, and D. Thévenin, “Direct-forcing immersed boundary lattice Boltzmann simulation of particle/fluid interactions for spherical and non-spherical particles,” *Particuology*, vol. 25, pp. 93–103, 2016.

[88] A. Abdelsamie, A. E. Fard, T. Oster, and D. Thévenin, “Impact of the collision model for fully resolved particles interacting in a fluid,” in *ASME 2014 Fluids Engineering Division Summer Meeting*, (Chicago, Illinois), American Society of Mechanical Engineers.

[89] C. S. Peskin, “The immersed boundary method,” *Acta Numerica*, vol. 11, pp. 479–517, 2002.

[90] Z.-G. Feng and E. E. Michaelides, “Robust treatment of no-slip boundary condition and velocity updating for the lattice-Boltzmann simulation of particulate flows,” *Computers & Fluids*, vol. 38, pp. 370–381, 2009.

[91] Z. Guo, C. Zheng, and B. Shi, “Discrete lattice effects on the forcing term in the lattice Boltzmann method,” *Physical Review E*, vol. 65, p. 046308, 2002.

[92] L.-S. Luo, “Analytic solutions of linearized lattice Boltzmann equation for simple flows,” *Journal of Statistical Physics*, vol. 88, pp. 913–926, 1997.

[93] S. K. Kang, *Immersed boundary methods in the lattice Boltzmann equation for flow simulation.* PhD thesis, Texas A&M University, 2010.

[94] S. Di and W. Ge, “Simulation of dynamic fluid-solid interactions with an improved direct-forcing immersed boundary method,” *Particuology*, vol. 18, pp. 22–34, 2015.

[95] Y. Chen, Q. Cai, Z. Xia, M. Wang, and S. Chen, “Momentum-exchange method in lattice Boltzmann simulations of particle-fluid interactions,” *Physical Review E*, vol. 88, p. 013303, 2013.

[96] Z. Xia, K. W. Connington, S. Rapaka, P. Yue, J. J. Feng, and S. Chen, “Flow patterns in the sedimentation of an elliptical particle,” *Journal of Fluid Mechanics*, vol. 625, pp. 249–272, 2009.

[97] A. Ten Cate, C. Nieuwstad, J. Derksen, and H. Van den Akker, “Particle imaging velocimetry experiments and lattice-Boltzmann simulations on a single sphere settling under gravity,” *Physics of Fluids*, vol. 14, pp. 4012–4025, 2002.

[98] E. B. Saff and A. B. Kuijlaars, “Distributing many points on a sphere,” *The Mathematical Intelligencer*, vol. 19, pp. 5–11, 1997.

[99] R. Glowinski, T. Pan, T. Hesla, D. Joseph, and J. Periaux, “A fictitious domain approach to the direct numerical simulation of incompressible viscous flow past moving rigid bodies: application to particulate flow,” *Journal of Computational Physics*, vol. 169, pp. 363–426, 2001.

[100] N. Sharma and N. A. Patankar, “A fast computation technique for the direct numerical simulation of rigid particulate flows,” *Journal of Computational Physics*, vol. 205, pp. 439–457, 2005.

[101] W.-P. Breugem, “A second-order accurate immersed boundary method for fully resolved simulations of particle-laden flows,” *Journal of Computational Physics*, vol. 231, pp. 4469–4498, 2012.

[102] H. Gan, J. Chang, J. J. Feng, and H. H. Hu, “Direct numerical simulation of the sedimentation of solid particles with thermal convection,” *Journal of Fluid Mechanics*, vol. 481, pp. 385–411, 2003.

[103] Z. Yu, X. Shao, and A. Wachs, “A fictitious domain method for particulate flows with heat transfer,” *Journal of Computational Physics*, vol. 217, pp. 424–452, 2006.

[104] J. Kim and H. Choi, "An immersed-boundary finite-volume method for simulation of heat transfer in complex geometries," *Korean Society of Mechanical Engineers International Journal*, vol. 18, pp. 1026–1035, 2004.

[105] J. R. Pacheco, A. Pacheco-Vega, T. Rodi, and R. E. Peck, "Numerical simulations of heat transfer and fluid flow problems using an immersed-boundary finite-volume method on nonstaggered grids," *Numerical Heat Transfer, Part B: Fundamentals*, vol. 48, pp. 1–24, 2005.

[106] Z.-G. Feng and E. E. Michaelides, "Heat transfer in particulate flows with direct numerical simulation (DNS)," *International Journal of Heat and Mass Transfer*, vol. 52, pp. 777–786, 2009.

[107] C. Dan and A. Wachs, "Direct numerical simulation of particulate flow with heat transfer," *International Journal of Heat and Fluid Flow*, vol. 31, pp. 1050–1057, 2010.

[108] S. K. Kang and Y. A. Hassan, "A comparative study of direct-forcing immersed boundary-lattice Boltzmann methods for stationary complex boundaries," *International Journal for Numerical Methods in Fluids*, vol. 66, pp. 1132–1158, 2011.

[109] A. Wachs, "Rising of 3D catalyst particles in a natural convection dominated flow by a parallel DNS method," *Computers & Chemical Engineering*, vol. 35, pp. 2169–2185, 2011.

[110] N. G. Deen, S. H. Kriebitzsch, M. A. van der Hoef, and J. Kuipers, "Direct numerical simulation of flow and heat transfer in dense fluid-particle systems," *Chemical Engineering Science*, vol. 81, pp. 329–344, 2012.

[111] H. Ström and S. Sasic, "A multiphase DNS approach for handling solid particles motion with heat transfer," *International Journal of Multiphase Flow*, vol. 53, pp. 75–87, 2013.

[112] R. Weiwei, *Development of immersed boundary methods for isothermal and thermal flows.* PhD thesis, Nanjing University of Aeronautics and Astronautics, 2014.

[113] J. Xia, K. Luo, and J. Fan, "Simulating heat transfer from moving rigid bodies using high-order ghost-cell based immersed-boundary method," *International Journal of Heat and Mass Transfer*, vol. 89, pp. 856–865, 2015.

[114] H. Zhang, A. Yu, W. Zhong, and Y. Tan, "A combined TLBM–IBM–DEM scheme for simulating isothermal particulate flow in fluid," *International Journal of Heat and Mass Transfer*, vol. 91, pp. 178–189, 2015.

[115] A. Eshghinejadfard and D. Thévenin, "Numerical simulation of heat transfer in particulate flows using a thermal immersed boundary lattice Boltzmann method," *International Journal of Heat and Fluid Flow*, vol. 60, pp. 31–46, 2016.

[116] Y. Shi, T. Zhao, and Z. Guo, "Thermal lattice Bhatnagar-Gross-Kkrook model for flows with viscous heat dissipation in the incompressible limit," *Physical Review E*, vol. 70, p. 066310, 2004.

[117] T. Seta, "Implicit temperature-correction-based immersed-boundary thermal lattice Boltzmann method for the simulation of natural convection," *Physical Review E*, vol. 87, p. 063304, 2013.

[118] Q. Zou and X. He, "On pressure and velocity boundary conditions for the lattice Boltzmann BGK model," *Physics of Fluids*, vol. 9, pp. 1591–1598, 1997.

[119] S. Haeri and J. Shrimpton, "A new implicit fictitious domain method for the simulation of flow in complex geometries with heat transfer," *Journal of Computational Physics*, vol. 237, pp. 21–45, 2013.

[120] E. Charlaix, A. Kushnick, and J. Stokes, "Experimental study of dynamic permeability in porous media," *Physical Review Letters*, vol. 61, p. 1595, 1988.

[121] A. Kumar, B. Maini, P. Bishnoi, M. Clarke, O. Zatsepina, and S. Srinivasan, "Experimental determination of permeability in the presence of hydrates and its effect on the dissociation characteristics of gas hydrates in porous media," *Journal of Petroleum Science and Engineering*, vol. 70, pp. 114–122, 2010.

[122] L. Zuo, S. Krevor, R. W. Falta, and S. M. Benson, "An experimental study of CO_2 exsolution and relative permeability measurements during CO_2 saturated water depressurization," *Transport in Porous Media*, vol. 91, pp. 459–478, 2012.

[123] S. Succi, *The Lattice Boltzmann Equation for Fluid Dynamics and Beyond.* Oxford, 2001.

[124] M. Junk, A. Klar, and L.-S. Luo, "Asymptotic analysis of the lattice Boltzmann equation," *Journal of Computational Physics*, vol. 210, pp. 676–704, 2005.

[125] S. Succi, E. Foti, and F. Higuera, "Three-dimensional flows in complex geometries with the lattice Boltzmann method," *Europhysics Letters*, vol. 10, pp. 433–438, 1989.

[126] C. Pan, L.-S. Luo, and C. T. Miller, "An evaluation of lattice Boltzmann schemes for porous medium flow simulation," *Computers & Fluids*, vol. 35, pp. 898–909, 2006.

[127] W. Degruyter, A. Burgisser, O. Bachmann, and O. Malaspinas, "Synchrotron X-ray microtomography and lattice Boltzmann simulations of gas flow through volcanic pumices," *Geosphere*, vol. 6, pp. 470–481, 2010.

[128] C. Chukwudozie and M. Tyagi, "Pore scale inertial flow simulations in 3-d smooth and rough sphere packs using lattice Boltzmann method," *AIChE Journal*, vol. 59, pp. 4858–4870, 2013.

[129] H. Cho, N. Jeong, and H. J. Sung, “Permeability of microscale fibrous porous media using the lattice Boltzmann method,” *International Journal of Heat and Fluid Flow*, vol. 44, pp. 435–443, 2013.

[130] B. Jelinek, M. Eshraghi, S. Felicelli, and J. F. Peters, “Large-scale parallel lattice Boltzmann-cellular automaton model of two-dimensional dendritic growth,” *Computer Physics Communications*, vol. 185, pp. 939–947, 2014.

[131] A. Komrakova, O. Shardt, D. Eskin, and J. Derksen, “Lattice Boltzmann simulations of drop deformation and breakup in shear flow,” *International Journal of Multiphase Flow*, vol. 59, pp. 24–43, 2014.

[132] A. Eshghinejadfard, L. Daróczy, G. Janiga, and D. Thévenin, “Calculation of the permeability in porous media using the lattice Boltzmann method,” *International Journal of Heat and Fluid Flow*, vol. 62, pp. 93–103, 2016.

[133] H. Darcy, *Les fontaines publiques de la ville de Dijon.* 1856.

[134] A. Chapman and J. Higdon, “Oscillatory Stokes flow in periodic porous media,” *Physics of Fluids A*, vol. 4, pp. 2099–2116, 1992.

[135] A. Nabovati and A. Sousa, “Fluid flow simulation in random porous media at pore level using lattice Boltzmann method,” in *New Trends in Fluid Mechanics Research*, pp. 518–521, Springer, 2007.

[136] J. Kozeny, “Über kapillare Leitung des wassers im boden,” *Akad Wiss. Wien*, vol. 136, pp. 271–306, 1927.

[137] P. C. Carman, “Fluid flow through granular beds,” *Transactions-Institution of Chemical Engineers*, vol. 15, pp. 150–166, 1937.

[138] J. Bear, *Dynamics of Fluids in Porous Media.* Courier Corporation, 1972.

[139] R. McGregor, “The effect of rate of flow on rate of dyeing II–The mechanism of fluid flow through textiles and its significance in dyeing,” *Journal of the Society of Dyers and Colourists*, vol. 81, pp. 429–438, 1965.

[140] R. Gore and C. T. Crowe, “Effect of particle size on modulating turbulent intensity,” *International Journal of Multiphase Flow*, vol. 15, pp. 279–285, 1989.

[141] J. Kussin and M. Sommerfeld, “Experimental studies on particle behaviour and turbulence modification in horizontal channel flow with different wall roughness,” *Experiments in Fluids*, vol. 33, pp. 143–159, 2002.

[142] Y. Sato, K. Hishida, and M. Maeda, “Effect of dispersed phase on modification of turbulent flow in a wall jet,” *Journal of Fluids Engineering*, vol. 118, pp. 307–315, 1996.

[143] D. Khalitov and E. Longmire, “Simultaneous two-phase PIV by two-parameter phase discrimination,” *Experiments in Fluids*, vol. 32, pp. 252–268, 2002.

[144] D. Kaftori, G. Hetsroni, and S. Banerjee, “Particle behavior in the turbulent boundary layer. I. motion, deposition, and entrainment,” *Physics of Fluids*, vol. 7, pp. 1095–1106, 1995.

[145] A. D. Paris, *Turbulence attenuation in a particle-laden channel flow.* PhD thesis, Stanford University, 2001.

[146] W. Hwang and J. K. Eaton, “Homogeneous and isotropic turbulence modulation by small heavy (St $\sim$ 50) particles,” *Journal of Fluid Mechanics*, vol. 564, pp. 361–393, 2006.

[147] Y. Suzuki, M. Ikenoya, and N. Kasagi, “Simultaneous measurement of fluid and dispersed phases in a particle-laden turbulent channel flow with the aid of 3-D PTV,” *Experiments in Fluids*, vol. 29, pp. 185–193, 2000.

[148] M. Rashidi, G. Hetsroni, and S. Banerjee, “Particle-turbulence interaction in a boundary layer,” *International Journal of Multiphase Flow*, vol. 16, pp. 935–949, 1990.

[149] Y. Pan and S. Banerjee, “Numerical simulation of particle interactions with wall turbulence,” *Physics of Fluids*, vol. 8, pp. 2733–2755, 1996.

[150] G. Mallouppas and B. van Wachem, “Large eddy simulations of turbulent particle-laden channel flow,” *International Journal of Multiphase Flow*, vol. 54, pp. 65–75, 2013.

[151] Y. Pan and S. Banerjee, “Numerical investigation of the effects of large particles on wall-turbulence,” *Physics of Fluids*, vol. 9, pp. 3786–3807, 1997.

[152] I. Lashgari, F. Picano, and L. Brandt, “Transition and self-sustained turbulence in dilute suspensions of finite-size particles,” *Theoretical and Applied Mechanics Letters*, vol. 5, pp. 121–125, 2015.

[153] T. Kajishima, S. Takiguchi, H. Hamasaki, and Y. Miyake, “Turbulence structure of particle-laden flow in a vertical plane channel due to vortex shedding,” *JSME International Journal Series B Fluids and Thermal Engineering*, vol. 44, pp. 526–535, 2001.

[154] M. Uhlmann, “Interface-resolved direct numerical simulation of vertical particulate channel flow in the turbulent regime,” *Physics of Fluids*, vol. 20, p. 053305, 2008.

[155] X. Shao, T. Wu, and Z. Yu, “Fully resolved numerical simulation of particle-laden turbulent flow in a horizontal channel at a low Reynolds number,” *Journal of Fluid Mechanics*, vol. 693, pp. 319–344, 2012.

[156] F. Picano, W.-P. Breugem, and L. Brandt, “Turbulent channel flow of dense suspensions of neutrally buoyant spheres,” *Journal of Fluid Mechanics*, vol. 764, pp. 463–487, 2015.

[157] W. Fornari, A. Formenti, F. Picano, and L. Brandt, “The effect of particle density in turbulent channel flow laden with finite size particles in semi-dilute conditions,” *Physics of Fluids*, vol. 28, p. 033301, 2016.

[158] A. Abdelsamie, G. Fru, T. Oster, F. Dietzsch, G. Janiga, and D. Thévenin, “Towards direct numerical simulations of low-mach number turbulent reacting and two-phase flows using immersed boundaries,” *Computers & Fluids*, vol. 131, pp. 123–141, 2016.

[159] A. Banari, Y. Mauzole, T. Hara, S. T. Grilli, and C. F. Janßen, “The simulation of turbulent particle-laden channel flow by the lattice Boltzmann method,” *International Journal for Numerical Methods in Fluids*, vol. 79, pp. 491–513, 2015.

[160] L.-P. Wang, C. Peng, Z. Guo, and Z. Yu, “Lattice Boltzmann simulation of particle-laden turbulent channel flow,” *Computers & Fluids*, vol. 124, pp. 226–236, 2016.

[161] A. Eshghinejadfard, A. Abdelsamie, S. A. Hosseini, and D. Thévenin, “Immersed boundary lattice Boltzmann simulation of turbulent channel flows in the presence of spherical particles,” *International Journal of Multiphase Flow*, vol. 96, pp. 161–172, 2017.

[162] J. Kim, P. Moin, and R. Moser, “Turbulence statistics in fully developed channel flow at low Reynolds number,” *Journal of Fluid Mechanics*, vol. 177, pp. 133–166, 1987.

[163] R. D. Moser, J. Kim, and N. N. Mansour, “Direct numerical simulation of turbulent channel flow up to $\mathrm{Re}_\tau = 590$,” *Physics of Fluids*, vol. 11, pp. 943–945, 1999.

[164] A. Vreman and J. Kuerten, “Comparison of direct numerical simulation databases of turbulent channel flow at $\mathrm{Re}_\tau = 180$,” *Physics of Fluids*, vol. 26, p. 015102, 2014.

[165] X. Wang, Y. Shangguan, N. Onodera, H. Kobayashi, and T. Aoki, “Direct numerical simulation and large eddy simulation on a turbulent wall-bounded flow using lattice Boltzmann method and multiple GPUs,” *Mathematical Problems in Engineering*, vol. 2014, pp. 1–10, 2014.

[166] A. Soldati and C. Marchioli, “Physics and modelling of turbulent particle deposition and entrainment: Review of a systematic study,” *International Journal of Multiphase Flow*, vol. 35, pp. 827–839, 2009.

[167] A. G. Kidanemariam, C. Chan-Braun, T. Doychev, and M. Uhlmann, “Direct numerical simulation of horizontal open channel flow with finite-size, heavy particles at low solid volume fraction,” *New Journal of Physics*, vol. 15, p. 025031, 2013.

[168] K. Kiger and C. Pan, “Suspension and turbulence modification effects of solid particulates on a horizontal turbulent channel flow,” *Journal of Turbulence*, vol. 3, pp. 1–17, 2002.

[169] J. Zhou, R. J. Adrian, S. Balachandar, and T. Kendall, “Mechanisms for generating coherent packets of hairpin vortices in channel flow,” *Journal of Fluid Mechanics*, vol. 387, pp. 353–396, 1999.

[170] S. Elghobashi, “An updated classification map of particle-laden turbulent flows,” in *IUTAM Symposium on Computational Approaches to Multiphase Flow*, pp. 3–10, Springer, 2006.

[171] S. Elghobashi, “On predicting particle-laden turbulent flows,” *Applied Scientific Research*, vol. 52, pp. 309–329, 1994.

[172] F. Zhao, W. George, and B. van Wachem, “Four-way coupled simulations of small particles in turbulent channel flow: The effects of particle shape and Stokes number,” *Physics of Fluids*, vol. 27, p. 083301, 2015.

[173] E. Ding and C. K. Aidun, “The dynamics and scaling law for particles suspended in shear flow with inertia,” *Journal of Fluid Mechanics*, vol. 423, pp. 317–344, 2000.

[174] D. Qi and L.-S. Luo, “Rotational and orientational behaviour of three-dimensional spheroidal particles in Couette flows,” *Journal of Fluid Mechanics*, vol. 477, pp. 201–213, 2003.

[175] Z. Yu, N. Phan-Thien, and R. I. Tanner, “Rotation of a spheroid in a Couette flow at moderate Reynolds numbers,” *Physical Review E*, vol. 76, p. 026310, 2007.

[176] H. Huang, X. Yang, M. Krafczyk, and X.-Y. Lu, “Rotation of spheroidal particles in Couette flows,” *Journal of Fluid Mechanics*, vol. 692, pp. 369–394, 2012.

[177] G. B. Jeffery, “The motion of ellipsoidal particles immersed in a viscous fluid,” *Proceedings of the Royal Society of London. Series A, Containing papers of a mathematical and physical character*, pp. 161–179, 1922.

[178] H. Huang, X. Yang, and X. Lu, “Sedimentation of an ellipsoidal particle in narrow tubes,” *Physics of Fluids*, vol. 26, p. 053302, 2014.

[179] F. Lucci, A. Ferrante, and S. Elghobashi, “Modulation of isotropic turbulence by particles of Taylor length-scale size,” *Journal of Fluid Mechanics*, vol. 650, pp. 5–55, 2010.

[180] I. Lashgari, F. Picano, W. P. Breugem, and L. Brandt, “Channel flow of rigid sphere suspensions: Particle dynamics in the inertial regime,” *International Journal of Multiphase Flow*, vol. 78, pp. 12–24, 2016.

[181] F.-G. Fan and G. Ahmadi, “A sublayer model for turbulent deposition of particles in vertical ducts with smooth and rough surfaces,” *Journal of Aerosol Science*, vol. 24, pp. 45–64, 1993.

[182] S. Parsa, E. Calzavarini, F. Toschi, and G. A. Voth, “Rotation rate of rods in turbulent fluid flow,” *Physical Review Letters*, vol. 109, p. 134501, 2012.

[183] M. Shin and D. L. Koch, “Rotational and translational dispersion of fibres in isotropic turbulent flows,” *Journal of Fluid Mechanics*, vol. 540, pp. 143–173, 2005.

[184] H. Zhang, G. Ahmadi, F.-G. Fan, and J. B. McLaughlin, “Ellipsoidal particles transport and deposition in turbulent channel flows,” *International Journal of Multiphase Flow*, vol. 27, pp. 971–1009, 2001.

[185] P. Mortensen, H. Andersson, J. Gillissen, and B. Boersma, “Dynamics of prolate ellipsoidal particles in a turbulent channel flow,” *Physics of Fluids*, vol. 20, p. 093302, 2008.

[186] C. Marchioli, M. Fantoni, and A. Soldati, “Orientation, distribution, and deposition of elongated, inertial fibers in turbulent channel flow,” *Physics of Fluids*, vol. 22, p. 033301, 2010.

[187] H. I. Andersson, L. Zhao, and M. Barri, “Torque-coupling and particle–turbulence interactions,” *Journal of Fluid Mechanics*, vol. 696, pp. 319–329, 2012.

[188] F. Zhao and B. van Wachem, “Direct numerical simulation of ellipsoidal particles in turbulent channel flow,” *Acta Mechanica*, vol. 224, pp. 2331–2358, 2013.

[189] M. Do-Quang, G. Amberg, G. Brethouwer, and A. V. Johansson, “Simulation of finite-size fibers in turbulent channel flows,” *Physical Review E*, vol. 89, p. 013006, 2014.

[190] A. Eshghinejadfard, S. A. Hosseini, and D. Thévenin, “Fully-resolved prolate spheroids in turbulent channel flows: A lattice Boltzmann study,” *AIP Advances*, vol. 7, p. 095007, 2017.

[191] T. Rosén, F. Lundell, and C. Aidun, “Effect of fluid inertia on the dynamics and scaling of neutrally buoyant particles in shear flow,” *Journal of Fluid Mechanics*, vol. 738, pp. 563–590, 2014.

[192] N. R. Challabotla, L. Zhao, and H. I. Andersson, “Orientation and rotation of inertial disk particles in wall turbulence,” *Journal of Fluid Mechanics*, vol. 766, p. R2, 2015.

[193] D. O. Njobuenwu and M. Fairweather, “Simulation of inertial fibre orientation in turbulent flow,” *Physics of Fluids*, vol. 28, p. 063307, 2016.

[194] G. A. Voth and A. Soldati, “Anisotropic particles in turbulence,” *Annual Review of Fluid Mechanics*, vol. 49, pp. 249–276, 2017.

[195] P. Mortensen, H. Andersson, J. Gillissen, and B. Boersma, “On the orientation of ellipsoidal particles in a turbulent shear flow,” *International Journal of Multiphase Flow*, vol. 34, pp. 678–683, 2008.

[196] J. Latt, *Hydrodynamic limit of lattice Boltzmann equations.* PhD thesis, University of Geneva, 2007.

Appendix A

Chapman-Enskog Expansion

Let us consider the SRT-LBM equation governed by

$$f_i(\boldsymbol{x} + \boldsymbol{c}_i \Delta t, t + \Delta t) - f_i(\boldsymbol{x}, t) = -\frac{1}{\tau}\left[f_i(\boldsymbol{x}, t) - f_i^{eq}(\boldsymbol{x}, t)\right], \tag{A.1}$$

with the equilibrium distribution function given by a Maxwellian one in order to recover the Navier-Stokes equation:

$$f_i^{eq} = \omega_i \rho \left[1 + \frac{\boldsymbol{c_i} \cdot \boldsymbol{u}}{c_s^2} + \frac{(\boldsymbol{c_i} \cdot \boldsymbol{u})^2}{2c_s^4} - \frac{|\boldsymbol{u}|^2}{2c_s^2}\right]. \tag{A.2}$$

The left-hand side of Eq. (A.1) can be expanded by a second-order Taylor series as follows:

$$f_i(\boldsymbol{x} + \boldsymbol{c}_i, t + 1) = f_i(\boldsymbol{x}, t) + (\partial_t + \nabla \cdot \boldsymbol{c}_i) f_i + \frac{1}{2}\left(\partial_t^2 + 2\partial_t \nabla \cdot \boldsymbol{c}_i + \nabla\nabla : \boldsymbol{c}_i \boldsymbol{c}_i\right) f_i \tag{A.3}$$

In the next step, the time scale of different physical phenomena should be separated.

$$\partial_t = \epsilon \partial_{t1} + \epsilon^2 \partial_{t2} + \mathcal{O}(\epsilon^3) \tag{A.4}$$

The space derivative is expanded in the same manner:

$$\nabla = \epsilon \nabla_1 + \epsilon^2 \nabla_2 + \mathcal{O}(\epsilon^3) \tag{A.5}$$

The particle distribution functions are also expanded, starting with a zeroth order. It means that the non-equilibrium part of the distribution function is considered as small perturbation from equilibrium state, with the scale of Knudsen number ($\mathcal{O}(\epsilon)$).

$$f_i = f_i^{(0)} + \epsilon f_i^{(1)} + \epsilon^2 f_i^{(2)} + \mathcal{O}(\epsilon^3) \tag{A.6}$$

where $f^{(0)}$ is the equilibrium distribution function. According to Latt [196], the ϵ is the Knudsen number and as a result of truncated multi-scale expansion, the LB equation is only valid for a continuum phase (low Kn numbers). The expansion up to second order satisfies the

Navier-Stokes equation. However, making the expansion up to higher orders can recover the Burnett equation. By replacing Eqs. (A.3)-(A.6) into Eq. (A.1) we would have

$$\begin{aligned}
&\left(\epsilon\partial_{t1}+\epsilon^2\partial_{t2}+\epsilon\nabla_1\cdot\boldsymbol{c}_i+\epsilon^2\nabla_2\cdot\boldsymbol{c}_i\right)\left(f_i^{(0)}+\epsilon f_i^{(1)}+\epsilon^2 f_i^{(2)}\right)\\
&+\frac{1}{2}\left(\epsilon\partial_{t1}+\epsilon^2\partial_{t2}\right)\left(\epsilon\partial_{t1}+\epsilon^2\partial_{t2}\right)\left(f_i^{(0)}+\epsilon f_i^{(1)}+\epsilon^2 f_i^{(2)}\right)\\
&+\frac{1}{2}\left(2\left(\epsilon\partial_{t1}+\epsilon^2\partial_{t2}\right)\left(\epsilon\nabla_1\cdot\boldsymbol{c}_i+\epsilon^2\nabla_2\cdot\boldsymbol{c}_i\right)\right)\left(f_i^{(0)}+\epsilon f_i^{(1)}+\epsilon^2 f_i^{(2)}\right)\\
&+\left(\epsilon\nabla_1\cdot\boldsymbol{c}_i+\epsilon^2\nabla_2\cdot\boldsymbol{c}_i\right)\left(\epsilon\nabla_1\cdot\boldsymbol{c}_i+\epsilon^2\nabla_2\cdot\boldsymbol{c}_i\right)\left(f_i^{(0)}+\epsilon f_i^{(1)}+\epsilon^2 f_i^{(2)}\right)\\
&=-\frac{1}{\tau}\left(\epsilon f_i^{(1)}+\epsilon^2 f_i^{(2)}\right)
\end{aligned} \tag{A.7}$$

Keeping only the terms up to second order and equating the terms with the same power of ϵ leads to the following equation

$$\epsilon\left(\partial_{t1}+\nabla_1\cdot\boldsymbol{c}_i\right)f_i^{(0)}=-\frac{1}{\tau}\epsilon f_i^{(1)} \tag{A.8}$$

Similar approach holds for the terms with ϵ^2 coefficient

$$\epsilon^2\left(\left(\partial_{t1}+\nabla_1\cdot\boldsymbol{c}_i\right)f_i^{(1)}+\left(\partial_{t2}+\nabla_2\cdot\boldsymbol{c}_i\right)f_i^{(0)}+\frac{1}{2}\left(\partial_{t1}^2+2\partial_{t1}\nabla_1\cdot\boldsymbol{c}_i+\nabla_1\nabla_1:\boldsymbol{c}_i\boldsymbol{c}_i\right)f_i^{(0)}\right)=-\frac{\epsilon^2 f_i^{(2)}}{\tau} \tag{A.9}$$

The moments of Eqs. (A.8) and (A.9) now need to be calculated with the following properties based on the selected equilibrium distribution of Eq. (A.2).

$$\sum_i f_i^{(0)}=\rho \tag{A.10}$$

$$\sum_i \boldsymbol{c}_i f_i^{(0)}=\rho\boldsymbol{u} \tag{A.11}$$

$$\sum_i \boldsymbol{c}_i\boldsymbol{c}_i f_i^{(0)}=\boldsymbol{\Pi}^{(0)}+\rho c_s^2\mathbf{I} \tag{A.12}$$

$$\sum_i f_i^{(m)}=0 \qquad for\ m\neq 0 \tag{A.13}$$

$$\sum_i \boldsymbol{c}_i f_i^{(m)}=0 \qquad for\ m\neq 0 \tag{A.14}$$

Mass conservation: Now computing the zeroth moment of Eq. (A.8):

$$\partial_{t1}\sum_i f_i^{(0)}+\nabla_1\cdot\sum_i \boldsymbol{c}_i f_i^{(0)}=-\frac{1}{\tau}\sum_i f_i^{(1)} \tag{A.15}$$

$$\Rightarrow \boxed{\partial_{t1}\rho+\nabla_1\cdot(\rho\boldsymbol{u})=0} \tag{A.16}$$

Then we compute the zeroth moment of Eq. (A.9). To do so, it should be noted that the zeroth moment of the third parenthesis on the LHS of Eq. (A.9) is equal to zero because

$$\left(\partial_t^2 + 2\partial_t \nabla \cdot \boldsymbol{c}_i + \nabla\nabla : \boldsymbol{c}_i\boldsymbol{c}_i\right) \sum_i f_i^{(0)} = \left(\partial_{t1} + \nabla_1 \cdot \boldsymbol{c}_i\right)\left(\partial_{t1} + \nabla_1 \cdot \boldsymbol{c}_i\right) \sum_i f_i^{(0)}$$
$$\xRightarrow{A.15} \left(\partial_t^2 + 2\partial_t \nabla \cdot \boldsymbol{c}_i + \nabla\nabla : \boldsymbol{c}_i\boldsymbol{c}_i\right) \sum_i f_i^{(0)} = -\frac{1}{\tau}\left(\partial_{t1} + \nabla_1 \cdot \boldsymbol{c}_i\right) \sum_i f_i^{(1)} \overset{A.13}{=} 0 \tag{A.17}$$

Then we have

$$\partial_{t1} \sum_i f_i^{(1)} + \nabla_1 \cdot \sum_i \boldsymbol{c}_i f_i^{(1)} + \partial_{t2} \sum_i f_i^{(0)} + \nabla_2 \cdot \sum_i \boldsymbol{c}_i f_i^{(0)} + 0 = -\frac{1}{\tau} \sum_i f_i^{(2)} \tag{A.18}$$

The first two terms on the LHS of above equation and the RHS are zero (see Eqs. (A.13), (A.14)). Based on this, above equation can be simplified as

$$\boxed{\partial_{t2}\rho + \nabla_2 \cdot (\rho \boldsymbol{u}) = 0} \tag{A.19}$$

In the final step, Eqs. (A.16) and (A.19) are multiplied by ϵ and ϵ^2, respectively, and are summed up to recover the continuity equation:

$$\boxed{\partial_t \rho + \nabla \cdot (\rho \boldsymbol{u}) = 0} \tag{A.20}$$

Momentum conservation: In order to recover the Navier-Stokes equation, the first-order moments are required. The first-order moment of Eq. (A.8) is calculated as:

$$\partial_{t1} \sum_i \boldsymbol{c}_i f_i^{(0)} + \nabla_1 \cdot \sum_i \boldsymbol{c}_i \boldsymbol{c}_i f_i^{(0)} = -\frac{1}{\tau} \sum_i \boldsymbol{c}_i f_i^{(1)} = 0 \tag{A.21}$$
$$\Rightarrow \partial_{t1}(\rho \boldsymbol{u}) + \nabla_1 \cdot \sum_i \boldsymbol{c}_i \boldsymbol{c}_i f_i^{(0)} = 0 \tag{A.22}$$
$$\Rightarrow \boxed{\partial_{t1}(\rho \boldsymbol{u}) + \nabla_1 \cdot \left(\boldsymbol{\Pi}^{(0)} + \rho c_s^2 \mathbf{I}\right) = 0} \tag{A.23}$$

Equation (A.23) is the well-known Euler equation. The first-order moment of Eq. (A.9) is calculated as well:

$$\begin{aligned} &\left(\partial_{t1} + \nabla_1 \cdot \boldsymbol{c}_i\right) \sum_i \boldsymbol{c}_i f_i^{(1)} + \left(\partial_{t2} + \nabla_2 \cdot \boldsymbol{c}_i\right) \sum_i \boldsymbol{c}_i f_i^{(0)} \\ &+ \frac{1}{2}\left(\partial_{t1}^2 + 2\partial_{t1}\nabla_1 \cdot \boldsymbol{c}_i + \nabla_1\nabla_1 : \boldsymbol{c}_i\boldsymbol{c}_i\right) \sum_i \boldsymbol{c}_i f_i^{(0)} = -\frac{1}{\tau} \sum_i \boldsymbol{c}_i f_i^{(2)} \end{aligned} \tag{A.24}$$

Similar to what was observed before and by using Eqs. (A.8) and (A.14) the third parenthesis of the LHS is calculated

$$\begin{aligned}\frac{1}{2}\left(\partial_{t1}^2 + 2\partial_{t1}\nabla_1\cdot\boldsymbol{c}_i + \nabla_1\nabla_1 : \boldsymbol{c}_i\boldsymbol{c}_i\right)\sum_i \boldsymbol{c}_i f_i^{(0)} &= \frac{1}{2}\left(\partial_{t1} + \nabla_1\cdot\boldsymbol{c}_i\right)\left(\partial_{t1} + \nabla_1\cdot\boldsymbol{c}_i\right)\sum_i \boldsymbol{c}_i f_i^{(0)} \\ &= \frac{-1}{2\tau}\left(\partial_{t1} + \nabla_1\cdot\boldsymbol{c}_i\right)\sum_i \boldsymbol{c}_i f_i^{(1)} = 0 - \frac{1}{2\tau}\nabla_1\cdot\sum_i \boldsymbol{c}_i\boldsymbol{c}_i f_i^{(1)} \qquad \text{(A.25)}\end{aligned}$$

Therefore,

$$\partial_{t1}\sum_i \boldsymbol{c}_i f_i^{(1)} + \nabla_1\cdot\sum_i \boldsymbol{c}_i\boldsymbol{c}_i f_i^{(1)} + \partial_{t2}\sum_i \boldsymbol{c}_i f_i^{(0)} + \nabla_2\cdot\sum_i \boldsymbol{c}_i\boldsymbol{c}_i f_i^{(0)} - \frac{1}{2\tau}\nabla_1\cdot\sum_i \boldsymbol{c}_i\boldsymbol{c}_i f_i^{(1)} = 0 \qquad \text{(A.26)}$$

Above equation is further simplified as:

$$0 + \left(1 - \frac{1}{2\tau}\right)\nabla_1\cdot\sum_i \boldsymbol{c}_i\boldsymbol{c}_i f_i^{(1)} + \partial_{t2}(\rho\boldsymbol{u}) + \nabla_2\cdot\left(\boldsymbol{\Pi}^{(0)} + \rho c_s^2\mathbf{I}\right) = 0 \qquad \text{(A.27)}$$

The second-order moment of $f_i^{(1)}$ in Eq. (A.27) is calculated from the second-order moment of Eq. (A.8):

$$\partial_{t1}\sum_i \boldsymbol{c}_i\boldsymbol{c}_i f_i^{(0)} + \nabla_1\cdot\sum_i \boldsymbol{c}_i\boldsymbol{c}_i\boldsymbol{c}_i f_i^{(0)} = -\frac{1}{\tau}\sum_i \boldsymbol{c}_i\boldsymbol{c}_i f_i^{(1)} \qquad \text{(A.28)}$$

$$\Rightarrow \partial_{t1}(\boldsymbol{\Pi}^{(0)} + \rho c_s^2\mathbf{I}) + \nabla_1\cdot\sum_i \boldsymbol{c}_i\boldsymbol{c}_i\boldsymbol{c}_i f_i^{(0)} = -\frac{1}{\tau}\sum_i \boldsymbol{c}_i\boldsymbol{c}_i f_i^{(1)} \qquad \text{(A.29)}$$

Based on the Eq. (A.16):

$$\partial_{t1}\rho = -\nabla_1\cdot(\rho\boldsymbol{u}) \qquad \text{(A.30)}$$

By replacing Eq. (A.30) in Eq. (A.29):

$$\sum_i \boldsymbol{c}_i\boldsymbol{c}_i f_i^{(1)} = -\tau\left(\partial_{t1}\boldsymbol{\Pi}^{(0)} - \nabla_1\cdot(\rho\boldsymbol{u})c_s^2\mathbf{I} + \nabla_1\cdot\sum_i \boldsymbol{c}_i\boldsymbol{c}_i\boldsymbol{c}_i f_i^{(0)}\right) \qquad \text{(A.31)}$$

Now, the term with time derivative in Eq. (A.31) can be converted to a space derivative by:

$$\begin{aligned}\partial_{t1}\boldsymbol{\Pi}^{(0)} &= \partial_t\rho u_i u_j = u_i\partial_t\rho u_j + u_j\partial_t\rho u_i - u_i u_j\partial_t\rho \\ &\overset{A.23}{=} -u_i\frac{\partial}{\partial x_k}\left(\rho c_s^2\delta_{jk} + \rho u_j u_k\right) - u_j\frac{\partial}{\partial x_k}\left(\rho c_s^2\delta_{ik} + \rho u_i u_k\right) + u_i u_j\frac{\partial(\rho u_k)}{x_k} \\ &= -u_i c_s^2\frac{\partial\rho}{\partial x_j} - u_j c_s^2\frac{\partial\rho}{\partial x_i} - u_i\frac{(\rho u_j u_k)}{x_k} - u_j\frac{(\rho u_i u_k)}{x_k} + u_i u_j\frac{\partial(\rho u_k)}{x_k} \qquad \text{(A.32)} \\ &= -u_i c_s^2\frac{\partial\rho}{\partial x_j} - u_j c_s^2\frac{\partial\rho}{\partial x_i} - \frac{(\rho u_i u_j u_k)}{\partial x_k},\end{aligned}$$

and for the last term on the RHS of Eq. (A.31)

$$\begin{aligned}
&\nabla_1 \cdot \sum_i \boldsymbol{c}_i \boldsymbol{c}_i \boldsymbol{c}_i f_i^{(0)} = \frac{\partial}{\partial x_k} \sum_\alpha c_i c_j c_k f_\alpha^{(0)} = \frac{\partial}{\partial x_k} \left[\rho c_s^2 \left(\delta_{ij} u_k + \delta_{ik} u_j + \delta_{jk} u_i \right) \right] \\
&= c_s^2 \delta_{ij} \frac{\partial (\rho u_k)}{\partial x_k} + u_j c_s^2 \frac{\partial \rho}{\partial x_i} + c_s^2 \rho \frac{\partial u_j}{\partial x_i} + u_i c_s^2 \frac{\partial \rho}{\partial x_j} + c_s^2 \rho \frac{\partial u_i}{\partial x_j}.
\end{aligned} \tag{A.33}$$

Substituting Eqs. (A.33) and (A.32) into Eq. (A.31), we get:

$$\sum c_i c_j f_i^{(1)} = -\tau \left[\rho c_s^2 \left(\frac{\partial u_j}{\partial x_i} + \frac{\partial u_i}{\partial x_j} \right) - \frac{\partial}{\partial x_k} (\rho u_i u_j u_k) \right]. \tag{A.34}$$

and then replacing Eq. (A.34) in Eq. (A.27) and combining the resulting equation with Eq. (A.23) we have:

$$\partial_t (\rho \boldsymbol{u}) + \nabla \cdot \left(\boldsymbol{\Pi}^{(0)} + \rho c_s^2 \mathbf{I} \right) = \left(1 - \frac{1}{2\tau} \right) \tau c_s^2 \nabla \cdot \left(\rho \nabla \boldsymbol{u} + \rho \nabla \boldsymbol{u}^{\mathrm{T}} \right) + \mathcal{O}(\mathrm{Ma}^2) \tag{A.35}$$

We rearrange the equation in the final form:

$$\partial_t (\rho \boldsymbol{u}) + \nabla \cdot (\rho \boldsymbol{u} \boldsymbol{u}) = -\boldsymbol{\nabla} \cdot (\rho c_s^2 \mathbf{I}) + \left(1 - \frac{1}{2\tau} \right) \tau c_s^2 \nabla \cdot \left(\rho \nabla \boldsymbol{u} + \rho \nabla \boldsymbol{u}^{\mathrm{T}} \right) + \mathcal{O}(\mathrm{Ma}^2) \tag{A.36}$$

Above equation is similar to Navier-Stokes equation if density variations are small and if we choose

$$\nu = (\tau - 0.5) c_s^2 \Delta t \tag{A.37}$$

List of Relevant Publications & Talks

[1] **A. Eshghinejadfard**, S. A. Hosseini, and D. Thévenin, “Fully-resolved prolate spheroids in turbulent channel flows: A lattice Boltzmann study,” *AIP Advances*, vol. 7, p. 095007, 2017.

[2] **A. Eshghinejadfard**, A. Abdelsamie, S. A. Hosseini, and D. Thévenin, “Immersed boundary lattice Boltzmann simulation of turbulent channel flows in the presence of spherical particles,” *International Journal of Multiphase Flow*, vol. 96, pp. 161-172, 2017.

[3] S. A. Hosseini, **A. Eshghinejadfard**, N. Darabiha, and D. Thévenin, “Weakly compressible Lattice Boltzmann simulations of reacting flows with detailed thermo-chemical models,” *Computers and Mathematics with Applications*, in press.

[4] **A. Eshghinejadfard**, K. Sharma, and D. Thévenin, “Effect of polymer and fiber additives on pressure drop in a rectangular channel,” *Journal of Hydrodynamics*, vol. 29, pp. 871-878, 2017.

[5] **A. Eshghinejadfard**, A. Abdelsamie, G. Janiga, and D. Thévenin, “Direct-forcing immersed boundary lattice Boltzmann simulation of particle/fluid interactions for spherical and non-spherical particles,” *Particuology*, vol. 25, pp. 93-103, 2016.

[6] **A. Eshghinejadfard** and D. Thévenin, “Numerical simulation of heat transfer in particulate flows using a thermal immersed boundary lattice Boltzmann method,” *International Journal of Heat and Fluid Flow*, vol. 60, pp. 31-46, 2016.

[7] **A. Eshghinejadfard**, L. Daróczy, G. Janiga, and D. Thévenin, “Calculation of the permeability in porous media using the lattice Boltzmann method,” *International Journal of Heat and Fluid Flow*, vol. 62, pp. 93-103, 2016.

[8] A. Abdelsamie, **A. Eshghinejadfard**, T. Oster, and D. Thévenin, “Impact of the collision model for fully resolved particles interacting in a fluid,” In *Proceedings of ASME 2014 Fluids Engineering Division Summer Meeting*, Chicago, Illinois, 2014.

[9] **A. Eshghinejadfard**, G. Janiga, and D. Thévenin. “Calculation of the permeability in porous media using the Lattice Boltzmann method,” In: *Conference on Modelling Fluid Flow*, Budapest, Hungary, 052/1-7, 2015.

[10] **A. Eshghinejadfard**, A. Abdelsamie, and D. Thévenin. “Lattice Boltzmann simulation of turbulent channel flows in the presence of spherical particles,” In *13th International Conference for Mesoscopic Methods in Engineering and Science*, ICMMES, Hamburg, Germany, 2016.

[11] S. A. Hosseini, **A. Eshghinejadfard**, D. Thévenin, and N. Darabiha, “Lattice Boltzmann simulation of multi-species reactive flows,” In *13th International Conference for Mesoscopic Methods in Engineering and Science*, ICMMES, Hamburg, Germany, 2016.

[12] **A. Eshghinejadfard**, and D. Thévenin, “Modeling the sedimentation behavior of single and multiple spheroidal particles using lattice Boltzmann method,” In *24th International Conference on Discrete Simulation of Fluid Dynamics (DSFD)*, Edinburgh, UK, 2015.

[13] **A. Eshghinejadfard**, and D. Thévenin, “Immersed boundary lattice Boltzmann modeling of particulate flows using different discrete delta functions and force schemes,” In *23rd International Conference on Discrete Simulation of Fluid Dynamics (DSFD)*, Paris, France, 2014.